

Understanding the [Fe-Fe]-Hydrogenase H-Cluster: Insights From Chemical Modelling and Advanced Spectroscopy

A thesis submitted to the University of East Anglia

For the degree of Doctor of Philosophy

Submitted June 2014

Aušra Jablonskytė

Energy Materials Laboratory

School of Chemistry, UEA

Norwich

This copy of the thesis has been supplied on condition that anyone who consults it is understood to recognise that its copyright rests with the author and that use of any information derived therefrom must be in accordance with current UK Copyright Law. In addition, any quotation or extract must include full attribution. ©

Abstract

Hydrogenase enzymes are nature's catalysts for hydrogen production and uptake. Understanding how they work may lead to new materials as alternatives for precious metals currently used in H₂-utilizing fuel and producer cells. Work described in this thesis focuses on synthetic mimics of the active site of [Fe–Fe]-hydrogenases and explores their reactivity towards protons and electrons.

Chapter 1 gives a brief overview of the chemistry taking place in hydrogenase enzymes with a particular focus on the [Fe–Fe]-hydrogenase. The evolution of synthetic models mimicking the structure and function of the enzyme from the late 1990s to the current state of the art is discussed.

Chapter 2 describes synthesis of the first {2Fe3S} hydride together with new active site mimics in which bulky substituents are incorporated into the dithiolate bridgehead. A comprehensive examination of their structural features and spectroscopic properties is provided.

Chapter 3 reports extensive stopped-flow UV-vis, IR and electrochemical studies for a range of subsite models exploring the relationship between the structure and the reactivity towards protons. It is shown that there is a direct linear free energy relationship between the activation energy for protonation and the energy level of the HOMO.

Chapter 4 describes the first characterisation of paramagnetic (mixed-valence) Fe(I)(μ-H)-Fe(II) species which is implicated in metallo-sulfur enzymes as an intermediate in electrocatalytic H₂ evolution. An unprecedented *super-reduced* state is detected and characterised using a custom-built spectroelectrochemical cell.

Chapter 5 shows how muon spectroscopy may provide a new approach for exploring metallo-hydride chemistry. Future avenues of research in the field of [Fe–Fe] chemistry arising from the work described in this thesis are also briefly discussed.

Acknowledgements

This PhD thesis did not come into this world without the guidance of many talented and supportive people. I owe my deepest gratitude to Professor Christopher Pickett, who has been inspiring me to do science since I was a meagre undergraduate. I am thankful for many opportunities given.

My heartfelt thanks goes out to Dr. Joseph A. Wright for unwavering help, a mountain of knowledge and a weekly nourishment of delicious cakes. Thank you for putting time and energy in teaching me LaTeX. It was a major tool in helping this thesis look amazing and becoming the best it can be.

My love and gratitude to my amazing fellow PhD students Amanda and Mark. You have been an unfailing source of laughter and joy on rainy days. Thanks to an outstanding friend Ira, who trekked miles in summer and winter just to have a lunch and a chat together. You brightened up my days. I owe you each a drink. Or twelve.

An additional huge thank you goes out to all the current and former members of the EML, for your encouragement and friendship.

Thank you Mom and Dad for showing me that the best way to get through life is with hard work and curiosity. The words I write would not be half as bright without all of you in my life.

And lastly, my sincerest thanks to Lee. This thesis would have never been written without your patience, love and unfailing encouragement. Thank you for being not just a part of my life, but the very best part. I love you. x

I demand a trial by combat.

– Tyrion Lannister

Contents

1 Biomimetic Catalysts for H₂ Generation: From Natural to Synthetic [Fe–Fe] Systems	1
1.1 Hydrogen as Alternative Fuel	1
1.2 Biological Role and Structure of Hydrogenases	2
1.3 [Fe–Fe]-Hydrogenase Active Site and Catalytic Mechanism	6
1.4 From Iron-Sulfur Carbonyls to Sophisticated Models of the H-cluster . .	13
1.4.1 Early Synthetic {2Fe2S} Complexes	13
1.4.2 Later Synthetic {2Fe2S} Complexes	17
1.4.3 Rotated State and Mixed-Valence Systems	19
1.4.4 {2Fe3S} Assemblies	24
1.4.5 Hydrides and Their Formation	25
1.4.6 Complete H-Cluster Mimicking Assemblies	32
1.5 Catalysts for Biomimetic Hydrogen Evolution and Uptake	34
1.5.1 Proton Reduction	34
1.5.2 Hydrogen Oxidation	40
1.6 Outstanding Challenges and Ongoing Research Directions	44
1.6.1 Objectives of the Project	45
2 New {2Fe2S} and {2Fe3S} Systems: Synthesis, Structure and Spectroscopic Properties	47
2.1 General Pathways to Synthetic [Fe–Fe]-Systems	47
2.2 Routes to New Dithiolate Ligands	49

2.3	Synthesis of Functionalised {2Fe2S} and {2Fe3S} Subsite Analogues	54
2.3.1	General Aspects	54
2.3.2	{2Fe2S} Frameworks	54
2.3.3	{2Fe3S} Frameworks	58
2.4	Synthesis of Hydride Complexes	61
2.4.1	General Aspects	61
2.4.2	{2Fe2S} and {2Fe3S} Hydrides	61
2.5	Comparative Structural Data and Spectroscopic Properties	64
2.6	Experimental	72
3	Protonation Studies of Diiron Dithiolate Assemblies: Effect of the Bridge Structure on the Rates and Mechanism	85
3.1	Early Protonation Studies of [Fe–Fe]-Hydrogenase Models	85
3.2	Relationship Between the Structure and Protonation Rates of Diiron Complexes	88
3.2.1	General Aspects of Kinetic Analysis	88
3.2.2	Stopped-Flow UV	91
3.2.3	Stopped-Flow FT-IR	98
3.2.4	Electrochemical Studies	103
3.3	Analysis: Electronic Influence	113
3.3.1	Inductive Effects	113
3.3.2	HOMO Energy Levels	116
3.4	Analysis: Steric Effects	118
3.4.1	Transient Species and Intermediates	118
3.4.2	Further Mechanistic Considerations	120
3.5	Summary	122
3.6	Experimental	123
4	(Super)Reduced Hydride States at {2Fe2S} and {2Fe3S} Cores	128
4.1	Hydrides at Metallo-Sulfur Centres	128

4.2	Mixed-Valence Fe(I)–Fe(II) Hydrides	129
4.2.1	CV Measurements	129
4.2.2	EPR Experiments	132
4.2.3	FT-IR Spectroelectrochemistry (SEC)	135
4.2.4	DFT Computational Simulations	143
4.3	Evidence for Super-Reduced Hydride States	152
4.3.1	SEC Measurements	152
4.3.2	Stopped-Flow IR Spectroscopy and DFT Simulations	156
4.3.3	Attempted (Electro)Chemical Synthesis of the <i>Super-Reduced</i> State	158
4.3.4	Related Studies	160
4.4	Summary	162
4.5	Experimental	163
5	Exploratory Studies and Future Directions	166
5.1	Probing the [Fe–Fe]-Hydrogenase Subsite Using Muon Spectroscopy . .	166
5.2	Future Avenues	169

Chapter 1

Biomimetic Catalysts for H₂ Generation: From Natural to Synthetic [Fe-Fe] Systems

1.1 Hydrogen as Alternative Fuel

Developing new ways to power the modern world is one of the most urgent and challenging issues our society is facing today. The widespread use of oil, gas and coal is causing serious ecological and environmental damage through the emission of greenhouse gases such as CO₂.¹ As of 2008 as much as 85 % of the world's energy needs were met by burning fossil fuels, this is despite their unreplenished and finite stock.² Even though supply predictions vary considerably,³⁻⁵ it is undoubtedly important that we eventually have the technologies to harness energy from alternative sources.

To mitigate pollution and climate change, a great deal of effort has been put into exploiting clean, sustainable, renewable energy such as solar, wind, hydroelectric or biomass.⁶ However, the output from these alternative power supplies in most cases is variable and comes in the form of electricity, which is difficult to store and transport.

Molecular fuels such as hydrocarbons and hydrogen are the most attractive solution to this problem owing to the high energy density that can be stored in their chemical bonds.⁷ Nature has been using sunlight to generate these solar fuels for over a billion years. With the amount of sunlight that falls on Earth far exceeding the global energy requirement, it

is an ideal and practically inexhaustible power source.⁸ Harnessed sunlight paired with an appropriate water oxidation or proton reduction catalyst can yield a viable practical solution for the generation of 'solar fuels'.

Hydrogen is a particularly good candidate as a solar fuel since it has the largest energy density by mass and is also clean and carbon free, the only by-product of its combustion being water.⁷ It has attractive characteristics such as potential storage as liquid, gas or solid, easy transportation over long distances and relatively high efficiency in conversion to electricity. It can also be produced in a sustainable way from renewable energy sources such as sunlight:⁹ this would be attractive if the very high price of fuel cells was not the major drawback. The most efficient hydrogen fuel cells (HFCs) use platinum as a catalyst, which is steadily increasing in price and is very limited in supply.¹⁰ As a result, many researchers have shifted their attention to nature for inspiration.

Nature exhibits exquisite examples of catalysts in the form of metalloenzymes known as hydrogenases. These utilise earth-abundant metals such as nickel and iron to reversibly interconvert protons to dihydrogen (Eq. 1). They do so at low overpotentials, displaying high efficiencies and activities with turnover frequencies of up to 21,000 s⁻¹ measured in the most active cases.¹¹



The remaining issues that prevent the widespread use of these complex macromolecules include the low density of their metal active sites compared to their overall size, long-term instability and low tolerance to oxygen.¹² However, none of these challenges should be viewed as unsurmountable. Understanding the fascinating chemistry of hydrogenases can lead to exciting possibilities in the sustainable energy technologies which will undoubtedly play an important role in enhancing 'Life after Oil'.¹³

1.2 Biological Role and Structure of Hydrogenases

Many microbial communities have developed enzymatic pathways to manipulate hydrogen. It is either used as an energy source in anaerobic environments, providing

the organism with the reducing power for carbon fixation, or produced as a result of recycling reduced electron carriers that accumulate during fermentation or photosynthesis.¹⁴ In nature, interconversion of protons and H₂ is catalysed by metalloenzymes called hydrogenases; based on their metal content they fall into three distinct classes: [Fe]-, [Fe-Fe]-, and [Ni-Fe]-hydrogenases.

The [Fe]-hydrogenase, formally known as H₂-forming methylene-tetrahydromethanopterin dehydrogenase (Hmd), was long thought to be metal-free due to its redox-inactivity and EPR (electron paramagnetic resonance) silence.¹⁵ The enzyme is also often referred to as iron-sulfur cluster-free hydrogenase to highlight an important structural difference from the [Fe-Fe]- and [Ni-Fe]-hydrogenases. Hmd catalyses reversible hydride transfer from dihydrogen to methenyltetrahydromethanopterin using a unique iron-containing cofactor (Figure 1).¹⁶ It is an intermediate step in the reduction of carbon dioxide to methane by methanogens, which grow under nickel-deficient conditions.

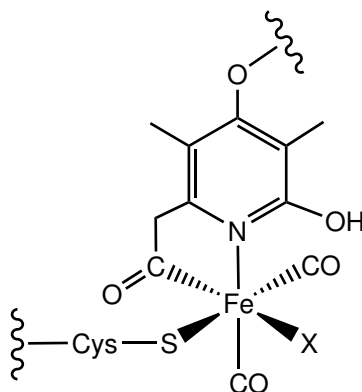


Figure 1: Active site of [Fe]-hydrogenase, X is currently modelled as H₂O in the crystal structure¹⁷

Whilst both the [Ni-Fe]- and the [Fe-Fe]-hydrogenases catalyse reversible oxidation of molecular hydrogen to protons and electrons, their primary functions are distinct. The physiological role of [Ni-Fe]-hydrogenases generally involves uptake of H₂ and they also appear to be less sensitive to inhibition by oxygen and carbon monoxide.¹⁸ The [Fe-Fe]-hydrogenases display the highest turnover frequencies for H₂ production

and are more susceptible to CO and O₂ poisoning.¹⁹ Another difference between the two enzymes is their activities, which are 10 to 100 times higher for [Fe–Fe]- than for [Ni–Fe]-hydrogenases for both proton reduction and hydrogen oxidation.²⁰

Although the two hydrogenases are phylogenetically unrelated, they share unifying features at their catalytic centres that are not observed elsewhere in biology. The active sites of both [Ni–Fe]- and [Fe–Fe]-hydrogenases harbour two metal centres buried deep within the protein, connected together through thiolate bridges (Figure 2). In the former the thiolates are provided by cysteines, while the latter utilises a small organic 2-azapropanedithiolate ligand, which provides a local base for proton binding in the vicinity of the active site. The low redox states of the metal ions are stabilised by coordinating π -acceptor ligands CO and CN⁻. This arrangement is intriguing from both the biological and the chemical perspective: carbon monoxide and cyanide are highly unusual as endogenous ligands in biology due to their toxicity, and the metals cycle through oxidation states that are uncommon in coordination chemistry.

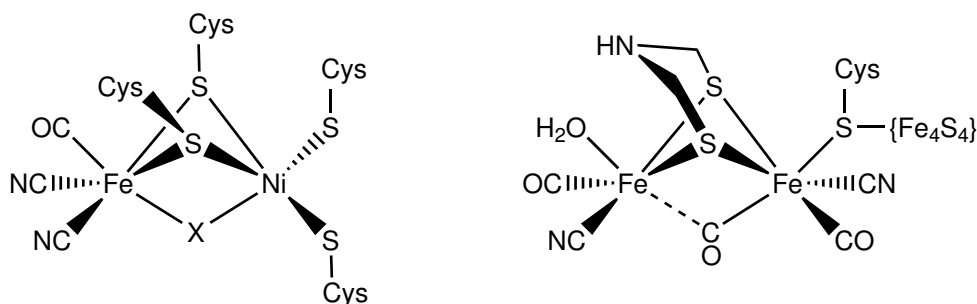


Figure 2: Left: Active site of [Ni–Fe]-hydrogenase ($X = \text{HOO}^-$, HO^- or H^- depending on the state);²¹ Right: Active site of [Fe–Fe]-hydrogenase²²

The protein environment provides more than just a protective scaffold for the oxygen- and carbon monoxide-sensitive catalytic centres. It stabilises the active sites in the optimum geometrical arrangement as they cycle through the catalytically active states. It accommodates a special relay system comprised of {4Fe4S} clusters which aid in fast electron transfer between the buried catalytic centres and the surface of the protein (Figure 3). Analysis of crystal structures also reveal networks of hydrophobic channels

that form pathways all the way to the metal centres for small gas molecules to tunnel in and out of the active sites (Figure 4).^{23,24} For the [Fe–Fe]-hydrogenase these can facilitate diffusion of H₂ produced or consumed at the {2Fe2S} centre, CO which results in reversible inhibition²⁵ or O₂ which leads to irreversible cluster destruction.²⁶

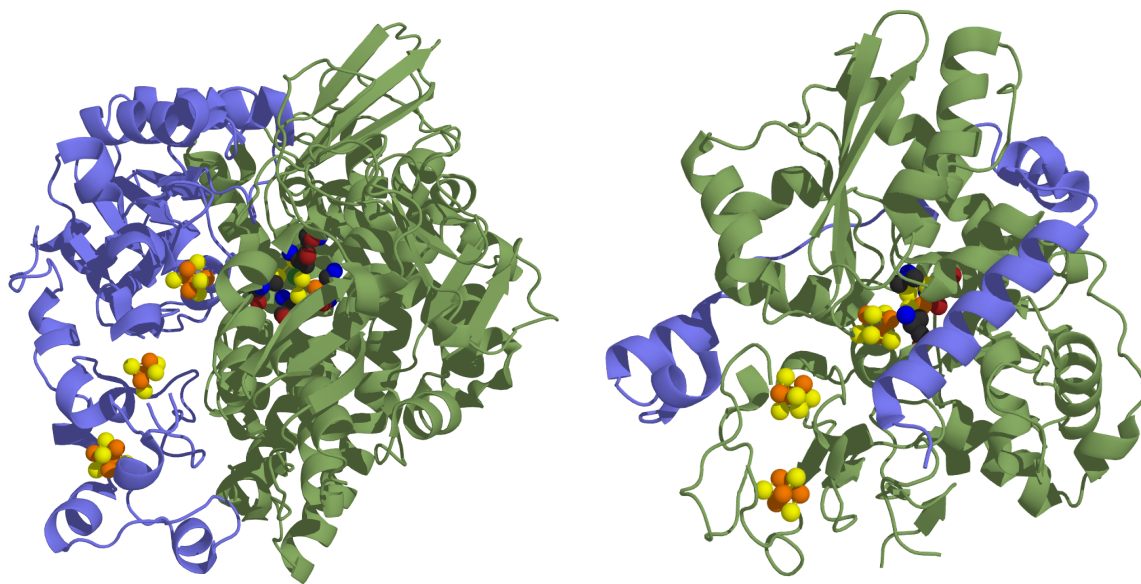


Figure 3: X-Ray structures of *Desulfovibrio gigas* [Ni–Fe]-hydrogenase (PDB code: 1YRQ)²⁷ (left) and *Desulfovibrio desulfuricans* [Fe–Fe]-hydrogenase (PDB code: 1HFE)²³ (right); some residues have been omitted for clarity

Although hydrogenases constitute exceptional catalysts for hydrogen generation and uptake, their delicate handling, challenging purification and sensitivity to oxygen severely hinder their studies and potential use as electrocatalysts. In the attempts to overcome these problems, research has been focused on engineering enzymes with increased tolerance to O₂ by selective mutations²⁹ or discovering new air-compatible hydrogenases.³⁰ Even though the latter tend to display lower turnover frequencies for H₂, all are mostly insensitive to gases that poison platinum catalysts such as CO. However difficult their production is, the recent advances in the field and their extraordinary potential grounds hydrogenases as one of the most attractive catalysts in future hydrogen fuel cell technologies.

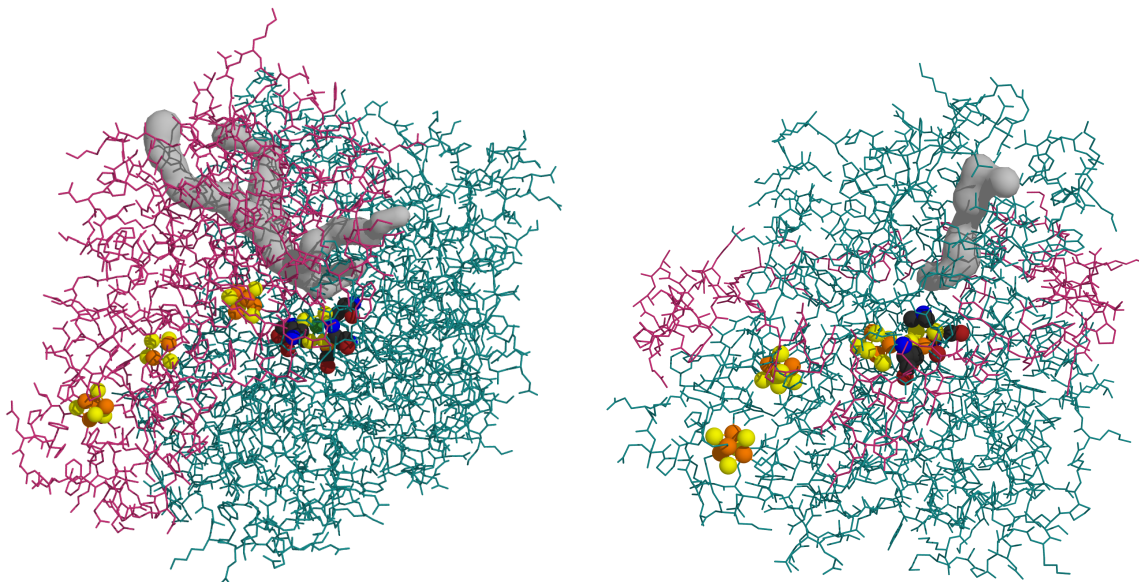


Figure 4: Structure of [Ni–Fe]-hydrogenase from *Desulfovibrio gigas* (PDB code: 1YRQ)²⁷ (left) and [Fe–Fe]-hydrogenase from *Desulfovibrio desulfuricans* (PDB code: 1HFE)²³ (right); gas channels modelled using MOLE 2.0 are depicted in grey²⁸

1.3 [Fe–Fe]-Hydrogenase Active Site and Catalytic Mechanism

While hydrogenases were first discovered in 1931 in colon bacteria,³¹ examples have now been identified in all kingdoms of life. It was not until the late 1990s that X-ray crystal structures of the enzymes became available. To date, the crystallographic characterisations of the [Fe–Fe]-hydrogenase assembly have only been reported for three organisms. The first came from anaerobic soil bacterium *Clostridium pasteurianum* (CpI)²² in 1998, whilst the second was published a year later from sulfate-reducing bacterium *Desulfovibrio desulfuricans* (DdH).²³ The most recent addition to the structural library of [Fe–Fe]-hydrogenases came from the green algae *Chlamydomonas reinhardtii* (Cr) in 2010, however, it has been expressed as apoenzyme lacking the active catalytic site, thus rendering it not pertinent to the work discussed here.³²

Whilst the crystallographic determination of the first two enzyme systems came from

two unrelated microorganisms, their structures appear to show considerable homology. The active sites of both CpI and DdH reveal the unique six Fe atom structure also known as the H-cluster, at which catalysis takes place (Figure 5). The two resolved structures, H_{ox} and H_{ref} (*vide infra*), differ only in the presence of the terminally coordinating solvent molecule and the bridging mode of the carbon monoxide ligand.

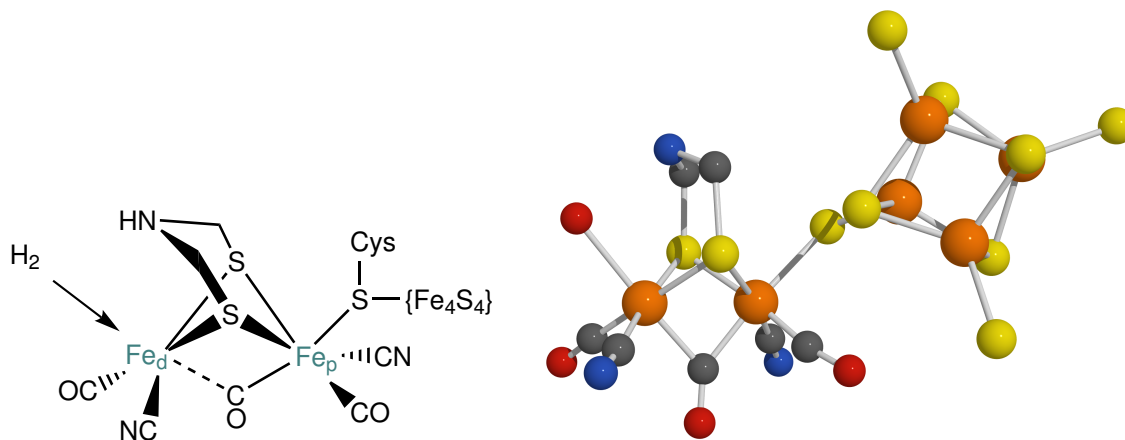


Figure 5: Schematic representation and the X-ray structure of the active site of [Fe-Fe]-hydrogenase from *Clostridium pasteurianum* (PDB code: 3C8Y);²² the bridgehead atom is represented here as nitrogen on the basis of current consensus: in the original report it was modelled as oxygen; the vacant site was occupied by a water molecule

The H-cluster consists of a {4Fe4S} electron transfer unit connected *via* a single bridging cysteine thiol to a binuclear {2Fe2S} subsite. The {2Fe2S} site contains a ‘distal’ iron atom (Fe_d) and a ‘proximal’ iron (Fe_p). The Fe_d centre is positioned farthest from the cubane, possesses a ‘rotated state’ geometry and is coordinated by a labile water molecule in the resting state of the enzyme, whilst the Fe_p is ligated by cysteinyl sulfur, connecting the metal to the electron transfer unit. Both the iron atoms are coordinated by CO and CN^- ligands as well as a bridging carbonyl, keeping the metal centres in low oxidation and spin states. Thus, in its resting state the subsite is mixed-valence Fe(I)–Fe(II) with a spin $S = 1/2$. The ‘butterfly’ diiron dithiolate arrangement accommodates two sulfur atoms

which comprise the azadithiolate bridge. It positions itself perfectly above the vacant coordination site and acts as a shuttle for protons transferring to and from the catalytic centre.

The coordination sphere around each iron atom in the active site of the [Fe–Fe]-hydrogenase enzyme is best defined as square pyramidal (Figure 6). The base of the square pyramid at the proximal iron is made up of two thiolates, a CO and a CN[−]: these can be referred to as the ‘basal’ ligands. The top (‘apical’) position of the pyramid is occupied by the cysteinyl sulfur. Similarly, the base of the square pyramid around the distal iron also consists of two thiolates, a CO and a CN[−]. The apical position at this iron is occupied by the CO ligand which is in the semi-bridging position to the proximal iron. Thus, the two square pyramids are inverted with respect to each other. This geometrical arrangement of ligands around the Fe_d atom is referred to as the ‘rotated’ state, distinguishing it from common arrangements observed in synthetic complexes which possess ‘uninverted’ edge-sharing square pyramids. This term was introduced by Darensbourg to explain the relationship between the apical/terminal arrangement and the bridging or semi-bridging form observed in the enzyme and in certain complexes in a mixed-valence Fe(I)–Fe(II) state.³³

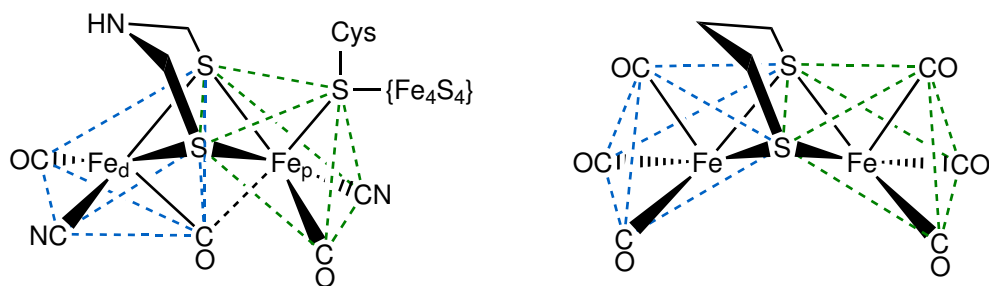


Figure 6: The active site of the [Fe–Fe]-hydrogenase enzyme showing the ‘rotated’ geometry with inverted square pyramid/square pyramid arrangement (left) and synthetic mimic with square pyramid/square pyramid arrangement (right)

First modelled as a carbon, later argued as an oxygen or a nitrogen, the identity of the bridgehead atom has been a matter of controversy for quite some time.^{23,34,35} Nonetheless,

evidence obtained by the hyperfine sub-level correlation (HYSCORE) and electron nuclear double resonance (ENDOR) spectroscopies as well as theoretical modelling and quantum refinement of existing X-ray data give strong support to the presence of the amine cofactor.^{35–37} This was dramatically reinforced by a very recent study conducted by Fontecave, Happe and co-workers on the apo-hydrogenase enzyme HydA1.^{38,39} They demonstrated that three synthetic mimics containing different bridging thiolate ligands could be transferred and successfully reinserted into an apo-enzyme (Figure 7). However, full activation of the H-cluster and hydrogen production at rates comparable to the biological system was only achieved with the mimic **2** possessing an azadithiolate bridge. This appears to accentuate the essential role of the bridgehead amine and confirm its presence in the active site of the native [Fe–Fe]-hydrogenase.

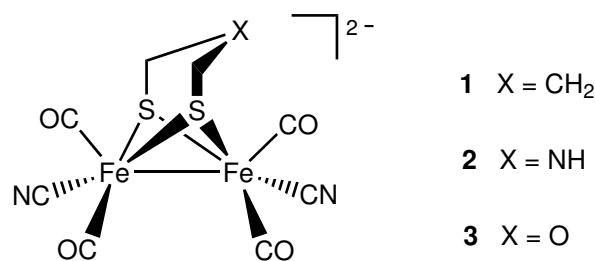
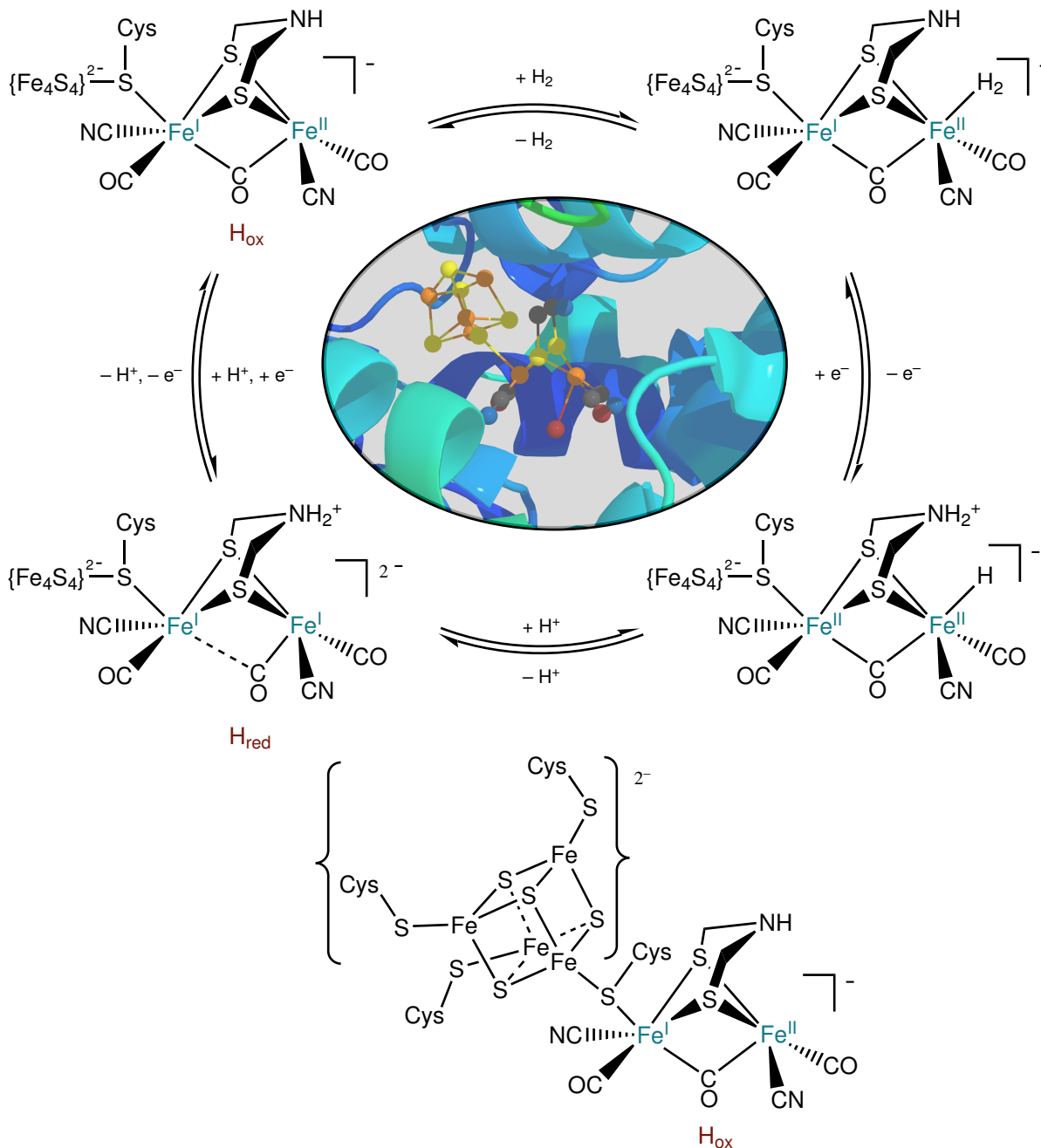


Figure 7: Synthetic mimics employed by Fontecave, Happe and co-workers^{38,39}

Various spectroelectrochemical, EPR, Mössbauer and FT-IR (Fourier transform infrared) techniques as well as detailed DFT (density functional theory) calculations have been employed by many groups in the attempt to elucidate numerous redox states of the H-cluster.^{25,40–42} Thus far only two functional states of the active site of [Fe–Fe]-hydrogenase have been definitively identified by crystallographic means. The first one (**H_{ox}**) was obtained from the air-isolated enzyme and is poised to oxidise H₂, whereas the second one (**H_{red}**) was identified under reducing conditions and is poised to accept protons. Other biologically relevant intermediates in the cycle for hydrogen evolution have only been partially characterized due to the complexity of the systems under investigation. The catalysis taking place in the protein is so fast that getting any

structural or spectroscopic data of the active centre whilst it is turning over is almost an unassailable challenge. Nonetheless, numerous experiments modelled and conducted on synthetic and biological systems enabled the current model of the catalytic H₂ production to be constructed (Scheme 1). It includes assignments of the oxidation states of the H-cluster and represents a consensus view of the catalytic cycle to date. The oxidation states in Scheme 1 are assigned according to IUPAC nomenclature wherein a metal-H compound H is assigned a formal 1- charge *i.e.* hydride. For clarity of assignment of the oxidation states of the subsite, the net charge on the subsite core is represented after the partial bracket to the right of the complex. The charge on the dialkyl ammonium bridgehead group (in the second coordination sphere) is placed on the N atom. The overall charge on the H-cluster is the sum of the cationic NH₂, the core and the cluster anionic charges. Thus, the overall charge on **H_{red}** in the proposed scheme is 3-.



Scheme 1: Top: Proposed catalytic cycle for H₂ catalysis in the [Fe-Fe]-hydrogenase active site;⁴³ Centre: catalytic site of the H-cluster present in reduced [Fe-Fe]-hydrogenase DdH (PDB code: 1HFE);²³ Bottom: figure showing bonding in the [4Fe4S] cluster in which the cysteinate groups are part of the peptide backbone

The mixed-valence paramagnetic H_{ox} state is considered to be the resting state of the enzyme. Its key features include a bridging CO ligand, the 'rotated' state at the distal iron, a weakly bound water molecule and hydrogen-bonded cyanide ligands. This state can be inhibited by carbon monoxide which displaces the bound solvent and reversibly binds to the H-cluster.^{25,44} Upon reduction the subsite retains the rotated state but the CO ligand is no longer bound in the fully bridging mode and water is no longer coordinated to the distal iron. Due to the limited capabilities of protein X-ray crystallography, it is not possible to locate hydrogen atoms in their structures, therefore the position of the protons can not be fully ascertained. For this reason it is still unclear whether the vacant site in the H_{red} state is occupied by a terminal hydride or whether the proton rests on a doubly protonated amine bridgehead atom.

Intriguingly, studies on synthetic mimics of the active site enabled the characterization of other catalytic intermediates thought to be involved in the biological cycle of H₂ production. Infrared and EPR data suggests that one-electron reduction of H_{red} leads to formation of a 'super-reduced' state of the H-cluster (H_{sred}) (Figure 8).⁴¹ Whilst formation of this state has been reported as irreversible in *Desulfovibrio desulfuricans* (DdH),⁴² leading to a catalytically inactive system, full reversibility has been detected in *Clostridium acetobutylicum* (CaHydA),⁴⁵ potentially arguing the importance of H_{sred} in the biological cycle.

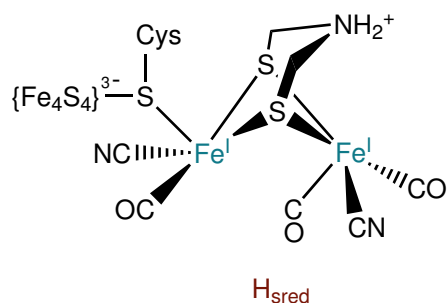


Figure 8: Suggested 'super-reduced' state of the H-cluster⁴¹

There are still many unanswered questions about the catalytic cycle of hydrogen evolution and the corresponding intermediates involved. Whilst H_{ox} , H_{red} and even

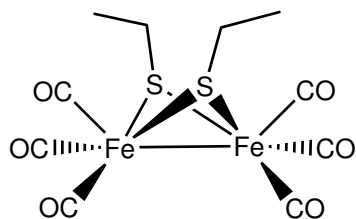
H_{sred} have been characterised by a variety of electrochemical and spectroscopic methods, there is still no unequivocal evidence of where these states protonate and how many more unidentified intermediates play a biologically significant role in H₂ evolution.

1.4 From Iron-Sulfur Carbonyls to Sophisticated Models of the H-cluster

1.4.1 Early Synthetic {2Fe2S} Complexes

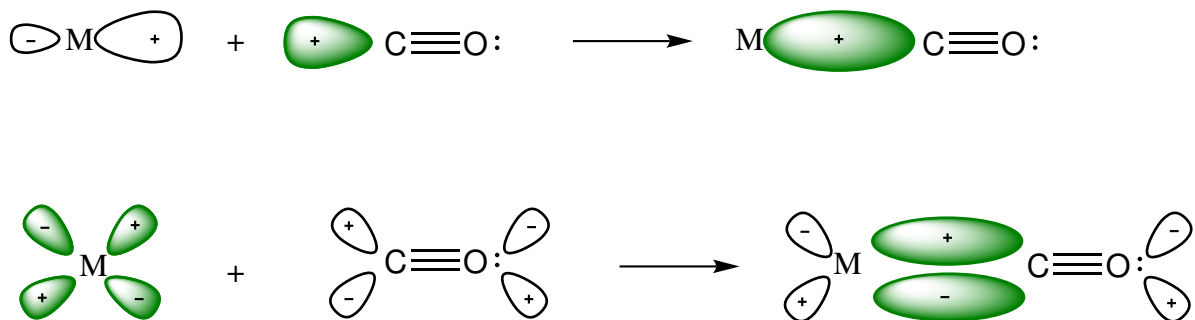
It has been postulated that the ultimate ancestor of the unusual organometallic active site of the [Fe–Fe]-hydrogenase is the diiron disulfide hexacarbonyl, *i.e.* a fragment of the mineral iron sulfide rendered mobile by carbon monoxide.^{46,47} The limited attachment of the {2Fe2S} subsite to the protein scaffold suggests that over the course of 4 billion years it was developed by nature and imported into the enzyme as an already functioning unit, evolving to be protected from the oxidising environment of the maturing Earth.^{23,48} This was followed by sophisticated and controlled biosynthesis of the extraordinary catalytic site immobilising ligands such carbon monoxide and cyanide, resulting in formation of the H-cluster as we know it today. It is the ease by which these structures can form that aid the chemists aiming for effortless synthetic access to compounds that model the active site of [Fe–Fe]-hydrogenase.

The fundamental principles of the metal carbonyl chemistry were effectively established in the inorganic chemistry archives well before the crystal structure of the active site of [Fe–Fe]-hydrogenase became available. The simplest dinuclear iron complex (μ -SEt₂)₂Fe₂(CO)₆ was first synthesised in 1929 by Reihlen and co-workers, who were intrigued by the rich reactivity of these systems (Figure 9).⁴⁹

Figure 9: First $(\mu\text{-SEt}_2)_2\text{Fe}_2(\text{CO})_6$ complex synthesised by Reihlen *et al.*⁴⁹

Nature of Bonding in $\{2\text{Fe}2\text{S}\}$ Complexes

The way in which carbon monoxide ligands engage in bonding to a metal can be viewed in Scheme 2. The overlap of a filled carbon σ orbital with an empty σ -type orbital on the metal forms a σ metal–carbon bond.⁵⁰ CO ligands are also excellent π -acids and can accept electron density from the metal into their π^* antibonding orbitals. This is known as ‘backbonding’ and is the reason why CO stretching frequencies in infrared spectroscopy are taken as a good measure of electron density surrounding the metal centre(s) to which they are bonded.

Scheme 2: Top: formation of metal–carbon σ bond; Bottom: formation of a metal–carbon π bond⁵⁰

Dahl has rationalised the basic geometry around $(\mu\text{-SEt}_2)_2\text{Fe}_2(\text{CO})_6$ and similar complexes by proposing a ‘bent’ Fe–Fe bond.^{51,52} This was conceptually viewed as completing an octahedral-like coordination around each iron atom. The bent metal–metal bond was described as arising from the overlap of octahedral-type iron orbitals, with the two d_{z^2}

orbitals making the largest contribution.

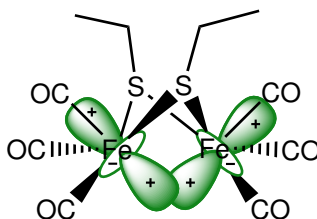


Figure 10: Formation of metal–metal bond

The two thiol ligands coordinate to two metal centres in a bridging fashion and each of the sulfur atoms is considered as an overall three–electron donor to two metal centres. This is represented in Figure 11 as an anionic bond to one centre and a dative bond to the other. In reality the two Fe–S bond distances are very similar and the motif is better represented as a 3–centre 3–electron bond. These thiolates carry a negative charge and the formal oxidation state of the two iron atoms in a $(\mu\text{-SEt}_2)_2\text{Fe}_2(\text{CO})_6$ complex is Fe(I)–Fe(I). Since Fe is in group 8 and has a +1 oxidation state, the total d electron count on each iron is 7. The stability of organometallic complexes may often be rationalised through the 18–electron rule.⁵³ Each iron centre can be viewed as having 18 valence electrons: 8 from iron, 6 from CO ligands, 3 from thiolates and 1 from the metal–metal bond. However, since the molecule contains two of these metals, the overall electron count for the complex is 34 as the electrons from iron–iron bond are not recounted.

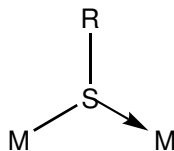


Figure 11: Coordination mode of thiolate

The number of infrared active bands expected from a dithiolate hexacarbonyl complex can be calculated using group theory.⁵³ For instance, the $\text{Fe}_2(\text{S}_2\text{C}_2\text{H}_4)(\text{CO})_6$ complex (**edt-CO**) (Figure 12) contains three symmetry elements: a C_2 rotation axis passing

vertically through the centre of the metal–metal bond and two vertical mirror planes (one perpendicular and one passing through the Fe–Fe bond). Thus the molecule is in point group C_{2v} with the symmetry elements: $E, C_2, \sigma_v, \sigma'_v$. With respect to the CO vectors in the molecule, these symmetry elements lead to a reducible representation (Γ_{CO}) given in Table 1.

Table 1: Reducible representation of the CO vectors in $Fe_2(S_2C_2H_4)(CO)_6$ complex (**edt-CO**)

$$\Gamma_{CO} = \begin{array}{cccc} & E & C_2 & \sigma_v & \sigma'_v \\ \hline & 6 & 0 & 0 & 2 \end{array}$$

A reducible representation can be resolved into its constituent irreducible representation using the ‘reduction formula’.⁵³ For the case in hand it gives:

$$\Gamma_{CO} = 2A_1 + A_2 + B_1 + 2B_2$$

where $A_1, A_2, etc.$ are the symmetry species of the C_{2v} point group. Examining the character table for this point group Table 2 shows that vibrations with A_1, B_1 and B_2 symmetry are infrared active.

Table 2: Point group character table for C_{2v} ⁵³

	E	C_2	σ_v	σ'_v	
A_1	1	1	1	1	z
A_2	1	1	-1	-1	
B_1	1	-1	1	-1	x
B_2	1	-1	-1	1	y

This predicts five IR active CO stretches ($2A_1 + B_1 + 2B_2$). Figure 12 shows the experimental infrared spectrum of **edt-CO** molecule in hexane. As essentially predicted 5 strong bands (one a shoulder) are observed with an additional weak band at 1956

cm⁻¹. This approach does not predict the position, overlap or intensity of the bands. However, *ab initio* methods such as DFT can be used to predict infrared data. Applied to this complex, DFT using the TPSS level of theory (see experimental Chapter 3) predicts five strong bands with observed *unscaled* frequencies in the gas phase close to those observed experimentally in hexane. In polar solvents such as MeCN the IR stretches are broadened with those close to 2000 cm⁻¹ forming an unresolved band.

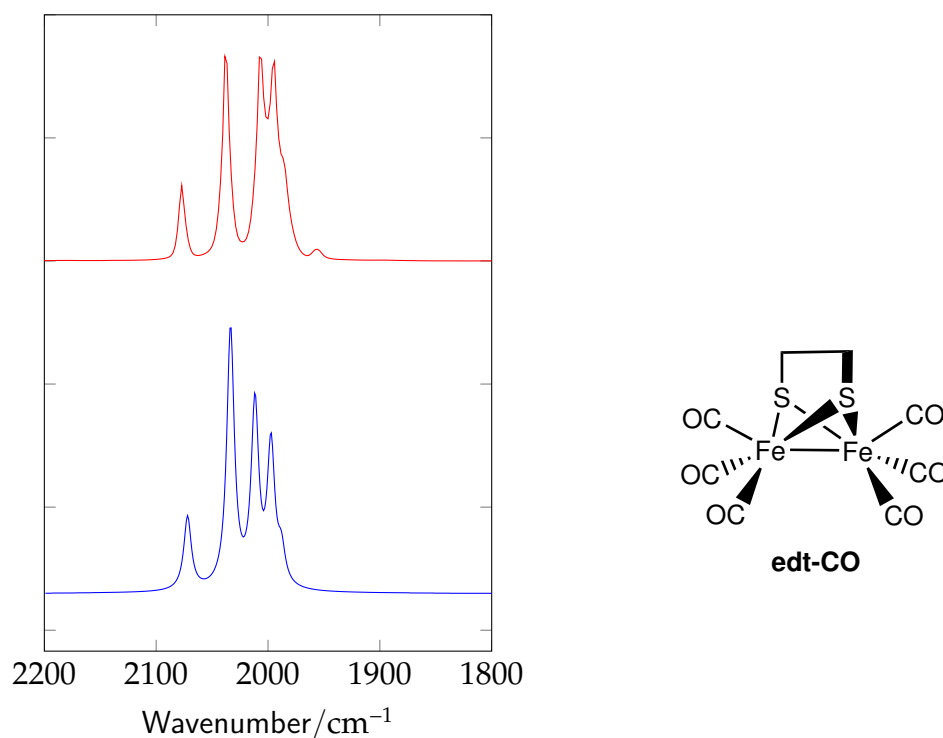


Figure 12: Red: IR spectrum of **edt-CO** in hexane obtained experimentally; Blue: IR spectrum of **edt-CO** in gas phase as calculated by DFT

1.4.2 Later Synthetic {2Fe2S} Complexes

In the next 50 years, following the synthesis of $(\mu\text{-SEt}_2)_2\text{Fe}_2(\text{CO})_6$, the diiron chemistry was further extended by Hieber,⁵⁴ Poilblanc,⁵⁵ Seyferth⁵⁶ and others.⁵⁷⁻⁵⁹ They produced a rich variety of diiron models possessing mainly {2Fe2S} cores that have been investigated towards a number of nucleophilic and electrophilic agents, noting their reactivity,

behaviour, structural and spectroscopic features. Whilst an array of coordination forms were explored in this period, these predominantly featured non-chelating sulfur ligands (Figure 13).

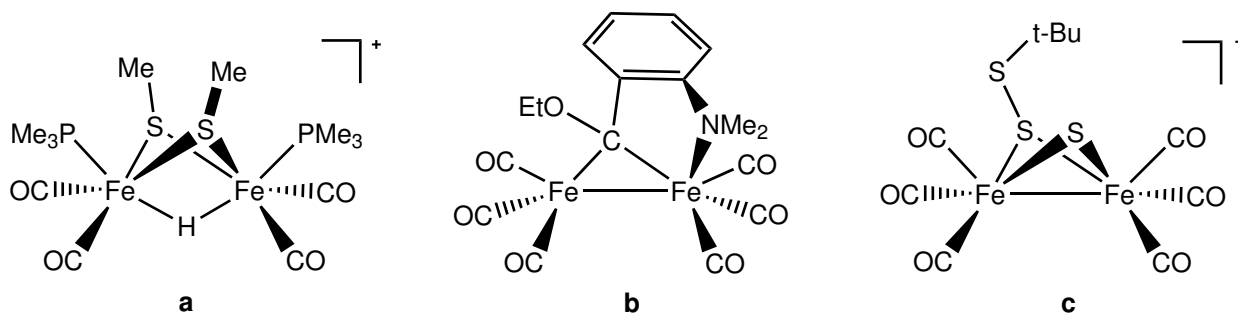


Figure 13: Some of the early diiron complexes investigated for their fundamental reactivity: **a**,⁵⁵ **b**,⁵⁸ **c**⁵⁹

This pattern was broken in 1987 by Seyferth *et al.* who reported isolation of $Fe_2(\mu\text{-pdt})(CO)_6$ (pdt = 1,3-propanedithiolate) in which the two sulfur atoms are linked reproducing the $\{2Fe_2S\}$ core fairly faithfully (Figure 14).⁶⁰ It was the ease of manipulation of this complex that later led to extensive synthetic efforts to reproduce structural and spectroscopic features of the catalytic centre of the $[Fe-Fe]$ -hydrogenase and allowed exploitation of these mimics for electrocatalysis.⁶¹

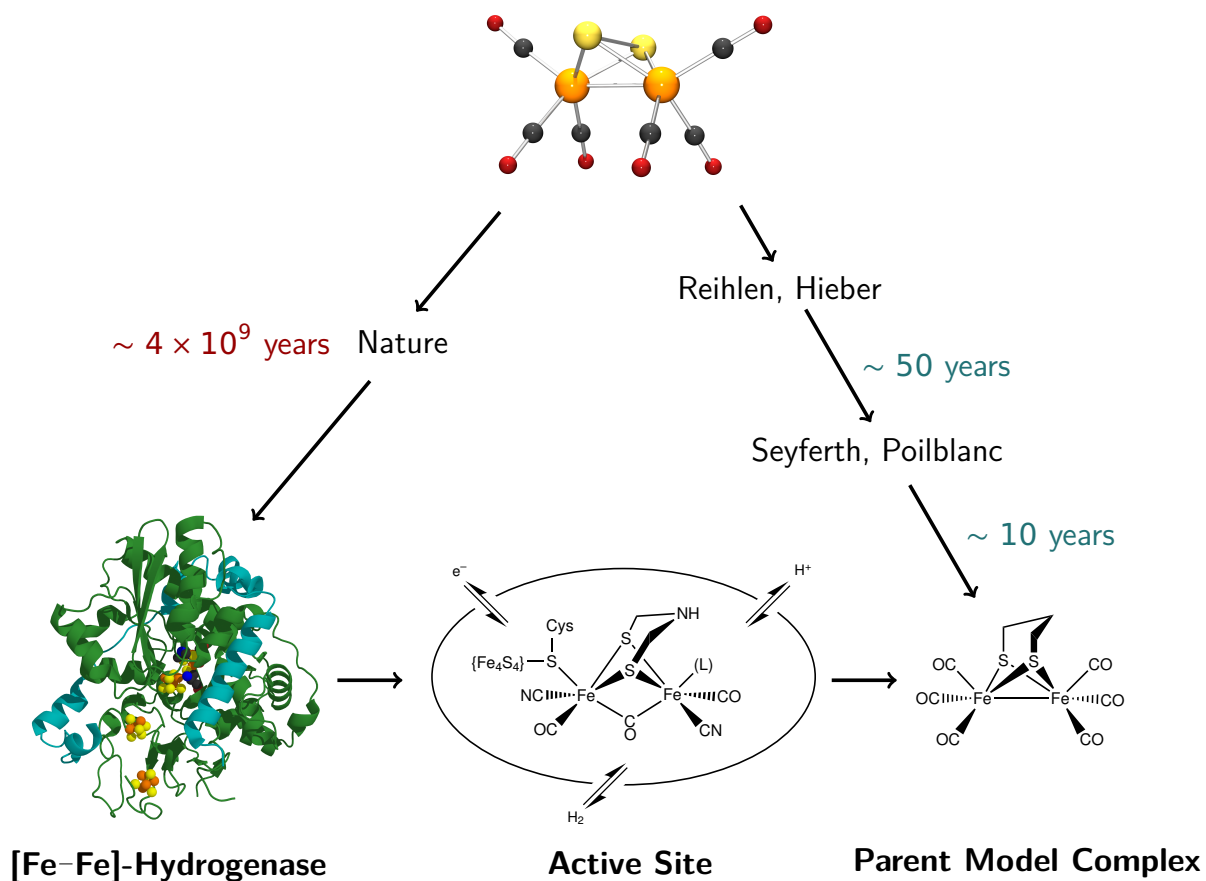


Figure 14: Evolution of CO-mobilized iron sulfide in nature to yield the active site of [Fe-Fe]-hydrogenase and in chemists' laboratories to yield model complexes. (Adapted from ref. 48)

1.4.3 Rotated State and Mixed-Valence Systems

Elucidation of the X-ray crystal structure of the active site of [Fe-Fe]-hydrogenase in 1998²² underlined the remarkable resemblance of the diiron subsite in the H-cluster to the well established organometallic complexes explored in the past 70 years. This has enabled synthetic chemists to skillfully construct some several hundred small molecule models which aim to better mimic the structure and ultimately the function of hydrogenase enzyme without the protein superstructure. Research in the following 15 years involving a myriad of modifications of the parent model complex have provided steady progress towards a complete working model of the H-cluster (Figure 15). The most significant ad-

vances yielded structures modified to include cyanide ligands,^{62,63} pendant amine groups capable of shuttling protons and affording terminal hydrides^{64–66} and mixed-valent diiron units with the rotated state arrangement.^{67–69} Even the {4Fe4S} cluster or its analogues have been reproduced in a more complete assembly of the H-cluster framework.^{70,71}

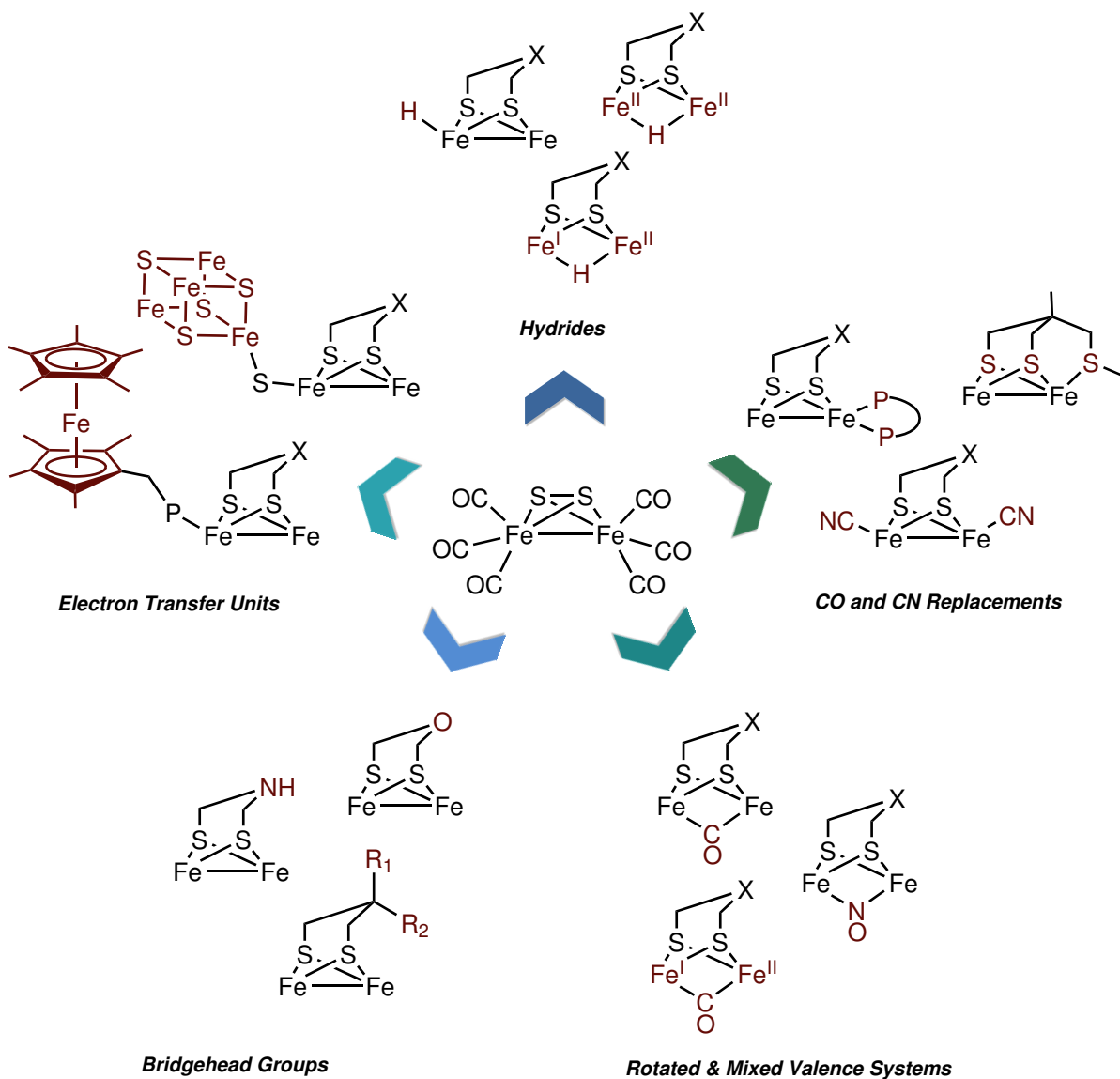
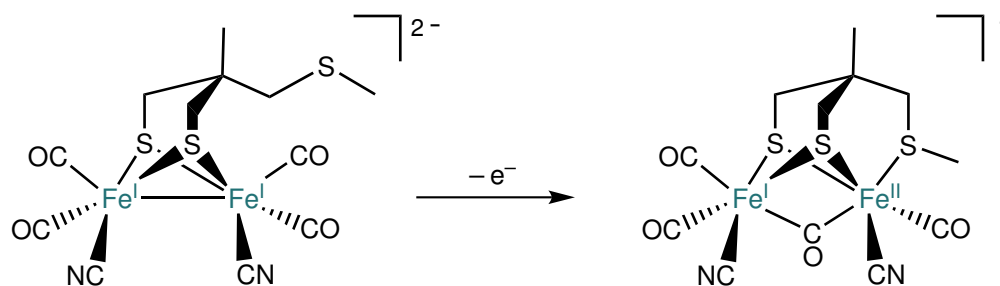


Figure 15: Key areas of research on the synthetic [Fe-Fe]-hydrogenase subsite analogues, ranging from mixed-valence and terminal hydride systems to total synthesis of the H-cluster

A major target for researchers has been assembly of molecules that contain the structural features of biologically relevant states of the H-cluster, with the expectation that the function will follow form. A great deal of effort has been focused on attempts to reproduce the H_{ox} and H_{red} , primarily replicating the rotated geometry, vacant coordination site and mixed-valence diiron centres. In the natural systems this geometry is enforced by the secondary coordination sphere and steric effects from the surrounding protein matrix. Hydrogen bonding of the cyanide ligands to nearby lysine or alanine residues as well as the proximity of several other hydrophobic chains to the open and rotated sites maintain the catalytically active configuration of the H-cluster (Figure 16).²² However, stabilizing synthetic analogues in a rotated stereochemistry is difficult and examples of the Fe(I)–Fe(II) systems are rare.

The first experimental evidence for a mixed-valence bridging-CO complex was observed *in situ* from one electron oxidation of {2Fe3S} model by the Pickett group, revealing IR and EPR signatures closely resembling those of the CO-inhibited enzyme (Scheme 3).⁷² This remains the only dicyanide system observed in an Fe(I)–Fe(II) rotated geometry thus far. Such studies are hindered by the inherent reactivity of the CN^- , which is known to be unstable, protonate readily and even bridge to nearby metal centres.



Scheme 3: Mixed-valence {2Fe3S} dicyanide system⁷²

Even though the biologically relevant subsite models with cyanide coligands remain elusive, the modelling efforts of the H_{ox} state have advanced significantly through the use of abiological constituents in the first coordination sphere. Stable mixed-valent small molecule analogues have been isolated through the use of strongly electron donating

carbenes,⁶⁸ rigid diphosphines^{73–75} or sterically demanding bridgehead groups.^{33,69} Upon oxidation all of these structural features have been shown to enforce a bridging CO geometry, exposing a free coordination site (Figure 17).

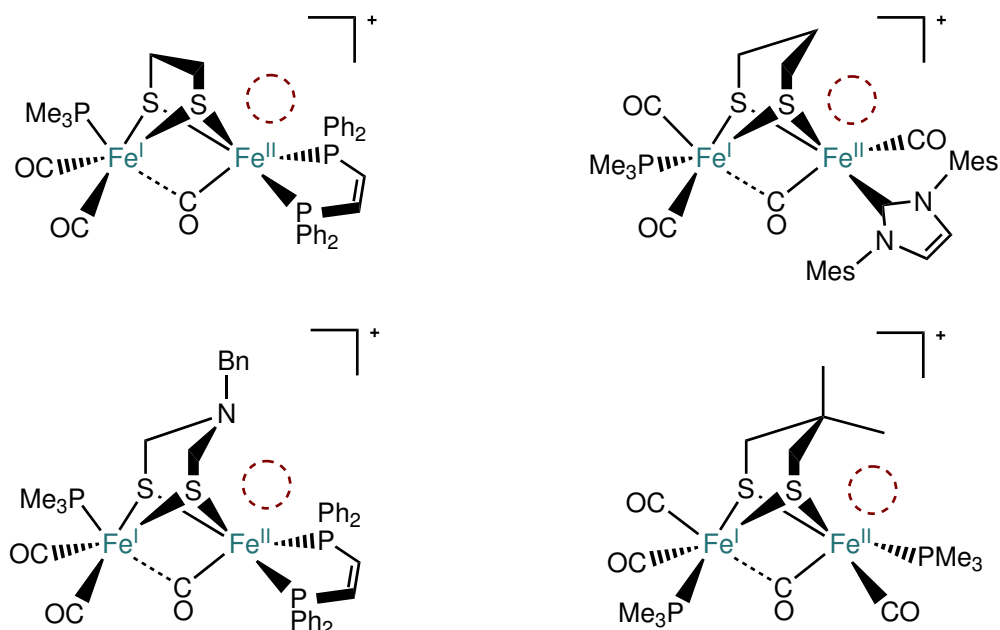


Figure 17: Mixed-valence {2Fe₂S} systems bearing (semi)bridging CO and vacancy at the distal iron (Mes = 2,4,6-trimethylphenyl, Bn = benzyl)^{33,68,73,75}

There is a small number of other interesting attempts to replicate some of the **H_{ox}** or **H_{red}** features. One of these showcase the use of bidentate carboranes to stabilise the mixed-valence species, with the added benefits of full electrochemical reversibility, relatively long lifetime of the oxidised species and very mild overpotential (Figure 18).⁷⁶ In another case, external Lewis acids have been employed to enforce and maintain the rotated structure, demonstrating how non-bonding ligand-ligand interactions may also influence the basicity of other ligands.⁶⁷

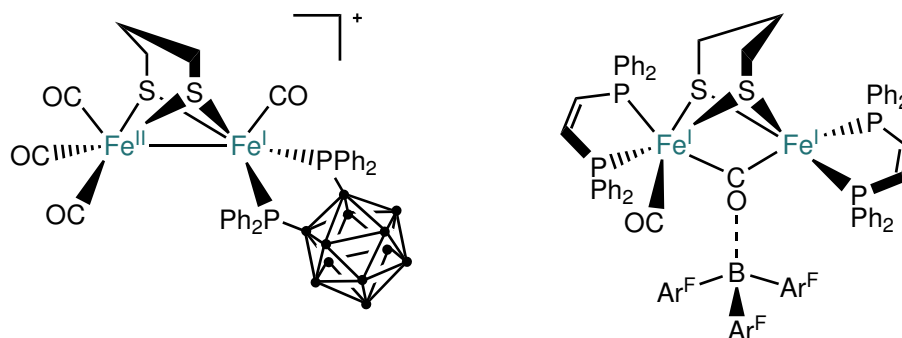


Figure 18: Some of the other approaches employed in the attempt to mimic H_{ox} and H_{red} features (Ar^F = pentafluorophenyl)^{67,76}

1.4.4 {2Fe3S} Assemblies

Whilst numerous successful modelling studies have been carried out on the active site of [Fe–Fe]-hydrogenase, the vast majority of them have been confined to easily accessible complexes with the {2Fe2S} core. Even though the natural system possesses a {2Fe3S} arrangement, catalysts which replicate this sulfur environment are far and few between. The surrogate sulfur for the cysteine residue, coordinating to the proximal iron in the biological system, has been modelled using monodentate thioethers or azadithiolate-bridging ligands with various thiol functionalities (Figure 19).^{77–82} Some of them have demonstrated some electrochemical activity towards proton reduction, others have been synthesised purely with the aim of establishing procedures for incorporation of proton relay units such as amine functionalities.

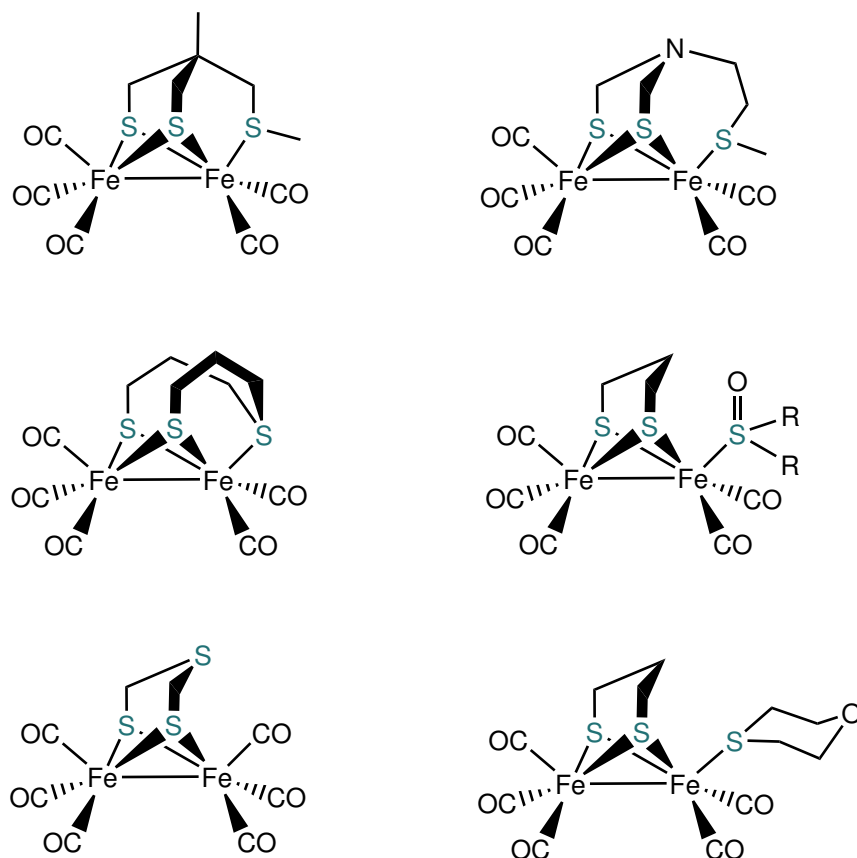


Figure 19: Complexes containing various thiol/thioether functionalities, and modelling {2Fe3S} core of the H-cluster⁷⁷⁻⁸²

1.4.5 Hydrides and Their Formation

Protonation of the active site is a central step in the production of dihydrogen catalyzed by the [Fe–Fe]-hydrogenases.⁸³ Even though hydride species have eluded detection by FT-IR, EPR/ENDOR or other spectroscopic methods in the enzymatic system, they have been postulated as key intermediates in the catalytic cycle. Unsurprisingly, this has led to many protonation studies of synthetic models of the natural subsite, providing vital crystallographic and spectroscopic data on diiron dithiolate hydride complexes. It has also supplied chemists with kinetic data and mechanistic information on factors related to their formation.

Addition of protons to the vast majority of synthetic mimics leads to direct attack on

the metal–metal bond, forming a bridging (μ') hydride (Figure 20).^{84–90} Even though there is no biological evidence implicating these μ -hydrides in the H₂ production by the [Fe–Fe]-hydrogenases, they have been undoubtedly observed in the [Ni–Fe] active redox states and are involved in the nitrogen fixation mechanism by the nitrogenases.^{91,92} As a result, bridging hydrides remain widely studied species not only for their fundamental chemistry, but also in anticipation to produce models that show catalytic activity towards H₂ production.

To bind protons complexes must have strong donor ligands, which provide sufficiently nucleophilic iron centres, and employ adequately strong acids. The resulting Fe(II)–Fe(II) hydrides have distinctive chemical ¹H NMR signals between –8 ppm and –20 ppm, characteristic CO shifts of around 70 cm^{–1} to higher frequencies compared to the non-protonated parent complex and typically elongated Fe–Fe bonds in the crystal structure.⁹³ In general, bridging hydride complexes also exhibit lower reactivity towards further addition of protons following an electron transfer, and are reduced at more negative potentials than their terminal hydride isomers.⁸³

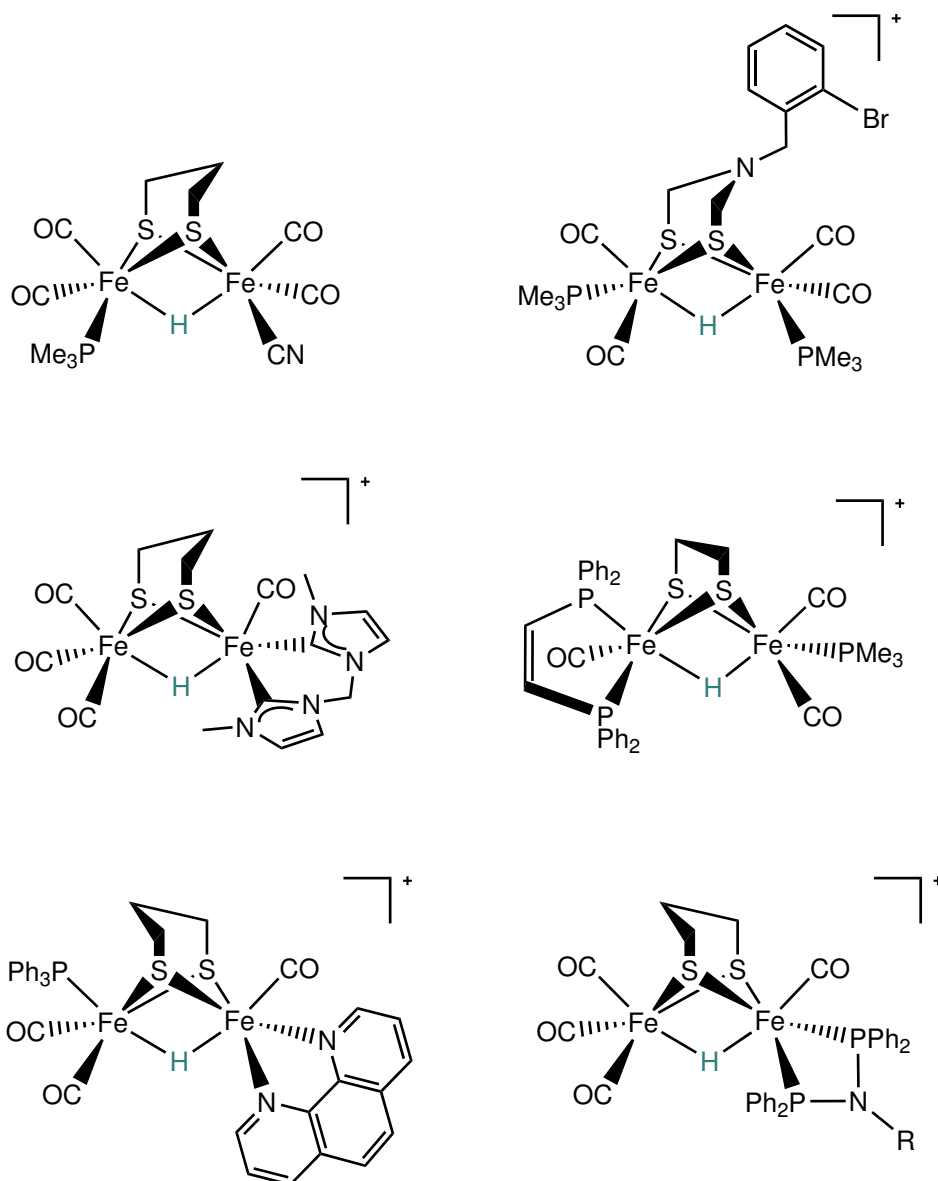


Figure 20: Examples of structurally characterised bridging hydride model systems^{84–89}

In sharp contrast to these synthetic models, the vacant site in the enzymatic H-cluster is thought to be occupied by a hydride ligand bound in the terminal fashion. There is a consensus that such terminal hydrides occur, if not in the **H_{red}** state itself, then as transient species during the catalytic production and oxidation of H₂. Despite their significance in biological function, synthetic electron-rich rotated diiron dithiolates are rare and challenging to produce. The first structurally-characterized terminal hydride

of {2Fe2S} system was prepared by Rauchfuss in 2005 using hydride reagents and not by protonation (Figure 21, left).⁹⁴ He later reported two more terminal-hydride-bearing systems, which remain the only structurally characterised species of this kind to date.^{95,96} A significant achievement has been crystallization of the doubly protonated diiron model that contains both a terminal hydride at the iron centre and a proton on the amine bridge (Figure 21, middle). This complex is of great interest to chemists as it represents the closest structural analogue of the H_{red} state thus far reported. An important outcome of these studies has been the key spectroscopic information distinguishing terminal and bridging hydrides with the same {2Fe2S} cores. All terminal hydrides were shown to feature a diagnostic signal in ¹H NMR spectroscopy within the narrow range –3 ppm to –5 ppm.

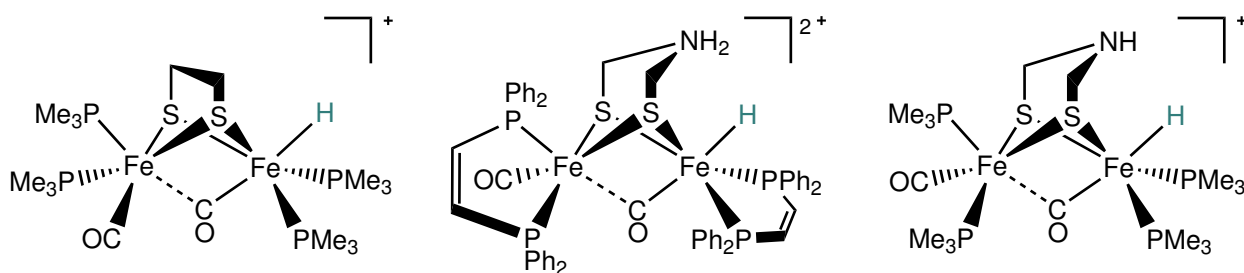


Figure 21: Crystallographically characterised terminal hydride systems^{94–96}

Interest in these biologically-relevant intermediates expanded in 2007 when Schollhammer and co-workers published the first spectroscopic evidence for the direct formation of terminal hydrides by protonation.⁹⁷ Even though a small number of other diiron complexes with terminal hydride ligands have been observed at low temperatures, all of them were short-lived and tended to isomerize to a more thermodynamically stable bridging position above –30 °C (Figure 22).^{87,98} Model complexes with either asymmetric substitution or exceptionally electron rich phosphine ligands are thus far the only examples of model complexes with terminal hydrides. Biologically more relevant terminally-protonated species bearing cyanide coligands has thus far eluded detection.

A compelling solution to the ‘terminal hydride problem’ – their tendency to isomerise

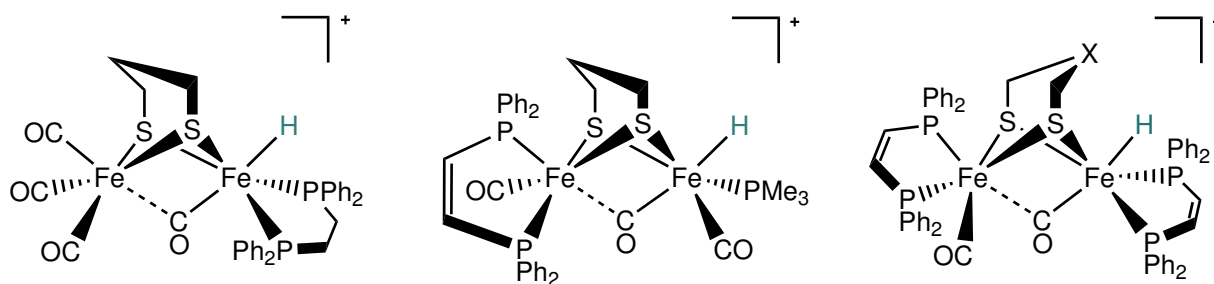


Figure 22: Spectroscopically characterized terminal hydride systems ($X = \text{O}, \text{NH}, \text{CH}_2$)^{87,97,98}

to the μ -hydride form – was reported by Rauchfuss and co-workers earlier this year.⁹⁹ They have spectroscopically characterised a complex featuring *both* a terminal and a bridging hydride (Figure 23). Intriguingly, the assignment of the ¹H NMR chemical shifts for the two hydrides does not follow the pattern observed thus far for other diiron hydrides. On the basis of spin–spin couplings, a signal at –12 ppm was assigned to the μ -hydride, whereas a shift at –19 ppm was attributed to the terminal one. This atypical behaviour might arise from the fact that in this case the terminal hydride rests not in the (usual) apical but in the basal position. In addition, the uncharged nature of this dihydride is in contrast to the positive charge borne by all other terminal hydride species characterised to date. The occurrence of basal terminal hydrides is unprecedented in the chemistry of diiron compounds and gives support to the existence of a long-postulated intermediate in the conversion of terminal apical hydrides to μ -hydride species.

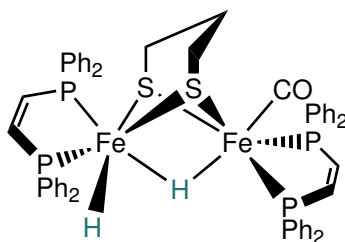
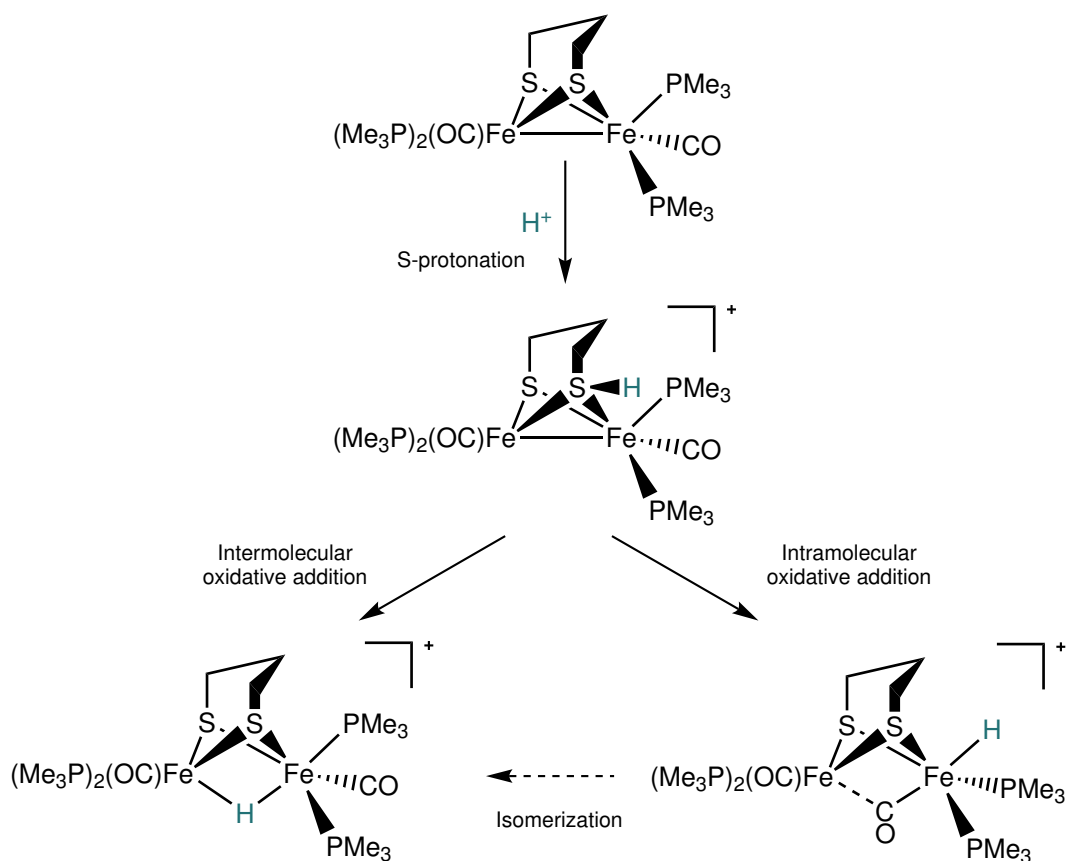


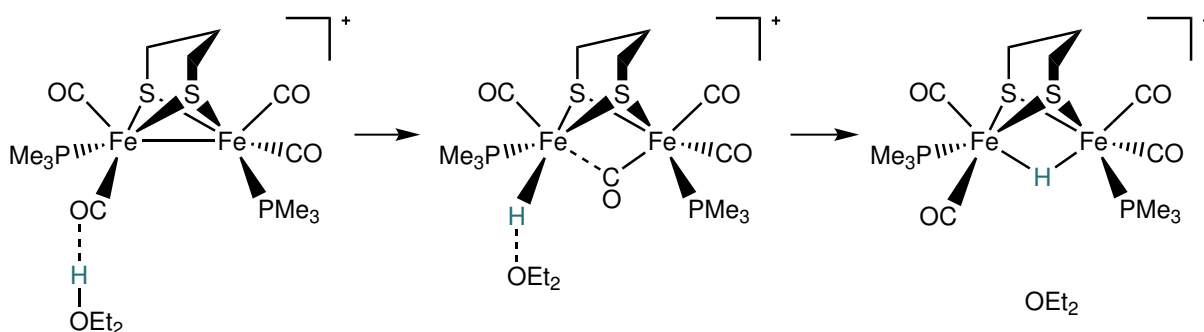
Figure 23: The first and only example of a complex bearing both the terminal basal and the bridging hydride⁹⁹

It was initially believed that terminal hydrides were the kinetic product of a protonation step and that these intermediates were on the pathway to more thermodynamically favoured μ -hydride species. However, it is puzzling that when symmetrically distributed complexes were treated with acid, evidence for terminal hydride formation was absent. Stopped-flow kinetic studies on a range of different {2Fe2S} models have clearly revealed the metal–metal bond as the initial and exclusive site of protonation followed by a rearrangement of phosphine ligands to the most stable isomer.^{100,101} In support of this, contrasting to his earlier assertions, Rauchfuss has provided compelling evidence showing that protonation of diiron dithiolates can proceed without such intermediates. His work has thus dispelled the idea that μ -hydrides necessarily arise from their terminal precursors.⁹⁶ He also supplied evidence that sulfur-protonated species might be implicated in the formation of hydrides (Scheme 4).



Scheme 4: Protonation mechanism proposed by Rauchfuss⁹⁶

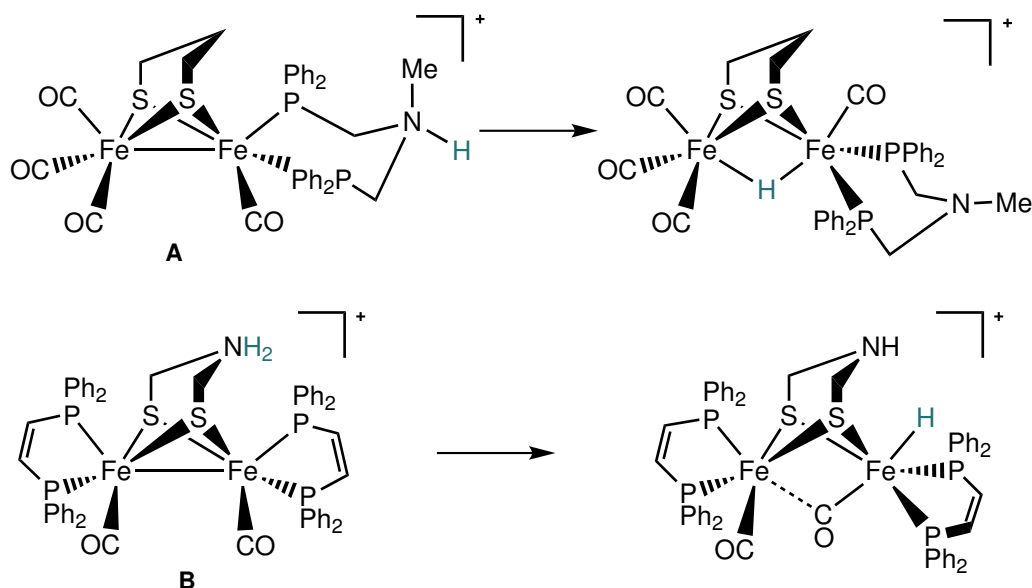
On the other hand, DFT calculations performed by Hall and co-workers demonstrate that sulfur-hydrides are much less stable than the terminal ones, which in turn are less favourable than their bridging counterparts.¹⁰² They have proposed a mechanism in which the solvent plays an important role as the proton carrier (Scheme 5). A crucial feature of this work is the interaction between the acidic proton and the CO (not S), prior to an attack of the 'underside' of the iron–iron bond. This forms a short-lived basal terminal hydride intermediate which is geometrically distinct from the other terminal hydrides that form in the apical rotated state arrangement.



Scheme 5: Protonation mechanism mediated by solvent as proposed by Hall¹⁰²

With increasing biophysical evidence for the presence of NH group in the subsite of the H-cluster, it is unsurprising that the amine cofactor is believed to play an important role in protonation. Synthetic models possessing bridghead NH or related pendant basic sites act as proton transfer relays to the more basic iron site resulting in terminal or bridging species, thus greatly increasing the rate of protonation (Scheme 6). For example, CV (cyclic voltammetry) experiments conducted on complex **A** and its analogues revealed that the rate of formation of the protonated species was greatly enhanced when the model was ligated by PNP (PNP = (Ph₂PCH₂)₂NCH₃) compared to when dppe ligand was used (dppe = (Ph₂PCH₂)₂).⁶⁵ Due to the similar electron donating properties of both, the higher rate was attributed to proton shuttling capabilities of nitrogen atom and not the increased basicity of the Fe–Fe bond. Another interesting study carried out on complex **B** confirmed the capabilities of the heteroatom in the dithiolate bridge to strongly facilitate

proton transfer to and from the empty coordination site on the Fe atom. It was observed that while a similar system possessing an oxygen atom exhibits relay-like behaviour, only the azadithiolate enables hydride formation from weak acids, which is relevant to catalysis at low overpotentials.¹⁰³



Scheme 6: Complexes capable of enhancing rates of protonation due to pendant amine functionalities^{65,98}

1.4.6 Complete H-Cluster Mimicking Assemblies

In the [Fe–Fe]-hydrogenase both proton reduction and hydrogen oxidation occur at very fast rates with negligible overpotentials. The active site of the biological system is thought to operate by supplying redox equivalents through the {4Fe4S} cluster and the {2Fe2S} unit providing a site for proton binding. Even though most modelling efforts are focused on replicating the essential features of the diiron subsite, the entire H-cluster is required for efficient turnover.

The first and thus far the most complete model of the entire H-cluster was prepared in 2005 by Pickett and co-workers.⁷⁰ In addition to representing a significant synthetic achievement, this unique 6Fe assembly aids in understanding of the intimate chemistry

of the natural process and provides insights relevant to engineering more sophisticated biomimetic catalysts. Unfortunately, the linkage between the {4Fe4S} cluster and the subsite is prone to breaking upon reduction. This emphasizes the importance of the neighbouring residues in the protein which support and maintain this geometrical arrangement of the H-cluster. Attempts to look beyond the naturally occurring clusters for alternative 'electron reservoirs' has led to use of ferrocenium-derived structures that exhibit greater stability and productivity (Figure 24).

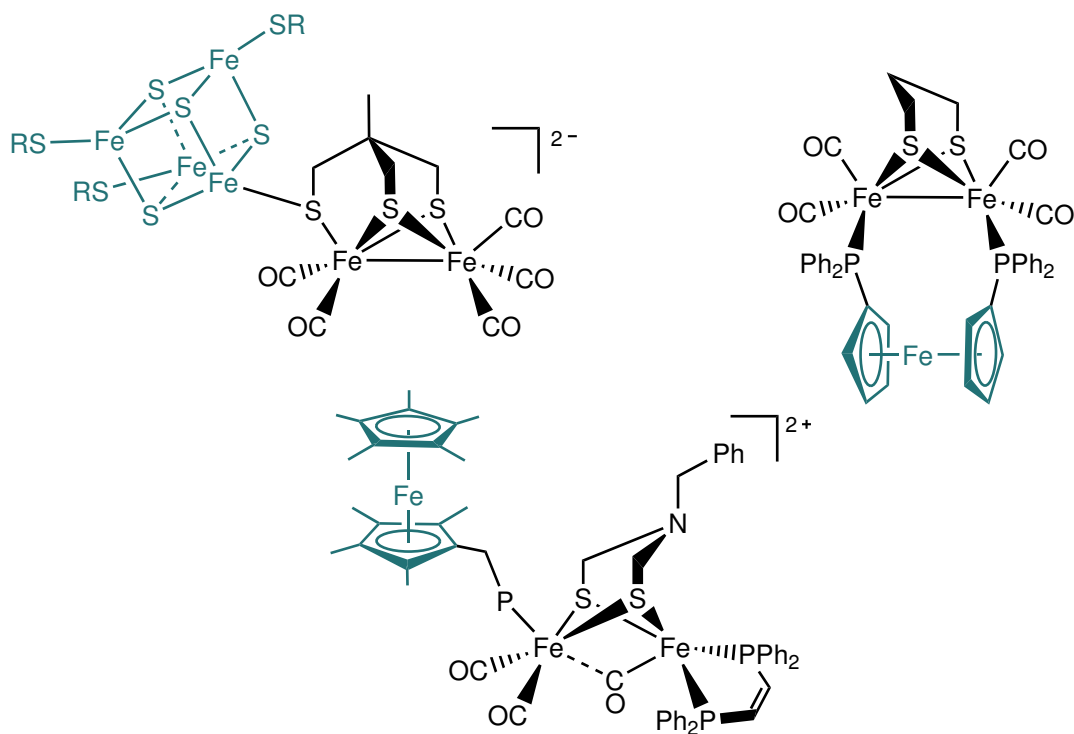


Figure 24: Synthetic models with pendant cluster or ferrocenium as redox auxiliaries^{70,71,104}

Another approach to replicating the redox auxiliary of the H-cluster has been to employ light-harvesting chromophores that serve as antennae (Figure 25).^{105–107} Excitation of these sensitizers is expected to generate electrons which, when passed onto diiron subsite assemblies, can generate hydrogen. The challenge that remains in this field is matching the properties of the photoreductant – lifetimes, quantum yields and reducing properties

– with the redox properties of the {2Fe2S} centres.

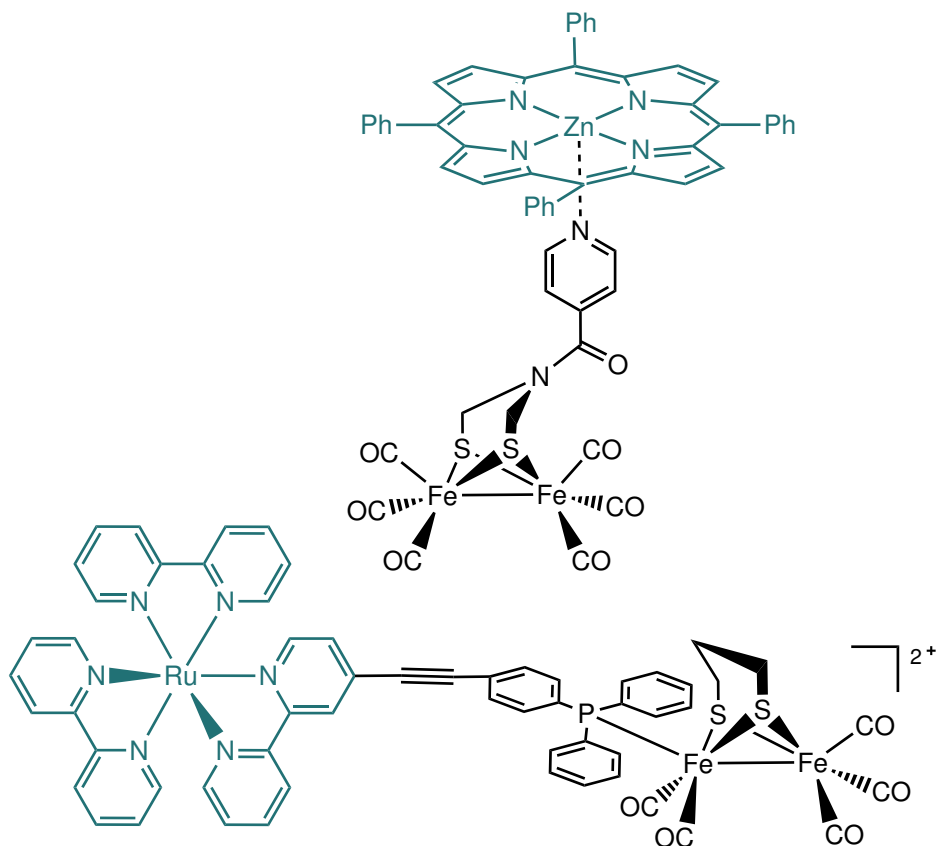


Figure 25: Synthetic models with incorporated photosensitizers as redox auxiliaries^{106,107}

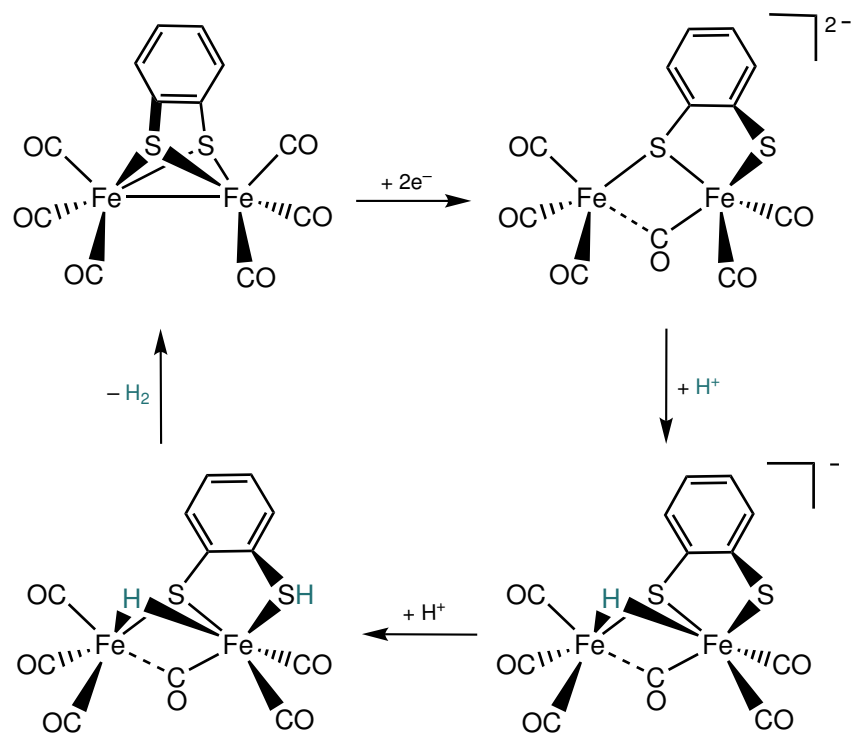
1.5 Catalysts for Biomimetic Hydrogen Evolution and Uptake

1.5.1 Proton Reduction

Guided by the structural features unveiled by the X-ray characterization of [Fe–Fe]-hydrogenases, a great number of catalysts have been developed that resemble the active site to a varying degree. However, only a few exhibit significant rates or low overpotentials and none exhibit both.^{83,95} Provided the diiron unit is sufficiently electron rich to be protonated and given a large enough overpotential, all models of the [Fe–Fe]-hydrogenase

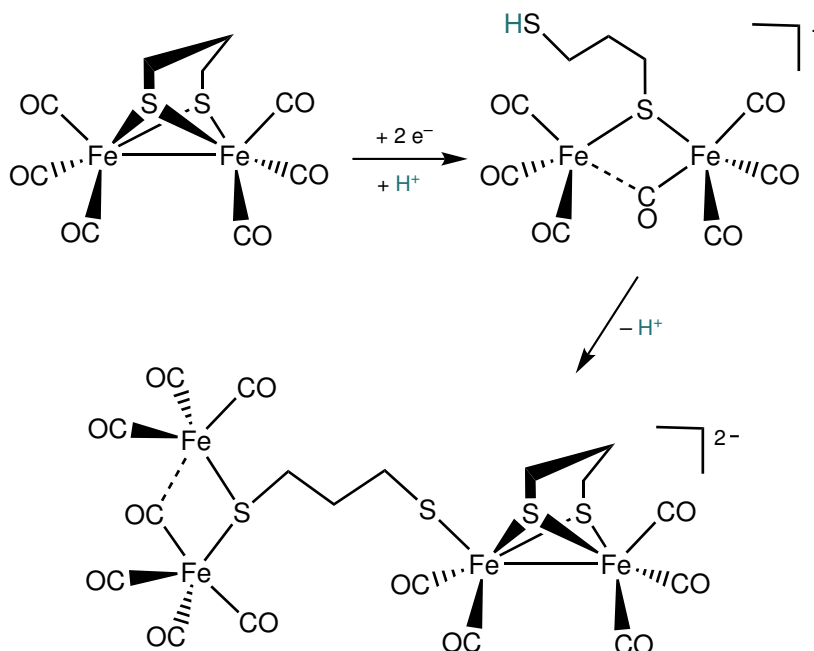
will catalyse proton reduction to some extent. However, the vast majority of them either degrade during the catalytic cycle or produce insufficient hydrogen to be of practical interest. None of them are fully water soluble, an important prerequisite for catalysts that are aiming to produce H₂ from water-splitting cycles. Chemists have a long way to go before truly efficient biomimetic catalysts are made.

When considering biomimetic hydrogen evolution, most of the model complexes can be classified according to the mechanistic features of their catalytic cycle. For instance, the CO-rich diiron complexes are poor bases and thus resist protonation. They do, however, reduce at relatively mild potentials, generating anions which readily protonate, thus initiating catalysis. Mechanistic studies performed on diiron hexacarbonyls also demonstrate that opening up of one of the sulfur bridges and/or loss of CO are characteristic features of these systems. As is demonstrated in the case of Fe₂(μ-bdt)(CO)₆ (bdt = benzenedithiolate), two electron reduction leads to a catalytically-active intermediate capable of reacting with protons.¹⁰⁸ The doubly reduced diiron dithiolate first undergoes protonation on the iron–iron bond then on the sulfur, before regenerating the parent complex (Scheme 7).¹⁰⁹

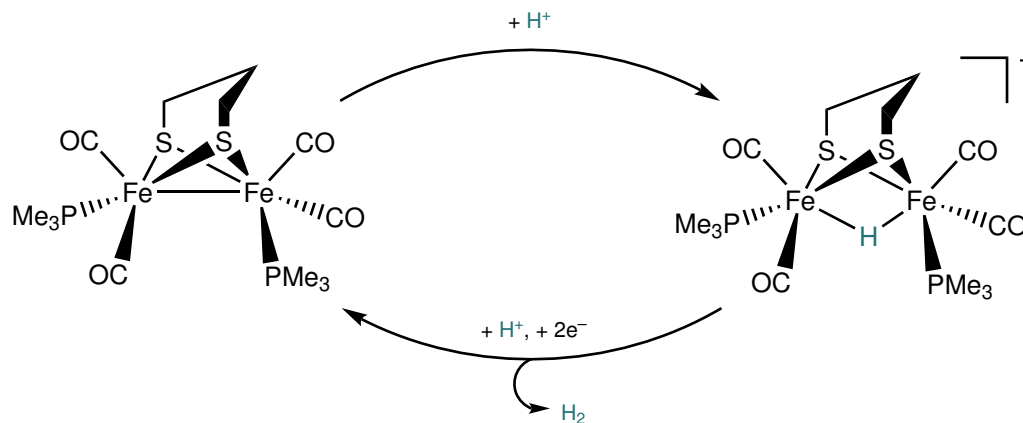


Scheme 7: Proposed reaction pathway of $\text{Fe}_2(\mu\text{-bdt})(\text{CO})_6$ complex in electrocatalytic proton reduction¹⁰⁹

Proton reduction by the related $\text{Fe}_2(\mu\text{-pdt})(\text{CO})_6$ complex occurs at a more negative potential than is required for the bdt derivative, but it does exhibit faster catalytic turnover.¹¹⁰ A one-electron reduced species was shown to be involved in several subsequent chemical reactions, one of which eventually gives a Fe_4 product that was also shown to be catalytically active (Scheme 8).

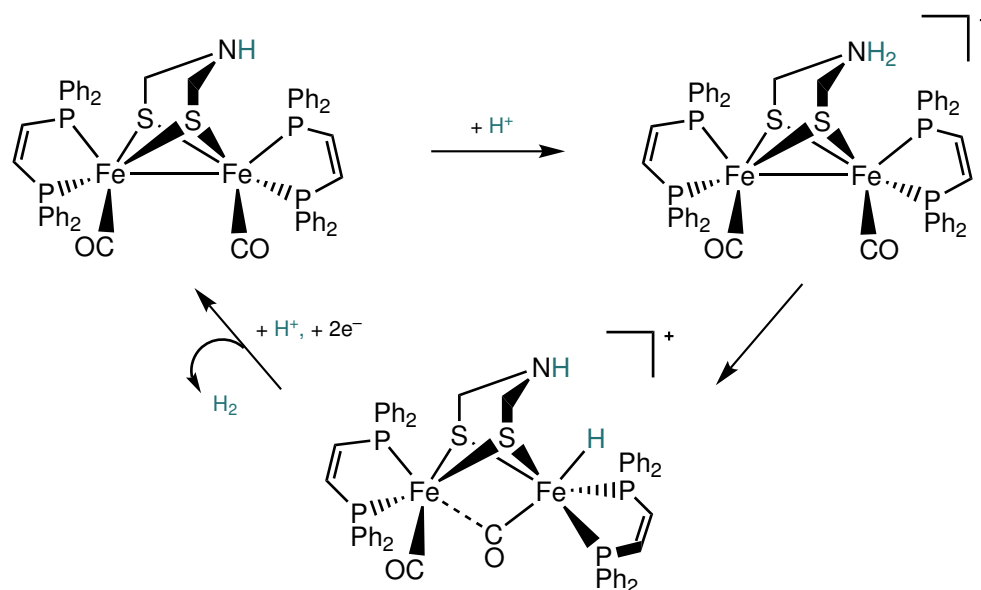
Scheme 8: Proposed reduction pathway of $\text{Fe}_2(\mu\text{-pdt})(\text{CO})_6$ complex¹¹⁰

Another major class of catalysts are the substituted diiron dithiolates in which electron rich groups model the cyanide ligands found in the native active site. They possess substantially more basic iron centres and are clearly more relevant to the H-cluster. These models are sufficiently electron rich to undergo direct protonation of the metal–metal bond forming bridging hydrides. Such intermediates are consequently susceptible to reduction and with a following protonation can engage in the catalytic H₂ production (Scheme 9).



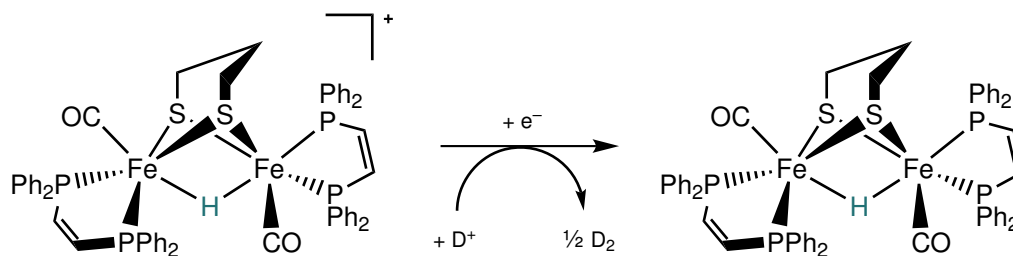
Scheme 9: Proposed catalytic cycle for substituted diiron complexes protonating in bridging fashion⁸⁴

The final class of catalysts also feature electron-rich donor ligands in place of CN. However, they are often described as being the most biologically relevant due to the fact that they undergo protonation at a single iron centre forming a terminal hydride (Scheme 10). These models also often contain an amine cofactor to mediate the proton transfer step.



Scheme 10: Proposed catalytic cycle for substituted diiron complexes protonating in terminal fashion⁹⁵

In general, it has been observed that reduction of protonated complexes enhances their susceptibility to a following proton attack, enabling hydrogen evolution. However, very recent studies performed by Rauchfuss and co-workers on a bridging hydride complex demonstrated that reduction of D^+ affords D_2 leaving the hydride ligand intact (Scheme 11).¹¹¹ This has led to a compelling conclusion that in some electrocatalytic cycles the μ -hydride species are merely acting as spectator ligands.

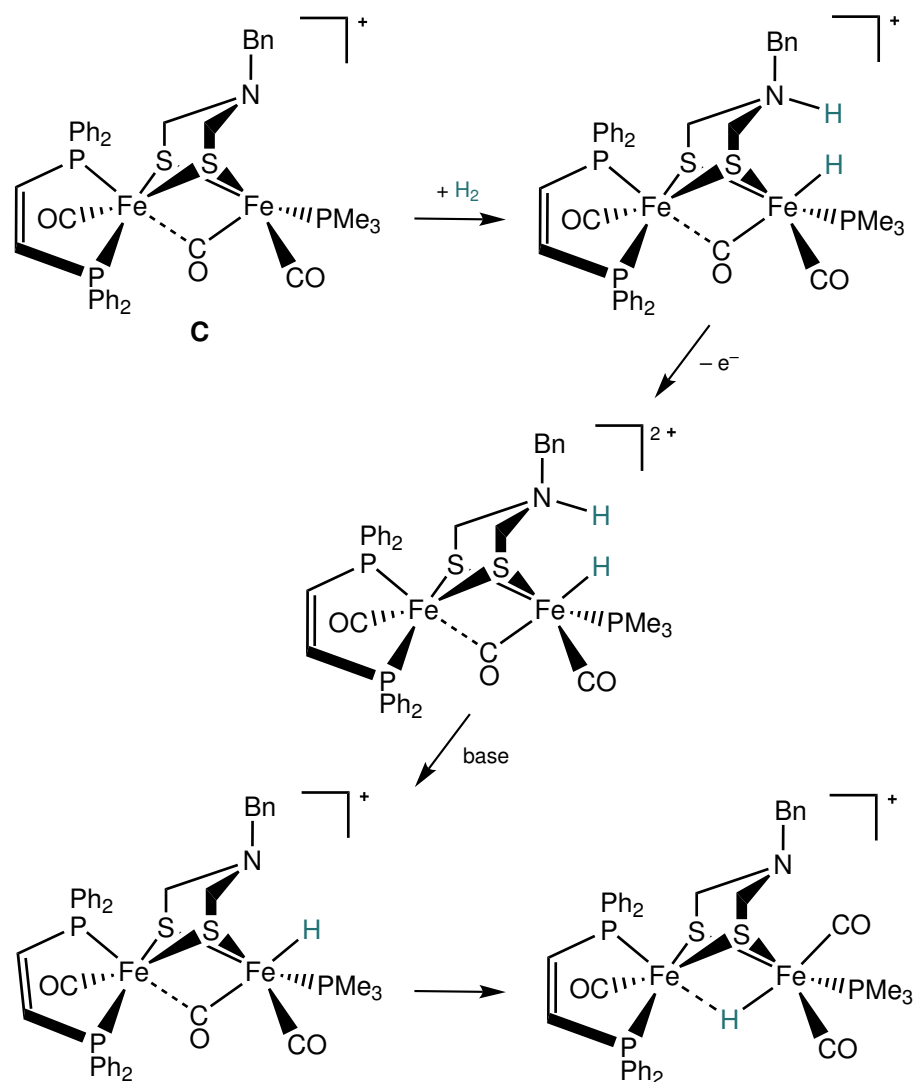


Scheme 11: Proposed catalytic cycle for D_2 evolution involving a spectator hydride¹¹¹

1.5.2 Hydrogen Oxidation

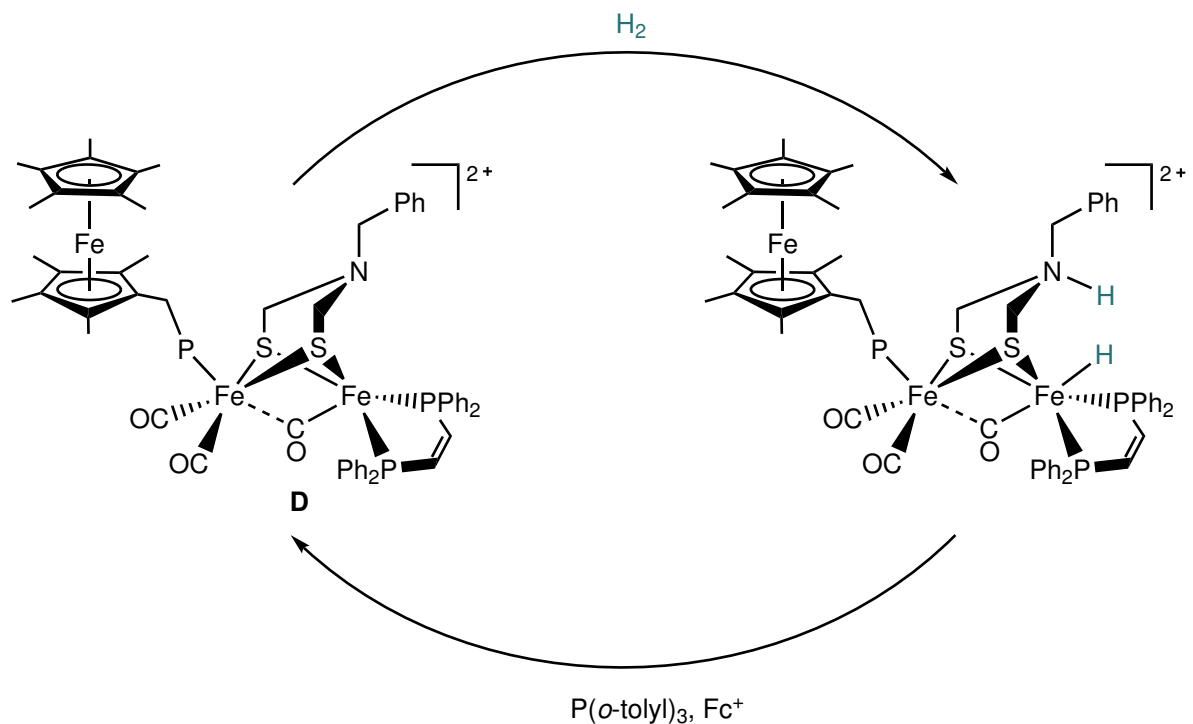
Although [Fe–Fe]-hydrogenases are usually engaged in catalyzing proton reduction, they are also highly efficient catalysts for the oxidation of H₂. Over the last decade studies have been focused mostly on reproducing H_{red} state and studying their function and reactivity, resulting in numerous synthetic models. However, modelling of the H_{ox} state and its oxidation function has been paid much less attention.

The first model of H_{ox} state that exhibited reactivity towards H₂ was reported in 2009 by Rauchfuss and co-workers (Scheme 12).¹¹² The azadithiolate containing diiron model was shown to cleave dihydrogen but only under significantly forcing conditions (12.4 MPa). Importantly, the related complexes bearing O or CH₂ groups as a central bridgehead atom were unreactive under the same conditions, once again highlighting the importance of the amine cofactor in catalysis. The same complex was later reported to allow for a much more facile oxidation of H₂ under much milder conditions (14 kPa) when the reaction was performed in the presence of decamethylferrocinium as an external oxidant.⁷⁵ The latter functioned as an ‘electron sink’, a role which in the natural system is performed by pendant {4Fe4S} clusters. Oxidation of H₂ was shown to be only stoichiometric as the stable μ -hydride formed in the reaction was not susceptible to deprotonation by a base.

Scheme 12: Proposed mechanism for stoichiometric oxidation of dihydrogen¹¹²

A dramatic breakthrough was made by the same group when they coupled a related diiron complex to a derivative of decamethylferrocenium relay unit acting as a surrogate for a cubane 'electron sink' (Scheme 13).⁷¹ This extraordinary system was able to achieve *catalytic* hydrogen oxidation in the presence of base and excess oxidant. This is in contrast to the previously reported complex **C** which, under identical conditions, activates H₂ stoichiometrically and proceeds four times slower than the new system **D**. Even though the actual turnover of the latter complex is extremely slow, showing rate of 0.0001 s⁻¹ compared to 21,000 s⁻¹ for the enzyme, the system remains the first example of *catalytic* H₂

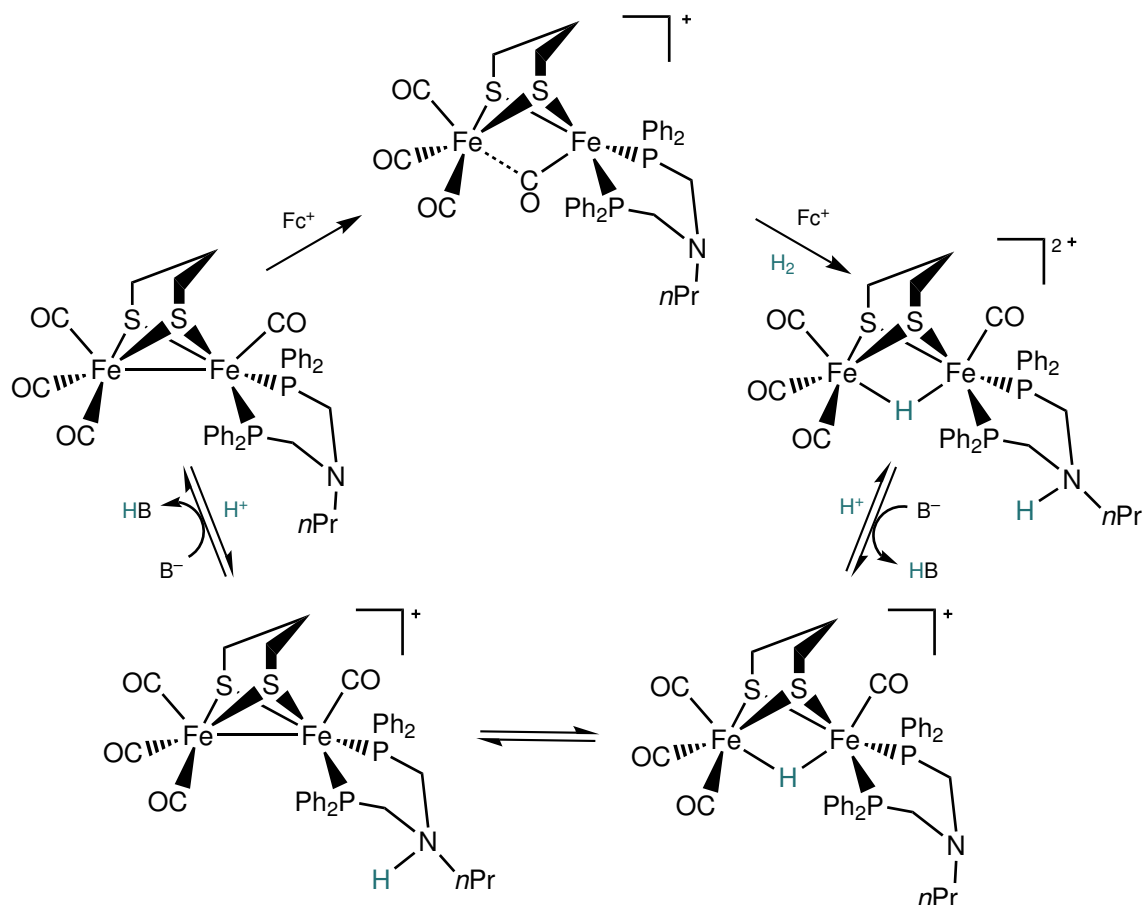
activation under mild conditions, hopefully inspiring future developments in biomimetic catalysis.



Scheme 13: Hydrogen oxidation catalyst operating in the presence of external base and oxidant (Fc⁺ = ferrocenium)⁷¹

Whilst all of these systems have been shown to rely on terminal hydride–pendant amine interactions, Sun and co-workers have recently reported a system which is believed to oxidise dihydrogen via catalytically active μ -hydride intermediates (Scheme 14).¹¹³ In the presence of external oxidant and a weak base the complex turns over very slowly, at a rate comparable to that of the Rauchfuss system described above. It was postulated that the activity of the μ -hydride species was distinct from those in diiron models bearing an azadithiolate bridge due to the short distance between the built-in amine of the bidentate phosphine ligand and the bridging hydride. However, it has to be noted that μ -hydrides are known to be the thermodynamic sink of protonation reactions and terminal hydrides are notoriously short-lived and thermally unstable. For this reason some caution must

be taken when interpreting the mechanistic aspects of H₂ oxidation by this system.



Scheme 14: Proposed pathway for H₂ oxidation in the presence of oxidant and base¹¹³

The latest addition to the growing number of H₂ oxidation catalysts is the diiron dithiolate system reported by Holt and co-workers earlier this year, capable of both reducing protons and oxidising dihydrogen.¹⁰⁴ They too employed a ferrocene-containing ligand as redox auxiliary anchored to the metal centres by two phosphine ligands (Figure 26). Whilst neither mechanism has been unveiled, the reduction is speculated to proceed *via* bridging hydride intermediate and oxidation has been tentatively proposed to generate a cationic dihydride. The one major disparity between the native system and this synthetic model is the potentials at which they operate. Whilst the catalysis in the enzyme occurs over the same redox levels, Holt's system operates at two different potentials for

hydrogen oxidation and proton reduction. Though more investigations are pending, the complex nonetheless offers exciting possibilities and brings the efforts of biosynthetic community one step closer to a truly biomimetic catalyst resembling the H-cluster both in structure and in function.

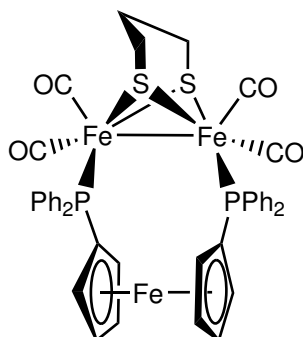


Figure 26: First diiron catalyst reported to engage in both proton reduction and H₂ oxidation¹⁰⁴

1.6 Outstanding Challenges and Ongoing Research Directions

In the past few decades, astounding progress has been made in the preparation of structural models for the active site of [Fe–Fe]-hydrogenase and in lifting the veil on the enzymatic mechanism. Crucial structural features such as CN[−] ligands, bridgehead NH, semi-bridging CO and even the cysteine-tethered {4Fe4S} cluster have been successfully translated into synthetic complexes. More encouragingly, some very critical model intermediates relevant to biological hydrogen oxidation and uptake have been isolated. These include mixed-valence Fe(I)–Fe(II) states and terminal hydride intermediates.

In spite of the tremendous achievements, there are still significant challenges that need to be overcome. The assembly of competent and economically-viable catalysts based on diiron subsite chemistry remains a realistic goal for inorganic chemists. However, it is clear that the mechanism of H₂ production and uptake are still insufficiently understood.

Elucidating how the protein scaffold tunes the chemical properties of the H-cluster remains one of the unanswered questions, stressing the need for exploration of the second coordination sphere interactions.

Most existing models require significantly large driving forces, display low activities and lack crucial electron-transfer units. Understanding how the enzyme achieves such immense production rates and bridging this performance gap between the natural system and synthetic models is of paramount importance to produce practical devices. Clearly, for the bio-inspired functional models of the H_{ox} state to be truly effective the presence of both the basic proton relay group and a suitably tuned redox cofactor is required. Doing this while minimising the overpotential, increasing water solubility and improving overall stability is to this day a severe challenge for the bioinorganic chemists. However, with new and exciting systems emerging every year building on improved mechanistic understanding, the outlook for viable hydrogen transduction using biomimetics is bright.

1.6.1 Objectives of the Project

The first objective of the project was to investigate aspects of the protonation of certain complexes possessing {2Fe2S} and {2Fe3S} cores that are related to the subsite of [Fe–Fe]-hydrogenase.

This entailed: (i) determining the reaction order with respect to complex and acid in reactions which lead to the formation of μ -hydride products;

(ii) determining the rate constants for the protonation of a range of complexes which possessed (a) different ligand substituents at the iron centres (b) different dithiolate groups linking the two iron centres;

and (iii) considering how rate constants for protonation might be rationalised in terms of the molecular and electronic structures of the complex.

This objective involved the synthesis and characterisation of 9 new diiron complexes, the crystallographic structures of 8 of which have been determined.

The second objective was to examine the reduction chemistry of cationic {2Fe2S} and {2Fe3S} bridging hydride complexes. In particular, the application of spectroelectrochem-

ical and stopped-flow FTIR and EPR methods to detect intermediates that might bear upon electrocatalysis of hydrogen evolution and how this might relate to the possible role of low-valent iron hydrides in hydrogenase and nitrogenase chemistry.

The third objective was to undertake preliminary studies of muon spectroscopy of {2Fe2S} complexes. A muonium (μ^+e^- or Mu) can be considered as a light hydrogen atom (H \cdot). Its addition to a diiron dithiolate complex is equivalent a concerted proton and an electron transfer. Understanding the structure of short-lived muonium adducts may shed light on transient species occurring during catalytic turnover of hydrogen in the natural and synthetic systems.

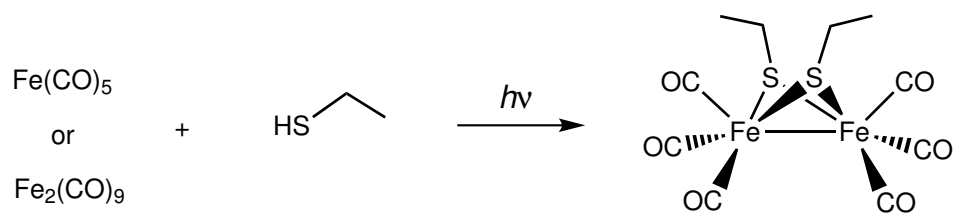
Chapter 2

New {2Fe2S} and {2Fe3S} Systems: Synthesis, Structure and Spectroscopic Properties

2.1 General Pathways to Synthetic [Fe–Fe]-Systems

Synthetic routes to simple diiron hexacarbonyls such as $[\text{Fe}_2(\mu\text{-SEt})_2(\text{CO})_6]$ were first described by Reihlen in 1929,⁴⁹ who showed that the general pathway to these structures involves the use of simple thiol ligands (Scheme 15). This chemistry was further extended by Hieber, Seyferth and others who investigated the reactivity of these complexes towards a variety of nucleophilic and electrophilic reagents.^{54–56} When the first crystallographic characterisation of the H-cluster was reported in 1998²² the striking similarity between the active site of the enzyme and the diiron systems developed over the past 70 years became apparent. It was the availability of these complexes that provided the basis of building an extensive library of close structural analogues for the subsite of the enzyme (see Chapter 1).

Following the structural characterisation of the H-cluster there was an outburst of publications reporting new diiron dithiolate and related systems mimicking structural and functional features of the active site. These models featured different substituents on the metal centres, altered bridgehead ligands and functionalised backbone structures with photoactive or anchoring groups.⁶¹ Recently more attention has been focused on



Scheme 15: Synthetic route to first diiron dithiol hexacarbonyl as reported by Reihlen and co-workers⁴⁹

producing synthetic models which replicate structural elements found in the enzymatic system: an amine bridge to assist in proton shuttling, bridging carbonyl to produce a vacant coordination site, and mixed-valence Fe(I)–Fe(II) centres.^{41,69,114}

Whilst the vast majority of active site mimics have been confined to the synthetically accessible {2Fe2S} assemblies, structural models reproducing sulfur ligation at the proximal iron in the natural system are under-represented. Pickett and co-workers have outlined the procedure of modifying the backbone of a propanedithiolate ligand with an appended thioether group, allowing access to complexes with {2Fe3S} cores (Figure 27).^{114,115} These models not only share close structural features with the H-cluster of the enzyme, but also represent the first spectroscopically characterised examples of a mixed-valence bridging-CO species.^{72,77}

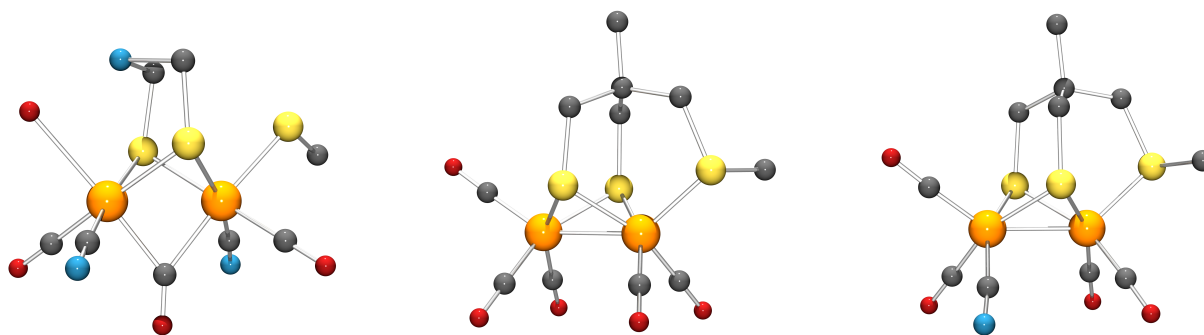


Figure 27: Left: Crystal structure of the H-cluster; Middle and Right: complexes possessing {2Fe3S} moieties reported by Pickett and co-workers^{77,115}

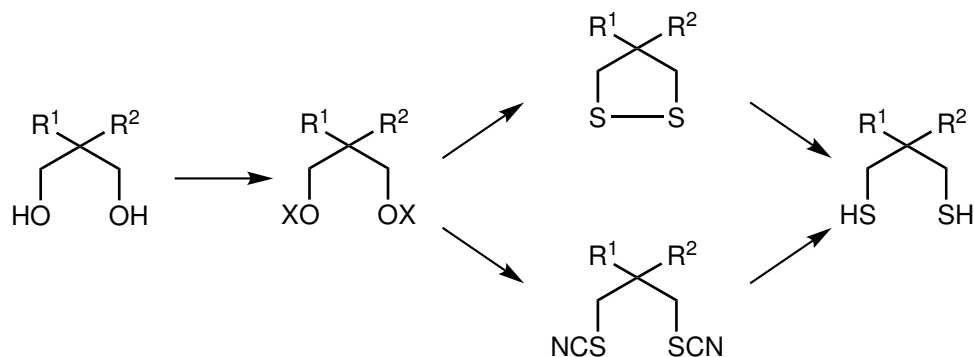
Stable mixed-valence Fe(I)–Fe(II) complexes possessing a rotated state geometry are

few and far between. Darensbourg and co-workers have observed that increasing the steric bulk of the bridgehead group can help stabilise such species.⁶⁹ While they have found no link between the bridgehead substitution and the electron richness of the diiron centres, the subtle control exerted by this remote structural element has not been fully exploited (see Chapter 3).

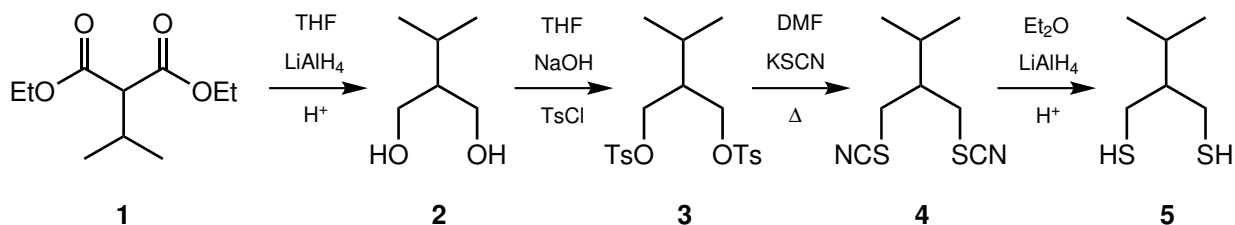
The work described in this chapter has been focused on extending the family of known {2Fe2S} and {2Fe3S} model complexes, with the intention of revealing new reactivity of these assemblies. The need to determine the role of dithiol unit on the protonation kinetics has inspired synthesis of new mimics possessing sterically demanding groups. Protonated derivatives of these mimics not only allowed the paramagnetic hydride systems to be probed, but also granted an unprecedented access to the *super-reduced* states (see Chapter 4).

2.2 Routes to New Dithiolate Ligands

The general approach to synthesising diiron systems with {2Fe2S} cores is to reflux $\text{Fe}_3(\text{CO})_{12}$ and the appropriate dithiol HS-X-SH (where X is a 2 or 3 carbon chain) in a non-coordinating solvent. This route usually affords the desired product in high yields ($\approx 90\%$).⁶⁰ The linear alkyl thiols such as pdt (1,3-propanedithiol) and edt (1,2-ethanedithiol) are commercially available. However, further variations of the μ -dithiolate group by introduction of one or two substituents on the central bridgehead carbon requires synthetic effort. Mono- and dialkylated 1,3-dithiolates have been synthesised before using the general procedure outlined in Scheme 16.^{116,117} This was achieved through a multistep reaction starting from the desired dialcohol, activating it with para-tosyl (Ts) or mesyl (Ms) chloride, then replacing $-\text{OH}$ with a sulfur containing group and finally reducing to give the anticipated dithiol compound.

Scheme 16: General route to dithiols from the corresponding diols (X = Ts, Ms)^{116,117}

The new 2-isopropyl-1,3-dithiol ligand (**5**) was readily synthesised starting from commercially available diethyl isopropyl malonate (**1**) (Scheme 17). This was converted to the corresponding dialcohol by reduction with LiAlH₄ according to the literature procedure.¹¹⁸

Scheme 17: Synthetic route to 2-isopropyl-1,3-dithiolate **5**

Following the general method outlined above, the resulting diol (**2**) was tosylated to give **3**. The formation of **3** was confirmed by ¹H NMR spectroscopy which shows the appearance of two doublets in the aromatic proton region at 7.33 ppm and 7.73 ppm as well as a single CH₃ resonance at 2.43 ppm corresponding to the tosyl group. Formation of **3** was followed by incorporation of a thiocyanate group to obtain **4**. The ¹H NMR spectrum of compound **4** is illustrated in Figure 28. The doublet at 1.00 ppm arises from coupling of 6 chemically and magnetically equivalent protons *a* to a single proton *b*. In addition to the six protons *a*, proton *b* also couples to the single proton *c*. If the two coupling constants have very similar magnitudes, as is likely in an acyclic alkyl system,

then in practice an octet will be observed. Proton *c* exhibits coupling to one *b*, two *d* and two *e* protons. Since *d* and *e* are diastereotopic, the resonance for *c* is expected to appear as a doublet of doublets of doublets. In practice both signals for *b* and *c* overlap, thus only a multiplet at 2.02 ppm is observed. Finally, protons *d* couple to *e* and *c* giving rise to a doublet of doublets at 3.04 ppm. Similarly, the doublet of doublets for protons *e* can be observed at 3.30 ppm. In the infrared spectrum of **4** an intense band at 2157 cm⁻¹ confirmed the incorporation of the thiocyanate group.

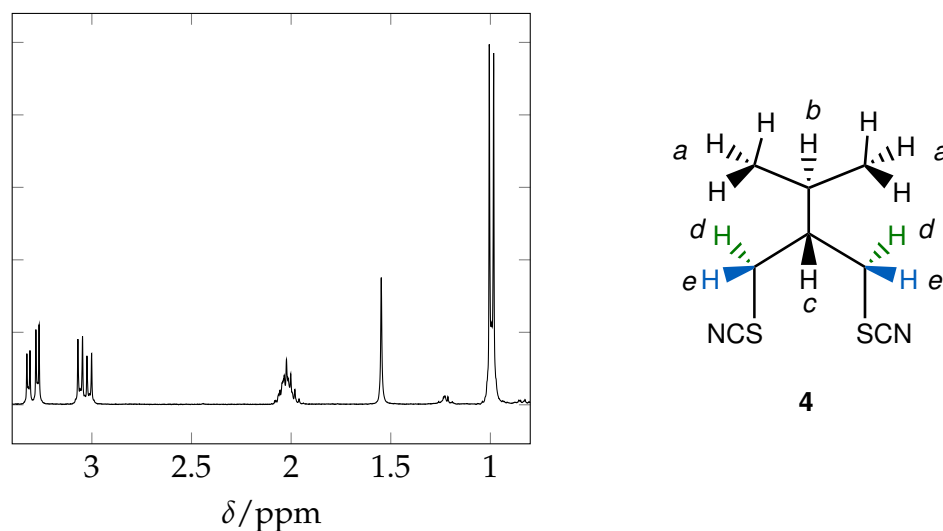
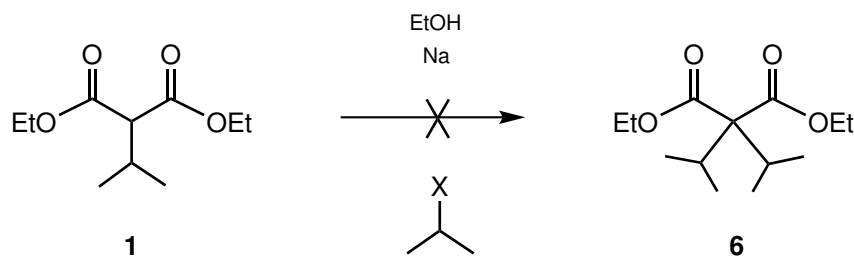


Figure 28: ¹H NMR spectrum of compound **4** in CD₃Cl; a signal at 1.55 ppm was assigned as arising from the residual water

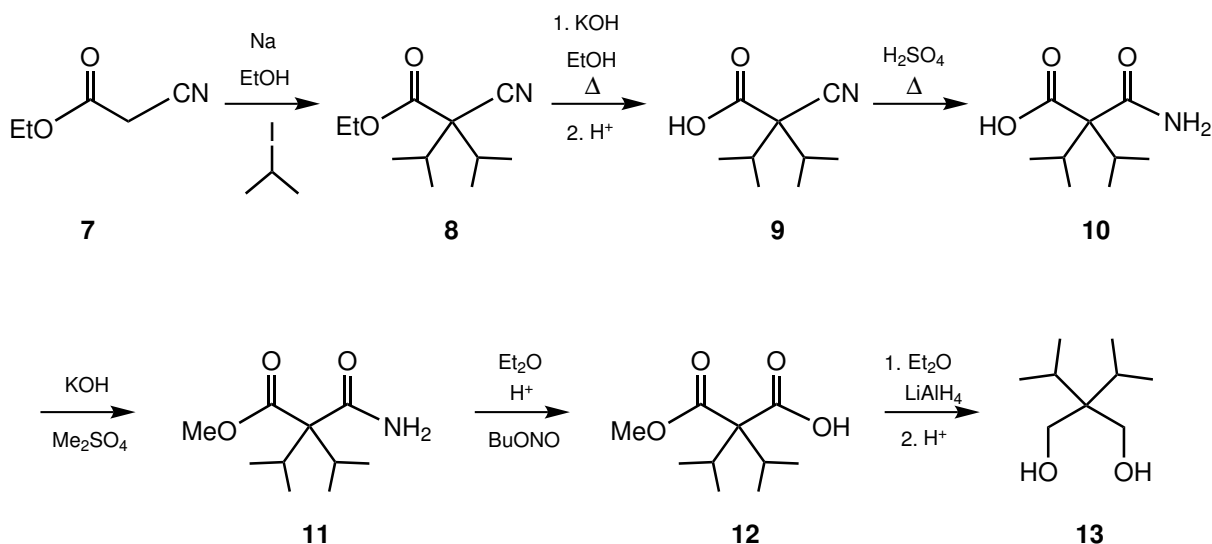
The reduction of **4** yields the desired thiol (**5**). Purification of **5** is challenging, thus only a crude material is used for the following step. Nonetheless, a crude sample of **5** gives a distinct triplet in ¹H NMR spectrum at 1.23 ppm arising from the SH protons coupling to CH₂ protons.

Synthesis of 2-diisopropyl-1,3-dithiolate (**6**) was attempted following the same procedure as for **5** (Scheme 18). However, introduction of a second isopropyl group at the α-carbon proved unsuccessful, presumably due to the steric crowding around the tertiary carbon centre, inhibiting the S_N2 attack.



Scheme 18: Unsuccessful substitution (X = Cl, Br)

An alternative route to alcohol (**13**) starting from ethyl cyanoacetate (**7**) has been described by Newman and Harper (Scheme 19).¹¹⁹ In contrast to reaction with **1**, it was possible to introduce two isopropyl groups in this molecule. This may be due to the small size of the cyano group in **7** relative to that of the ester in **1**, the latter inhibiting access of the electrophile to the anionic centre. Conversion of nitrile functionality (**7**) to a corresponding carboxylic acid (**12**) was carried out according to literature procedure, thus allowing for easy reduction of both the carboxylic acid and the ester groups to the dialcohol (**13**).

Scheme 19: Synthetic route to 2,2-diisopropyl-1,3-dialcohol **13**¹¹⁹

Subsequent conversion of **13** to the new dithiol (**16**) has been carried out following

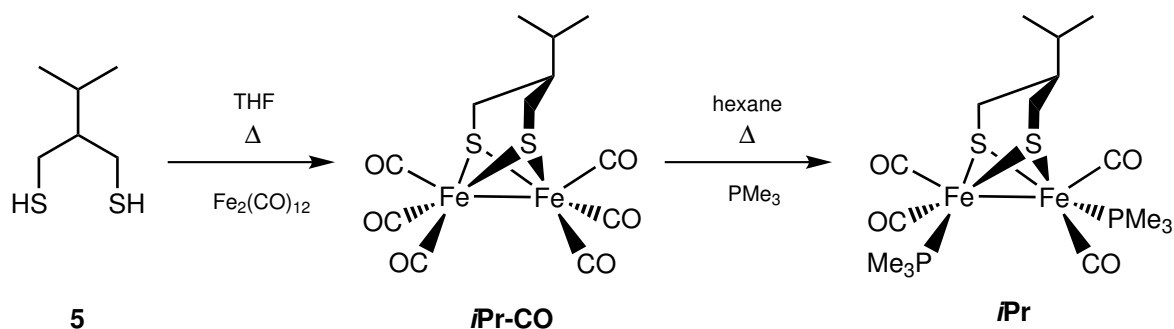
2.3 Synthesis of Functionalised {2Fe2S} and {2Fe3S} Sub-site Analogues

2.3.1 General Aspects

The diiron dithiolate complexes used in this study were prepared by the literature methods as referenced, or by adaptation of these for the synthesis of the 6 new hexacarbonyl and PMe_3 -substituted complexes. The new species were all characterised by five data points. The materials were analytically pure by C and H microanalysis and all were characterised by X-ray crystallography.

2.3.2 {2Fe2S} Frameworks

Synthesis of new substituted diiron dithiolate complexes has been achieved following established literature procedures.⁶⁰ The monoisopropyl dithiolate (**5**) was refluxed with $\text{Fe}_3(\text{CO})_{12}$ in dry THF (tetrahydrofuran) under an inert atmosphere for 1.5 hours after which time the colour change from dark green to deep red indicated completeness of the reaction (Scheme 21). Purification by column chromatography afforded ***i*Pr-CO** in good yield (72 %). Treatment of ***i*Pr-CO** with 2 equivalents of PMe_3 and reflux in hexane for 24 hours produced ***i*Pr** in high yield (86 %).



Scheme 21: Synthetic route to ***i*Pr**

Exchange of two CO groups for two electron-rich phosphines led to a shift in the

carbonyl frequencies of around 95 cm^{-1} to lower values (Figure 29). The shift of CO bands to lower frequencies arises from a greater extent of back-bonding of metal to the empty π^* antibonding orbitals of carbonyl ligands. This is a result of increased electron density around the two iron centres by the addition of two electron-rich, strong σ -donor PMe_3 groups. The greater back-bonding to carbonyls weakens the CO bond and thus the stretching occurs at lower energies.

The ^1H NMR of all-carbonyl or PMe_3 -substituted diiron complexes were found to be undiagnostic as they displayed broadened and overlapping signals at room temperature in which the couplings could not be resolved. This arises from the dynamic behaviour of ligands surrounding the metals *i.e.* a fast bridge-flip from one side to the other and a turnstile motion of CO and/or PMe_3 ligands around the iron atoms. This dynamic behaviour was more fully examined by Darensbourg and co-workers employing low-temperature NMR studies.^{120,121} This group found that at $-80\text{ }^\circ\text{C}$ the ^1H NMR of the $\text{Fe}_2(\text{pdt})_2(\text{CO})_6$ complex was partially resolved showing non-equivalent axial and equatorial CH_2 resonances, but at room temperature overlapping multiplets were observed.

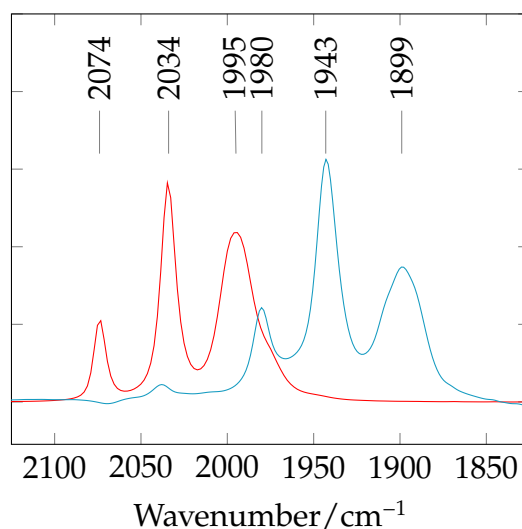


Figure 29: IR spectrum of *iPr*-CO in MeCN (red) and *iPr* in MeCN (blue)

The ^{13}C NMR spectrum of *iPr*-CO is provided in Figure 30 (left): it shows 6 singlets. The two very closely spaced singlets at 207.97 and 207.61 ppm have chemical shifts

consistent with CO resonances. With a fast rotation of the CO groups around the Fe centres a single resonance would be expected, however if the bridge flip is slow then different environments of the Fe(CO)₃ centres may result. If the bridge flip is fast then the apical and basal CO groups might be distinguished. The signal at 19.20 ppm can be assigned to a CH₃ group, as the chemical shift is typical for this type of sp³ carbon. In order to distinguish the remaining environments of carbon a ¹³C DEPT experiment was carried out (Figure 30 right). The negative peak indicates a CH₂ environment, positive resonances correspond to CH and/or CH₃ groups and the carbons with no attached protons (CO) do not give signals in a ¹³C DEPT experiment. Thus the signal at 26.30 ppm can be assigned as arising from the CH₂ carbon. The remaining two carbon signals (49.74 ppm and 33.74 ppm) are due to the two adjacent CH groups in *iPr*-CO. The proton signals for these two groups are overlapping multiplets, and this means further assignment, for example by use of a 2D proton-carbon correlation experiment, is not possible.

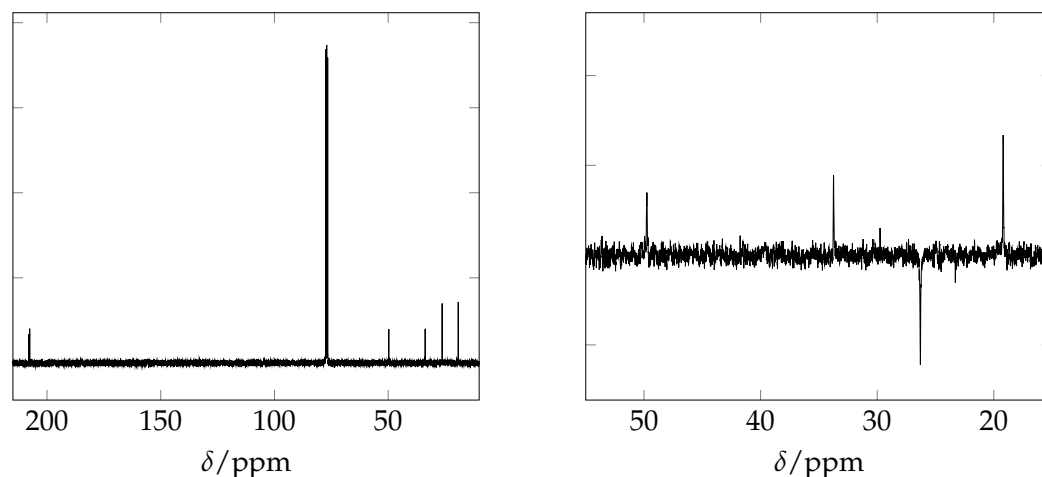
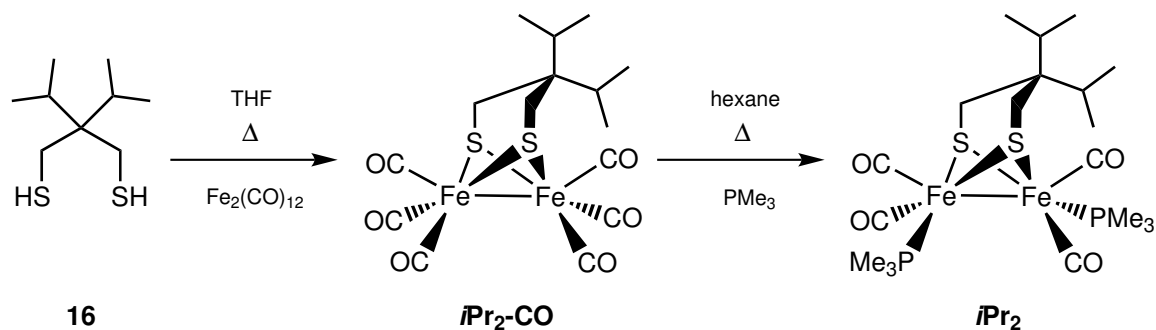


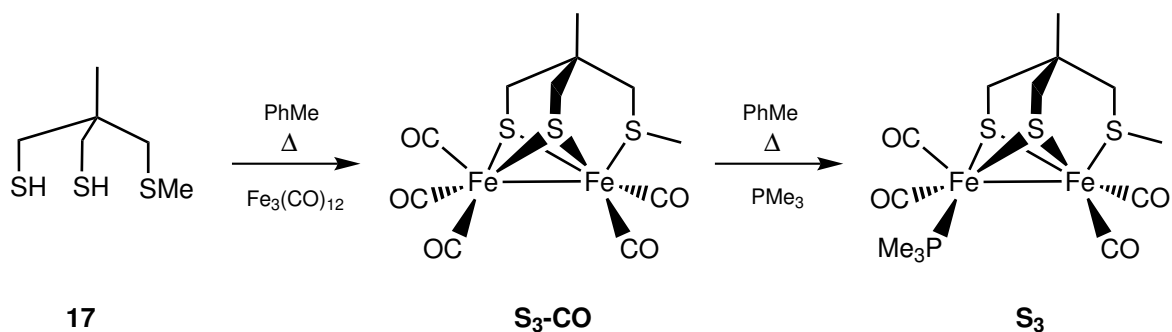
Figure 30: Left: ¹³C NMR spectrum of *iPr*-CO in CD₃Cl; Right: DEPT ¹³C NMR spectrum of *iPr*-CO in CD₃Cl

Preparation of diisopropyl hexacarbonyl *iPr*₂-CO and its substituted derivative *iPr*₂ was carried out using the same procedure as described above (Scheme 22). In contrast to the formation of *iPr*, an IR spectrum after 24 hours showed that the reaction to pro-

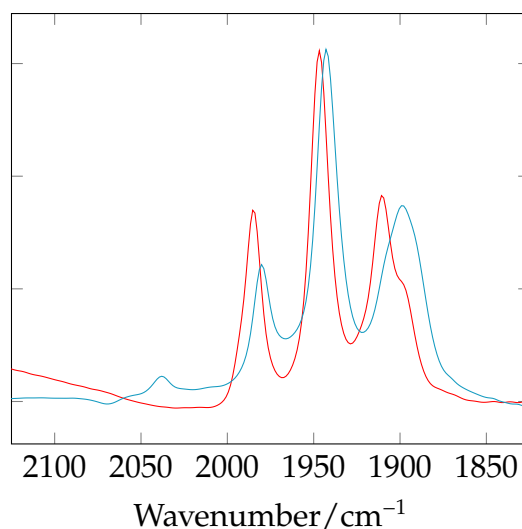
duce iPr_2 was not complete and a significant amount of the starting material remained. However, continuing under the same conditions for additional 5 days led to complete consumption of iPr_2 -CO. The considerably slower substitution of this complex is presumably due to steric hindrance slowing the rate of phosphine attack on the Fe centres. The shift of CO bands in IR spectrum is nearly identical to that observed for the monoisopropyl derivative.

Scheme 22: Synthetic route to iPr_2

Two mono-substituted diiron complexes (**edt-P** and **pdt-P**) were also prepared for a systematic study of the influence of phosphine ligands on the protonation rate and redox potentials, examined in Chapter 3 (Scheme 23). Both of them were synthesized from their corresponding hexacarbonyl complexes (**edt-CO** and **pdt-CO**) following a general literature method.¹²² Mono-substitution was achieved using 1.5 equivalents of trimethylphosphine and in the absence of the external heating. The reaction was accompanied by a shift of IR frequencies in the carbonyl region by *ca* 40 cm^{-1} as expected for introduction of only one PMe_3 ligand.

Scheme 24: Synthetic route to {2Fe3S} model S_3

The substitution of a CO by PMe_3 results in an average of 40 cm^{-1} shift of CO peaks to lower frequencies in the carbonyl region as they experience more back-donation from the metal centres. Interestingly, complex S_3 has a very similar IR spectrum to that of isopropyl ($i\text{Pr}$) or diisopropyl ($i\text{Pr}_2$) derivatives (Figure 31). At first glance this is suggestive of similar electron density around the two metal centres, provided by either two PMe_3 ligands or a PMe_3 and a thioether group. This electronic influence will be discussed in more detail in Chapter 3.

Figure 31: IR spectra in MeCN of S_3 (red) and $i\text{Pr}$ (blue)

It was anticipated that due to chirality at sulfur the complex S_3 would exist in two

isomeric forms. Variable temperature ^{31}P NMR spectroscopy was performed to probe this dynamic behaviour. At room temperature a singlet was observed for the PMe_3 , which coalesced into one broad signal at $-40\text{ }^\circ\text{C}$. Decreasing the temperature to $-90\text{ }^\circ\text{C}$ resulted in appearance of two closely positioned singlets indicative of two distinct species (Figure 32).

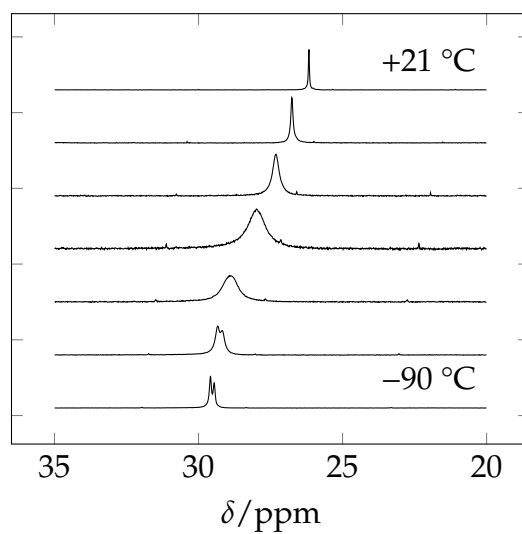


Figure 32: Variable temperature ^{31}P NMR spectrum of S_3 in $(\text{CD}_3)\text{C}=\text{O}$

The shift of the signals upfield and the close proximity between them suggests that this is due to freezing out the inversion of the tethered methyl group at sulfur and not the rotation of PMe_3 . The two resulting diastereomers were assigned as $\text{S}_{3\text{-trans}}$ where PMe_3 and Me group are *transoid* to one another and $\text{S}_{3\text{-cis}}$ where both PMe_3 and Me are *cisoid* (Figure 33).

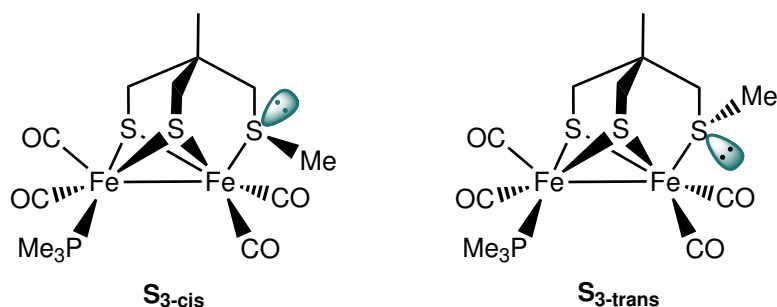


Figure 33: Schematic representation of two diastereomers of complex S_3 due to chirality at sulfur

2.4 Synthesis of Hydride Complexes

2.4.1 General Aspects

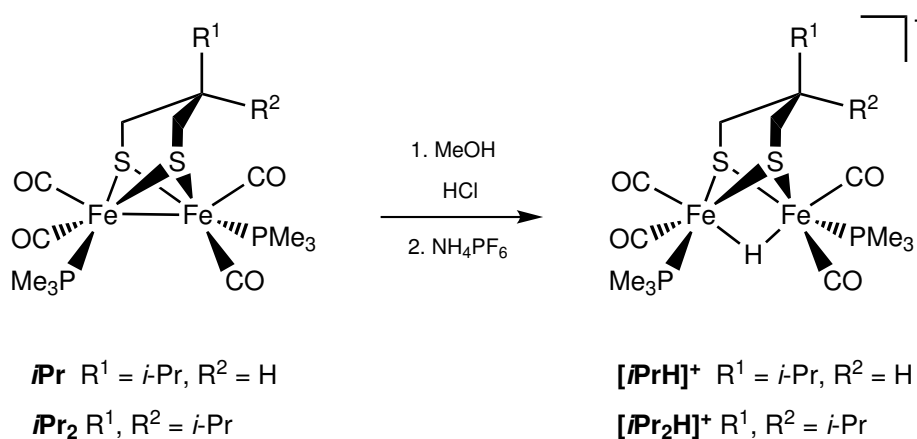
The hydride complexes used in this study were prepared by the literature methods as referenced, or by adaptation of these. All three of the new hydride species were analytical pure by C and H microanalysis. Five and six data points were obtained for complexes $[iPrH]^+$ and $[S_3H]^+$ respectively; crystals suitable for X-ray analysis of compound $[iPr_2H]^+$ could not be obtained and its characterisation is limited to four data points.

2.4.2 {2Fe2S} and {2Fe3S} Hydrides

Metal hydride species have been postulated as intermediates in the catalytic mechanism of hydrogen evolution/uptake of hydrogenases, but thus far have not been observed spectroscopically in the natural system. Synthetic models of the subsite do readily protonate and have been studied extensively to gain mechanistic understanding of their formation as well as establish their viability as electrocatalysts for hydrogen evolution.

Protonation of the vast majority of Fe(I)–Fe(I) models leads to a direct attack on a metal–metal bond resulting in a formation of a bridging hydride Fe(II)(μ -H)Fe(II) species. However, when sufficiently electron donating ligand arrangements are used, terminal hydrides have been isolated.^{94–96} Synthesis of a bridging hydride species is

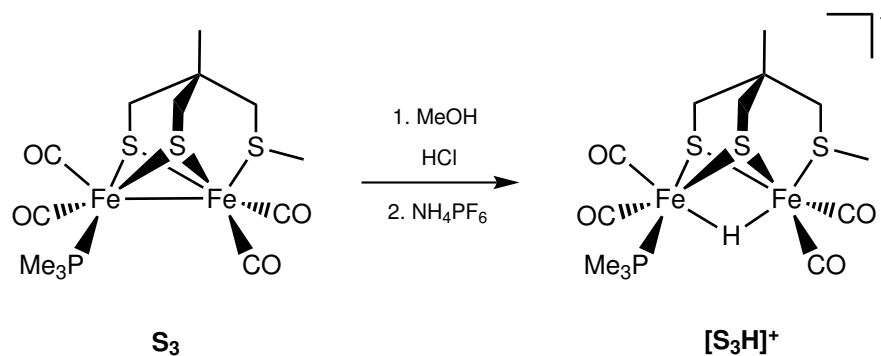
a well-established procedure: the complex is stirred in acidified methanol, then precipitated with NH_4PF_6 to give the desired μ -hydride species.¹²⁹ Compounds $[\mathbf{iPrH}]^+$ and $[\mathbf{iPr}_2\text{H}]^+$ were produced following this general method (Scheme 25). Following the reactions, IR spectra gave an anticipated shift of CO frequencies of around 90 cm^{-1} to higher wavenumbers for both systems.¹⁰¹ Both exhibit triplets at around -15 ppm , typical for isolated bridging hydride species.⁹⁷ The coupling constants of 22 Hz are consistent with a basal phosphine geometry.



Scheme 25: Synthetic route to new {2Fe2S} hydride complexes

While synthetic bridging hydrides at {2Fe2S} cores are structurally well-established, protonation of related {2Fe3S} moieties, which resemble the active site of [Fe–Fe]-hydrogenase more closely, have never been explored. Pleasingly, such species can be generated by protonation of S_3 using conditions described above to give the first hydride species at a well-defined {2Fe3S} core (Scheme 26). In the hydride region of a ^1H NMR $[\text{S}_3\text{H}]^+$ gives rise to a doublet at around -20 ppm , around 5 ppm more negative than seen for $[\mathbf{iPrH}]^+$ and $[\mathbf{iPr}_2\text{H}]^+$, but still consistent with its identification as a μ -hydride. As for $[\mathbf{iPrH}]^+$, the coupling constant of 21 Hz supports formulation with PMe_3 in a basal position. The average shift of CO bands following a protonation are identical to that observed for the {2Fe2S} complex \mathbf{iPr} , however, the pattern is different (Figure 34). This is presumably due to the rigidity and enforced asymmetry of the tripodal thioether ligand in $[\text{S}_3\text{H}]^+$ in

comparison with $[iPrH]^+$.



Scheme 26: Synthetic route to a first {2Fe3S} hydride complex

Details of the protonation mechanisms for all the new complexes will be discussed in Chapter 3.

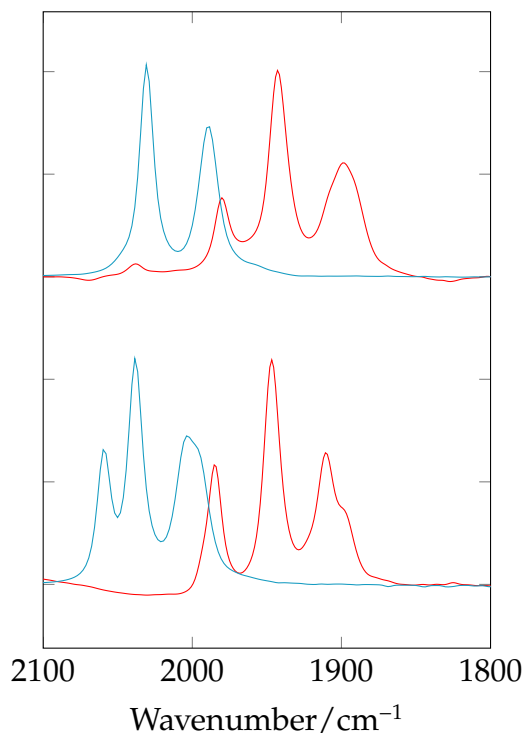


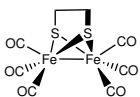
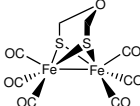
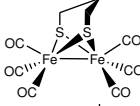
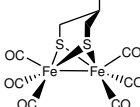
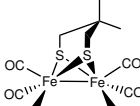
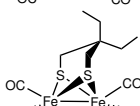
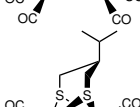
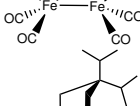
Figure 34: Top: protonation of {2Fe2S} complex iPr in MeCN; Bottom: protonation of {2Fe3S} complex S_3 in MeCN; Red traces: unprotonated complexes; Blue traces: protonated complexes

2.5 Comparative Structural Data and Spectroscopic Properties

The isolated structure of the active site of [Fe–Fe]-hydrogenase in its resting state (\mathbf{H}_{ox}) clearly exhibits a bridging CO ligand linking the two iron atoms.²² Thus far most of the reported synthetic analogues of the subsite that aim to mimic both the structure and the function of the enzyme do not possess this rotated geometry.⁶¹ Very recently a few groups have succeeded in replicating this significant feature in synthetic models by introducing geometrically or electronically demanding groups.^{69,130} This was in part elicited in DFT calculations performed by Tye *et al.*, which revealed that both the substitution of CO by more electron-donating ligands and the steric bulk built into the bridgehead carbon stabilizes the rotated state.¹³¹

Many of the precursors to the bis- PMe_3 diiron complexes display nearly identical infrared band patterns and positions in their solution spectra regardless of the bulkiness of the substituents on the bridge (Table 3). These systems exhibit dynamic behaviour in solution at room temperature *i.e.* the dithiolate bridge is flipping back and forth and the co-ligands around the iron metals are rotating a turnstile motion. As noted earlier Darensbourg and co-workers have undertaken low temperature ^1H NMR studies of these systems and shown the bridge-flip can be frozen out at $-80\text{ }^\circ\text{C}$.^{120,121} However, the X-ray structures of $i\text{Pr-CO}$ and $i\text{Pr}_2\text{-CO}$ confirm the observation that the bulk of the bridge alone in the hexacarbonyl series is not sufficient to distort the geometry around the two iron centres *i.e.* formation of a semi-bridging CO state is not observed (Figure 35).

Table 3: Comparative table of Fe–Fe bond lengths and infrared CO frequencies (hexane) for selected {2Fe2S} complexes with increasingly bulky bridgehead groups

Name	Structure	Fe–Fe/Å	$\tilde{\nu}_{\max}/\text{cm}^{-1}$
edt-CO		–	2078, 2038, 2008, 1995, 1985
odt-CO		2.5113(13) ¹³²	2080, 2043, 2006, 1989
pdt-CO		2.5103(11) ⁶²	2076, 2035, 2006, 1992, 1982
Me-CO		2.4877(9) ¹³³	2076, 2036, 2006, 1992, 1982 ¹³³
Me₂-CO		2.494(6) ¹³⁴	2075, 2034, 2005, 1992, 1980 ¹³⁴
Et₂-CO		2.501(4) ¹³⁴	2073, 2031, 2005, 1990, 1979 ¹³⁴
iPr-CO		2.5097(3)	2075, 2035, 2006, 1991, 1981
iPr₂-CO		2.5100(8)	2074, 2033, 2006, 1990, 1978

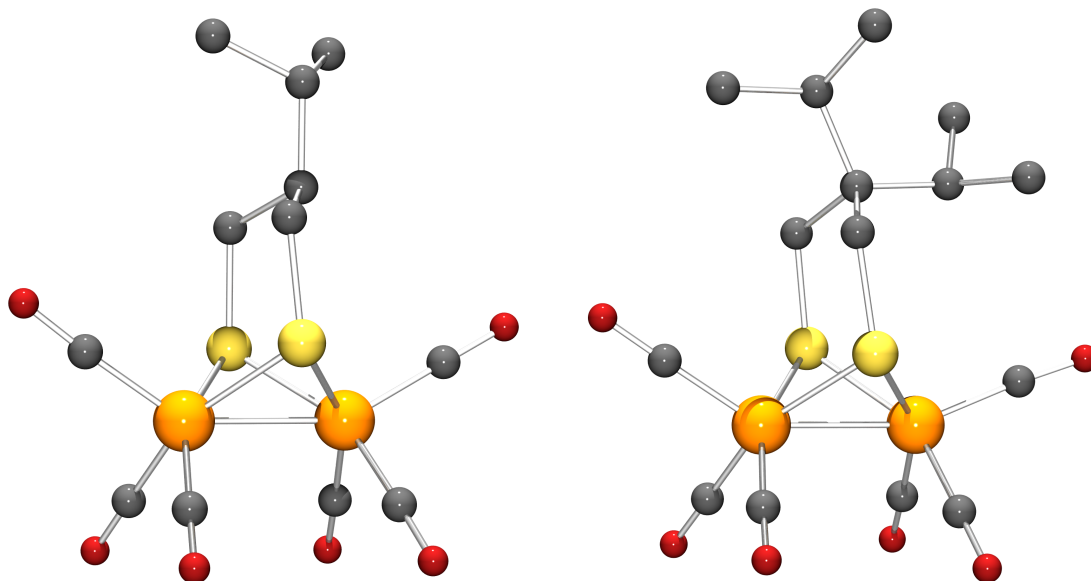


Figure 35: X-ray crystal structures of *i*Pr-CO (left) and *i*Pr₂-CO (right) with spheres of arbitrary size; hydrogen atoms have been omitted for clarity

Replacement of CO by the stronger donor ligand PMe₃ results in an increase of Fe-Fe bond lengths by between 0.010(2) Å (pdt bridge) and 0.1048(11) Å (monoisopropyl bridge). However, there appears to be no systematic variation upon substitution, *i.e.* the PMe₃ group does not add a predictable amount to the metal-metal distance (Table 4). This is in sharp contrast to the IR, where there is a systematic trend: an average 100 cm⁻¹ shift in the CO region upon coordination of the strongly σ -donating PMe₃.

Table 4: Comparative table of Fe–Fe bond lengths and infrared CO frequencies for selected {2Fe2S} complexes with PMe₃ substituents

Name	Structure	Fe–Fe/Å	$\tilde{\nu}_{\max}/\text{cm}^{-1}$
edt		2.5159(6) ¹²¹	1981, 1944, 1897 ^{a,101}
odt		2.5235(5) ¹³⁵	1984, 1947, 1898 ^{a,135}
pdt		2.555(2) ¹²²	1980, 1943, 1898 ^{a,100}
Me		2.585(3)	1980, 1943, 1899 ^{a,133}
Me₂		2.5690(7) ³³	1980, 1940, 1899 ^{b,33}
Et₂		2.5367(17) ⁶⁹	1980, 1938, 1899 ^{b,69}
iPr		2.6145(8)	1980, 1943, 1899 ^a
iPr₂		2.5392(5)	1982, 1945, 1909 ^a

^a CH₃CN; ^b CH₂Cl₂

Notably, the majority of PMe₃-substituted complexes adopt a ‘pseudo-symmetrical’ arrangement of CO ligands, where both of the Fe atoms rest in an unrotated state. The presence of the substituted bridgehead in most of these complexes means that there is no formal mathematical symmetry in position of metal substituents. Ignoring the bridgehead part of the molecule one can imagine a C₂ axis passing vertically through the metal–metal bond. In that case the substituents lie very close to idealised in this analysis and thus the arrangement is referred to as *pseudo-symmetrical*.

Intriguingly, the combination of steric bulk at the bridgehead and electron richness imparted by the PMe_3 ligands does result in the adoption of an enzyme-like semi-rotated geometry at one iron centre in the solid state structure of $i\text{Pr}_2$ (Figure 36). This contrasts with both the parent hexacarbonyl $i\text{Pr}_2\text{-CO}$ and the bis-phosphine $i\text{Pr}$, which features only one isopropyl group, emphasizing the importance of the optimal combination of steric and electronic parameters. The semi-rotated geometry is characterised by a shortened distance between the basal CO and the remote Fe centre, descended apical carbonyl and an increased angle between the apical CO and the metal–metal bond. In fact, the structure is in close agreement with the reduced state of the enzyme (H_{red}), which exhibits apical CO–proximal iron distance of 2.807 Å.²³ This altered geometry in $i\text{Pr}_2$ is not evident in the solution phase due to dynamic behaviour of the system, where fast ligand rotation around the metal centres is expected. This is entirely consistent with the general pattern observed for the bridgehead substituted complexes.

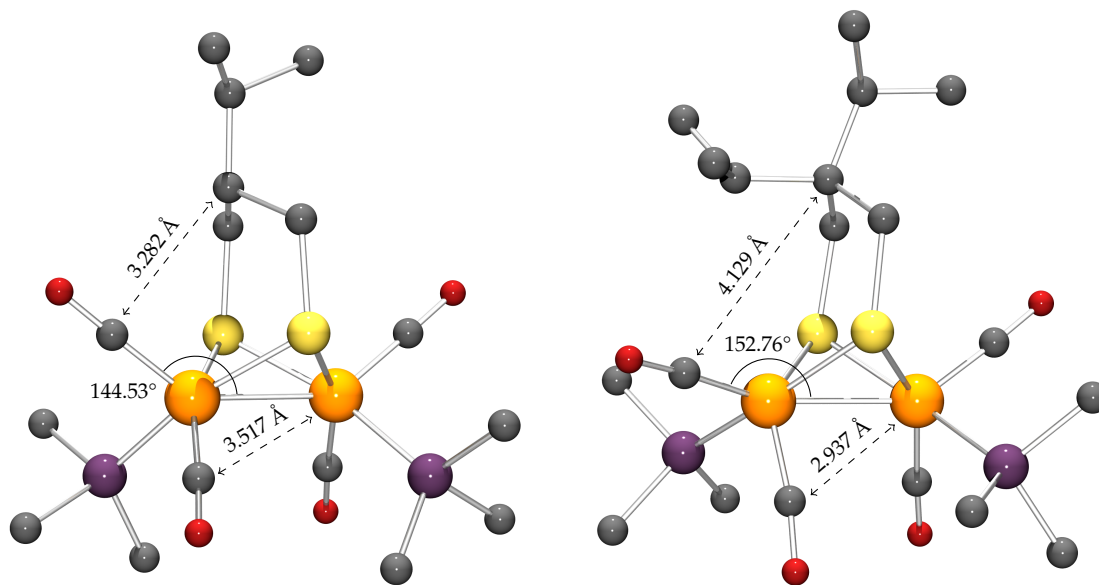


Figure 36: X-ray crystal structures of $i\text{Pr}$ (left) and $i\text{Pr}_2$ (right) with spheres of arbitrary size, showing selected angles and distances; hydrogen atoms have been omitted for clarity

Whilst the substitution of CO ligands by phosphines yields an increase in the Fe–Fe

bond distance in all mentioned cases, there is no such trend accompanying protonation. For example, protonated complexes with edt, pdt and dimethyl bridges exhibit an elongated metal···metal vector, however systems possessing monomethyl and monoisopropyl bridges display a decrease in the Fe···Fe distance when compared to their unprotonated parent complexes (Tables 4 and 5). That the differences in bond lengths of the unprotonated and protonated pairs is statistically significant can be judged in the following way.

The standard deviation (σ) for the bond length is the bracketed value in the listed data (Tables 4 and 5). Accepted criteria of statistical significance when comparing bond data is expressed in Equation 2.

$$L_A - L_B > 3(\sigma_A + \sigma_B) \quad (2)$$

where L_A and L_B are the bonds compared and σ_A and σ_B are the respective standard deviations for these bonds. Three times the sum of the sigma values embraces 99% of the distribution curve for the bond length data. This criteria establishes whether or not there is significant 'overlap' of bond distances L_A and L_B at the 3σ level. For example, the difference in the Fe···Fe bond distances between complex **pdt** and its protonated derivative [**pdtH**]⁺ is 0.0237. The values of σ are 0.002 and 0.0008 respectively, giving a total 3σ of 0.0084. Thus the criteria given in Equation 2 is met, the Fe–Fe bond significantly lengthens on protonation. In contrast the difference in the Fe···Fe bond distances between complex **iPr** and its protonated derivative [**iPrH**]⁺ is -0.0281. The values of σ are 0.008 for both, giving a total 3σ of 0.0048. The criteria given in Equation 2 is met, and the Fe–Fe bond significantly decreases on protonation.

This is in stark contrast to IR, where addition of a proton systematically shifts CO peaks by an average 70 cm⁻¹ (Table 5). Whilst all complexes fall within the hydride region of ¹H NMR typical for a μ -hydride species,⁹³ the signals range from -13 ppm to -17 ppm. Notably, the hydride shifts for model systems possessing a three-carbon bridge, all cluster around -15 ppm.

Table 5: Comparative table of Fe...Fe distances, infrared CO frequencies and hydride shifts for selected {2Fe2S} complexes

Name	Structure	Fe...Fe/Å	$\tilde{\nu}_{\max}/\text{cm}^{-1}$	$\delta_{\text{H}}/\text{ppm}$
[edtH] ⁺		2.5742(13) ¹²¹	2034, 1990 ^{a,101}	-17.33 ^{c,101}
[odtH] ⁺		2.5770(15)	2037, 1997 ^{a,135}	-13.40 ^{c,135}
[pdtH] ⁺		2.5787(8) ¹²⁹	2031, 1990 ^{a,100}	-15.27 ^{c,100}
[MeH] ⁺		2.5836(4) ¹³³	2032, 1989 ^{a,133}	-15.45 ^c
[Me2H] ⁺		2.5880(8) ¹³³	2030, 1988 ^a	-15.14 ^c
[Et2H] ⁺		—	—	—
[iPrH] ⁺		2.5864(8)	2032, 1990 ^b	-15.35 ^d
[iPr2H] ⁺		—	2029, 1987 ^b	-15.22 ^d

^a CH₃CN; ^b CH₂Cl₂; ^c CD₃CN; ^d CD₂Cl₂

In the case of {2Fe3S} complex **S**₃, substitution of CO by a single PMe₃ ligand results in a small increase of the Fe–Fe distance, and a shift of CO bands in IR by an average of 40 cm⁻¹. The structural similarities between **S**₃ and the subsite of the enzyme are evident from Figure 37. The Fe–Fe distance and the average bridging Fe–S lengths in the synthetic complex are similar to those estimated for the protein. Whilst the thioether Fe–S distance is shorter than the corresponding subsite Fe–S_{cysteine} length, the angles

between the sulfurs are in good agreement.

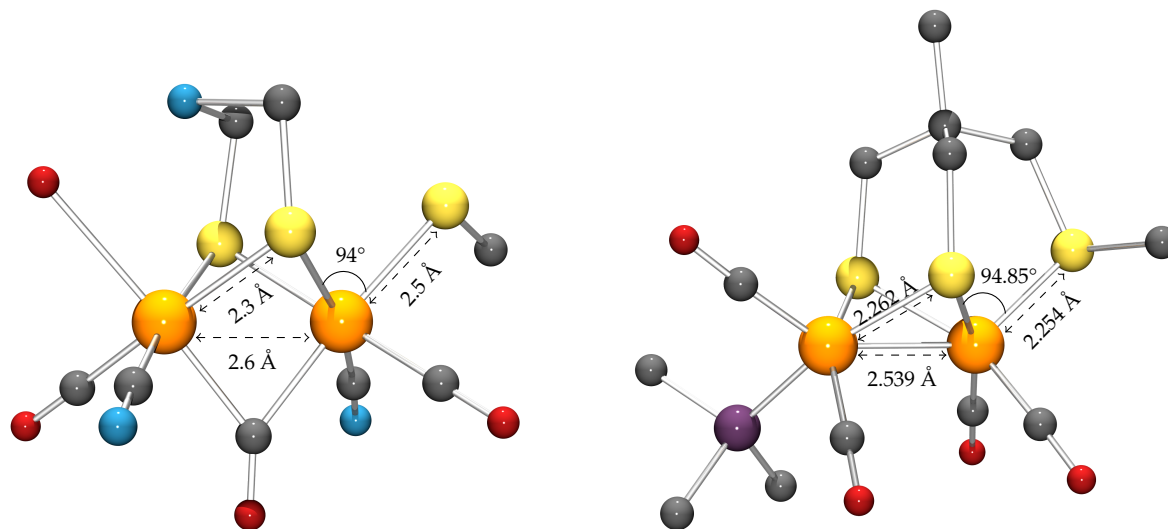
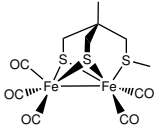
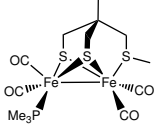
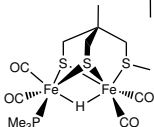


Figure 37: X-ray crystal structures of the active site of [Fe-Fe]-hydrogenase²² (left) and S₃ (right) with spheres of arbitrary size, showing selected angles and distances; hydrogen atoms have been omitted for clarity

As for {2Fe2S} systems, following the addition of a proton, CO peaks move to higher frequencies by around 70 cm⁻¹ (Table 6). Whilst [S₃H]⁺ displays the most upfield hydride shift in ¹H NMR of all the aforementioned complexes, exhibiting a signal at -20 ppm, it still falls within the region typical for a bridging hydride species.

Table 6: Comparative table of Fe...Fe distances and infrared CO frequencies (CH₃CN) for {2Fe3S} complexes

Name	Structure	Fe...Fe/Å	$\tilde{\nu}_{\max}/\text{cm}^{-1}$
S₃-CO		2.5158(10) ¹¹⁵	2046, 1979, 1925 ¹¹⁵
S₃		2.5387(4)	1984, 1947, 1910
[S₃H]⁺		2.5659(4)	2060, 2038, 2003

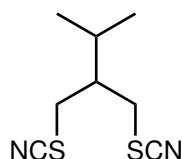
2.6 Experimental

Unless otherwise stated, all reactions were carried out under nitrogen atmosphere using conventional air-sensitive techniques. Solvents were degassed using a nitrogen purge and dried using an M. Braun solvent purifier unit before use. Starting materials were of reagent grade and were used as purchased from Sigma-Aldrich or Alfa Aesar. NMR spectra were collected at room temperature on a Bruker Avance 300 spectrometer operating at 300 MHz. FT-IR spectra were recorded on a Bruker Vertex 80 spectrometer. Elemental analysis and mass spectrometry were performed at London Metropolitan University and Swansea University, respectively. Compounds **2**,¹¹⁸ **13**,¹¹⁹ **17**,⁷⁷ **edt-CO**,⁶⁰ **pdt-CO**,⁶⁰ **odt-CO**,¹³² **S₃-CO**,¹¹⁵ **edt**,¹²¹ **pdt**,¹²⁹ **odt**¹³⁵ and **pdt-P**¹²² were prepared according to literature procedures.

The X-ray crystal structures for complexes **edt-P**, **S₃** and **[S₃H]⁺** were determined by the author and Dr. J. A. Wright at the University of East Anglia. The X-ray crystal structures for complexes **[iPr]-CO**, **[iPr₂]-CO**, **[iPr]**, **[iPr₂]** and **[iPrH]⁺** were determined by the National Crystallography Service, Southampton. For X-ray crystallography crystals were suspended in oil and mounted on a glass fibre or MiTeGen micromount and fixed in the

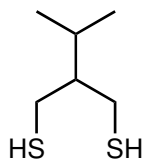
(CDCl₃) δ 19.81 (CH₃), 21.72 (CH₃), 25.86 (CH), 43.78 (CH), 67.62 (CH₂), 127.93 (aromatic CH), 129.98 (aromatic CH), 132.45 (aromatic C), 145.06 (aromatic C). m/z (orbitrap) calcd for C₂₀H₂₆O₆S₂NH₄ (M⁺ + NH₄) 444.1509, found 444.1497.

1,3-Bis(thiocyanato)-2-(propan-2-yl)propane (4)



Compound **3** (3.10 g, 7.27 mmol) and KSCN (7.06 g, 72.7 mmol) were dissolved in DMF (100 mL) and stirred at 140 °C for 12 hours. The reaction mixture was allowed to cool before adding it to water (200 mL) to give a cloudy yellow solution. This was extracted with CH₂Cl₂ (3 × 100 mL), washed with HCl (1 M, 100 mL), sat. NaHCO₃ (100 mL), brine (100 mL) and dried over MgSO₄. The solution was filtered and the solvent removed *in vacuo* to give yellow oil. Column chromatography (hexane : diethyl ether 3 : 2) gave (**4**) as white feathery crystals (0.70 g, 48 %). Crystals suitable for X-ray analysis were grown by slow evaporation of a solution of **4** in hexane : diethyl ether 3 : 2. Anal. found (calcd) for C₈H₁₂N₂S₂: C, 47.88 (47.99); H, 6.13 (6.05); N, 14.14 (14.00) %. $\tilde{\nu}_{\max}/\text{cm}^{-1}$ (MeCN) 2157 (SCN). ¹H NMR (CDCl₃) δ 1.00 (6H, d, $J_{HH} = 6.6$ Hz, CH₃), 2.02 (1H + 1H, m, CH-CH), 3.04 (dd, 2H, $J_{HH} = 7.0$ Hz, 13.6 Hz, CH₂), 3.30 (2H, dd, $J_{HH} = 4.7$ Hz, 13.6 Hz, CH₂). ¹³C NMR (CDCl₃) δ 19.40 (CH₃), 28.83 (CH), 34.60 (CH), 45.25 (CH₂), 111.65 (SCN). m/z (orbitrap) calcd for C₈H₁₂N₂S₂H (M⁺ + H) 201.0515, found 201.0515.

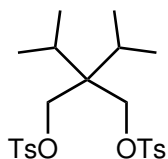
2-(Propan-2-yl)propane-1,3-dithiol (5)



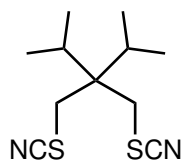
Compound **4** (1.80 g, 9.0 mmol) was dissolved in dry Et₂O (30 mL) and added drop wise *via* cannula to a cooled (0 °C) suspension of LiAlH₄ (0.68 g, 18.0 mmol) in Et₂O (50 mL).

On completion of addition, the solution was stirred for 12 hours at 50 °C. The reaction mixture was then cooled (0 °C) and quenched with drop wise addition of degassed water (40 mL) and HCl (6 M, 30 mL). The product was extracted with Et₂O (3 × 40 mL) and dried over MgSO₄. The solution was filtered and the solvent removed *in vacuo* to give **5** as a yellow oil (1.15 g, 85 %). ¹H NMR (CDCl₃) δ 0.89 (6H, d, *J*_{HH} = 6.8 Hz, CH₃), 1.23 (2H, t, *J*_{HH} = 8.2 Hz, SH), 1.39 (1H, m, CH-CH₂), 1.85 (1H, *pseudo*-octet., *J*_{HH} = 6.8 Hz, CH-CH₃), 2.62 (ddd, *J*_{HH} = 7.7 Hz, 13.5 Hz, 13.6 Hz, CH₂), 2.76 (ddd, 2H, *J*_{HH} = 5.0 Hz, 8.1 Hz, 13.5 Hz, CH₂). ¹³C NMR (CDCl₃) δ 19.80 (CH₃), 24.75 (CHCH₃), 28.33 (CHCH₂), 49.77 (CH₂).

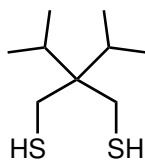
1,3-Bis(toluenesulfonyl)-2,2-bis(propan-2-yl)propane (**14**)



Potassium hydroxide (10.66 g, 190 mmol) was dissolved in THF (200 mL) and treated with a solution of **13** (3.31 g, 21 mmol) in THF (50 mL). The mixture was cooled in ice-salt bath with vigorous stirring and *p*-toluenesulfonyl chloride (22.88 g, 120 mmol) was added slowly. The yellow milky solution was stirred in ice bath for 2 hours and then at room temperature for 10 hours. The solvent was removed *in vacuo*. The resulting yellow residue was dissolved in CH₂Cl₂ (70 mL) and washed with water (3 × 60 mL). The aqueous washings were extracted with CH₂Cl₂ (2 × 60 mL). The combined organic phase was washed with brine (100 mL), dried over MgSO₄, filtered and solvent removed *in vacuo*. Column chromatography (hexane : ethyl acetate 8 : 1) gave **14** as a white powder (6.74 g, 69 %). Anal. found (calcd) for C₂₃H₃₂O₆S₂: C, 58.86 (58.95); H, 6.78 (6.89) %. ¹H NMR (CDCl₃) δ 0.81 (12H, d, *J*_{HH} = 7.0 Hz, CH₃), 1.86 (2H, sept., *J*_{HH} = 7.0 Hz, CH-CH₃), 2.44 (6H, s, aromatic CH₃), 3.88 (4H, s, CH₂), 7.33 (4H, d, *J*_{HH} = 8.3 Hz, aromatic CH), 7.73 (4H, d, *J*_{HH} = 8.3 Hz, aromatic CH). *m/z* (orbitrap) calcd for C₂₃H₃₂O₆S₂NH₄ (M⁺ + NH₄) 486.1979, found 486.1966.

1,3-Bis(thiocyanato)-2,2-bis(propan-2-yl)propane (15)

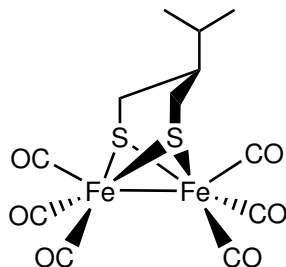
Compound **14** (3.20 g, 6.83 mmol) and KSCN (6.63 g, 68.3 mmol) were dissolved in DMF (100 mL) and stirred at 150 °C for 36 hours. The reaction mixture was allowed to cool before adding it to water (200 mL) to give a cloudy yellow solution. This was extracted with CH₂Cl₂ (3 × 100 mL), washed with HCl (1 M, 100 mL), sat. NaHCO₃ (100 mL), brine (100 mL) and dried over MgSO₄. The solution was filtered and the solvent removed *in vacuo* to give a yellow oil. Column chromatography (hexane : ethyl acetate 4 : 1) gave **15** as a white powder (0.75 g, 45 %). Anal. found (calcd) for C₂₃H₃₂O₆S₂: C, 54.57 (54.42); H, 7.28 (7.49), N 11.43 (11.57) %. $\tilde{\nu}_{\max}/\text{cm}^{-1}$ (MeCN) 2157 (SCN). ¹H NMR (CDCl₃) δ 1.02 (12H, d, $J_{\text{HH}} = 7.0$ Hz, CH₃), 2.00 (2H, sept., $J_{\text{HH}} = 7.0$ Hz, CH), 3.26 (4H, s, CH₂). ¹³C NMR (CDCl₃) δ 18.62 (CH₃), 32.45 (CH), 39.80 (CH₂), 44.82 (CH), 112.33 (SCN). m/z (orbitrap) calcd for C₁₁H₁₈N₂S₂NH₄ (M⁺ + NH₄) 260.1250, found 260.1248.

2,2-Bis(propan-2-yl)propane-1,3-dithiol (16)

Compound **15** (120 mg, 0.50 mmol) was dissolved in dry THF (40 mL) and added drop wise *via* to a suspension of LiAlH₄ (40 mg, 1.0 mmol) in THF (50 mL). On completion of addition, the solution was refluxed for 12 hours. The reaction mixture was then cooled (0 °C) and quenched with drop wise addition of degassed water (40 mL) and HCl (6 M, 30 mL). The product was extracted with Et₂O (3 × 40 mL) and dried over MgSO₄. The solution was filtered and the solvent removed *in vacuo* to give **16** as yellow oil (74 mg, 77 %). ¹H NMR (CDCl₃) δ 0.97 (12H, d, $J_{\text{HH}} = 7.1$ Hz, CH₃), 1.25 (2H, t, $J_{\text{HH}} = 8.1$ Hz,

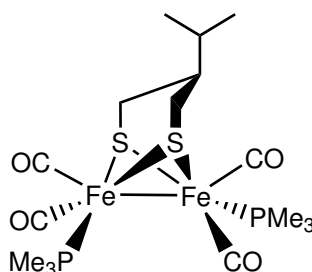
SH), 1.94 (2H, sept., $J_{HH} = 7.1$ Hz, CH), 2.73 (4H, d, $J_{HH} = 8.1$ Hz, CH₂).

Fe₂{μ-SCH₂CH(*i*-Pr)CH₂S}(CO)₆ (*i*Pr-CO)



A mixture of Fe₃(CO)₁₂ (670 mg, 1.33 mmol) and **5** (200 mg, 1.33 mmol) was dissolved in dry THF (60 mL) and refluxed under nitrogen for 1.5 hours until the colour changed from deep green to dark red. The solvent was removed *in vacuo* to give dark red solid. The complex was purified using column chromatography eluting with hexane and affording ***i*Pr-CO** as a red-orange solid (410 mg, 72 %). Single crystals suitable for X-ray were grown from hexane at -4 °C. Anal. found (calcd) for C₁₂H₁₂Fe₂O₆S₂: C, 33.64 (33.67); H, 2.78 (2.83) %. $\tilde{\nu}_{\max}/\text{cm}^{-1}$ (hexane) 2075, 2035, 2006, 1991, 1981 (CO). ¹³C NMR (CDCl₃) δ 19.20 (CH₃), 26.28 (CH₂), 33.74 (CH), 49.74 (CH), 207.61 (CO). *m/z* (orbitrap) calcd for C₁₂H₁₂Fe₂O₆S₂HO (M⁺ + H + O) 444.8796, found 444.8804.

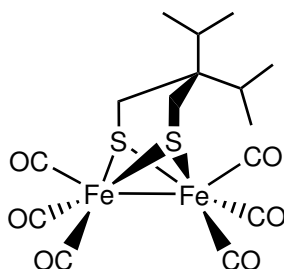
Fe₂{μ-SCH₂CH(*i*-Pr)CH₂S}(CO)₄(PMe₃)₂ (*i*Pr)



Trimethylphosphine (0.10 mL, 0.90 mmol) was added to a solution of ***i*Pr-CO** (110 mg, 0.26 mmol) in hexane (40 mL). The solution was heated to reflux for 24 hours after which time it became dark red. Filtration through Celite followed by removal of solvent *in vacuo* afforded crude product as dark red powder, which was purified by crystallisation from a

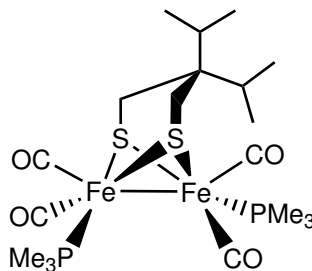
concentrated hexane solution at $-30\text{ }^{\circ}\text{C}$ (540 mg, 86 %). Single crystals suitable for X-ray were grown from hexane at $-4\text{ }^{\circ}\text{C}$. Anal. found (calcd) for $\text{C}_{16}\text{H}_{30}\text{Fe}_2\text{O}_4\text{P}_2\text{S}_2$: C, 36.55 (36.66); H, 5.87 (5.77) %. $\tilde{\nu}_{\text{max}}/\text{cm}^{-1}$ (MeCN) 1980, 1943, 1899 (CO). ^{13}C NMR (CDCl_3) δ 19.63 (d, $J_{\text{CP}} = 40.0$ Hz, CH_3P), 20.24 (CH_3CH), 20.45 (d, $J_{\text{CP}} = 30.2$ Hz, CH_3P), 27.55 (CH_2), 33.86 (CH), 49.52 (CH). ^{31}P NMR (CDCl_3) δ 24.85 (PMe_3).

$\text{Fe}_2\{\mu\text{-SCH}_2\text{C}(i\text{-Pr})_2\text{CH}_2\text{S}\}(\text{CO})_6$ (*iPr*₂-CO)



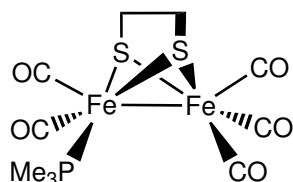
A mixture of $\text{Fe}_3(\text{CO})_{12}$ (260 mg, 0.52 mmol) and **16** (100 mg, 0.52 mmol) was dissolved in dry THF (50 mL) and refluxed under nitrogen for 2 hours until the colour changed from deep green to dark red. The solvent was removed *in vacuo* to give dark red solid. The complex was purified using column chromatography eluting with hexane and affording *iPr*₂-CO as a red solid (150 mg, 63 %). Single crystals suitable for X-ray were grown from hexane at $-4\text{ }^{\circ}\text{C}$. Anal. found (calcd) for $\text{C}_{15}\text{H}_{18}\text{Fe}_2\text{O}_6\text{S}_2$: C, 38.24 (38.32); H, 3.91 (3.86) %. $\tilde{\nu}_{\text{max}}/\text{cm}^{-1}$ (hexane) 2074, 2033, 2006, 1990, 1978 (CO). ^{13}C NMR (CDCl_3) δ 18.14 (CH_3), 25.37 (CHCH_3), 31.26 (CHCH_2), 42.03 (CH_2), 207.55 (CO). m/z (orbitrap) calcd for $\text{C}_{14}\text{H}_{19}\text{Fe}_2\text{O}_5\text{S}_2$ ($\text{M}^+ + \text{H}^+ - \text{CO}$) requires 442.9368, found 442.9372.

$\text{Fe}_2\{\mu\text{-SCH}_2\text{C}(i\text{-Pr})_2\text{CH}_2\text{S}\}(\text{CO})_4(\text{PMe}_3)_2$ (*iPr*₂)

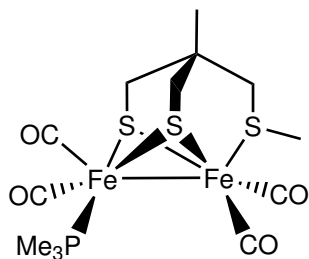


Trimethylphosphine (0.10 mL, 0.90 mmol) was added to a solution of **iPr₂-CO** (70 mg, 0.15 mmol) in hexane (30 mL). The solution was heated to reflux for 5 days after which time the IR confirmed almost quantitative conversion to the product. Filtration through Celite followed by removal of solvent *in vacuo* afforded crude product as dark red powder. It was purified by cooling the concentrated hexane solution to $-30\text{ }^{\circ}\text{C}$ (60 g, 71 %). Single crystals suitable for X-ray were grown from hexane at $-4\text{ }^{\circ}\text{C}$. Anal. found (calcd) for $\text{C}_{16}\text{H}_{30}\text{Fe}_2\text{O}_4\text{P}_2\text{S}_2$: C, 36.55 (36.66); H, 5.87 (5.77) %. $\tilde{\nu}_{\text{max}}/\text{cm}^{-1}$ (hexane) 1974, 1948, 1908, 1895 (CO). ^{13}C NMR (CDCl_3) δ 18.29 (CH_3), 19.60 (d, $J_{\text{CP}} = 111\text{ Hz}$, PCH_3), 26.67 (CHCH_3), 31.24 (CHCH_2), 42.19 (CH_2). ^{31}P NMR (CD_2Cl_2) δ 25.54 (PMe_3).

$\text{Fe}_2\{\mu\text{-SCH}_2\text{CH}_2\text{CH}_2\text{S}\}(\text{CO})_6(\text{PMe}_3)$ (**edt-P**)

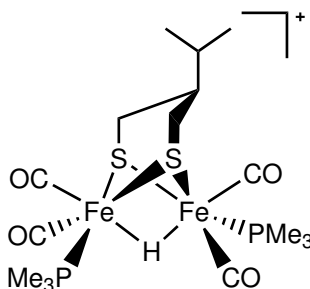


Trimethylphosphine (0.21 mL, 2.05 mmol) was added to a solution of **edt-CO** (390 mg, 1.05 mmol) in hexane (30 mL). The solution was stirred under N_2 for 24 hours. After the solution was concentrated by solvent evaporation *in vacuo*, the crude product was purified by column chromatography eluting with CH_2Cl_2 : hexane (1 : 6) to give **edt-P** as a red powder (230 mg, 52 %). Single crystals suitable for X-ray were grown from hexane at $-4\text{ }^{\circ}\text{C}$. Anal. found (calcd) for $\text{C}_{11}\text{H}_{20}\text{Fe}_2\text{O}_5\text{PS}_2$: C, 28.55 (28.6); H, 3.15 (3.12) %. $\tilde{\nu}_{\text{max}}/\text{cm}^{-1}$ (hexane) 2043, 1988, 1965, 1932 (CO). ^{13}C NMR (CDCl_3) δ 211.17 (CO), 35.96 (CH_2), 20.77 (d, $J_{\text{CP}} = 114\text{ Hz}$, CH_3). ^{31}P NMR (CDCl_3) δ 23.03 (PMe_3).

Fe₂{MeSCH₂C(Me)(CH₂S)₂}(CO)₄(PMe₃) (S₃)

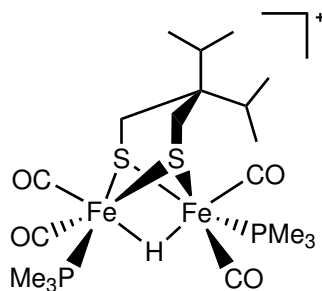
A solution of S₃-CO (700 mg, 1.7 mmol) in toluene (100 mL) was treated with PMe₃ (0.35 ml, 3.4 mmol). The dark red reaction mixture was refluxed under nitrogen for 2 hours. The solution was then filtered through Celite and the solvent removed *in vacuo* leaving dark red residue. It was purified by silica chromatography eluting with hexane/diethyl ether (1 : 1) mixture. The product was collected as second dark brown fraction. Removal of solvent gave S₃ as dark red-brown powder (300 g, 32 %). Single crystals suitable for X-ray were grown from diethyl ether at -4 °C. Anal. found (calcd) for C₁₃H₂₁Fe₂O₄PS₃ C, 32.85 (32.52); H, 4.29 (4.41) %. $\tilde{\nu}_{\max}/\text{cm}^{-1}$ (MeCN) 1984, 1947, 1910 (CO). ³¹P NMR (CD₃CN) δ 25.8 (PMe₃). EI-MS: m/z 480 [M]⁺, 452 [M-CO-P(CH₃)₃]⁺, 424 [M - 2 CO - P(CH₃)₃]⁺, 396 [M - 3 CO - P(CH₃)₃]⁺, 368 [M - 4 CO - P(CH₃)₃]⁺.

Note: ¹³C NMR of S₃ was attempted, however in the course of the experiment the complex precipitates from both CD₂Cl₂ and CD₃CN. The signals can be tentatively assigned as follows: ¹³C NMR (CD₂Cl₂) δ 19.52 (d, J_{CP} = 29.4 Hz, CH₃P), 31.74 (CH₃), 32.19 (br, CH₂), 33.05 (CH₃), 39.30 (C), CO signals were not observed.

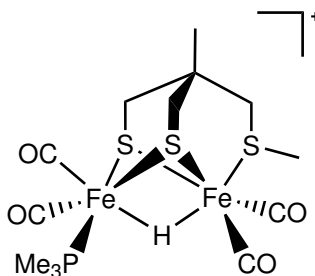
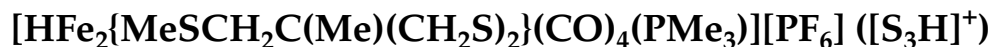
[HFe₂{ μ -SCH₂CH(*i*-Pr)CH₂S}(CO)₄(PMe₃)₂][PF₆] ([*i*PrH]⁺)

A solution of **iPr** (100 mg, 0.2 mmol) in methanol (20 mL) was treated with conc. HCl (3 mL) and left to stir under nitrogen for 1 hour. A dark orange solid precipitated upon addition of saturated aqueous solution of NH_4PF_6 . The solid was filtered, washed with water, diethyl ether and dried *in vacuo* to give product as dark orange powder (63 mg, 48 %). Single crystals suitable for X-ray were grown from CH_2Cl_2 at -4°C . Anal. found (calcd) for $\text{C}_{16}\text{H}_{31}\text{F}_6\text{Fe}_2\text{O}_4\text{P}_3\text{S}_2$: C, 28.57 (28.67); H, 4.75 (4.66) %. $\tilde{\nu}_{\text{max}}/\text{cm}^{-1}$ (CH_2Cl_2) 2032, 1990 (CO). ^1H NMR (CD_2Cl_2) δ 0.93 (6H, d, $J_{\text{HH}} = 6.7$ Hz, $\text{CH}(\text{CH}_3)_2$), 1.57 (9H, d, $J_{\text{HP}} = 10.3$ Hz, PMe_3), 1.62 (9H, d, $J_{\text{HP}} = 10.3$ Hz, PMe_3), 1.64 (2H, m, CH/CH₂), 2.05 (2H, m, CH/CH₂), 2.90 (2H, m, CH/CH₂), -15.35 (1H, t, $J_{\text{PH}} = 21.9$ Hz, Fe–H–Fe). ^{13}C NMR (CD_3CN) δ 17.27 (d, $J_{\text{CP}} = 32.5$ Hz, CH_3P), 17.39 (d, $J_{\text{CP}} = 33.2$ Hz, CH_3P), 18.50 (CH_3CH), 24.48 (CH_2), 33.48 (CH), 48.88 (CH). ^{31}P NMR (CD_2Cl_2) δ 21.84 (d, $J_{\text{PP}} = 8.5$ Hz, PMe_3), 19.78 (d, $J_{\text{PP}} = 8.5$ Hz, PMe_3), -144.45 (sept. $J_{\text{PF}} = 710.8$ Hz, PF_6).

$[\text{HFe}_2\{\mu\text{-SCH}_2\text{C}(\text{i-Pr})_2\text{CH}_2\text{S}\}(\text{CO})_4(\text{PMe}_3)_2][\text{PF}_6] ([\text{iPr}_2\text{H}]^+)$



A solution of **iPr₂** (130 mg, 0.2 mmol) in methanol (20 mL) was treated with conc. HCl (3 mL) and left to stir under nitrogen for 1 hour. A red-orange solid precipitated upon addition of saturated aqueous solution of NH_4PF_6 . The solid was filtered, washed with water, diethyl ether and dried *in vacuo* to give product as red-orange powder (53 mg, 32 %). Anal. found (calcd) for $\text{C}_{19}\text{H}_{37}\text{F}_6\text{Fe}_2\text{O}_4\text{P}_3\text{S}_2$: C, 31.92 (32.03); H, 5.55 (5.24) %. $\tilde{\nu}_{\text{max}}/\text{cm}^{-1}$ (CH_2Cl_2) 2029, 1987 (CO). ^1H NMR (CD_2Cl_2) δ 0.99 (12H, d, $J_{\text{HH}} = 7.0$ Hz, $\text{CH}(\text{CH}_3)_2$), 1.26 (2H, br s, CH_2), 1.53 (2H, br s, CH_2), 1.62 (18H, d, $J_{\text{HP}} = 10.3$ Hz, PMe_3), 2.26 (2H, m, CH), -15.22 (1H, t, $J_{\text{HP}} = 22.3$ Hz, Fe–H–Fe). ^{31}P NMR (CD_2Cl_2) δ 21.45 (s, PMe_3).



A solution of S_3 (63 mg, 0.1 mmol) in methanol (10 mL) was treated with conc. HCl (3 mL) and left to stir under nitrogen for 1 hour. A red solid precipitated upon addition of saturated aqueous solution of NH_4PF_6 . The solid was filtered, washed with water, diethyl ether and dried *in vacuo* to give product as dark red powder (58 mg, 71 %). Single crystals suitable for X-ray were grown from CH_2Cl_2 at $-4\text{ }^\circ\text{C}$. Anal. found (calcd) for $\text{C}_{13}\text{H}_{22}\text{F}_6\text{Fe}_2\text{O}_4\text{P}_2\text{S}_3$: C, 24.80 (24.93); H, 3.65 (3.54) %. $\tilde{\nu}_{\text{max}}/\text{cm}^{-1}$ (MeCN) 2060, 2038, 2003 (CO). ^1H NMR (CD_3CN) δ 1.17 (3H, s, S(CH_3) $_3$), 1.52 (9H, d, $J_{\text{HP}} = 10.7$ Hz, PMe_3), 2.11 (2H, m, CH_2), 2.41 (2H, m, CH_2), 2.55 (2H, m, CH_2), -19.95 (1H, d, $J_{\text{HP}} = 21.0$ Hz, Fe-H-Fe). ^{31}P NMR (CD_3CN) δ 20.19 (s, PMe_3), 19.74 (s, PMe_3), -144.64 (sept. $J_{\text{PF}} = 706.5$ Hz, PF_6). ^{13}C NMR (CD_3CN) δ 16.96 (d, $J_{\text{CP}} = 33.2$ Hz, CH_3P), 18.69 (CH_3), 19.08 (CH_3), 29.94 (CH_2), 30.60 (CH_2), 32.07 (CH_2), 38.76 (C), CO signals were not observed. EI-MS: m/z 480 $[\text{M} - \text{PF}_6 - \text{H}]^+$, 452 $[\text{M} - \text{CO} - \text{PF}_6 - \text{H}]^+$.

Compound	$i\text{Pr-CO}$	$i\text{Pr}_2\text{-CO}$	$i\text{Pr}$	$i\text{Pr}_2$
Formula	$\text{C}_{12}\text{H}_{12}\text{Fe}_2\text{O}_6\text{S}_2$	$\text{C}_{15}\text{H}_{18}\text{Fe}_2\text{O}_6\text{S}_2$	$\text{C}_{16}\text{H}_{30}\text{Fe}_2\text{O}_4\text{P}_2\text{S}_2$	$\text{C}_{19}\text{H}_{36}\text{Fe}_2\text{O}_4\text{P}_2\text{S}_2$
Formula weight	428.04	470.11	524.16	566.24
Crystal system	Triclinic	Triclinic	Monoclinic	Orthorhombic
Space group	$P\bar{1}$	$P\bar{1}$	$C2/c$	$P2_12_12_1$
$a/\text{\AA}$	9.11680(10)	7.792(2)	16.7840(7)	12.090(2)
$b/\text{\AA}$	9.65810(10)	11.571(3)	11.0945(5)	13.027(2)
$c/\text{\AA}$	9.82730(10)	11.826(2)	12.5523(8)	16.282(3)
$\alpha/^\circ$	74.585(3)	116.222(13)	90	90
$\beta/^\circ$	75.109(3)	101.170(17)	104.937(7)	90
$\gamma/^\circ$	89.144(4)	95.179(18)	90	90
$V/\text{\AA}^3$	804.84(2)	919.5(4)	2258.4(2)	2564.4(7)
Z	2	2	2	4
T/K	100(2)	100(2)	100(2)	100(2)
Crystal size/mm	$0.44 \times 0.22 \times 0.14$	$0.16 \times 0.04 \times 0.03$	$0.07 \times 0.03 \times 0.01$	$0.10 \times 0.06 \times 0.01$
$2\theta/^\circ$	27.5	27.5	27.5	27.5
Reflections measured	11 191	12 081	14 727	17 644
Unique reflections, R_{int}	3667, 0.023	4202, 0.021	2591, 0.074	5723, 0.025
Reflections with $I > 2\sigma(I)$	3606	3900	2004	5568
No. parameters	201	230	150	272
$R_1 [I > 2\sigma(I)]$	0.021	0.025	0.036	0.026
wR_2 (all data)	0.058	0.064	0.075	0.054

Compound	$[\text{iPrH}]^+$	S_3	$[\text{S}_3\text{H}]^+$	edt-P
Formula	$\text{C}_{16}\text{H}_{31}\text{Fe}_2\text{O}_4\text{P}_2\text{S}_2, \text{F}_6\text{P}$	$\text{C}_{13}\text{H}_{21}\text{Fe}_2\text{O}_4\text{PS}_3$	$\text{C}_{13}\text{H}_{22}\text{Fe}_2\text{O}_4\text{PS}_3, \text{F}_6\text{P}$	$\text{C}_{10}\text{H}_{13}\text{Fe}_2\text{O}_5\text{PS}_2$
Formula weight	670.14	480.15	626.13	419.19
Crystal system	Monoclinic	Monoclinic	Triclinic	Triclinic
Space group	$\text{C}2/c$	$\text{P}2_1/c$	$\text{P}\bar{1}$	$\text{P}\bar{1}$
$a/\text{\AA}$	18.7466(9)	14.1694(5)	8.2088(3)	8.4937(5)
$b/\text{\AA}$	11.1267(5)	13.2159(5)	11.6207(5)	9.4901(5)
$c/\text{\AA}$	25.7195(18)	10.2777(4)	13.0278(5)	11.7656(6)
$\alpha/^\circ$	90	90	97.952(3)	101.030(4)
$\beta/^\circ$	99.892(7)	99.350(4)	106.923(3)	104.003(5)
$\gamma/^\circ$	90	90	102.607(4)	113.074(5)
$V/\text{\AA}^3$	5285.0(5)	1899.05(12)	1132.82(8)	801.90(8)
Z	8	4	2	2
T/K	100(2)	140(2)	140(2)	140(2)
Crystal size/mm	$0.04 \times 0.03 \times 0.01$	$0.20 \times 0.20 \times 0.20$	$0.38 \times 0.07 \times 0.05$	$0.03 \times 0.03 \times 0.02$
$2\theta/^\circ$	27.5	27.50	27.00	27.50
Reflections measured	35458	26529	16537	13038
Unique reflections, R_{int}	6045, 0.101	4313, 0.038	4913, 0.037	3675, 0.0887
Reflections with $I > 2\sigma(I)$	3766	3654	4259	2652
No. parameters	312	213	280	184
$R_1 [I > 2\sigma(I)]$	0.047	0.029	0.033	0.057
wR_2 (all data)	0.100	0.064	0.076	0.094

Chapter 3

Protonation Studies of Diiron Dithiolate Assemblies: Effect of the Bridge Structure on the Rates and Mechanism

3.1 Early Protonation Studies of [Fe–Fe]-Hydrogenase Models

The hunt for terminal hydrides in the synthetic models of the [Fe–Fe]-hydrogenase subsite has been an outstanding challenge for chemists for quite some time. Not only have they been implicated in biological hydrogen production but they have also been long thought to be on the path to the more stable bridging hydride species.^{87,141} In an attempt to probe the detailed mechanism by which protonation occurs, Pickett and co-workers have undertaken a number of studies as part of wider efforts to produce competent artificial systems with high stability and activity.^{100,101,135,142} It was demonstrated that intimate chemistry of synthetic mimics related to the [Fe–Fe]-hydrogenase subsite can be conveniently probed using fast time-resolved FT-IR spectroscopy – a technique predominantly reserved for protein and enzyme systems.^{143,144}

A number of complexes have been subjected to stopped-flow studies (Figure 38). It was found that protonation of the metal–metal bond in a range of simple {2Fe2S} systems

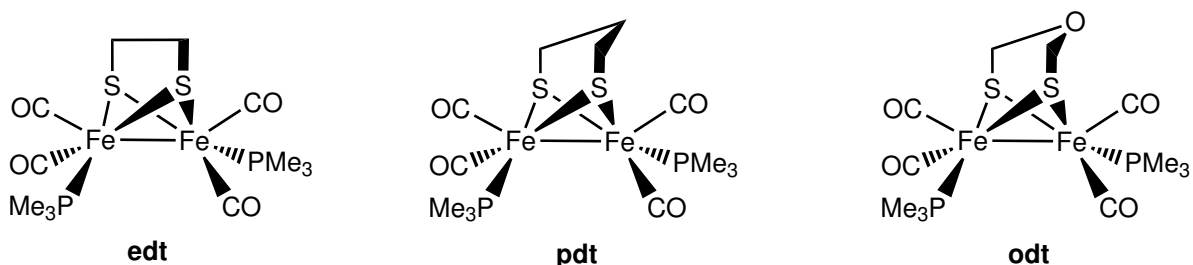
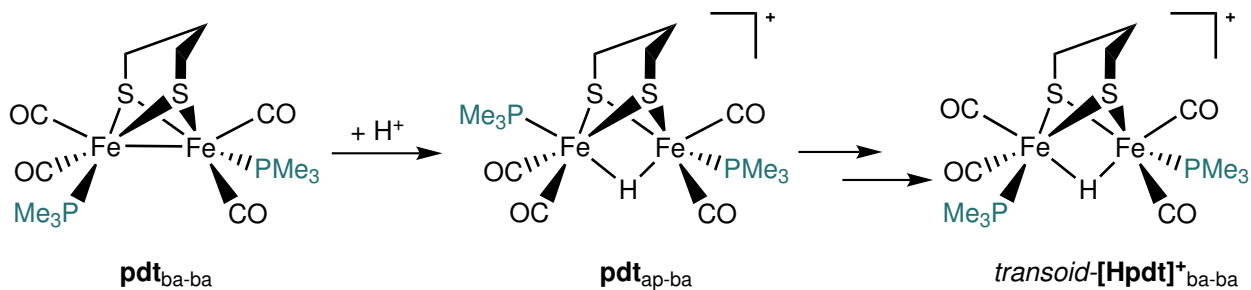


Figure 38: Model complexes examined by Pickett and co-workers in the stopped-flow kinetic studies^{101,135}

does not proceed through a simple one-step mechanism. At least one intermediate was detected in all cases, *i.e.* requiring a minimum of two steps to yield the isolable product. Initial protonation of all three complexes (**edt**, **pdt** and **odt**) leads to formation of a bridging hydride species in which one phosphine rests in the apical position. This is followed by a slow isomerisation to give the most thermodynamically stable product in which the PMe_3 ligands are *transoid*-dibasal (Scheme 27).



Scheme 27: Reaction mechanism for protonation of **pdt**¹⁰⁰

The studies revealed *no* evidence for terminal hydride formation. More interestingly, they uncovered an unexpected variation in the rate of protonation. Both steps of the reaction were an order of magnitude *slower* for **edt** and **odt** than for **pdt**. The apparent subtle difference between CH_2 and O in the bridgehead position has been found to have significant mechanistic implications. However, despite a major body of work, an open question remained as to why the protonation rates differ so dramatically. It has been suggested that, noting the minimal effect of CH_2 *vs* O on the infrared frequencies, neither

the length of the bridge nor the electronic influence of the bridgehead atom had any correlation to the rates of protonation.¹³⁵

The observation that altering the backbone structure of diiron subsite models does not influence the IR positions was also made by Darensbourg while examining complexes possessing sterically bulky bridgehead ligands (Figure 39).¹³⁴ Due to very similar infrared spectral signatures in the carbonyl region of both **Me**₂ and **Et**₂, it was concluded that the addition of alkyl groups to the bridgehead position does not increase the thiolate donor capacities or electron densities around the two iron atoms.⁶⁹ However, it was noted that addition of bridgehead bulk does lower the oxidation potential of **Me**₂ when compared to an unsubstituted subsite analogue **pdt**.³³ This was attributed solely to the influence of the steric effect from the two methyl groups, although further explanation has not been provided.

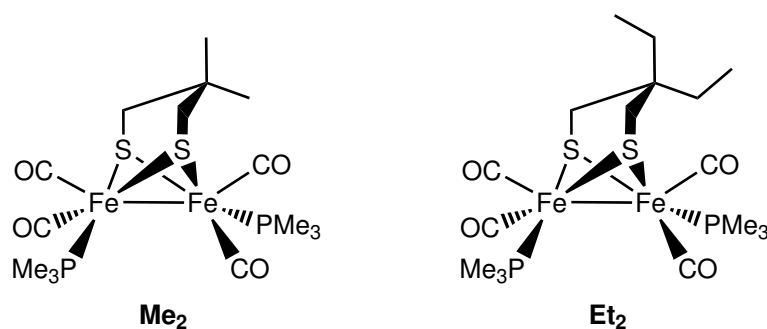


Figure 39: Model complexes with steric bulk on the bridgehead group examined by Darensbourg and co-workers¹³⁴

The work described in this chapter focuses on investigating the broader influence of the dithiolate bridge on the reactivity of related [Fe-Fe]-hydrogenase subsite models, something which has not been fully explored and understood thus far. A range of {2Fe2S} and {2Fe3S} models have been subjected to stopped-flow UV and IR studies to acquire primary protonation rates (Table 7). Both the steric bulk introduced into dithiolate bridge and the degree of substitution by the electron donating co-ligands were found to have a significant influence on the reactivity of these systems towards protons. A direct linear

free energy relationship between the activation energy for protonation and the energy level of the HOMO is uncovered. This allows predictions of protonation rates of systems which are too fast to measure experimentally.

Table 7: Diiron dithiolate complexes examined in this chapter

Compound	Structure	Compound	Structure
edt		iPr₂	
odt		pdt-P	
pdt		edt-P	
Me		bd_t	
Me₂		S₃-CO	
iPr		S₃	

3.2 Relationship Between the Structure and Protonation Rates of Diiron Complexes

3.2.1 General Aspects of Kinetic Analysis

In earlier studies it was shown that the diiron complexes have kinetics which are first order in complex and first order in proton concentration.¹⁰⁰ The general considerations of first and *pseudo*-first order kinetics are now discussed.

If a general first order reaction is considered:



then the rate of consumption of [A] can be expressed as follows:

$$-\frac{dA}{dt} = k[A] \quad (4)$$

The integrated first-order rate law is shown in Equation 5, where $[A]_t$ is the concentration of the complex at time t and $[A]_0$ is the concentration of the complex at time zero.

$$[A]_t = [A]_0 e^{-kt} \quad (5)$$

This data can then be analysed by taking the natural logarithm of both sides of Equation 5, which gives:

$$\ln[A]_t = \ln[A]_0 - kt \quad (6)$$

Thus a plot of $\ln[A]_t$ versus time will have a slope of $-k$ (Figure 40).

If a second-order protonation reaction is considered:



Then the rate of consumption of [A] can be expressed as:

$$-\frac{dA}{dt} = k_2[A][H^+] \quad (8)$$

If $[H^+] \gg [A]$ throughout the course of the reaction, then the concentration of $[H^+]$ remains essentially constant. That is, the reaction is carried out under *pseudo*-first order conditions and Equation 8 can be re-written as:

$$-\frac{dA}{dt} = k_{\text{obs}}[A] \quad (9)$$

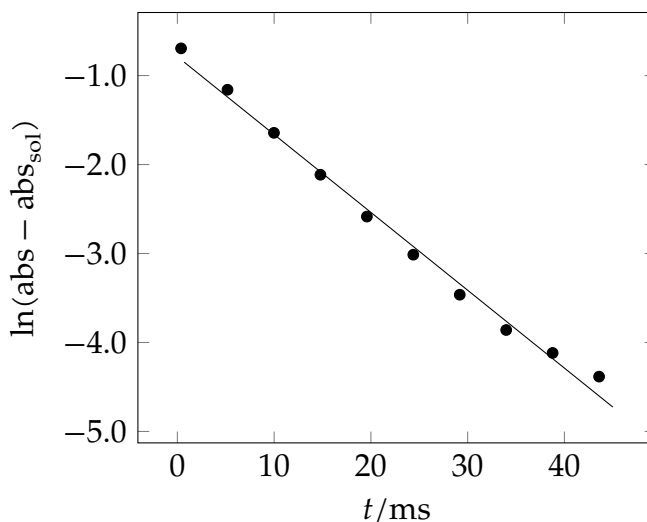


Figure 40: Linear dependence of $\ln[A]$ on time for protonation of *iPr* (circles) under *pseudo*-first order conditions; linear fit (line); $[iPr]_0$ 0.12 mM, $[HBF_4 \cdot Et_2O]_0$ 125 mM. The concentration of substrate, $[A]$, is proportional to the measured absorbance minus the background absorbance of the solvent; absorbances measured at 348 nm

Thence:

$$\ln[A]_t = \ln[A]_0 - k_{obs}t \quad (10)$$

where:

$$k_{obs} = k_2[H^+] \quad (11)$$

Thus monitoring the concentration of $[A]$ as a function of time can be analysed as for as for a simple first order reaction. The rate constant k_{obs} depends on the concentration of $[H^+]$. From Equation 11, a plot of k_{obs} versus $[H^+]$ should be linear with a slope equal to the second order rate constant and a zero intercept. Concentrations can be monitored with respect to time by spectrophotometry or other methods.

Whereas data analysis of determination of k_{obs} can be performed by $\ln[A]$ versus t plots, an alternative is directly fitting the concentration-time curves by computational methods to experimental function as described below.

3.2.2 Stopped-Flow UV

The stopped-flow UV-visible technique is most commonly employed to study rapid reactions as well as detect and identify formation of transient species. It can grant access to kinetic information on a short time scale – typically hundreds of microseconds. The protonation of dinitrogen in molybdenum and tungsten bis-diphosphine systems and of iron sulfur clusters are among the inorganic systems which have been probed by the kinetic stopped-flow studies.¹⁴⁵ More recently this technique has been successfully applied in a variety of small molecule studies, including the reactions of [Fe–Fe]-hydrogenase subsite models.¹¹⁴

Solutions of all substituted diiron complexes (such as **edt**, **odt**, **iPr**, *etc.*) exhibit a strong UV absorption peak at *ca* 340–360 nm. Their respective protonated products are featureless in this region, but have a significant background absorbance. This is illustrated by Figure 41 for **pdt** and **iPr** complexes. The extinction coefficients (ϵ) of these are 9865 and 8908 $\text{M}^{-1} \text{cm}^{-1}$, respectively. After protonation of **pdt** the absorbtion at 348 nm is 36 % of that for the parent species. Similarly, protonated product of **iPr** also has an absorbance at 348 nm of around the same amount as seen for the **pdt** complex. The stopped-flow UV-visible technique therefore provides excellent means of monitoring protonation.

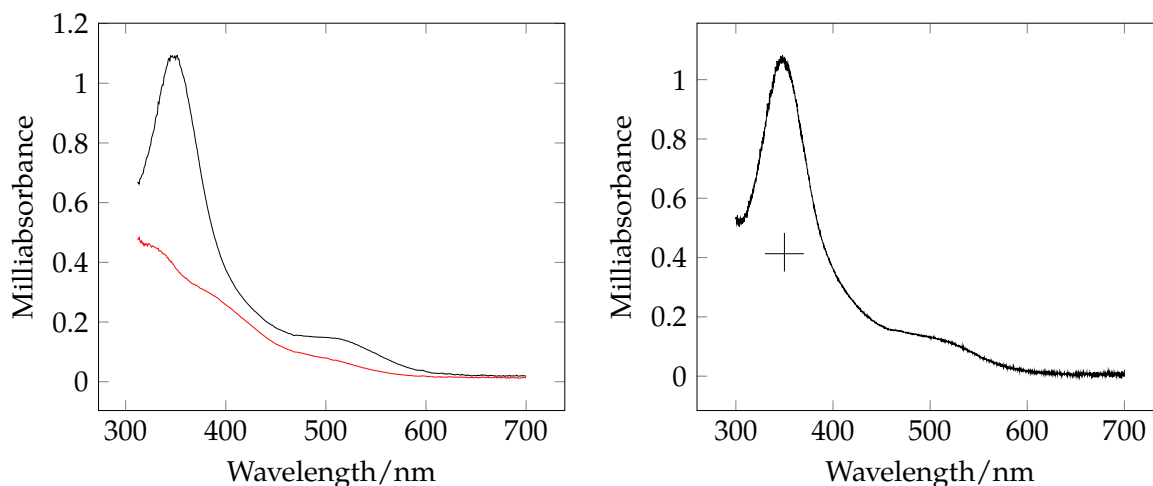


Figure 41: Left: UV spectrum of 0.11 mM **pdt** solution in MeCN before protonation (black) and after protonation (red); Right: UV spectrum of 0.12 mM **iPr** solution in MeCN before protonation (black) and a point the peak reaches after protonation (cross)

In a typical experimental protocol a solution of acid and a solution of diiron complex is prepared in a glove-box, where the stopped-flow UV instrument is housed under strict anaerobic conditions (<10 ppm of O_2). The reactants are then placed in separate syringes and the flow is initiated by by an automatic pushing block, delivering equal volume of each solution into a mixing chamber (Figure 42). This enables a rapid and smooth mixing of the two reactants. Once the sample mixture reaches the observation cell, the reaction is monitored by optical components attaining the first scan as fast as 500 microseconds.

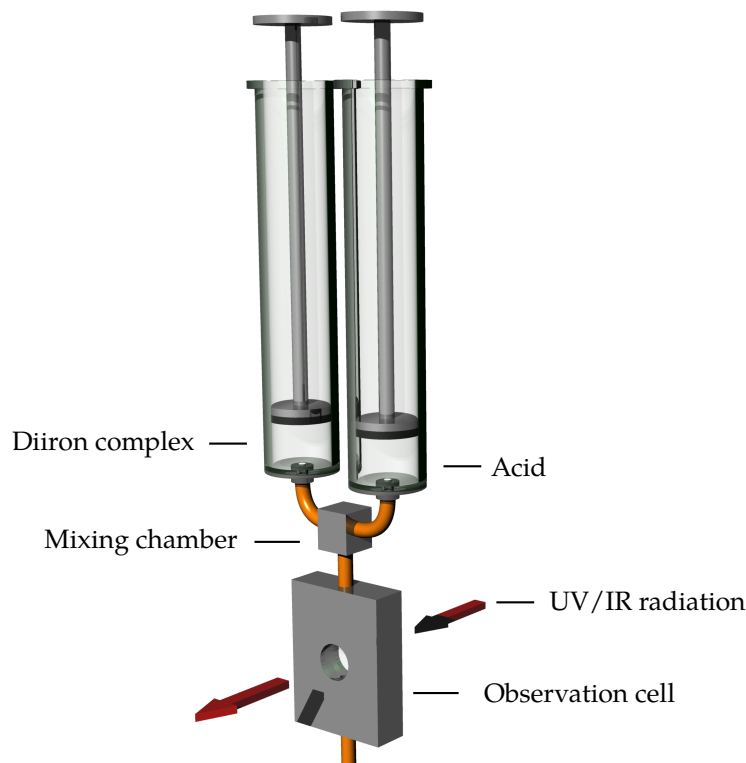


Figure 42: Schematic representation of the stopped-flow set-up

Protonation of *iPr* with $\text{HBF}_4 \cdot \text{Et}_2\text{O}$ in MeCN was monitored at 348 nm by stopped-flow UV-visible spectroscopy under *pseudo*-first order conditions: the concentration of acid was always retained in a large excess of the diiron complex. Over a range of acid concentrations (12.5 mM to 125 mM after mixing) the loss of the absorbance of *iPr* followed *pseudo*-first order kinetics and could be fitted by a single exponential decay over at least three half-lives. Figure 43 shows a typical time course for loss of UV signal from the starting material.

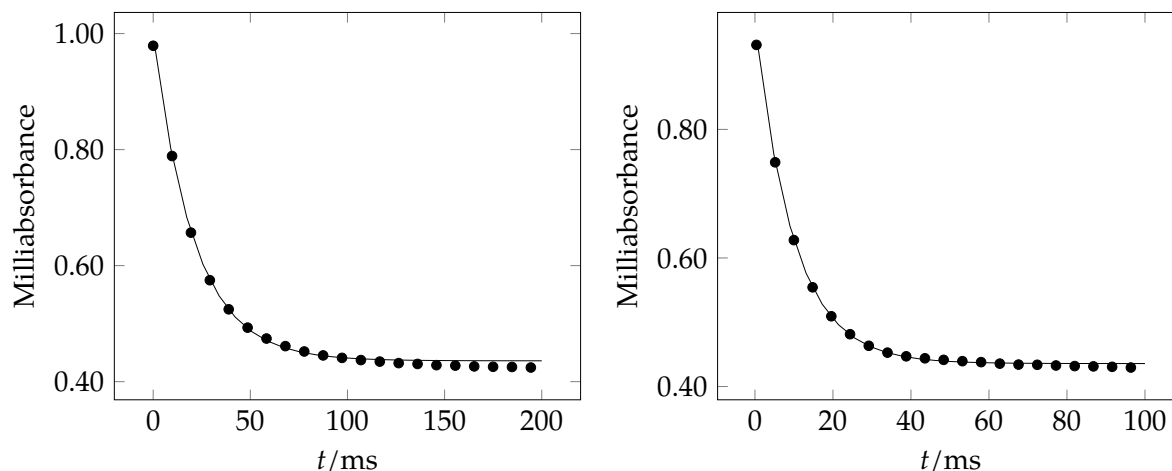


Figure 43: Decay of UV signal at 348 nm over time on protonation of *iPr* (circles); *pseudo*-first order fit (line); [*iPr*]₀ 0.12 mM, [HBF₄·Et₂O]₀ 25 mM (left); [HBF₄·Et₂O]₀ 125 mM (right)

An alternative approach to the analysis of kinetic data by manual means described in Section 3.2.1 is to directly fit the raw kinetic data to an exponential function. This is shown by the screen-shot in Figure 44, which illustrates the exponential fit and the parameters defining this fit.

The k_{obs} values obtained show a linear dependence on acid concentrations over a wide range (Figure 45) and are consistent with an overall bimolecular rate-limiting protonation on the metal–metal bond in *iPr*. A more detailed mechanism for this reaction was elucidated employing stopped-flow IR technique (*vide infra*).

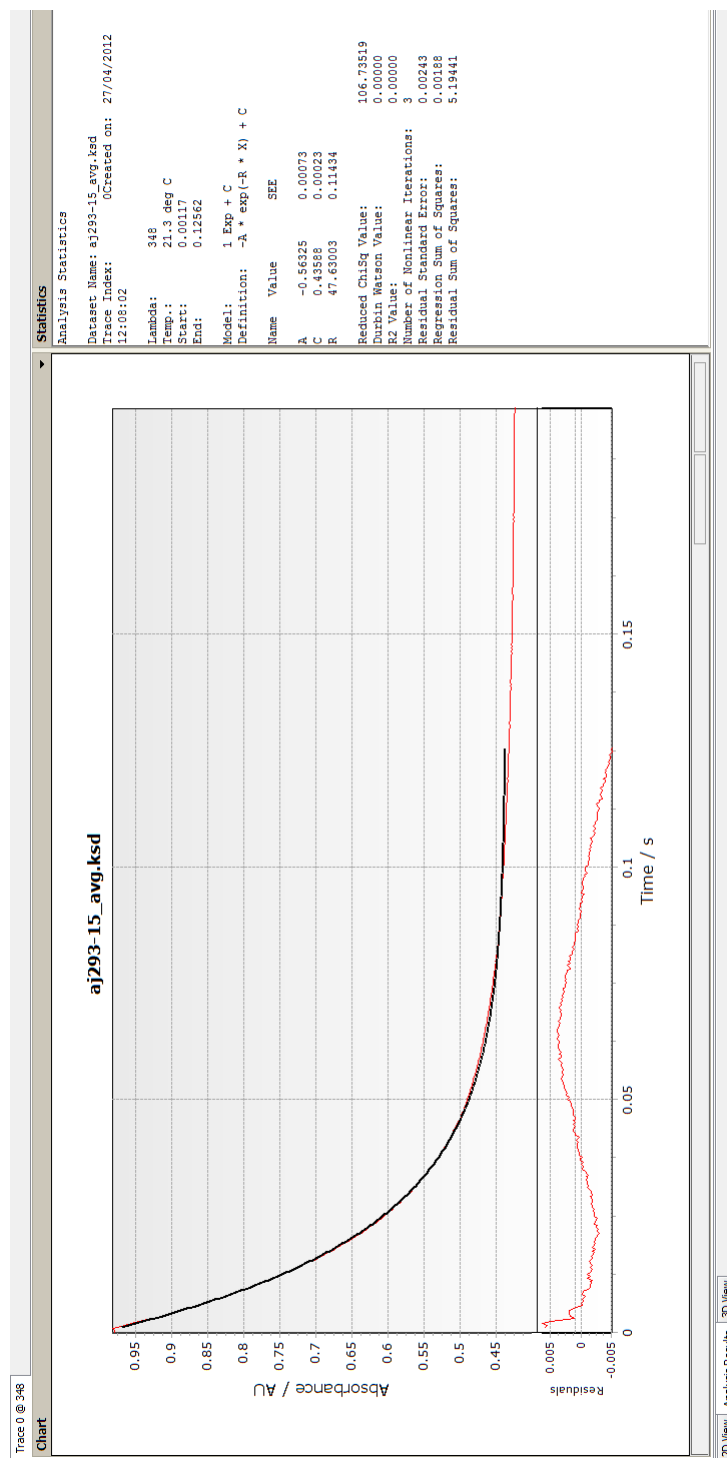


Figure 44: Fitting of the stopped-flow UV-vis data for *iPr* complex; [*iPr*]₀ 0.12 mM, [HBF₄ · Et₂O]₀ 25 mM

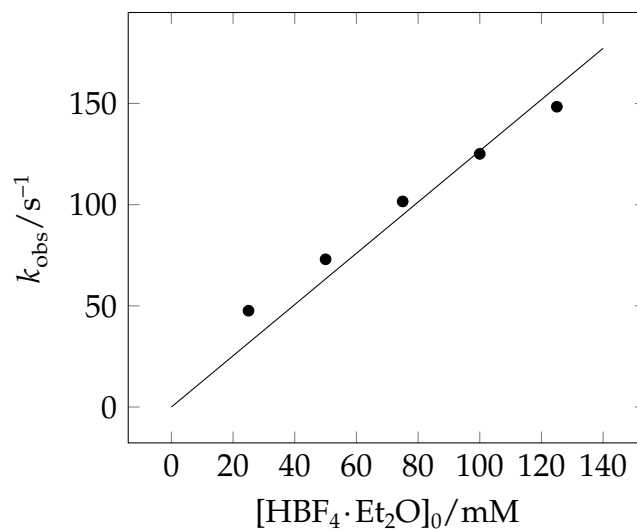


Figure 45: *Pseudo*-first order rate constants for *iPr* vs acid concentrations; measured in MeCN by stopped-flow UV; [*iPr*]₀ 0.12 mM

Protonation of **Me**, **Me₂**, ***iPr*₂** and **S₃** was monitored using the same procedure as for *iPr*. Loss of the signal of starting material in the UV followed *pseudo*-first order kinetics and exhibited linear relationship over a range of acid concentrations. However, the rates of protonation varied significantly between the different subsite analogues with ***iPr*₂** exhibiting the highest rate and **edt-P** showing the slowest (Table 8). In fact, due to a very slow nature of the reaction, protonation of **bdt**, **edt-P**, **pdt-P** and **S₃-CO** could not be measured by the stopped-flow UV technique. Prolonged exposure of diiron complexes to ultraviolet radiation leads to liberation of CO and eventually decomposition of the compound. The rate constants for protonation of the latter systems have therefore been determined using a stopped-flow IR, which avoids extended exposure of the sample to destructive radiation.

Table 8: Summary of second order rate constants for protonation of {2Fe2S} and {2Fe3S} complexes in MeCN at 21.0 °C

Compound	Structure	Rate constant of protonation/ $M^{-1} s^{-1}$
edt		83.7 ± 1.1^{101}
odt		102 ± 2^{135}
pdt		797 ± 16^{100}
Me		1040 ± 30
Me2		2500 ± 40
iPr		1266 ± 40
iPr2		4300 ± 150
pdt-P		0.0028 ± 0.0002
edt-P		0.0037 ± 0.0004
bdt		9.3 ± 0.3
S3-CO		0.060 ± 0.001
S3		36 ± 2

3.2.3 Stopped-Flow FT-IR

Whilst stopped-flow UV is an excellent method to probe fast reaction kinetics, it provides limited chemical insight. On the other hand, the stopped-flow IR technique has a poorer time resolution (typically hundreds of milliseconds), but can yield much greater amount of molecular information. UV spectroscopy is used to probe electronic transitions which are often hard to assign due to superposition of rotational and vibrational transitions, whereas IR absorption frequencies can be directly related to individual bonds and functional groups in the molecule. Time-resolved FT-IR spectroscopy complements the rapid stopped-flow UV-vis and provides a sensitive tool for monitoring even the smallest molecular changes taking place. Not only can it provide detailed information of the reaction and aid in identifying short-lived intermediates, but it can also grant access to kinetic information. Even though it has been predominantly used in examining enzyme kinetics and protein folding studies,^{144,146} stopped-flow IR is gaining attention for probing small molecule mechanisms.¹⁴⁷ This technique is particularly suited to study reactions of metal carbonyls due to the presence of strongly infrared-absorbing chromophores – CO ligands. Thus, the [Fe–Fe]-hydrogenase subsite models are ideal systems to be examined by time-resolved FT-IR.

In order to verify that the decay of UV signal in the stopped-flow experiments was indeed due to initial protonation on the iron–iron bond, stopped-flow IR studies have been carried out using the same experimental protocol. The runs were performed with similar acid concentrations (12.5 mM to 100 mM after mixing) under an inert atmosphere.

The starting material **iPr** exhibits strong IR maxima at 1980 cm⁻¹, 1943 cm⁻¹ and 1899 cm⁻¹ in MeCN. Protonation leads to the decay of these signals, with the formation of new maxima at 2054 cm⁻¹, 2032 cm⁻¹ and 1995 cm⁻¹ (Figure 46, left). A shift of CO bands by *ca* 80 cm⁻¹ to higher frequencies is indicative of a large structural change and can be assigned as a direct protonation of the Fe–Fe bond to produce μ -hydride species.

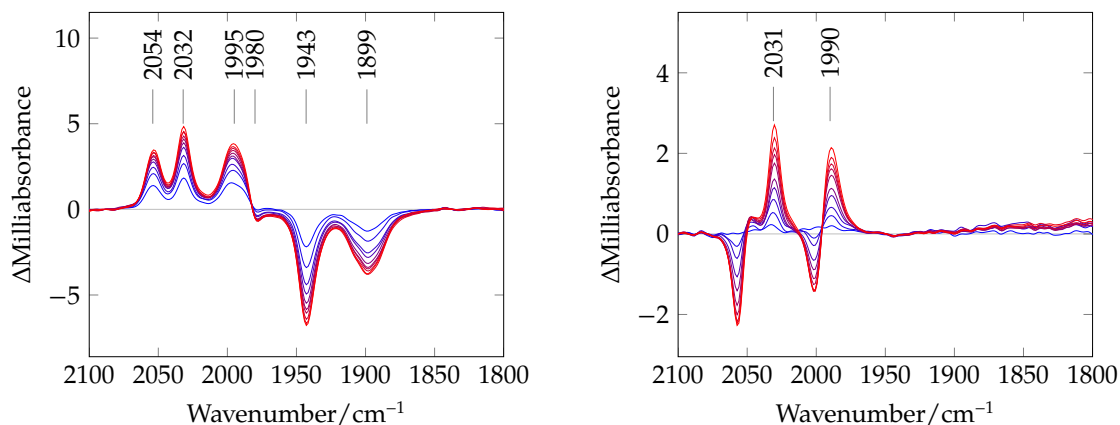
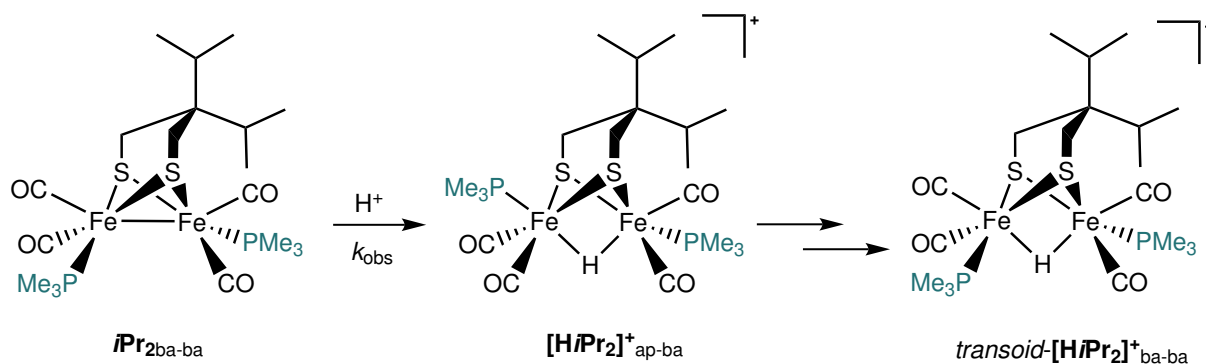


Figure 46: Left: difference spectrum for stopped-flow IR data in the time range 0.12 s (blue) to 0.9 s (red) *versus* a scan at 80 ms; [*i*Pr]₀ 0.05 mM, [HBF₄·Et₂O]₀ 25 mM; Right: data for reaction over time range 1 s (blue) to 27.6 s (red) *versus* a scan at 80 ms; [HBF₄·Et₂O]₀ 50 mM; MeCN solvent in both cases

The three maxima observed on protonation subsequently decay over time to only two signals at 2031 cm⁻¹ and 1990 cm⁻¹ under conditions where the UV-visible monitoring is 'blind' (Figure 46, right). The decay of intermediate and growth of the final product signals were independent of acid concentrations used and could be fitted using a two-term exponential function. This is indicative of formation of multiple isomers in which the phosphine ligands rest in either apical or basal positions, *cisoid* or *transoid* to one another. Over time, ligand isomerisation occurs to form the thermodynamically most stable isomeric form of the diiron complex (Scheme 28). No evidence for bridging carbonyls was detected.



Scheme 28: Proposed protonation mechanism of iPr_2 based on behaviour of similar diiron dithiolate systems

The data from the stopped-flow experiments is very similar to that observed for **edt**, **pdt** and **odt** complexes, and is consistent with a two-step mechanism. Whilst the protonation reactions of the latter complexes were slow enough to be monitored by a time-resolved NMR spectroscopy, the fast nature of the reaction with **Me**, **Me₂**, **iPr** and **iPr₂** complexes meant that this technique could not be employed to aid in assigning the isomeric structures. Although some of the subsite models such as **pdt-P**, **edt-P**, **S₃** and **S₃-CO** protonate slowly, the main purpose of investigation was to probe the primary protonation and the closer examination of isomerisation step was not pursued.

The stopped-flow UV for complexes which protonate very slowly could not be employed. This is due to the fact that prolonged exposure to ultraviolet radiation liberates CO and leads to decomposition of the complex. Instead, to obtain the *pseudo*-first order rate constants for protonation the stopped-flow IR data was used in the kinetic analysis. For **S₃-CO** complex the difference spectrum of the stopped-flow IR data is shown in Figure 47.

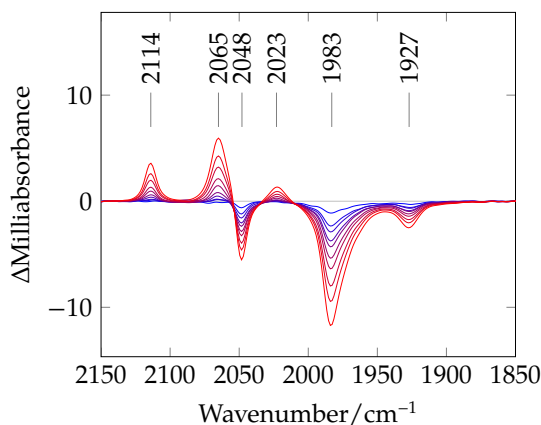


Figure 47: Difference spectrum for stopped-flow IR data in the time range 0.30 s (blue) to 25.6 s (red) *versus* a scan at 80 ms; $[\text{S}_3\text{-CO}]_0$ 0.05 mM, $[\text{HBF}_4 \cdot \text{Et}_2\text{O}]_0$ 150 mM in MeCN

The disappearance of the CO band at 1927 cm^{-1} could be fitted to a single exponential decay curve in the same way that the decay of the UV absorbance at 348 nm was fitted for other systems (Figure 48, left). The product IR band at 2114 cm^{-1} also exhibits first order exponential growth (Figure 48, right).

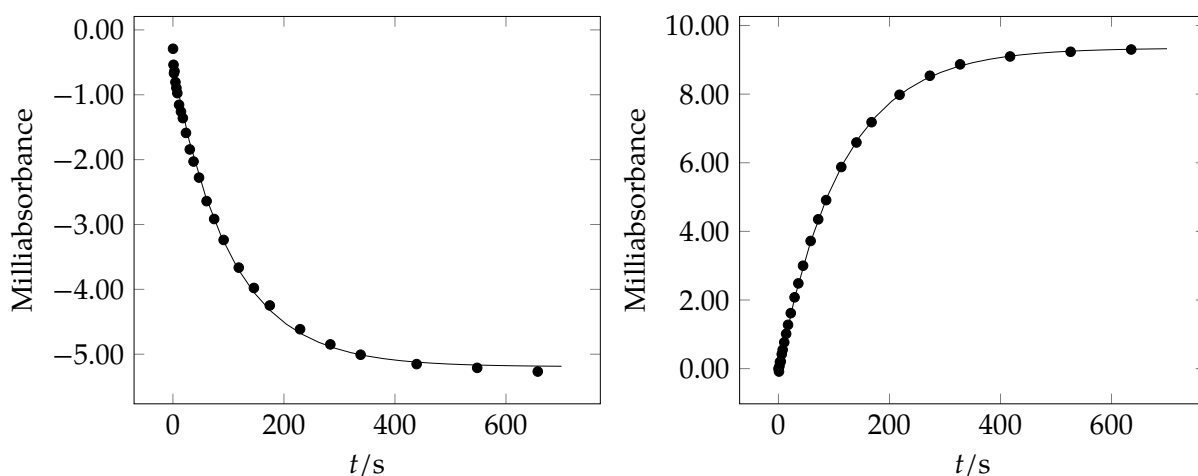


Figure 48: Left: decay of IR band at 1927 cm^{-1} over time following protonation of $\text{S}_3\text{-CO}$; Right: growth of IR band at 2114 cm^{-1} over time following protonation of $\text{S}_3\text{-CO}$; $[\text{S}_3\text{-CO}]_0$ 0.05 mM, $[\text{HBF}_4 \cdot \text{Et}_2\text{O}]_0$ 150 mM in MeCN

The k_{obs} values obtained show a linear dependence on acid concentrations over a wide range (Figure 49) and are consistent with an overall bimolecular rate-limiting protonation on the metal–metal bond in $\mathbf{S}_3\text{-CO}$.

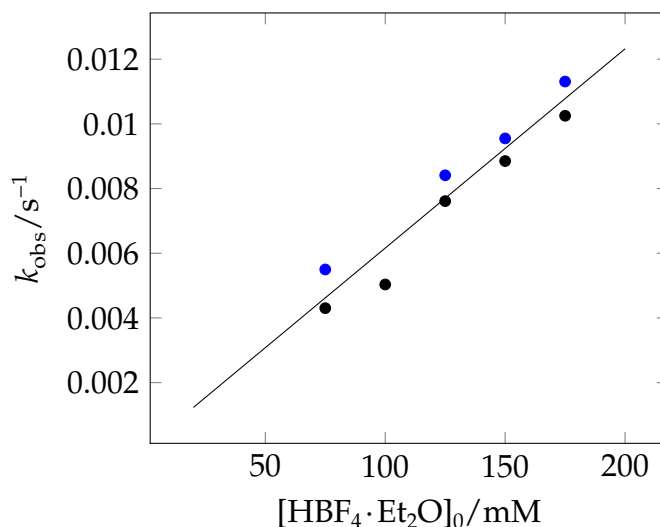


Figure 49: *Pseudo*-first order rate constants of $\mathbf{S}_3\text{-CO}$ obtained from fitting the decay of IR band at 1927 cm^{-1} (blue circles) and growth of IR band at 2114 cm^{-1} (black circles) *versus* acid concentrations

From the time-resolved FT-IR data it appears that protonation of $\mathbf{S}_3\text{-CO}$, \mathbf{S}_3 , $\mathbf{edt-P}$ and $\mathbf{pdt-P}$ complexes leads to formation of only one product without the discernible intermediate (Figure 50). In the case of $\mathbf{S}_3\text{-CO}$, \mathbf{S}_3 and $\mathbf{edt-P}$, this may reflect the rigidity of the backbone dithiolate. However, it is possibly a consequence of identical infrared signatures of different isomeric forms of the complexes and not necessarily an indication of a single-step mechanism, as this is not observed for any other subsite model.

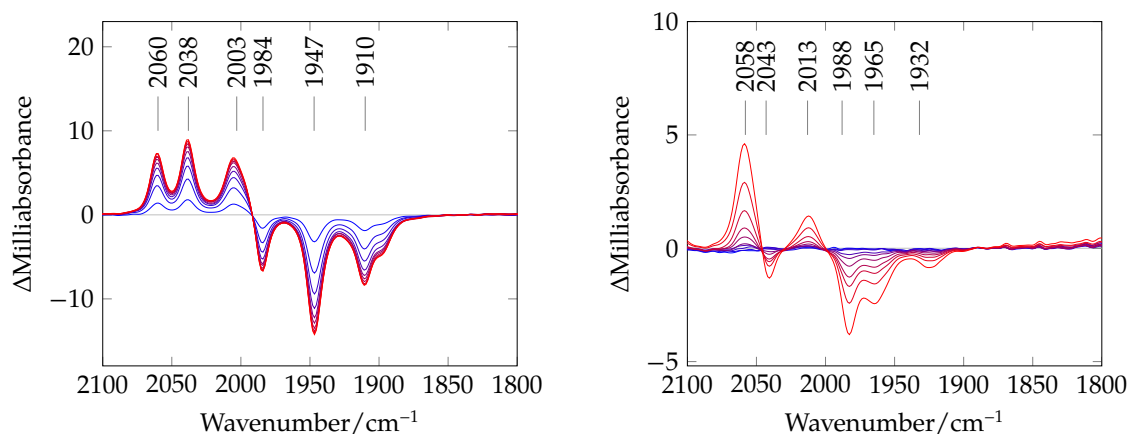


Figure 50: Left: difference spectrum for stopped-flow IR data in the time range 0.24 s (blue) to 3.4 s (red) *versus* a scan at 80 ms; $[S_3]_0$ 0.05 mM, $[HBF_4 \cdot Et_2O]_0$ 50 mM; Right: difference spectrum for stopped-flow IR data in the time range 0.24 s (blue) to 27.4 s (red) *versus* a scan at 80 ms; $[edt-P]_0$ 0.05 mM, $[HBF_4 \cdot Et_2O]_0$ 50 mM

3.2.4 Electrochemical Studies

Basic Aspects of Cyclic Voltammetry Experiments

Cyclic voltammetry (CV) is an electrochemical technique that is often employed to examine redox-active systems, offering a wealth of kinetic and thermodynamic information.¹⁴⁸ In a cyclic voltammetry experiment the applied potential with respect to a reference electrode is scanned at a fixed rate between selected limits and the direction of scan is reversed. The current which flows between the working and the secondary electrode is continuously monitored as a function of the applied potential. This provides a rapid location of the redox potentials for the electroactive species, determines reversibility of the system and aids in evaluation of the effect of media on the redox processes. CV also has the advantage of being broadly non-destructive due to a small amount of sample being oxidised/reduced at any given time within the confines of the diffusion layer, leaving the bulk of the solution unchanged.

For the work described in this chapter, cyclic voltammetry is used to determine the

oxidation potential $E_{1/2}^{\text{ox}}$ associated with the electrochemically reversible removal of an electron from the neutral closed-shell diiron dithiolate complexes in an electrolyte solution. The general characteristics of a cyclic voltammetric experiment are first described using ferrocene as a model complex. How the $E_{1/2}$ values are experimentally measured and how they relate to standard, formal potential and gas-phase ionisation potentials is then discussed.

Figure 51, left, shows a typical cyclic voltammogram for a 3.5 mM solution of ferrocene recorded at a vitreous carbon electrode in 0.1 M $[\text{NBu}_4][\text{BF}_4]$ at a scan rate of 100 mV s^{-1} against a non-aqueous Ag/AgCl reference electrode (*i.e.* the applied potential is measured relative to this electrode couple). Figure 51, right, shows the current potential response for a range of scan rates, ν , between 20–200 mV s^{-1} .

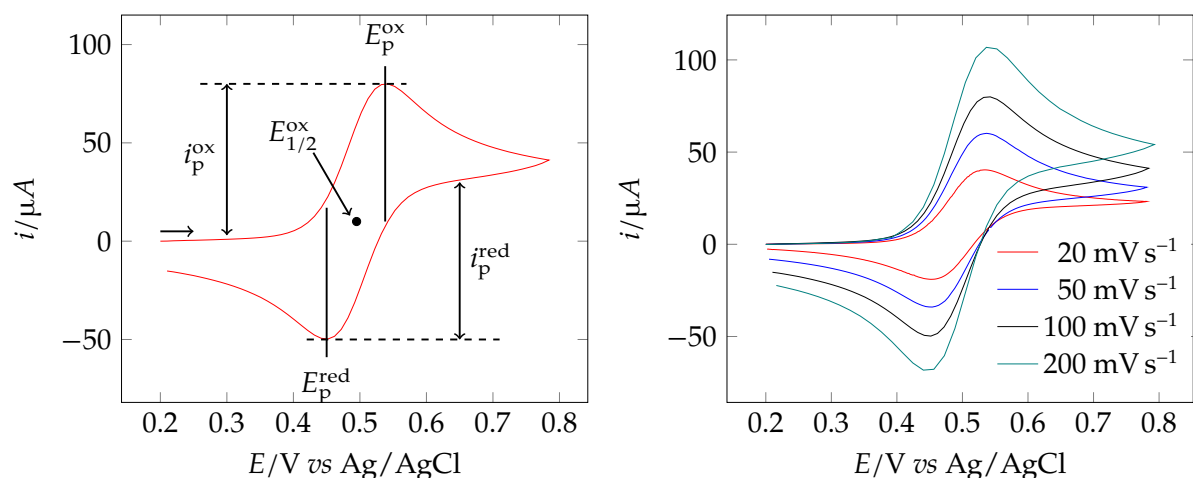


Figure 51: Left: CV of 3.5 mM ferrocene recorded at 100 mV s^{-1} vs Ag/AgCl in 0.1 M $[\text{Bu}_4\text{N}][\text{BF}_4]$ -MeCN at 25°C ; Right: CV of 3.5 mM ferrocene recorded at various scan rates vs Ag/AgCl in 0.1 M $[\text{Bu}_4\text{N}][\text{BF}_4]$ -MeCN at 25°C

The experimental parameters directly obtainable from the voltammograms are:

- (i) the peak current for the forward scan, i_p^{ox}
- (ii) the peak current for the reverse scan, i_p^{red}
- (iii) the peak potential for the forward scan, E_p^{ox}

- (iv) the peak potential for the reverse scan, E_p^{red}
- (v) the variation of i_p^{ox} with the scan rate, ν .

The position and values of (i)–(iv) are located on the experimental cyclic voltammogram shown in Figure 51. The diagnostic criteria derived from this data which shows that ferrocene undergoes diffusion controlled, reversible one-electron oxidation, as is well established, are the following.

- (a) The magnitude of the peak potential separation $\Delta E = |E_p^{\text{ox}} - E_p^{\text{red}}|$ at 100 mV s^{-1} is close to 60 mV. For a reversible redox process, the theoretical magnitude of $\Delta E = 59 \text{ mV}/n$ at 295K. The observed value is therefore consistent with a one-electron oxidation of the parent compound.¹⁴⁸
- (b) The forward peak current in a linear sweep voltammogram for a reversible system is given by the theoretical relationship, Equation 12:

$$i_p = 2.69 \times 10^5 n^{3/2} A D^{1/2} C^* \nu^{1/2} \quad (12)$$

where n is the number of electrons associated with the oxidation (or reduction step) of the parent species, A is the area of the electrode in cm^2 , D is the diffusion coefficient of the species in $\text{cm}^2 \text{ s}^{-1}$, C^* is the bulk concentration expressed in $\text{mol}^3 \text{ dm}^{-3}$, and ν is the potential scan rate, in V s^{-1} . For the set of voltammograms shown in Figure 51 (left) n , A , D and C^* have constant values, thus for a diffusion controlled process it would be expected that i_p^{ox} increases linearly with $\nu^{1/2}$, as is shown to be the case by the plot in Figure 52. If the process involved adsorption of the ferrocene couple on the electrode surface then i_p^{ox} would vary linearly with ν rather than $\nu^{1/2}$, which is not the case.

- (c) Figure 51 shows the ratio $i_p^{\text{red}}/i_p^{\text{ox}}$ is close to unity. Thus on the time scale of this cyclic voltammetric experiment (seconds) the product of one-electron oxidation is stable: the ferrocinium cation is not removed from the diffusion layer at the

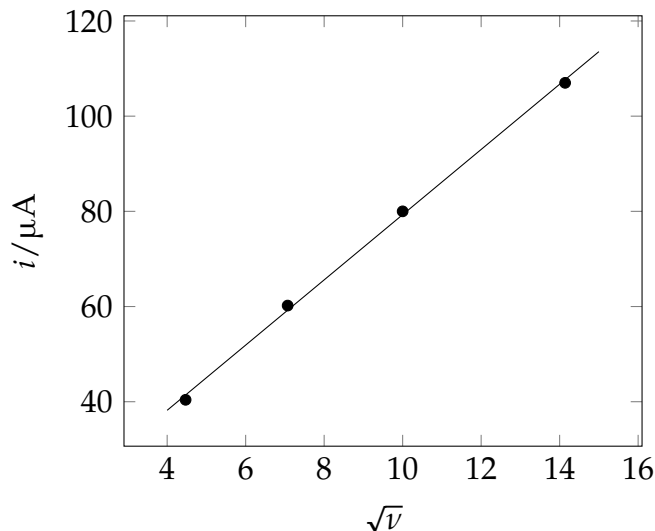


Figure 52: A plot of current peak i_p^{ox} vs the square root of scan rate $\nu^{1/2}$ for ferrocene oxidation

electrode by further reaction(s), the electrochemistry is reversible. A useful means of comparison of the cyclic voltammetric response at different scan rates is to normalise the current across the entire scan by dividing the i data by $\nu^{1/2}$. This is shown for the ferrocene system in Figure 53 for two scan rates, 20 and 200 mV s^{-1} . The double layer-charging (capacitive) and solution resistivity (iR -drop) effects are small in the 0.1 M $[\text{Bu}_4][\text{BF}_4]\text{-MeCN}$ thus the correspondence of the overlaid plots are close. This normalisation is particularly useful in visualising the consequence of chemistry following the primary electron-transfer, as is illustrated later in this Chapter and also in Chapter 4.

Figure 51 shows the position of the $E_{1/2}^{\text{ox}}$ potential for ferrocene, it is the mid-point between E_p^{ox} and E_p^{red} , *i.e.*:

$$E_{1/2}^{\text{ox}} = \frac{E_p^{\text{ox}} + E_p^{\text{red}}}{2} \quad (13)$$

The superscript for $E_{1/2}$ (ox or red) defines whether the oxidation ($E_{1/2}^{\text{ox}}$) of the reduced partner or reduction of the oxidised partner ($E_{1/2}^{\text{red}}$) of a redox couple is being experimentally determined. The values of $E_{1/2}^{\text{ox}}$ and $E_{1/2}^{\text{red}}$ are identical parameters and have the same

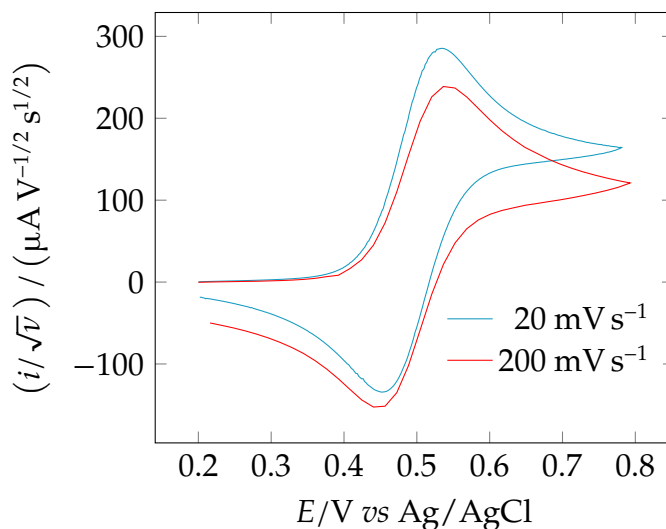


Figure 53: Scan rate-normalized CV of ferrocene (3.5 mM) recorded at a vitreous carbon working electrode containing 0.1 M $[\text{Bu}_4\text{N}][\text{BF}_4]$ -MeCN at 25 °C

sign.

Experimentally it is important to note that if the cyclic voltammetric scan is initiated at a potential where oxidation (or reduction) of the parent compound takes place at a diffusion controlled rate, then for a fully reversible system a cyclic voltammogram similar but not identical to that of one initiated (correctly) at a potential where the parent complex is not electroactive is observed. The current axis is displaced in a negative direction when the scan is initiated at a potential positive of $E_{1/2}^{\text{ox}}$ for an oxidation process. However, the similarity in behaviour of cyclic voltammograms initiated at potentials negative or positive of $E_{1/2}^{\text{ox}}$ for an oxidation process (or the converse for a reduction) has led to misassignments in the literature: a reversible oxidation being assigned to a reversible reduction of the parent species and *vice versa*. This is somewhat compounded in cyclic voltammetric measurements by a further misconception that species which apparently undergo a reversible redox process at a potential significantly negative of a conventional reference electrode, such as the saturated calomel electrode SCE, must involve the reversible reduction of the parent complex, and *vice versa*. This is clearly not the case for easily oxidised electron-rich species. In practice, distinguishing whether or not a compound undergoes a fully reversible oxidation or reduction is easily resolved in a

voltammetric experiment by vigorously stirring the solution or rotating the electrode at a slow potential scan-rate. Either process rapidly removes product from the diffusion layer and observed faradaic current on scanning in either direction shows a current plateau. If this plateau is anodic (positive of zero current) then unequivocally the process is an oxidation of the parent species, a cathodic (negative) plateau will similarly signify the process as a reduction.

Where the primary product undergoes further reaction on the time-scale of the voltammetric experiment it is similarly removed from the diffusion layer, and the current observed upon scan-reversal is diminished. Thus partially reversible (or irreversible) systems are readily assigned as oxidation or reduction processes. As discussed later in this chapter, the cyclic voltammetry of all the neutral diiron species studied show partial reversibility at slow scan rates unambiguously defining the process as an oxidation involving the removal of an electron to give a more or less unstable product.

The Thermodynamic Significance of Cyclic Voltammetric $E_{1/2}$ Values

The Nernst equation (14) defines the equilibrium potential E for a system as:

$$E = E^0 + \frac{RT}{nF} \ln \frac{a^{\text{ox}}}{a^{\text{red}}} \quad (14)$$

where a^{ox} and a^{red} are the thermodynamic activities of the redox partners and E^0 is the *standard potential*. This can be re-written as:

$$E = E^0 + \frac{RT}{nF} \ln \frac{\gamma^{\text{ox}} C^{\text{ox}}}{\gamma^{\text{red}} C^{\text{red}}} \quad (15)$$

where γ^{ox} , γ^{red} , C^{ox} , C^{red} are the respective activity coefficients and concentrations of the oxidised and reduced species. Rearranging (15) gives:

$$E = E^0 + \frac{RT}{nF} \ln \frac{C^{\text{ox}}}{C^{\text{red}}} + \frac{RT}{nF} \ln \frac{\gamma^{\text{ox}}}{\gamma^{\text{red}}} \quad (16)$$

Letting

$$E^{0'} = E^0 + \frac{RT}{nF} \ln \frac{\gamma^{\text{ox}}}{\gamma^{\text{red}}} \quad (17)$$

and, defining $E^{0'}$ as the *formal potential* we have an alternative form of the Nernst equation:

$$E = E^{0'} + \frac{RT}{nF} \ln \frac{C^{\text{ox}}}{C^{\text{red}}} \quad (18)$$

$E_{1/2}$ is related to $E^{0'}$ by the expression:¹⁴⁸

$$E_{1/2} = E^{0'} + \frac{RT}{nF} \ln \sqrt{\frac{D^{\text{red}}}{D^{\text{ox}}}} \quad (19)$$

The diffusion coefficients (D) of the redox partners of systems of moderate molecular mass (>200) are usually quite similar. If we consider a case where the reduced form of the redox pair has a diffusion coefficient as much as 20% greater than that of the oxidised species, then from Equation 19 for a one electron couple:

$$E_{1/2} = E^{0'} + 2.34 \text{ mV} \quad (20)$$

Thus to a reasonable approximation:

$$E_{1/2} \approx E^{0'} \quad (21)$$

Using similar arguments for activity coefficients in Equation 19 then we can use the approximation:

$$E_{1/2} \approx E^{0'} \approx E^0 \quad (22)$$

Variation in $E_{1/2}$ for Series of Closely Related Compounds

Consider the two Nernstian equilibrium shown in Equations 23 and 24 for two closely related species A and B with have associated formal potentials E_{A}^0 and E_{B}^0 respectively.





If E_A^0 is positive of E_B^0 relative to the same reference electrode then A^+ is clearly easier to reduce than is B^+ . The direct corollary of course is that B is easier to oxidise than A because the potential E_B^0 is negative of E_A^0 . In this chapter we report $E_{1/2}^{\text{ox}}$ values measured for a series of diiron dithiolate complexes which undergo reversible one electron oxidation. Unambiguously, if a species B in this series oxidises at a potential $E_{1/2}^{\text{ox},B}$ more negative of $E_{1/2}^{\text{ox},A}$ it is easier to oxidise B than A. This is the basis of comparison of oxidation potentials and their relationship to structure and reactivity.

Electrochemistry of Diiron Complexes

Photoelectron spectroscopy and DFT calculations have shown that in a typical $\text{Fe}_2\text{S}_2(\text{CO})_6$ unit the orbital character of the HOMO (highest occupied molecular orbital) corresponds closely to the classical 'bent' Fe–Fe bond (Chapter 1, Figure 10).^{149–151} Thus, the protonation of the metal–metal bond and the oxidation of diiron complexes engages the HOMO directly. If a reversible one-electron oxidation process in solution is considered, then the value of E^0 (close to $E_{1/2}$) can be viewed as a relative measure of the energy of the HOMO for a series of complexes where solvation energy differences between oxidised and reduced forms are very similar or vary systematically (see 3.3.2).

To this end, a series of electrochemical measurements have been carried out in order to investigate the effect of the bridgehead substituents on the ease by which the complexes are oxidised. The oxidation potentials of all diiron complexes were measured in 0.1 M $[\text{Bu}_4\text{N}][\text{BF}_4]$ -MeCN solution under an atmosphere of argon. Intriguingly, they show that the most sterically demanding complexes such as $i\text{Pr}_2$ are the easiest to oxidise, whilst systems bearing only one donor ligand such as **edt-P** and **S₃-CO** need much more energy to surrender an electron (Table 9).

Table 9: Summary of oxidation potentials of {2Fe2S} and {2Fe3S} complexes measured in 0.1 M [Bu₄N][BF₄]-MeCN; potentials reported *vs* the Fc⁺/Fc couple

Compound	Structure	$E_{1/2}^{\text{ox}}/\text{V}$
edt		-0.15
odt		-0.19
pdT		-0.24
Me		-0.20
Me₂		-0.27
iPr		-0.21
iPr₂		-0.31
pdT-P		+0.14
edt-P		+0.23
bdT		-0.15
S₃-CO		+0.23
S₃		-0.16

A series of cyclic voltammograms also demonstrate that the presence of sterically demanding groups results in a much more stable product. This is evident from Figure 54, left, in which the oxidation of iPr_2 appears to be fully reversible even at low scan rates as the ratio of the reverse peak (i_p^{red}) to the forward peak (i_p^{ox}) is close to 1. This is indicative of the absence of subsequent chemistry following a one-electron oxidation. The only other system exhibiting such behaviour is Me_2 susbite model.

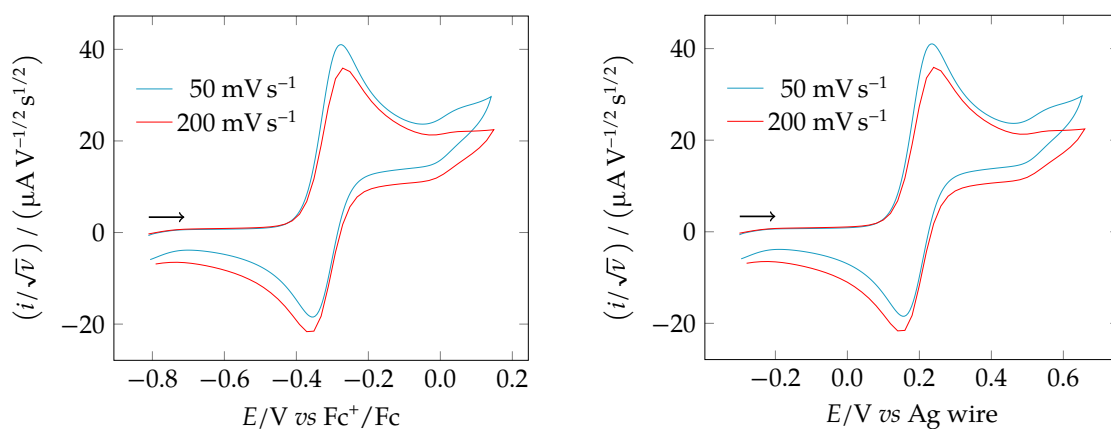


Figure 54: Scan rate-normalized CV of iPr_2 (0.5 mM) recorded at a vitreous carbon working electrode containing 0.1 M $[Bu_4N][BF_4]$ -MeCN at 25 °C; Left: *versus* Fc^+/Fc ; Right: *versus* Ag wire; arrows indicate the direction of the scans

In contrast, oxidation of other complexes is only a partially reversible process, implying the presence of a following chemistry. This is clearly noticeable in the CV obtained for iPr complex (Figure 55, right). Not only is the oxidation of the system irreversible at 50 mV s^{-1} scan rate, but daughter products can also be detected.

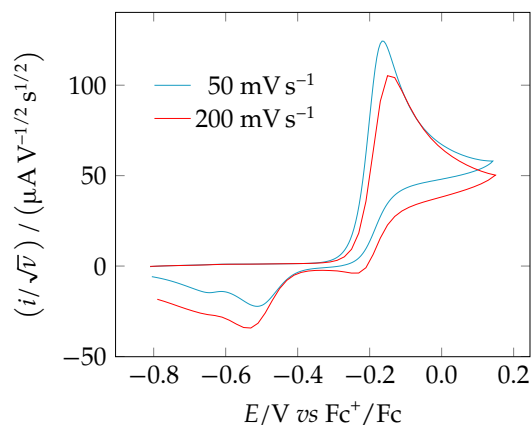


Figure 55: Scan rate-normalized CV of *iPr* (1 mM) (right) recorded at a vitreous carbon working electrode containing 0.1 M [Bu₄N][BF₄]-MeCN at 25 °C

3.3 Analysis: Electronic Influence

3.3.1 Inductive Effects

There is an explicit correlation between the rates of protonation of complexes of the type Fe₂(xdt)(CO)_(6-n)(PMe₃)_n (where xdt = alkyl dithiolate, *n* = 1, 2) and their oxidation potentials (Figure 56). This is a clear indication that different bridgehead substituents are influencing the electronic properties of the diiron complexes and also affecting the kinetics of protonation.

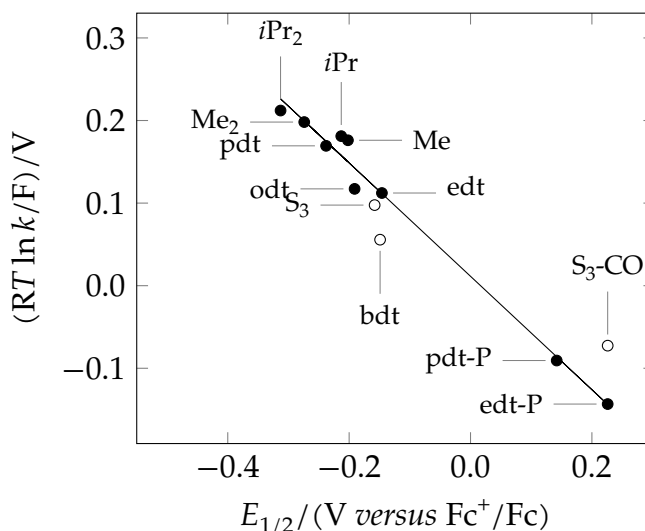


Figure 56: Correlation of rate of protonation with oxidation potential for {2Fe2S} and {2Fe3S} systems; the line shows the best fit for the filled circles; slope = -0.68

There is a clear difference in the electronic properties between the bis-phosphine and mono-phosphine complexes; IR bands for the former are approximately 80 cm^{-1} lower than for the latter. Moreover, diiron dithiolate hexacarbonyls containing no donor ligands can only be protonated by treatment with superacids.⁹⁰ Thus, there is no doubt that introduction of phosphine ligands increases the basicity of the metal–metal bond, in turn lowering the oxidation potential and favouring protonation.

The extent to which the oxidation potentials are altered upon the addition of electron donating substituents can be observed in Figure 57. From this, it can be estimated that introduction of one PMe_3 ligand translates in an increase of $E_{1/2}^{\text{ox}}$ by around 500 mV.

It is notable that the rate of protonation of the **pdt-P₄** complex is too fast to measure by the stopped-flow UV-vis spectroscopy. However, the correspondence between $\ln k$ and $E_{1/2}$ shown in the plot allows prediction of the rate constant for this and similar systems. In the **pdt-P₄** case the rate of protonation is estimated to be around $1.3 \times 10^{13}\text{ M}^{-1}\text{ s}^{-1}$. This is around 3 orders of magnitude larger than expected for a diffusion controlled reaction. However, taking into consideration the errors of the plot, the protonation of this system is likely to be diffusion controlled.

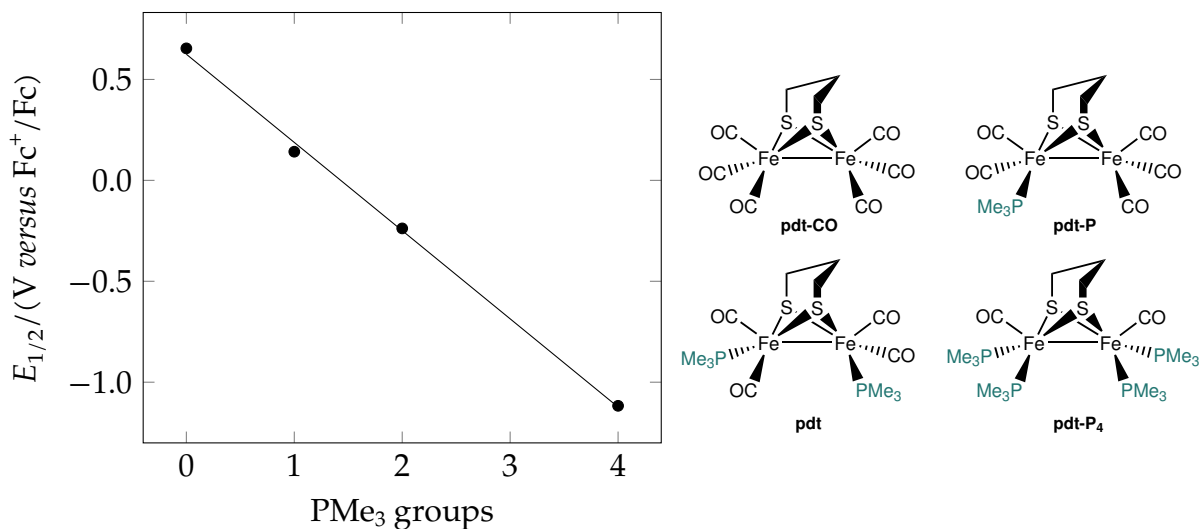
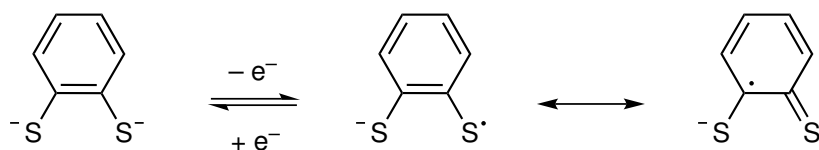


Figure 57: Left: Correlation of oxidation potential with degree of substitution, potentials recorded at vitreous carbon electrode in 0.1 M $[Bu_4N][BF_4]$ -MeCN vs Fc^+/Fc ; Right: Structures of complexes under investigation

Thus the difference in oxidation potentials and protonation rates between **edt-P** and **edt**, and between **pdt-P** and **pdt** arise due to additional electron-rich PMe_3 groups. The variation between **edt** and **pdt** can be attributed to the inductive effects of the bridgehead atoms exerted through sulfur ligands. However, similar oxidation potentials for **pdt**, **Me** and **iPr** suggest that the central alkyl groups are too far removed from the metal centres to exhibit any significant inductive effects. This implies that other factors such as sterics might be important.

In the **bdt** case, there are two possible factors contributing to its 'unusual' behaviour – sterics or electronics. The steric consideration encompasses a rigid and enforcing backbone structure, which accounts for the slower protonation rate of **bdt** system than the redox potential predicts. On the other hand, its oxidation potential is more negative than expected from its rate of protonation. This might be attributed to the electronic properties of benzene dithiolate. The ease of oxidation of **bdt** might arise from the stability of the radical cation in which the electron is delocalised within the aromatic backbone (Scheme 29).



Scheme 29: Oxidation of 1,2-dithiol ligand

Whilst the S_3 system appears to be in line with the $\{2Fe2S\}$ complexes, its unsubstituted precursor S_3-CO is not. Its oxidation potential is more positive than the rate would predict, presumably due to the weaker donative abilities of SMe ligand when compared to PMe_3 in complexes such as **edt-P** or **pdt-P**. On the other hand, the rate of protonation is faster than the oxidation potential suggests, potentially owing to an increased accessibility of $Fe-Fe$ bond, which is not obscured by the more bulky phosphine group. Even though these three subsite models do not fall directly on the trend line, they still follow the broad pattern where an increase in the sterics and electron-richness on the bridge translates into an accelerated protonation rate.

3.3.2 HOMO Energy Levels

An explanation for an observed difference in protonation rates of diiron subsite models rests with the energy level of orbitals engaged in the reaction. Protonation/oxidation is concerned with the removal of electrons from the $Fe-Fe$ bond and typically it is associated with HOMO (highest occupied molecular orbital) level. The energy of HOMO in a molecule can be directly measured by gas-phase techniques such as photoelectron spectroscopy, which provide a measurement of the ionisation potential.

The formal redox potential (E^0) can be generally obtained from the gas phase ionisation energy (I_E) and the solvation free energies of oxidised and reduced forms of compound $\Delta_{solv}G_{ox}$ and $\Delta_{solv}G_{red}$ respectively (Equation 25).

$$E^0 = \Delta_{solv}G_{ox} - \Delta_{solv}G_{red} + I_E \quad (25)$$

However, for a series of compounds in which ΔG_{solv} between the reduced and oxidised

forms change in a regular manner the oxidation potentials are linearly related to I_E . The measured oxidation potentials ($E_{1/2}^{ox}$) can therefore be viewed as 'solution' ionisation potentials, *i.e.* the energy of HOMO.

Correlation between HOMO and ($E_{1/2}^{ox}$) of transition metal complexes has a theoretical basis and has been examined before. For example, Sarapu and Fenske have shown that the HOMO energies of the complexes $[\text{Mn}(\text{CO})_{6-n}(\text{CNPh})_n]^+$ ($n = 1 - 6$) calculated *in silico* exhibit a linear relationship with experimentally determined $E_{1/2}^{ox}$.¹⁵²

If this is generally true then diiron dithiolate complexes that contain stronger electron-donating bridgehead substituents and low oxidation potentials will have the highest HOMO energy levels. Provided that the transition state of these systems are of similar energy, this would decrease the activation energy E_a required for the protonation reaction to occur (Figure 58). Thus, the inductive effects exerted by different substituents on the central bridgehead carbon or metal centres, which result in increased basicity of the metal-metal bond and raised HOMO levels can at least in part account for the observed vast difference in rates of protonation.

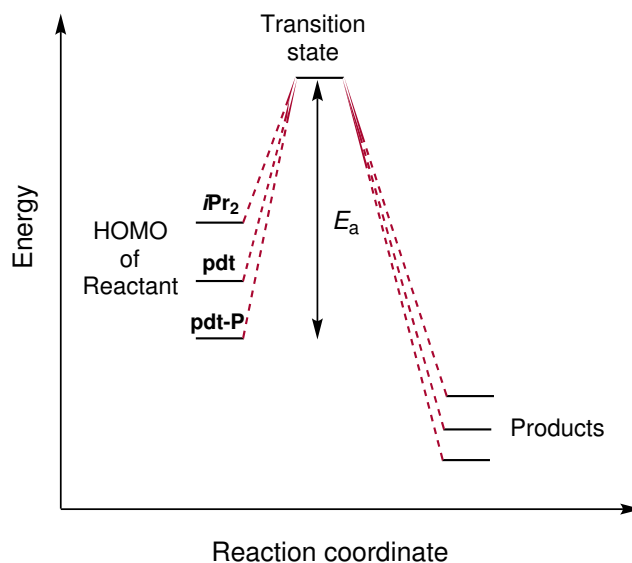
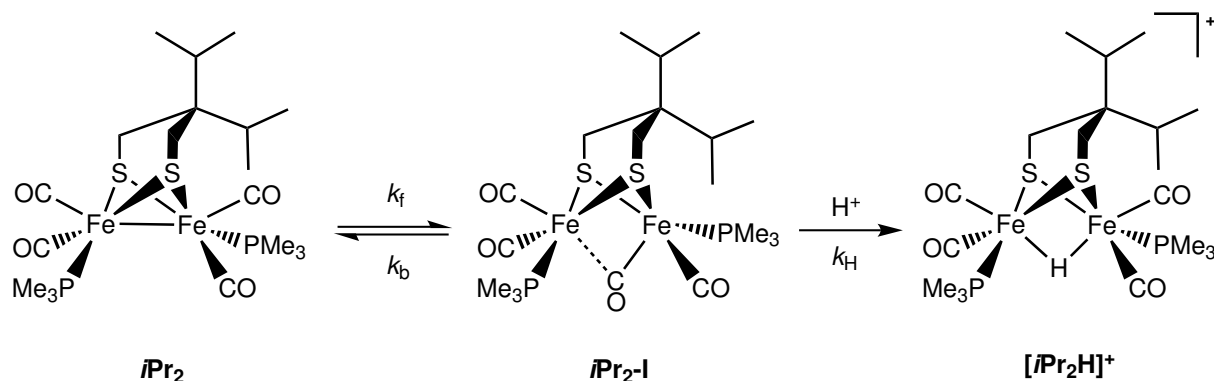


Figure 58: Potential energy diagram showing how different bridgehead substituents affect the HOMO levels and activation energy of protonation

3.4 Analysis: Steric Effects

3.4.1 Transient Species and Intermediates

Here the possible effect of steric bulk at the bridgehead of the diiron systems on the kinetics of protonation is considered. As evident from the solid state X-ray structure of iPr_2 , the complex exhibits a semi-bridging CO arrangement. It also yields the fastest protonation rate for $\{2Fe2S\}$ systems studied. It is possible that in the solution phase there is an equilibrium between the iPr_2 complex with all terminal CO ligands and a low concentration of intermediate iPr_2-I with a semi-bridging CO as observed in the solid state (Scheme 30). As quantified by the stopped-flow techniques, the overall rate of reaction is first order in the complex under *pseudo*-first order conditions. Thus, if the iPr_2-I species is on the pathway of formation of $[iPr_2H]^+$, the k_f must be much greater than k_H for protonation to be the rate-determining step, as is observed from the experimental methods.

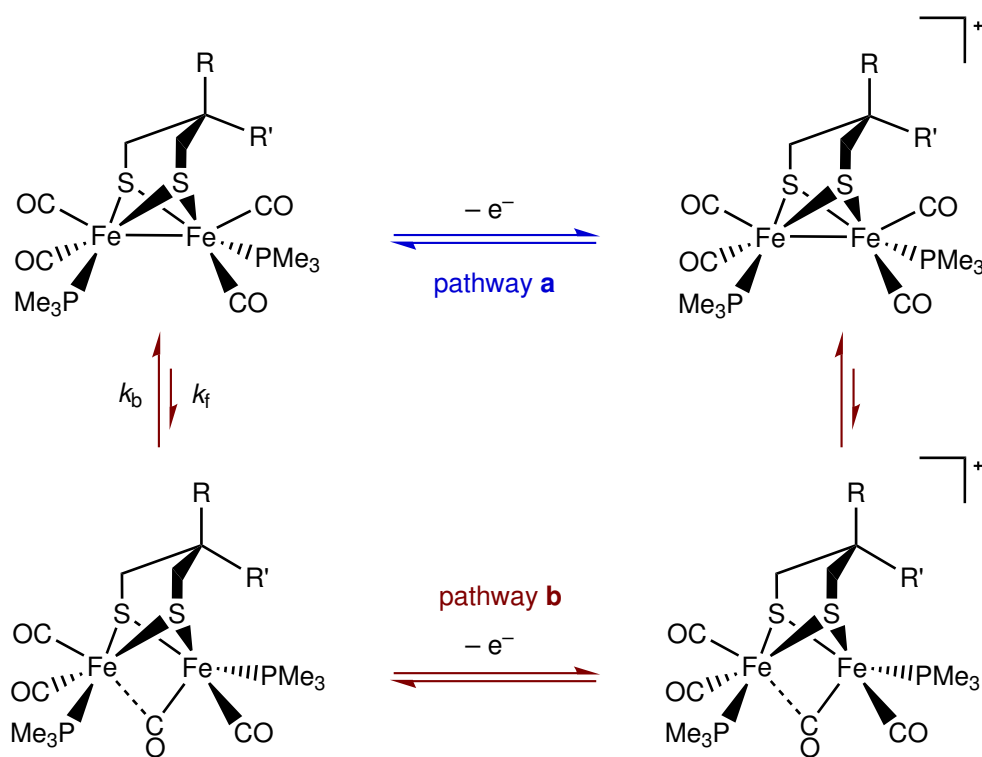


Scheme 30: Proposed iPr_2 states in solution phase

Interestingly, DFT simulations performed for Scheme 31 suggests that neutral structures in which $R = H$ or Me and $R' = H$ results in complexes with all-terminal carbonyl ligands, *i.e.* formation of a bridging CO species is calculated to be unfavourable. This implies that steric bulk on the bridgehead is not sufficient to enforce a rotated state geometry, thus the oxidation proceeds *via* pathway **a**. On the other hand, when both

R and R' = Me in the neutral complex, the only optimised structure which is stable possesses a semi-bridging CO. This implies that the pathway **b** is more favourable in dialkylated systems in which steric bulk on the bridge plays an imposing role on the structure.

That the experimentally measured $E_{1/2}$ for oxidation in the Me_2 and $i\text{Pr}_2$ systems is that for the semi-bridging CO molecule rather than the terminal form can be understood in terms of the 'scheme of squares' (Scheme 31). The fast equilibrium between the semi-bridged and terminal forms leads to a measured $E_{1/2}$ of the semi-bridging form, even though the equilibrium lies over to the terminal form, as evident from IR spectroscopy.



Scheme 31: Two pathways of formation for the oxidised diiron dithiolate complexes explored by DFT (J. A. Wright)

DFT simulations also shows that the HOMO in both the Me with all terminal CO ligands and the Me_2 possessing a semi-bridging CO is predominantly metal–metal bond in character (Figure 59). Thus the $E_{1/2}$ that is measured for the complex is the one for the

dominant form. Complexes with a rotated state geometry have been shown to oxidise at a lower potential than the related non-bridging systems.³³ Thus the presence of a semi-bridging CO form is expected to raise the energy level of HOMO, accounting for a more negative oxidation potentials and higher protonation rates for **Me**₂ and *iPr*₂ complexes.

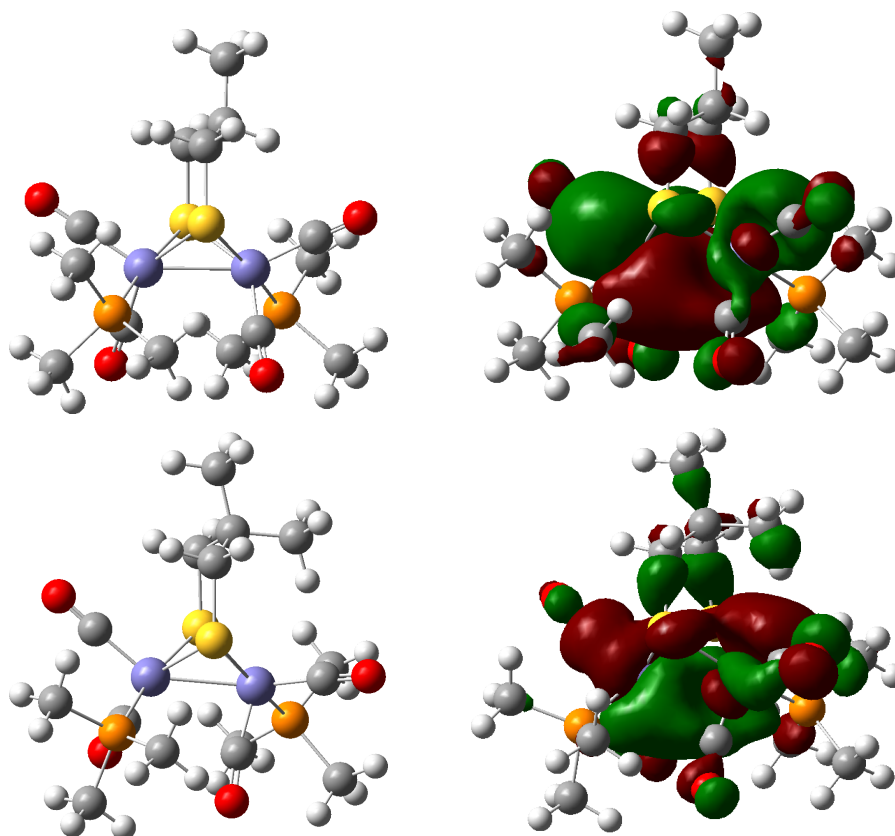
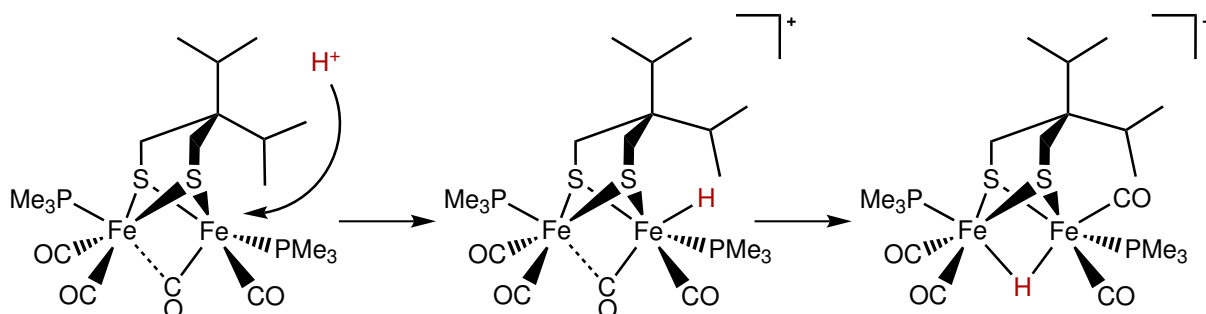


Figure 59: Left: structure of **Me** (top) and **Me**₂ (bottom) as optimised by DFT; Right: isosurface of spin density of HOMO

3.4.2 Further Mechanistic Considerations

The subsequent proton attack can proceed *via* two possible pathways: (i) terminal approach or (ii) approach from below. The terminal approach encompasses H⁺ attack from above, coordinating at the apical terminal position (Scheme 32). Such formation of

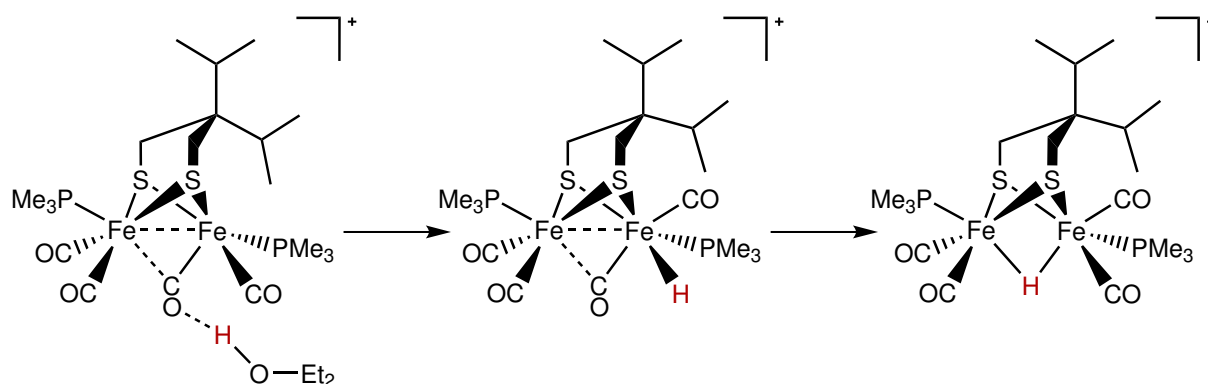
terminal hydride intermediates have been long thought to be on the pathway of a more thermodynamically stable bridging hydride species. This idea was based on a handful of occurrences when terminal hydrides were detected at or below $-40\text{ }^{\circ}\text{C}$.^{87,98} The lack of success in observing such species in the majority of protonation reactions have been attributed to the short-lived nature and instability of terminal hydrides. However, since then compelling evidence has been provided supporting the idea that protonation of diiron dithiolates can proceed without such intermediates.⁹⁶ Whilst the proton alone is generally small enough to circumvent the bulk of the bridge obscuring the terminal position, it most likely exists as solvated species in a solution, which greatly increases its size. This and the fact that terminal hydrides are not observed even in slow-protonating systems renders this pathway as unlikely.



Scheme 32: Protonation by terminal approach

The second possibility entails the proton approach from below the molecule, potentially guided by one of the carbonyl ligands (Scheme 33). The idea that ether (or solvent) might be acting as a proton carrier has been explored by De Gioia, Schollhammer, Hall and their co-workers.^{102,153,154} Employing DFT calculations Hall has determined that the most favourable protonation pathway of diiron subsite models involves an intermediate with $[\text{Et}_2\text{OH}]^+$ bound to a CO ligand followed by rearrangement to a terminal hydride in the basal position. This pathway is entirely consistent with the proposed approach from 'below'. The interaction between the solvated proton and carbonyl is most likely to occur at the semi-bridging CO site. The 'ketone-like' bridging carbonyl is much more basic

than the terminally-bound COs and is more likely to play a role in navigating the proton to its terminal basal position, presenting this pathway as the most plausible.



Scheme 33: Protonation by approach from below

The proposed protonation pathway would also account for the observed rise in rates with an increased bulkiness on the bridgehead position. Sterically demanding groups would favour semi-rotated carbonyl ligands, which in turn are more accessible for incoming protons.

3.5 Summary

A combination of stopped-flow UV-visible and IR studies on a range of {2Fe2S} subsite models, which possess bulky bridgehead substituents, revealed that protonation of the metal–metal bond does not proceed *via* a simple one-step mechanism. This is consistent with previous studies in which at least two phases were identified: initial protonation directly on the Fe–Fe bond followed by a slower ligand isomerisation to form the thermodynamically most stable product.

Surprisingly, the rate of protonation was found to increase with the steric demand of the bridgehead group. This was attributed to two factors: steric and electronic. The inductive effects appear to be the most prominent in complexes with a different degree of PMe_3 substitution and systems with different composition of the three-atom bridge. They

not only increased the basicity of the metal–metal bond, but also were found to raise the energy level of HOMO, thus decreasing the activation energy required for protonation to occur. The steric effect was found to be important mostly for the dialkylated bridgehead complexes. The bulkiness of the bridge was postulated to enforce the semi-rotated state geometries which aid in providing a site for proton to bind. The increased population of the minor bridging carbonyl form is thought to account for the rate enhancement with increased steric demand.

Here the first comprehensive study on rates and oxidation potentials of a family of the subsite models for the Fe–Fe-hydrogenase is provided. Lastly, an explanation has been put forward to account for the variation of the reactivity of diiron systems with an increased bulk on the backbone structure. The rotated state geometry in the protein is enforced by the neighbouring residues and has thus far been challenging to reproduce in synthetic models. Here we demonstrate that bulk introduced on the backbone structure of diiron dithiolates can aid in achieving this geometry. Not only does it stabilise the semi-bridging CO but also results in a vastly more reactive complex towards protons. Since the protonation plays a major role in biological hydrogen evolution cycle, this discovery has the potential to influence the future designs of diiron catalysts.

3.6 Experimental

Unless otherwise stated, reactions were carried out under nitrogen using conventional air-sensitive techniques. Solvents were degassed using a nitrogen purge and dried using an M. Braun solvent purifier unit before use. Starting materials were purchased from Aldrich or Alfa Aesar and were used without further purification. Compounds **edt**,¹²¹ **pdt**,¹²⁹ **odt**,¹³⁵ **bdt**,¹³³ **Me**,¹³³ **Me**₂,³³ **S**₃-**CO**,¹¹⁵ **pdt-P**,¹²² **pdt-PO**¹²² and **pdt-P**₄⁹⁶ were prepared according to literature procedures.

Stopped-flow measurements

Stock solutions for stopped-flow were prepared in a Belle Technology glove box (oxygen concentration <10 ppm), and were adjusted to the required concentration by dilution with acetonitrile.

UV-visible measurements were carried out using a Tgk Scientific stopped-flow system equipped with a xenon lamp, monochromator and photomultiplier tube detector. The cell and drive system were located inside the glove box, with fibre optic connection to the source and detector located outside the box. The flow syringes and cell were thermostated to $21.0\text{ }^{\circ}\text{C} \pm 0.2\text{ }^{\circ}\text{C}$ using a Thermo Scientific recirculating bath. For each experiment, three separate shots were carried out and the data averaged before further analysis. The initial concentration of substrate was typically 0.12 mM after mixing. Data collection and curve fitting were carried out using the Tgk Kinetic Studio application. Typically, data were collected such that 100 time points were recorded for each experiment.

IR measurements were carried out using a Tgk stopped-flow drive interfaced to a Bruker Vertex 80 spectrometer equipped with a custom-built flow cell (path length = 50 μm) fitted with CaF_2 windows (Tgk Scientific). The drive unit was located inside the glove box, with the reagents carried to the cell prior to mixing *via* a flexible conduit. The cell itself was mounted in a miniature anaerobic chamber fixed inside the sample compartment of the IR instrument. The conduit and cell were thermostated to $21.0\text{ }^{\circ}\text{C} \pm 0.2\text{ }^{\circ}\text{C}$ using a Thermo Scientific recirculating bath. Mixing of the two solutions occurred in a chamber within the cell body. The initial concentration of substrate was typically 0.50 mM after mixing. A Northumbria Optical Coatings filter (pass band 4.76 μm to 5.60 μm) was fitted in front of the cell, within the sample chamber. The stopped-flow system was controlled using the Tgk KinetaDrive and Bruker Opus 3D packages. IR data was processed and analysed using the Fit_3D application¹⁵⁵ and curve fitting was carried out using SciDAVis. Data were normally collected at 4 cm^{-1} resolution. Typically, between 60 and 180 time points were recorded for each experiment.

Electrochemical measurements

Cyclic voltammetry measurements were carried out in 0.1 M [Bu₄N][BF₄]-MeCN or 0.2 M [Bu₄N][BF₄]-THF using a three compartment cell fitted with a glassy carbon working electrode (diameter 3 mm, area 7.1 mm²), a platinum counter electrode and a silver wire pseudo-reference electrode interfaced with an Autolab PGSTAT30 potentiostat. Potentials were calibrated using ferrocenium/ferrocene as an internal standard.

DFT calculations

All calculations were performed using the Gaussian 09¹⁵⁶ computational package. Geometry optimisation and frequency calculations have been carried out using the Tao–Perdew–Staroverov–Scuseria¹⁵⁷ (TPSS) density functional. Phosphorus, sulfur and iron atoms are described by the the Hay and Wadt LANL2DZ^{158,159} basis set with effective core potential (ECP). In the case of iron, the two outermost p functions were replaced with reoptimised 4p functions.¹⁶⁰ For sulfur and phosphorus, additional p and d polarisation functions were added.¹⁶¹ All other atoms employ the all electron 6-31+G** basis set. Structures were geometry optimised in the gas phase with the default convergence criteria and confirmed as minima through frequency calculations.

Tables of *Pseudo-First Order Rate Constants*

Concentration of [HBF ₄ ·Et ₂ O]/ mM	<i>Pseudo</i> -first order rate constants k_{obs} for pdt / s ⁻¹
21.1	9.47 (5)
42.3	34.19 (4)
84.5	64.80 (18)
169.1	143.4 (2)
338.1	266.4 (9)

Concentration of [HBF ₄ ·Et ₂ O]/ mM	Pseudo-first order rate constants k_{obs} for edt / s ⁻¹
125	10.61 (1)
250	21.14 (2)
375	30.33 (4)
500	42.48 (7)

Concentration of [HBF ₄ ·Et ₂ O]/ mM	Pseudo-first order rate constants k_{obs} for odt / s ⁻¹
50	5.658 (9)
125	14.740 (8)
250	26.34 (3)
375	39.22 (6)
500	49.7 (1)

Concentration of [HBF ₄ ·Et ₂ O]/ mM	Pseudo-first order rate constants k_{obs} for Me / s ⁻¹
12.5	4.735 (9)
25	23.81 (4)
50	57.44 (11)
75	84.77 (12)
100	100.8 (3)
150	152.9 (2)

Concentration of [HBF ₄ ·Et ₂ O]/ mM	Pseudo-first order rate constants k_{obs} for Me₂ / s ⁻¹
12.5	27.82 (4)
25	66.72 (4)
50	121.63 (8)
75	189.9 (3)

Concentration of [HBF ₄ ·Et ₂ O]/ mM	Pseudo-first order rate constants k_{obs} for iPr / s ⁻¹
25	47.6 (1)
50	73.0 (2)
75	101.6 (2)
100	125.1 (2)
125	148.4 (3)

Concentration of [HBF ₄ ·Et ₂ O]/ mM	Pseudo-first order rate constants k_{obs} for iPr₂ / s ⁻¹
25	126 (3)
50	189 (1)
75	324 (4)
100	444 (16)

Concentration of [HBF ₄ ·Et ₂ O]/ mM	Pseudo-first order rate constants k_{obs} for S₃-CO / s ⁻¹
75	0.0043 (1)
100	0.0050 (1)
125	0.0076 (2)
150	0.0089 (5)
175	0.0103 (3)

Concentration of [HBF ₄ ·Et ₂ O]/ mM	Pseudo-first order rate constants k_{obs} for S₃ / s ⁻¹
25	1.248 (2)
50	1.963 (4)
75	2.88 (1)
125	4.32 (2)
150	5.118 (27)
200	7.568 (18)
250	8.652 (17)

Concentration of [HBF ₄ ·Et ₂ O]/ mM	Pseudo-first order rate constants k_{obs} for bdt / s ⁻¹
50	0.524 (4)
75	0.548 (7)
100	0.867 (3)
125	1.184 (6)
150	1.422 (9)
175	1.664 (4)

Concentration of [HBF ₄ ·Et ₂ O]/ mM	Pseudo-first order rate constants k_{obs} for edt-P / s ⁻¹
250	0.0013 (5)
250	0.0016 (2)
500	0.0018 (3)
1000	0.0034 (3)

Concentration of [HBF ₄ ·Et ₂ O]/ mM	Pseudo-first order rate constants k_{obs} for pdt-P / s ⁻¹
25	0.0008 (2)
50	0.0015 (3)
75	0.0024 (3)
100	0.0026 (4)

Chapter 4

(Super)Reduced Hydride States at {2Fe2S} and {2Fe3S} Cores

4.1 Hydrides at Metallo-Sulfur Centres

Hydrides at various metallo-sulfur cores have been widely postulated as key intermediates in biological catalytic cycles. Bridging hydride species have been recently identified at FeMo-co (iron-molybdenum cofactor) centres, the active sites of nitrogenases responsible for nitrogen fixation.⁹² They are thought to play a crucial role in hydrogen evolution and uptake by the [Fe–Fe]- and [Ni–Fe]-hydrogenases,⁶¹ as well as heterolytic hydrogen activation by the [Fe]-hydrogenase.¹⁶² Terminal hydrides bound to nickel centres in carbon monoxide dehydrogenases (CODH) have also been implicated in catalysis of the interconversion of CO₂ to CO.¹⁶³ Unsurprisingly, this has led to extensive protonation studies of synthetic biomimetic systems which model these natural processes.⁸³

With the aim to understand the chemistry taking place at the active site of the [Fe–Fe]-hydrogenase, much work has been done on isolating and spectroscopically characterising bridging and terminal hydride complexes. This has resulted in a wide library of Fe(II)–Fe(II)- μ -hydride systems^{86,129,164} and a handful of examples of terminally bound Fe(I)–Fe(II) species at {2Fe2S} cores.^{94–96}

Whilst enzymatic H₂ production have been assumed to proceed *via* an intermediacy of

terminal hydrides, de Gioia has noted from DFT simulations that this may also occur *via* mixed-valence μ -hydride species.¹⁶⁵ Since there has only been a small number of mixed-valence Fe(I)–Fe(II) hydrides observed and characterised spectroscopically, endeavouring to extend the library of these species and examine their reactivity is an exciting and important objective. It is these as-yet unisolated and spectroscopically uncharacterised Fe(I)(μ -H)Fe(II) states that will be the focus of this chapter. The complexes under investigation are depicted in Figure 60, ranging from an uncomplicated symmetrical edt system ([edtH]⁺) to a {2Fe3S} model ([S₃H]⁺) possessing a closer structural homology to the iron-sulfur core of the [Fe–Fe]-hydrogenase. A combination of various transient spectroscopic techniques not only allowed examination of the reductive chemistry of these subsite mimics, but also granted access to unprecedented *super-reduced* states.

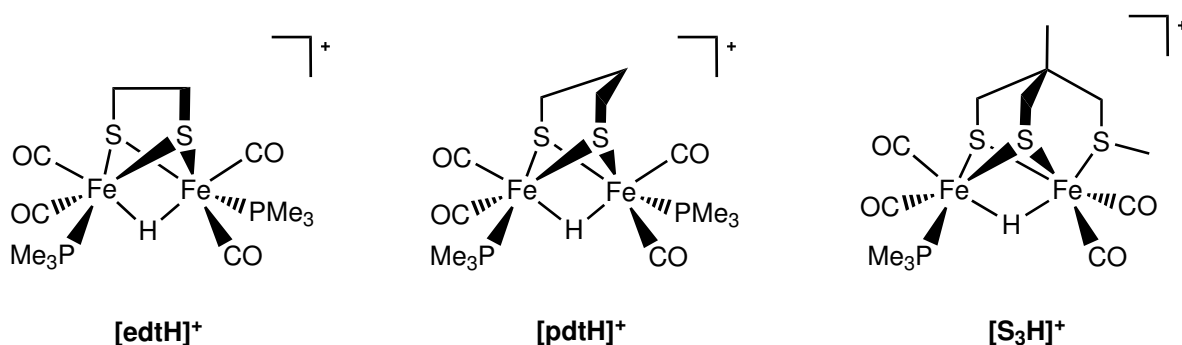


Figure 60: Structural models of the subsite of [Fe–Fe]-hydrogenase investigated in this chapter

4.2 Mixed-Valence Fe(I)–Fe(II) Hydrides

4.2.1 CV Measurements

Cyclic voltammetry experiments have provided primary evidence for the mixed-valence μ -hydride species.¹⁶⁶ Reduction of [pdtH]⁺ and [edtH]⁺ at 50 mV s⁻¹ recorded at 25 °C reveals a partially reversible process, which approaches full reversibility at 500 mV s⁻¹. Figure 61 shows CV data where the current i has been normalised by the square root of

scan rate. This allows a direct comparison of the effect of scan rate on the stoichiometry of electron transfer in fast and slow time frames.

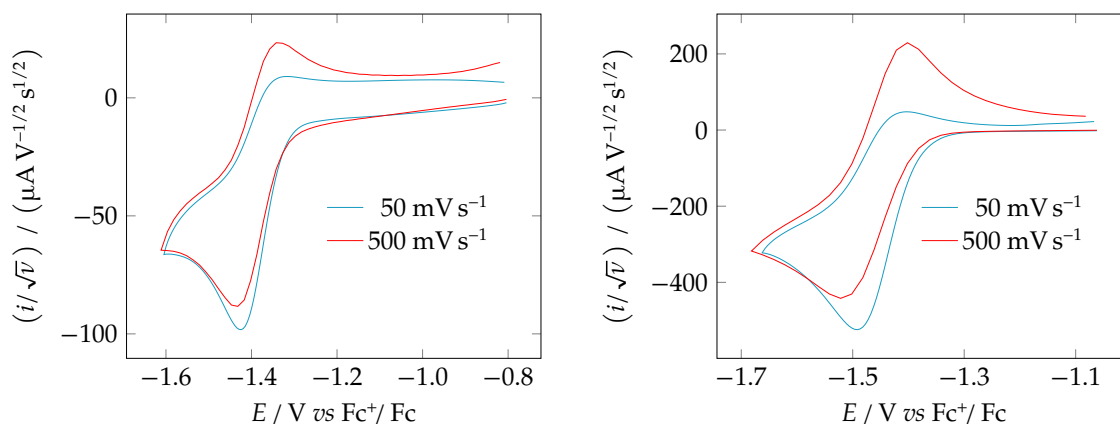
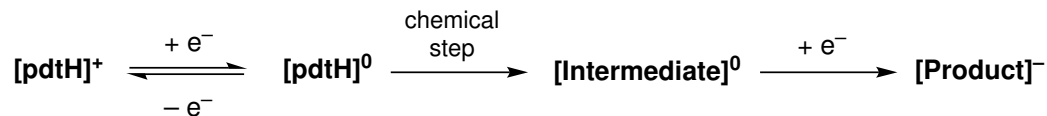


Figure 61: Scan rate-normalized CV of $[\text{pdtH}]^+$ (1 mM) (left) and $[\text{edtH}]^+$ (5 mM) (right) recorded at a vitreous carbon working electrode in 0.1 M $[\text{Bu}_4\text{N}][\text{BF}_4]\text{-MeCN}$ at 25 °C

CV measurements reveal that at higher scan rates the ratio of the reverse peak (i_p^{ox}) to the forward peak (i_p^{red}) approaches 1. The peak separation, ΔE_p is *ca* 63 mV for $[\text{pdtH}]^+$ and *ca* 68 mV for $[\text{edtH}]^+$ as measured at 50 mV s^{-1} . This is consistent with a one electron reduction according to the relationship depicted in Equation 26 (where n is the number of electrons involved in a redox process).

$$\Delta E_p = |E_p^{\text{ox}} - E_p^{\text{red}}| = \frac{59}{n} \text{ mV} \quad (26)$$

At slower scan rates $i_p^{\text{ox}}/i_p^{\text{red}}$ is less than 1, corresponding to the instability of a 35-electron product and a chemical step succeeding the initial electron transfer. Furthermore, the scan rate normalised current function i^{red}/\sqrt{v} at 50 mV s^{-1} is substantially greater than that at 500 mV s^{-1} , which suggests further electron transfer following a chemical step. These processes can be summarised by the ECE (electron transfer – chemical reaction – electron transfer) steps shown in Scheme 34.

Scheme 34: Proposed ECE mechanism for the reduction of $[\text{pdtH}]^+$

At 50 mV s^{-1} , the $[\text{pdtH}]^+$ system is partially reversible with i_p^{ox} approximately 50% of i_p^{red} . At this scan rate the time taken to scan from the forward to the reverse peak is *ca* $60 \text{ mV s}^{-1} / 50 \text{ mV s}^{-1} = 1.2 \text{ s}$ thus the half-life of the reduced species is of the order of one second.

Reduction of $[\text{edtH}]^+$ shows similar results, but the primary product is less stable under identical conditions. In addition, $[\text{edtH}]^+$ is reduced at slightly more negative potential, exhibiting $E_{1/2} = -1.41 \text{ V}$ (*vs* Fc^+/Fc) when compared to $E_{1/2} = -1.38 \text{ V}$ (*vs* Fc^+/Fc) for the $[\text{pdtH}]^+$ complex.

In contrast, CV of $[\text{S}_3\text{H}]^+$ demonstrates that the complex is reduced reversibly in a diffusion-controlled process even at lower scan rates (Figure 62). The peak separation $\Delta E_p = 50 \text{ mV}$ as measured at 20 mV s^{-1} , is somewhat under that expected for a one electron reduction. This correlates to a much more stable 35-electron product, which has the half-life around five times that of the corresponding $[\text{pdtH}]^+$ species. Moreover, reduction of $[\text{S}_3\text{H}]^+$ occurs at much less negative potentials ($E_{1/2} = -1.12 \text{ V}$ *vs* Fc^+/Fc) than the related {2Fe2S} subsite mimics. This parallels the oxidation potentials obtained for the unprotonated parent complexes, where it is found that the removal of an electron from **pdt** is easier by 80 mV than for **S₃** system, corresponding to a weaker donative ability of the SMe group.

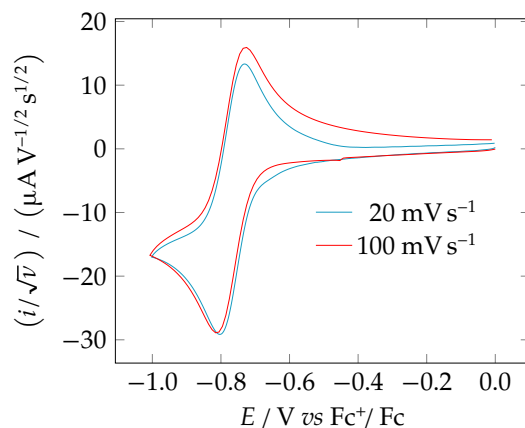


Figure 62: Scan rate-normalized CV of $[S_3H]^+$ (0.5 mM) recorded at a vitreous carbon working electrode in 0.1 M $[Bu_4N][BF_4]$ -MeCN at 25 °C

4.2.2 EPR Experiments

Since the reduction of $[pdth]^+$ and $[S_3H]^+$ complexes generates species possessing an unpaired electron, a convenient way to examine such systems is to employ electron paramagnetic resonance (EPR) spectroscopy. Similar to NMR technique, EPR examines the interactions between electromagnetic radiation and magnetic moments, but in the case of the latter, the magnetic moments arise from unpaired electrons rather than nuclei.¹⁶⁷ The technique is based on the absorption of this radiation, most frequently in the microwave frequency region, by a paramagnetic sample placed in a magnetic field. The position of the absorption, the separation, relative intensities, line shapes and widths can all provide information about the location of the unpaired electrons as well as structure and the dynamic processes of the species under investigation.

The EPR spectra of all the complexes were ran and analysed by Dr. Shirley A. Fairhurst. Due to the very short life-time of $[edth]^0$ species, it was not possible to examine it by EPR spectroscopy. However, greater stability of both the reduced $[pdth]^+$ and the $[S_3H]^+$ complexes meant that EPR could be employed. Reduction of $[pdth]^+$ was carried out using acenaphthylene monoanion radical ($E_{1/2} = -2.26$ V vs Fc^+/Fc)¹⁶⁸ in THF. The sample was rapidly frozen in liquid nitrogen to prolong the lifetime of reduced species. The

solution was then slowly warmed up to 165 K to give a well-defined isotropic spectrum for $S = 1/2$ species $[\text{pdtH}]^0$ (Figure 63, top left). Analysis of the spectrum gives g factor of 2.0066, which differs from the free electron value of $g_e = 2.0023$, due to interactions with local magnetic fields in the molecule. Thus, the unpaired electron exhibits strong hyperfine couplings with three nuclei: two equivalent phosphorus atoms giving rise to three cross-overs ($|A_{\text{iso}}| = 42$ MHz), and the bridging hydride resulting in 1 : 1 splitting ($|A_{\text{iso}}| = 76$ MHz). The assignment of the latter was confirmed by the reduction of $[\text{pdtD}]^+$ complex possessing a μ -deuteride. The spectrum of this species gave the anticipated 1 : 1 : 1 splitting due to coupling with bridging deuteride ($|A_{\text{iso}}| = 12$ MHz) with no change observed for the phosphorus coupling (Figure 63, bottom left). The reduced intensity between the protio and deutero spectra arises from a smaller magnetogyric ratio for deuterium (γ_{D}) compared to that of a proton (γ_{H}), which is six times larger for the latter. The EPR data is in accord with a symmetrical disposition of the radical character of 35-electron reduced $[\text{pdtH}]^0$ species. Simulated EPR spectra are also in good agreement with the experimental observations (Figure 63, right).

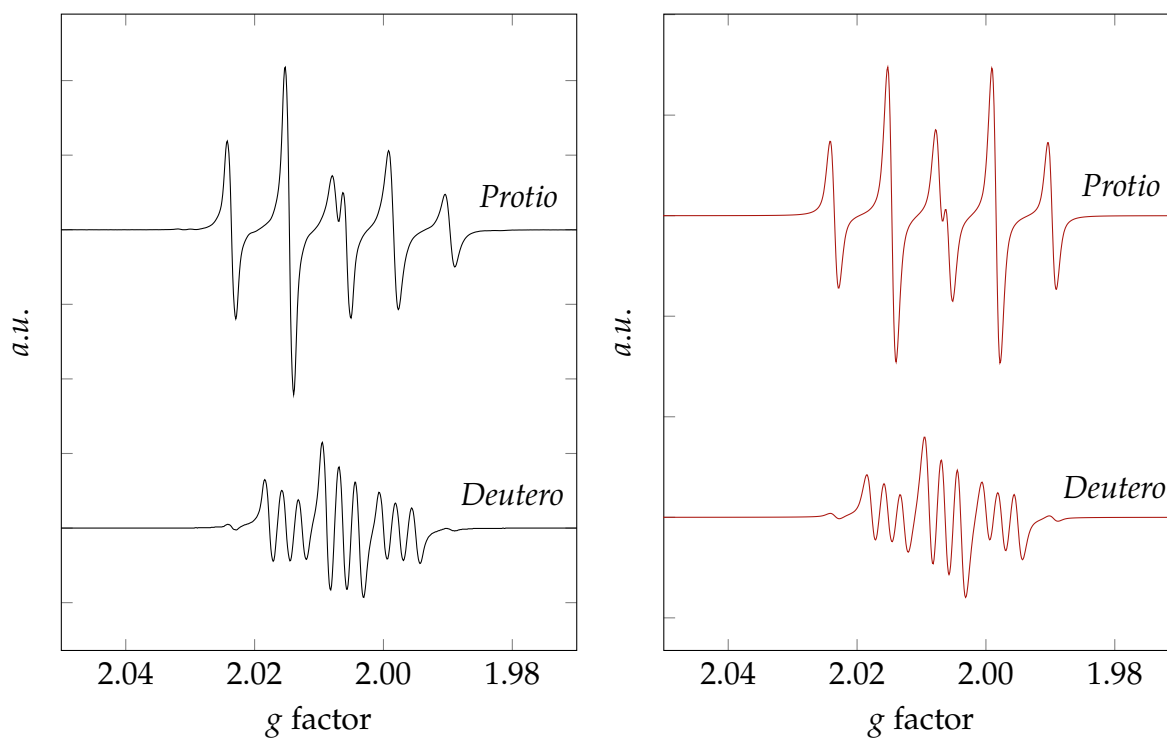


Figure 63: Left: experimental continuous wave X-band EPR spectra in THF: (top) reduced $[\text{pdtH}]^+$ at 165 K; (bottom) reduced $[\text{pdtD}]^+$ at 164 K. Right: simulated EPR spectrum for: (top) reduced $[\text{pdtH}]^+$; (bottom) reduced $[\text{pdtD}]^+$; experimental and simulated spectra were obtained and analysed by Dr. Shirley A. Fairhurst

Chemical reduction of $[\text{S}_3\text{H}]^+$ was carried out using the same procedure as described above. EPR spectrum of the reduced material at 165 K in THF gave a defined isotropic spectrum for the $S = 1/2$ species, with a g factor of 2.0209 (Figure 64, top left). The unpaired electron was found to exhibit strong hyperfine couplings to the bridging hydride ($|A_{\text{iso}}| = 41$ MHz) and to the phosphorus atom ($|A_{\text{iso}}| = 74$ MHz). The assignment of the two couplings was confirmed using a μ -deuteride complex $[\text{S}_3\text{D}]^+$, which exhibits expected change in the coupling patterns (Figure 64, bottom left). The coupling values are very similar to $[\text{pdtD}]^+$ complex and the EPR data are therefore fully in accord with the formulation of $[\text{S}_3\text{D}]^0$ as a mixed-valence 35-electron species. Simulated EPR data is also in good agreement with the experimental observations.

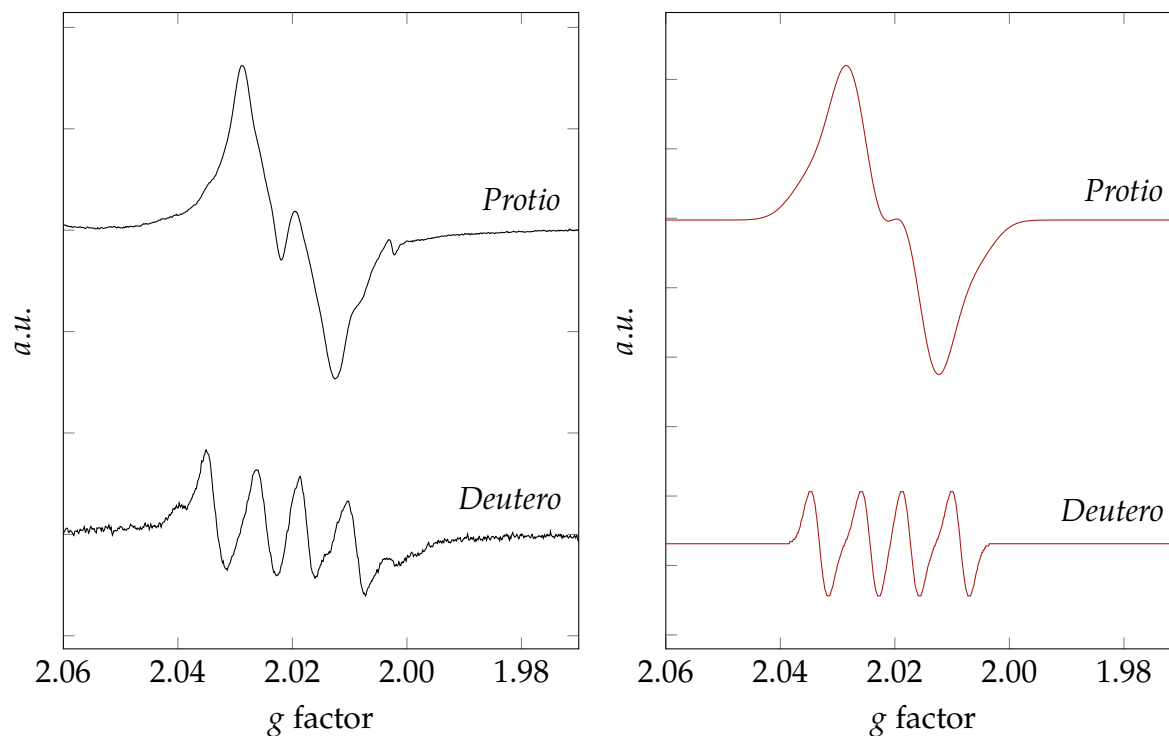


Figure 64: Left: experimental continuous wave X-band EPR spectra in THF: (top) reduced $[\text{S}_3\text{H}]^+$ at 165 K; (bottom) reduced $[\text{S}_3\text{D}]^+$ at 164 K. Right: simulated EPR spectrum for: (top) reduced $[\text{S}_3\text{H}]^+$; (bottom) reduced $[\text{S}_3\text{D}]^+$; experimental and simulated spectra were obtained and analysed by Dr. Shirley A. Fairhurst

4.2.3 FT-IR Spectroelectrochemistry (SEC)

Whilst electrochemistry provides excellent means of determining electron transfer kinetics, redox potentials and formal reaction mechanisms *via* kinetic analysis, this technique alone yields only a limited insight into the structure of the transient species. This has spawned a number of approaches designed to couple the electrochemical and spectroscopic measurements. Some of these exploit UV, IR or Raman scattering, whilst other less common techniques employ EPR, NMR, X-ray absorption spectroscopy (XAS) and luminescence in the UV or VIS regions.¹⁶⁹ Spectroelectrochemical (SEC) techniques permit *in situ* spectroscopic investigation of electrogenerated intermediates, providing crucial insights into the electronic, vibrational and magnetic structure of short-lived species.

SEC Cell Design and Assembly

Despite the many advantages, one of the main limitations with currently available IR-SEC cells is their response times. The majority of cells operate on the time frame of seconds or minutes, thus failing to detect transient intermediates. Due to the short-lived nature of the reduced [edtH]⁰, [pdtH]⁰ and [S₃H]⁰ species, none of the commercially available SEC cells were suitable in investigation of mixed-valence Fe(I)–Fe(II) complexes. As a result, a new FT-IR SEC cell was built, marrying the control offered by the electrochemistry with the fast response time accessible by the time-resolved ATR-IR (attenuated total reflectance infrared). The PEEK (polyether ether ketone) body was machined at the University of Cambridge, Department of Chemistry, with the design optimised following discussions with Richard Nightingale. The overall design and assembly of the electrode materials and ATR was undertaken in the Energy Materials Laboratory, University of East Anglia.

Figure 65 demonstrates the set-up of the SEC cell within the existing IR spectrometer. Since the model subsites bear strong IR chromophores (CO), time-resolved SEC has the potential to reveal significant detail about molecular changes accompanying electron transfer.

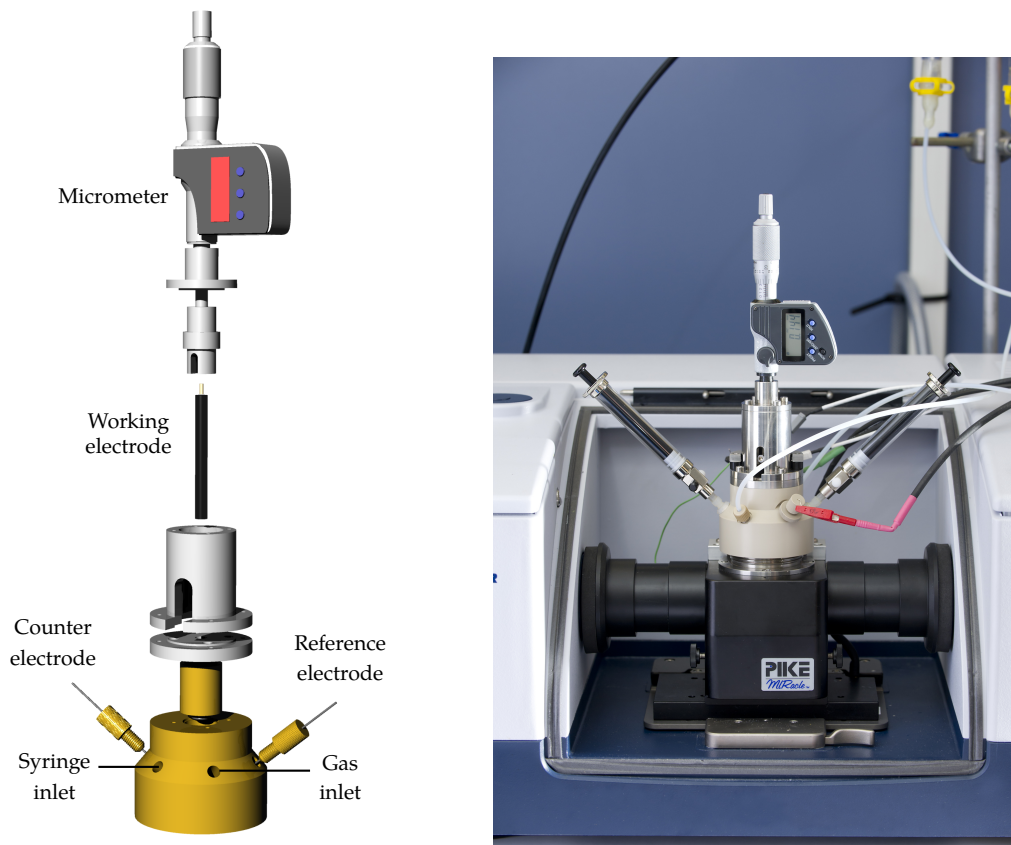


Figure 65: Left: schematic representation of FT-IR SEC cell; Right: ATR-SEC cell set-up

The cell is designed to fit a commercially available ATR plate, equipped with a silicon prism to give the best light throughput in the region of 1700 cm^{-1} and 2200 cm^{-1} . In order to gain the best time resolution and good signal-to-noise, the spectral range is restricted with an optical filter and the spectrometer is equipped with a mercury cadmium telluride (MCT) detector.

The cell comprises of a PEEK body coupled to a stainless steel mounting giving the system high chemical resistance and mechanical rigidity necessary to obtain reproducible data. It houses a silver wire *pseudo*-reference electrode placed in the bulk of the solution, thus making it less susceptible to potential shifts. It also accommodates a platinum counter electrode positioned close to the vitreous carbon working electrode, minimising the drop in voltage due to the resistance of the solution (*iR* drop). An important feature of this cell is the ability to control the solution thickness between the working electrode

and the ATR crystal using a micrometer (Figure 66). The thin layer (typically 10 μm) offers rapid generation of the electroactive species and a small diffusion distance to the evanescent wave region (0.85 μm) of the ATR-IR. This set-up paired with the fast detector allows spectral capture at a maximum frequency of 80 ms per spectrum. This is a 10 fold improvement from the best time resolution accomplished in FT-IR SEC experiments to date.¹⁷⁰ A major advantage of this design is not only the fast response time but also the low volume of analyte solution required to fill the sample chamber (<1 mL). The thin layer volume is small ($\approx 0.071 \mu\text{L}$) and can be rapidly changed, allowing many experiments to be carried out on a single 1 mL sample. Two gas ports keep the analyte under inert atmosphere while the two-syringe arrangement is available to allow flushing or mixing of solutions.

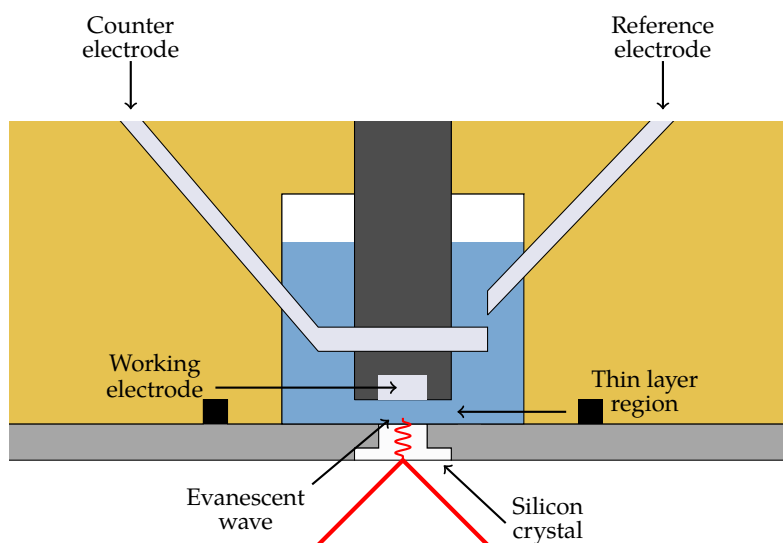


Figure 66: An expanded representation of the solution compartment within the SEC cell

SEC Results

SEC measurements of complex $[\text{pdtH}]^+$ were carried out under an atmosphere of dinitrogen in 0.1 M $[\text{Bu}_4\text{N}][\text{BF}_4]\text{-MeCN}$. The applied potential was stepped from *ca* 1100 mV positive of $E_{1/2}$, at which $[\text{H}][\text{pdt}]^+$ is inactive, to *ca* 300 mV negative of $E_{1/2}$, at which the complex is reduced in the thin layer at a diffusion-controlled rate. Upon reduction

the two peaks in the carbonyl region at 2031 cm^{-1} and 1989 cm^{-1} for the parent complex were rapidly replaced by two new bands at 1949 cm^{-1} and 1900 cm^{-1} (Figure 67, left). This primary product has a half-life of *ca* 1.2 seconds in MeCN, as measured by the loss of absorption at 1949 cm^{-1} . Reduction of $[\text{edtH}]^+$ under identical conditions yields the same peak shift and pattern, but the lifetime of the paramagnetic intermediate is much shorter having a half-life of *ca* 0.4 seconds in MeCN, as measured by the loss of absorption at 1951 cm^{-1} (Figure 67, right). SEC experiments also revealed that one-electron reduced products are more stable in THF than in MeCN, even though the higher resistivity of the former incurs longer cell response times.

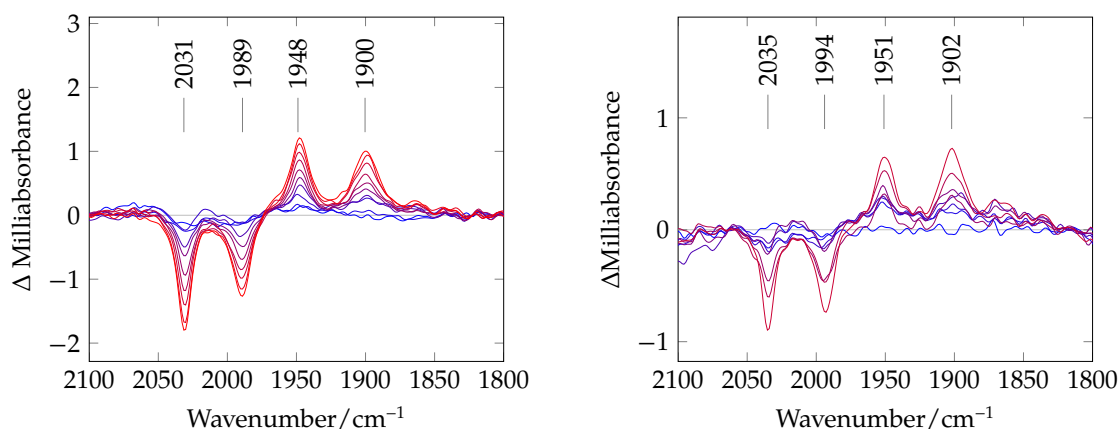


Figure 67: Left: difference spectrum for the reduction of $[\text{pdtH}]^+$ in the time range 0.25 s (blue) to 1.79 s (red) relative to a scan at 0.08 s. Right: difference spectrum for the reduction of $[\text{edtH}]^+$ in the time range 0.25 s (blue) to 1.62 s (red) relative to a scan at 0.08 s.

Figure 68 shows the absorbance-time course at 2031 cm^{-1} for consumption of $[\text{pdtH}]^+$ in the thin-layer spectroelectrochemical cell. In 2 s all of the parent material in the cell has been reduced to the primary one-electron reduction product. This is mirrored by the growth band at 1948 cm^{-1} which reaches a maximum at *ca* 2 s and subsequently falls off as it is converted to the super-reduced product (*vide infra*). The decay after 2 s does not fall to zero absorbance because there is a corresponding growth of the band for

product at 1944 cm^{-1} . The time-dependence of the loss of band at 2031 cm^{-1} reflects the time constant of the cell as the diffusion front advances towards the IR detection zone.

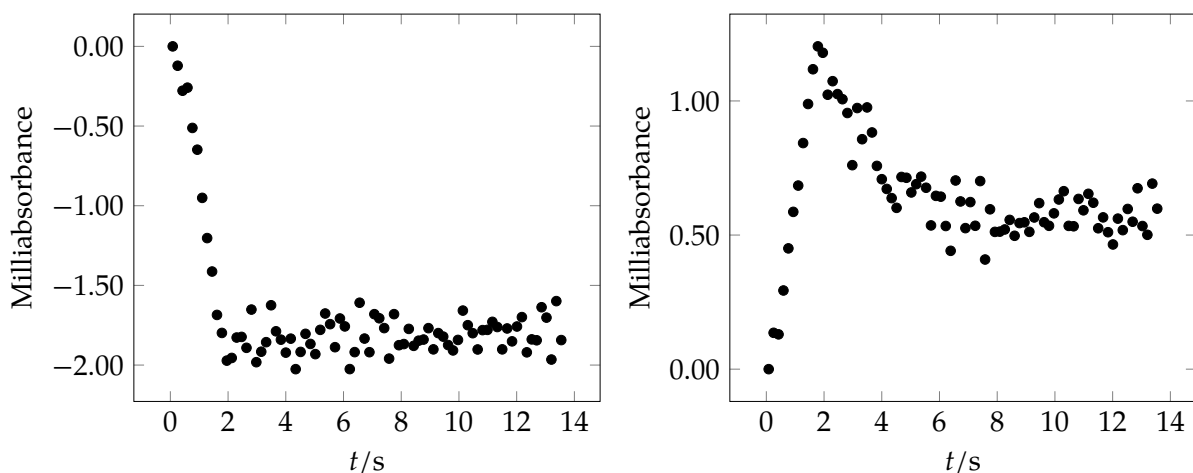
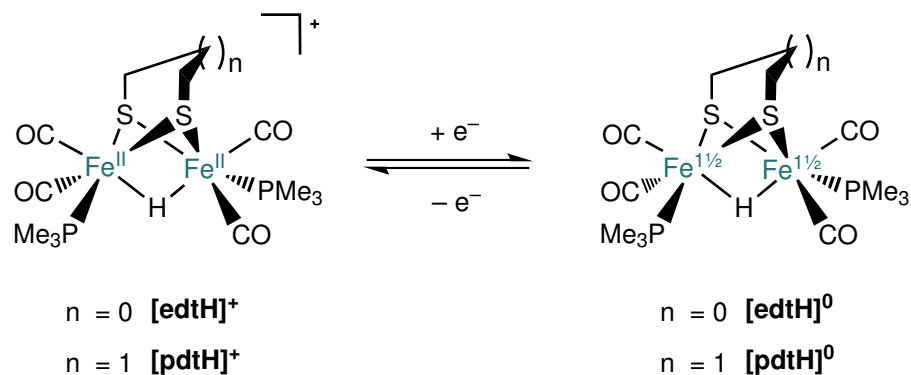


Figure 68: Left: decay of IR peak at 2031 cm^{-1} of $[\text{pdtH}]^+$; Right: growth of IR peak at 1948 cm^{-1} of $[\text{pdtH}]^0$

Retention of the peak pattern of the starting material following reduction suggests that the first-formed intermediate has the same geometry as the parent compound, *i.e.* that there is no gross structural change following a single-electron transfer. While the reduced intermediates are formally mixed-valence Fe(I)–Fe(II) species, the IR data suggests that they are better described as 35-electron valence-delocalized systems containing two iron atoms with an average oxidation state of 1.5 (Scheme 35). If the spin were localised, but rapidly oscillated between the two irons the CV experiment would not be able to distinguish this. The time scale of EPR experiment is in the order of nanoseconds and so any intervalence electron transfer must occur faster than this. In principle, the IR experiment examines processes on the vibrational (picosecond) timescale and is the fastest technique. However, for a molecule in solution at room temperature line broadening is likely to obscure small variations in stretching frequencies in a postulated localised Fe(I)Fe(II) structure.



Scheme 35: Formal oxidation states of iron atoms following reduction of **[edtH]⁺** and **[pdtH]⁺** complexes

SEC experiments performed on **[S₃H]⁺** shows very similar behaviour to that of **[edtH]⁺** and **[pdtH]⁺** systems. Reduction of the complex within the confines of the thin-layer SEC cell results in the shift of CO bands from 2061 cm⁻¹, 2038 cm⁻¹ and 2006 cm⁻¹ for the starting material to 1992 cm⁻¹, 1967 cm⁻¹ and 1915 cm⁻¹ for the one-electron reduced product **[S₃H]** (Figure 69).

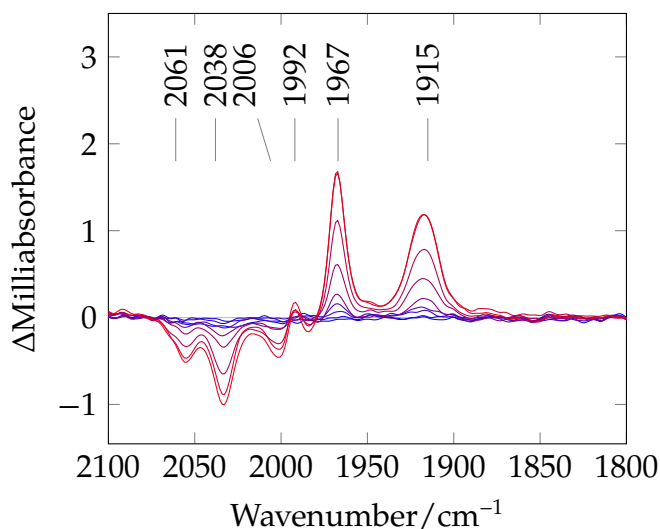
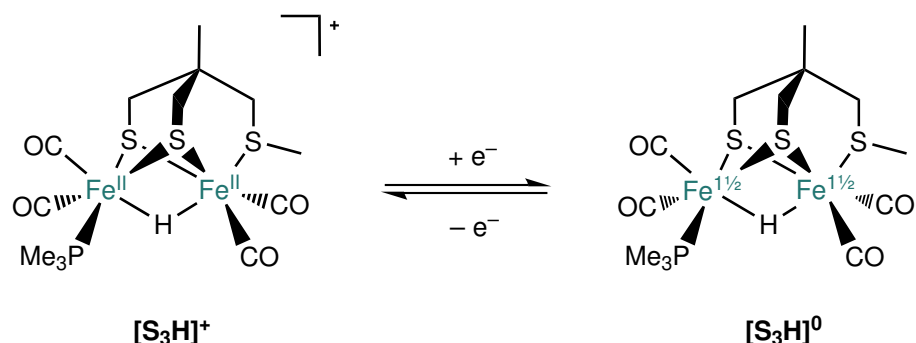


Figure 69: Difference spectrum for the reduction of **[S₃H]⁺** in THF in the time range 0.34 s (blue) to 5.8 s (red) relative to a scan at 0.08 s.

As observed before, retention of the peak pattern and intensities signifies no structural

change accompanying an electron transfer. The reduced species is stable for *ca* 3 seconds when the potential is switched to an open circuit following the generation of $[\text{S}_3\text{H}]^0$.



Scheme 36: Formal oxidation states of iron atoms following reduction of $[\text{S}_3\text{H}]^+$ complex

The reversibility of the systems following a one-electron reduction was also confirmed using SEC measurements. This was achieved employing a double potential step experiment. First, the reduction of $[\text{pdtH}]^+$ was carried out at -1.4 V to achieve full conversion to the reduced species. This was followed by a 0.9 s delay before the potential was changed to 0 V, regenerating around 90 % of the starting material (Figure 70). Reoxidation of the one-electron reduced species $[\text{edtH}]^0$ and $[\text{S}_3\text{H}]^0$ reveals identical behaviour with full conversion to the parent cation complexes $[\text{edtH}]^+$ and $[\text{S}_3\text{H}]^+$, respectively.

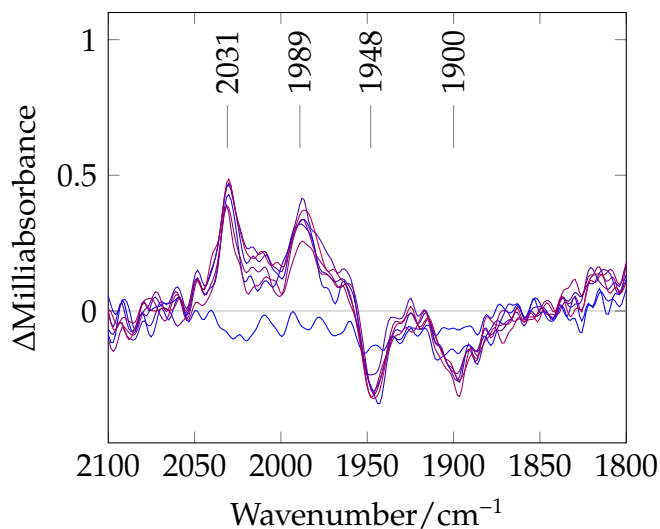


Figure 70: Difference spectrum for reoxidation of $[\text{pdthH}]^0$ (10 mM in MeCN) at 0 V from 0.9 s (blue) to 3.1 s (red), following reduction at -1.4 V (time zero)

When SEC measurements of $[\text{pdthH}]^+$ were carried out in the presence of a proton source ($\text{HBF}_4 \cdot \text{Et}_2\text{O}$), the turnover of the system resulted in a *ca* 9 s lag before the disappearance of the FT-IR bands of the parent complex $[\text{pdthH}]^+$. This is fully consistent with electrocatalysis involving the generation of 35-electron radical and fast protic attack to yield dihydrogen and restore the parent hydride cation $[\text{pdthH}]^+$. Only after exhaustion of the acid was depletion of the starting material in the thin-layer observed.

4.2.4 DFT Computational Simulations

Density functional theory (DFT) is a greatly successful computational approach able to provide a vast array of unique information on behaviour, structure and properties of individual atoms and molecules *in silico*. DFT simulations have rapidly grown from being a specialized technique practised by a handful of physicists to a tool used routinely by large numbers of researchers in chemistry, physics, materials science, chemical engineering, geology and other disciplines.¹⁷¹ It is an extremely complex and demanding approach employing cutting-edge wavefunction-based quantum mechanics and solutions to Schrödinger equation. DFT methods have been used to make important contributions

to scientific questions by providing vital information ranging from electronic nature of the excited states to giving ground to spectroscopic observations of transient species.

DFT simulations for complexes [**edtH**]⁺ and [**pdtH**]⁺, and their reduced forms were performed by J. N. T. Peck. Calculations on the [**S₃H**]⁺ system were undertaken by the author following the protocols established for {2Fe2S} species. These theoretical calculations were essential in lending support to some of the experimental observations.

{2Fe2S} Systems

All of the potential isomers calculated for the parent [**edtH**]⁺ and the paramagnetic species generated following a one-electron transfer are depicted in Figure 71.

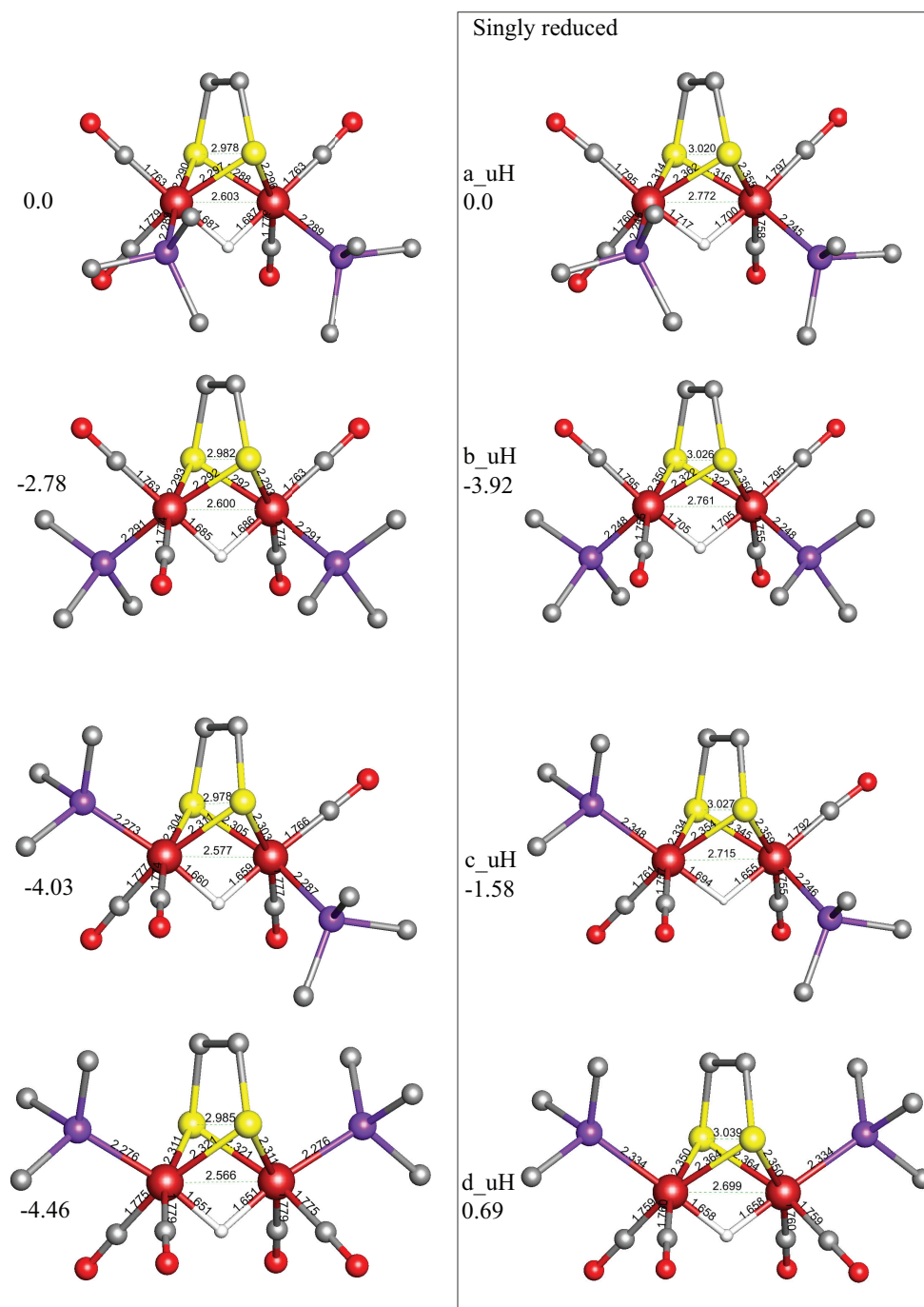


Figure 71: Geometry optimised structures of isomers of $[\text{edtH}]^+$ (left) and their reduced forms (right): bond lengths given in Å, energies are reported in kcal mol^{-1} relative to isomer a. Hydrogen atoms except hydride are omitted for clarity

From this, the lowest energy isomer for the reduced species is calculated to be isomer b,

where both of the trimethylphosphine ligands rest in the basal-basal geometry *transoid* to one another. Notably, it is also the only simulated species that produces the same infrared shift and pattern upon one-electron reduction as observed experimentally (Figure 72). The lowest energy isomer for the neutral parent complex is calculated to be isomer **d** with both of the trimethylphosphine ligands resting in the apical-apical positions. However, there is only a very small difference in relative energies between the two isomeric forms **d** and **b** ($< 2 \text{ kcal mol}^{-1}$). In addition, the DFT calculations are carried out in the gas phase and does not account for solvation, so some discrepancy from the experimental data is to be expected.

As calculated by DFT, the reduced form of [**pdtH**]⁺ shows identical behaviour with the most stable isomer possessing the same *transoid* dibasal ligand arrangement around the metal centres.

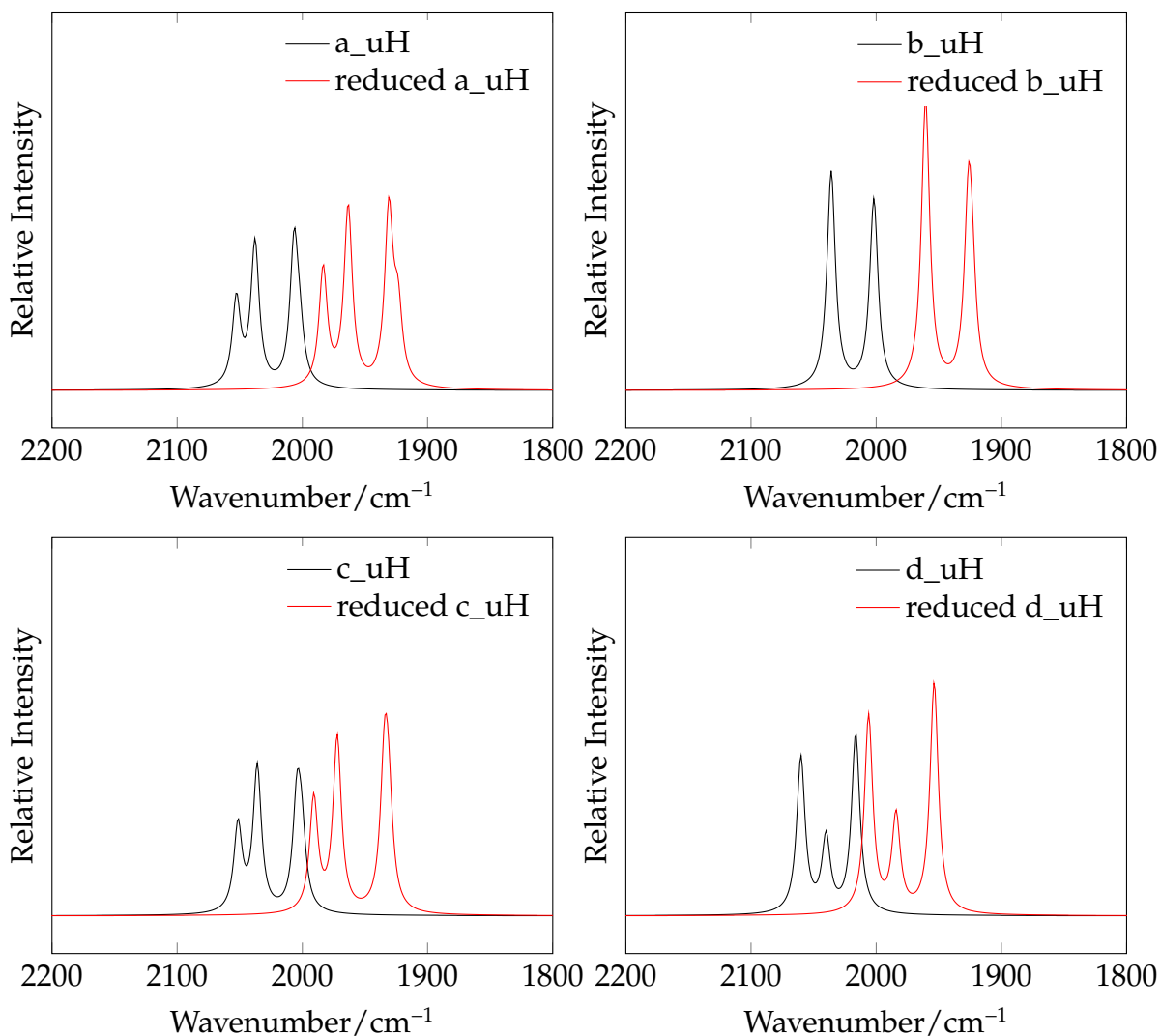


Figure 72: Comparison of the simulated IR spectra of $[\text{edtH}]^+$ isomers and their reduced forms; the calculated vibrational frequencies are *unscaled*

The DFT simulations support the experimental observation that reduction leads to a shift in the positions of the peak maxima but not to a development of any additional signals. This signifies that the structure of the parent complex remains unchanged upon generation of paramagnetic radical species. Figure 73 shows excellent agreement between the experimental CO band frequencies observed for protonated and reduced forms of {2Fe2S} complexes and the values obtained for the most stable isomers with *transoid* dibasal ligand arrangements calculated *in silico*.

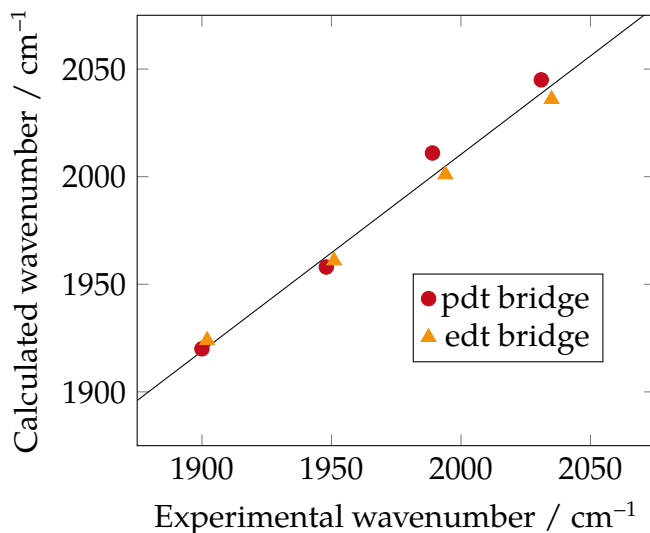


Figure 73: Relationship between experimental and calculated IR values. Theoretical values are for isomer **b** in all cases.

Computational simulations are also able to lend support to EPR measurements by calculating where the spin density of the unpaired-electron resides within the molecule. It indicates that the two iron atoms of the singly reduced [**pdtH**]⁰ form share approximately 70 % of spin density, 3 % is located on the bridging hydride, while the two phosphorus atoms carry a total of 0.5 % (Figure 74). These results are in accord with the experimental spin density dispositions estimated from EPR experiments: 5 % for the bridging hydride and 0.8 % for the two phosphorus atoms.

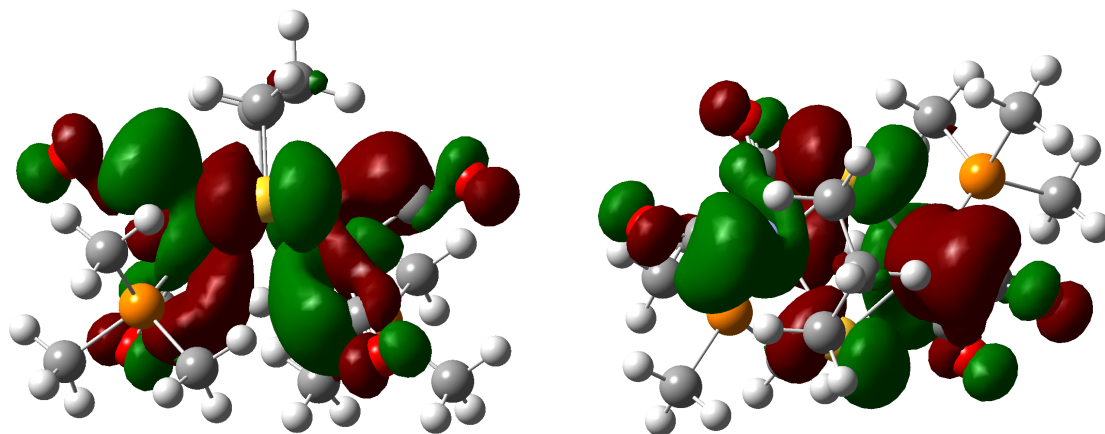


Figure 74: Isosurface of the spin density distribution of the singly reduced $[\text{pdtH}]^0$ species; views approximately perpendicular to (left) and parallel with (right) the plane containing the Fe-H-Fe unit; the spin density phases are indicated in green and red

{2Fe3S} Systems

All the potential isomers for both the parent cation $[\text{S}_3\text{H}]^+$ and its one electron reduced form $[\text{S}_3\text{H}]^0$ are depicted in Figure 75. The energies have been reported with respect to the most stable isomer **a** of the unreduced form of the complex.

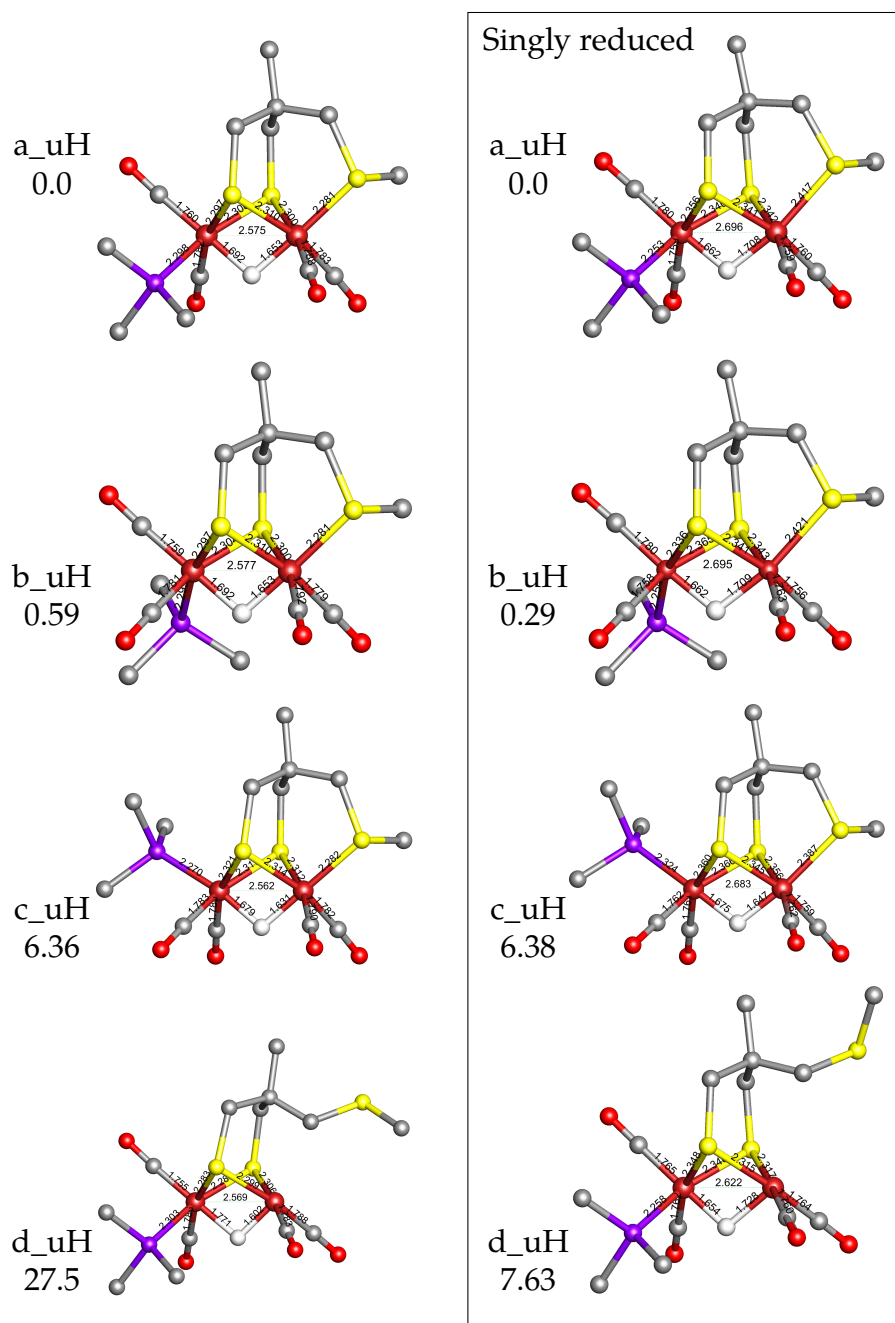


Figure 75: Geometry optimised structures of isomers of $[\text{S}_3\text{H}]^+$ (left) and their reduced forms (right): bond lengths given in Å, energies are reported in kcal mol^{-1} relative to isomer a. Hydrogen atoms except hydride are omitted for clarity

As calculated *in silico*, the lowest energy isomer is **a** in which the PMe_3 ligand rests in the basal position *transoid* to the methyl of the thioether group. Dissociation of the

thioether group is very high in energy, suggesting that this is an unlikely step in a one-electron reduction process. This is supported by the simulated IR spectra obtained for both the parent complexes and their reduced forms. Figure 76 evidently demonstrates that only the isomer **a** matches the experimentally observed pattern to a high degree.

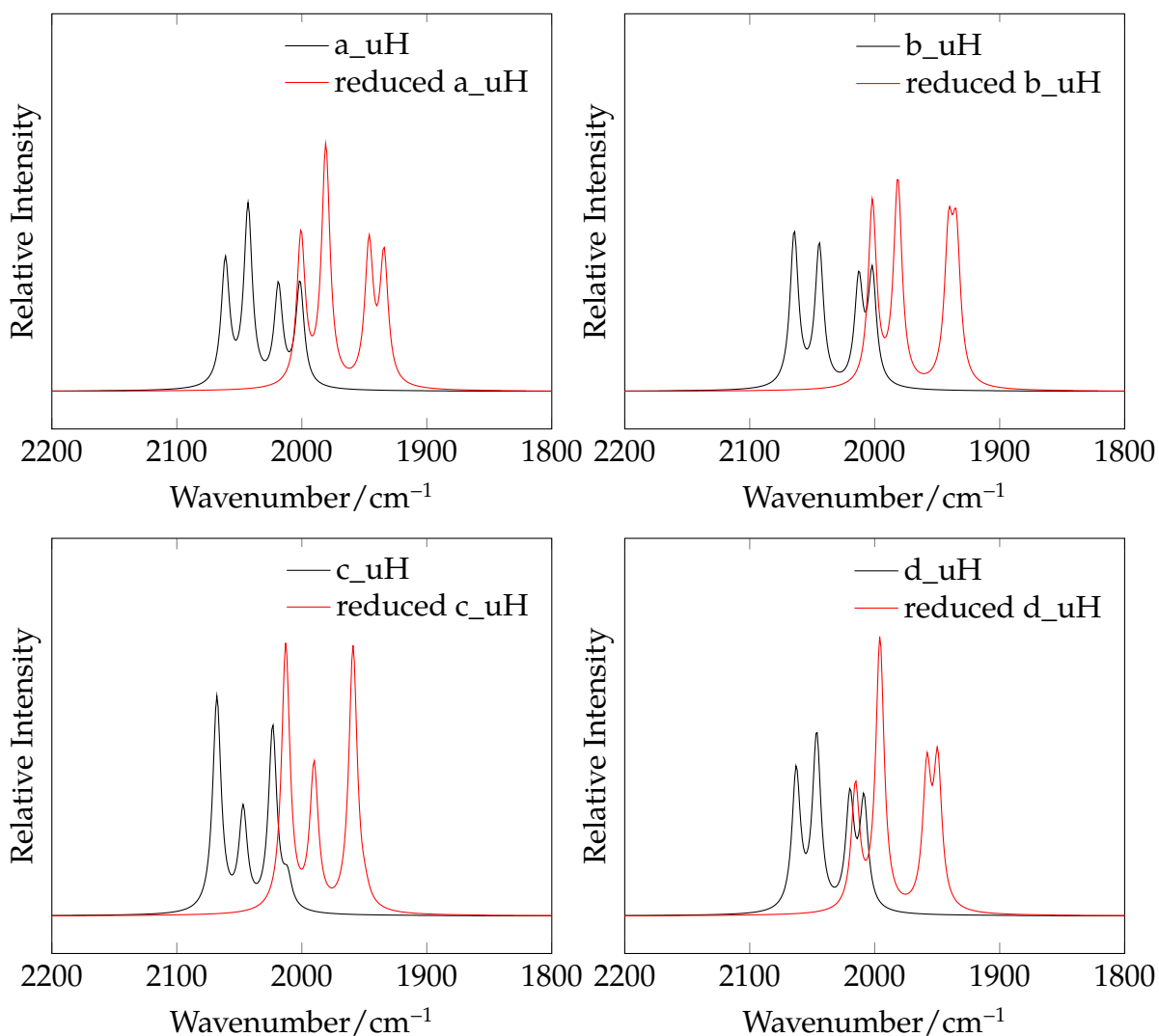


Figure 76: Comparison of the simulated IR spectra of $[\text{S}_3\text{H}]^+$ isomers and their reduced forms; the calculated vibrational frequencies are *unscaled*

Thus, the DFT simulations support formulation of $[\text{S}_3\text{H}]^0$ as the mixed-valence 35-electron species in which no ligand rearrangement has occurred.

4.3 Evidence for Super-Reduced Hydride States

4.3.1 SEC Measurements

SEC, CV and EPR spectroscopies have confirmed the accessibility of paramagnetic mixed-valence Fe(I)–Fe(II) bridging hydride species. It is now shown that these transient intermediates undergo further chemistry leading to the generation of unprecedented *super-reduced* states. As is evident from the cyclic voltammograms for the [pdtH]⁺ and [edtH]⁺ species in Figure 61, at slow scan rates the normalised current function $i^{\text{red}} / \sqrt{v}$ is greater than that at fast scans. This is indicative of further electron transfer arising from the ECE mechanism (Scheme 34). For the [S₃H]⁺ system this process is less evident because [S₃H]⁰ is more stable. However, partial reversibility is still observed at the slower scan rates.

The *super-reduced* species are also revealed in SEC experiments at longer runs when the one-electron reduced intermediate decays to a second product possessing CO bands at much lower IR frequencies. This is clearly evident from Figure 77 (left), in which two maxima in the carbonyl region of the [pdtH]⁰ complex is replaced by four distinct new bands: 1944 cm⁻¹, 1900 cm⁻¹, 1863 cm⁻¹ and 1841 cm⁻¹ (Figure 77, left). Surprisingly, longer runs of reduction of [S₃H]⁺ produces a product possessing an *identical* set of peaks (Figure 77, right).

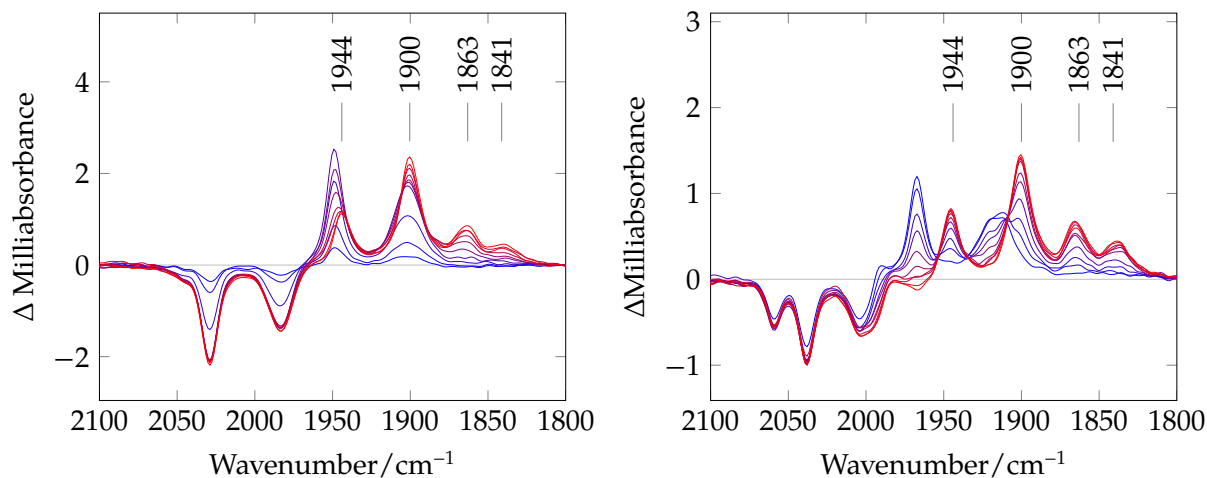


Figure 77: Left: difference spectrum for the reduction of $[\text{pdtH}]^+$ in THF in the time range 6.47 s (blue) to 24.87 s (red) relative to a scan at 0.08 s; Right: difference spectrum for the reduction of $[\text{S}_3\text{H}]^+$ in MeCN in the time range 0.34 s (blue) to 6.49 s (red) relative to a scan at 0.08 s

Plotting intensity of the peak at 1967 cm^{-1} for the one-electron reduced intermediate *versus* a peak at 1863 cm^{-1} of the final product exhibits a linear relationship (Figure 78). This is strongly suggestive that the conversion of one to the other is synchronous and the final set of four peaks correlates to one product.

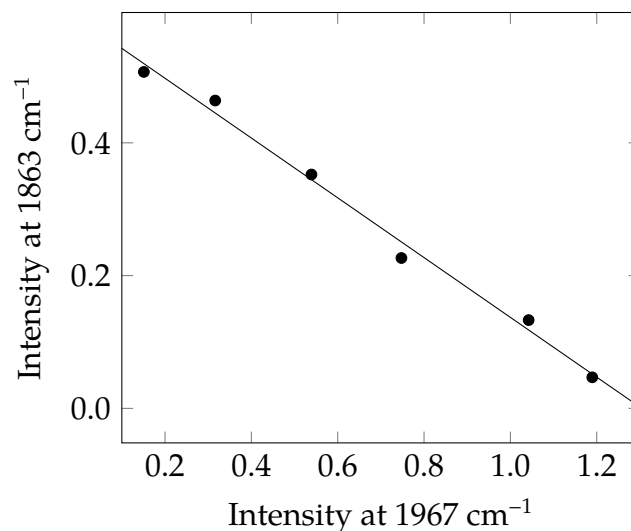
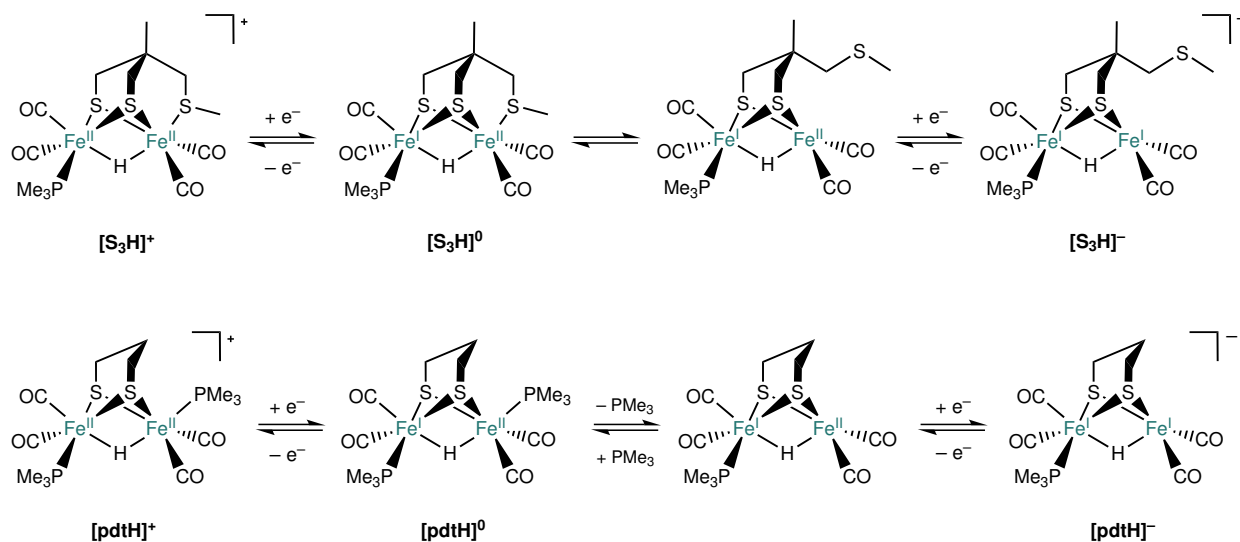


Figure 78: Relationship between the decay of intensity of $[\text{S}_3\text{H}]^0$ signal at 1967 cm^{-1} vs growth of intensity of the final product $[\text{S}_3\text{H}]^-$ signal at 1863 cm^{-1}

The shift of bands to lower frequencies is consistent with a further one-electron reduction of paramagnetic intermediates $[\text{pdtH}]^0$ and $[\text{S}_3\text{H}]^0$ to *super-reduced* $\text{Fe(I)}(\mu\text{-H})\text{Fe(I)}$ states. The appearance of equivalent carbonyl bands also indicates that both species share *identical* core frameworks. This is fully consistent with a dissociation of a thioether group in the {2Fe3S} complex and a loss of trimethylphosphine group in the {2Fe2S} case (Scheme 37).



Scheme 37: Proposed formation of *super-reduced* complexes $[S_3H]^-$ and $[pdtH]^-$

In support of this, following reoxidation of the *super-reduced* species, the $[pdtH]^+$ parent cation is regenerated in *ca* 60 % yield and recovery of $[S_3H]^+$ complex approaches *ca* 85 % (Figure 79).

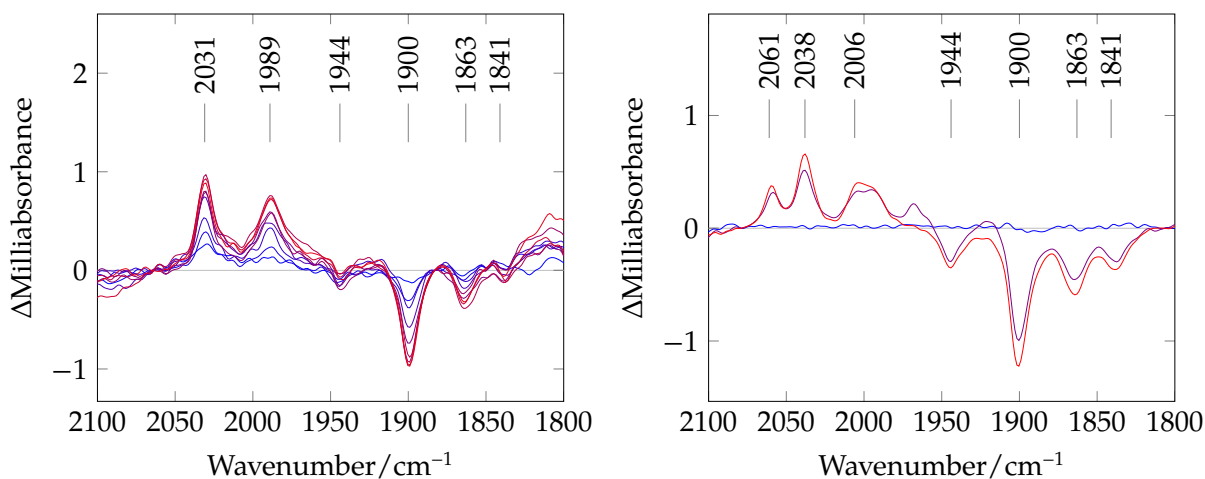


Figure 79: Left: difference spectrum for the reoxidation of *super-reduced* $[pdtH]^-$ in MeCN at -0.6 V following reduction at -1.4 V in the time range of 12.9 s (blue) to 15.6 s (red); Right: difference spectrum for the reoxidation of *super-reduced* $[S_3H]^-$ in MeCN at 0 V following reduction at -1.2 V in the time range of 11.3 s (blue) to 12.6 s (red)

The anchoring of the SMe group by the rest of the ligand accounts for the high chemical reversibility observed in the $[\text{S}_3\text{H}]^-$ complex, whereas loss of PMe_3 from the diffusion layer limits the recovery of $[\text{pdthH}]^+$. It also explains the reason why reoxidation of $[\text{S}_3\text{H}]^-$ appears to be instantaneous whilst the same process for $[\text{pdthH}]^-$ is much slower.

4.3.2 Stopped-Flow IR Spectroscopy and DFT Simulations

Another method of generating the *super-reduced* species is to employ chemical reduction under the stopped-flow conditions. Reaction of $[\text{S}_3\text{H}]^+$ or $[\text{pdthH}]^+$ with a strong reducing agent Cp^*_2Co (Cp^* = pentamethylcyclopentadienyl) in MeCN ($E_{1/2} = -1.91 \text{ V vs Fc}^+/\text{Fc}$)¹⁶⁸ yields $[\text{S}_3\text{H}]^-$ or $[\text{pdthH}]^-$ respectively in a flow cell, as observed from Figure 80.

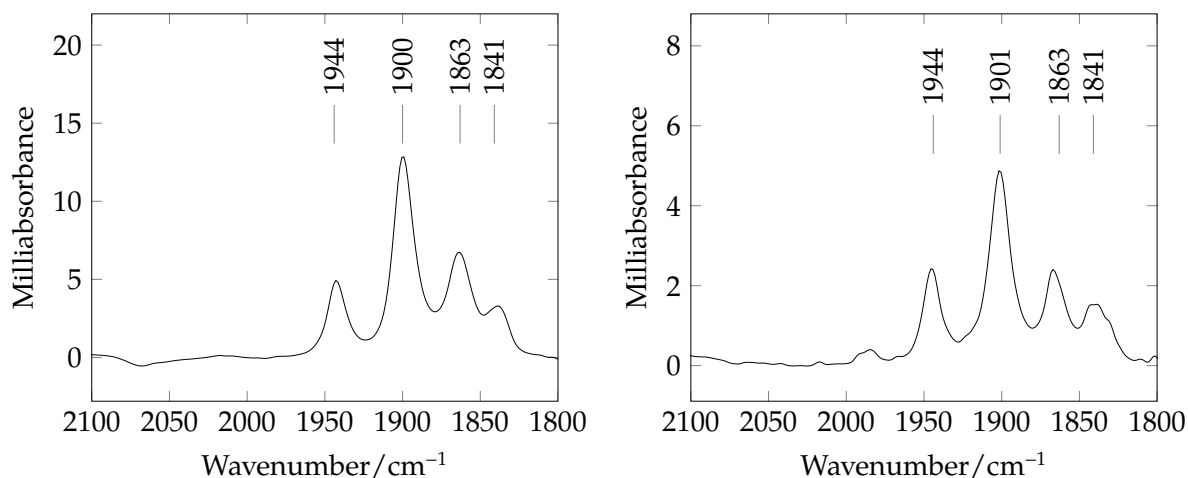


Figure 80: Left: IR spectrum of $[\text{pdthH}]^-$ obtained from reduction with Cp^*_2Co in a stopped-flow IR cell; Right: IR spectrum of $[\text{S}_3\text{H}]^-$ obtained from reduction with Cp^*_2Co in a stopped-flow IR cell

Efficient capillary mixing of the two solutions in a stopped-flow IR set-up allows for instantaneous conversion of the cationic parent material to the *super-reduced* state. This parallels SEC experiments where the electrochemical conversion of the analyte in the thin layer is fast, avoiding the complication of the reaction of reduced species with a parent material.

The DFT simulations of the infrared data for established structure of $[\text{S}_3\text{H}]^+$, its primary one-electron reduced product $[\text{S}_3\text{H}]^0$ and the proposed structure of $[\text{S}_3\text{H}]^-$ show good correlation between the experimental and the simulated data across all three redox states of the complex ($R^2 = 0.983$) (Figure 81).

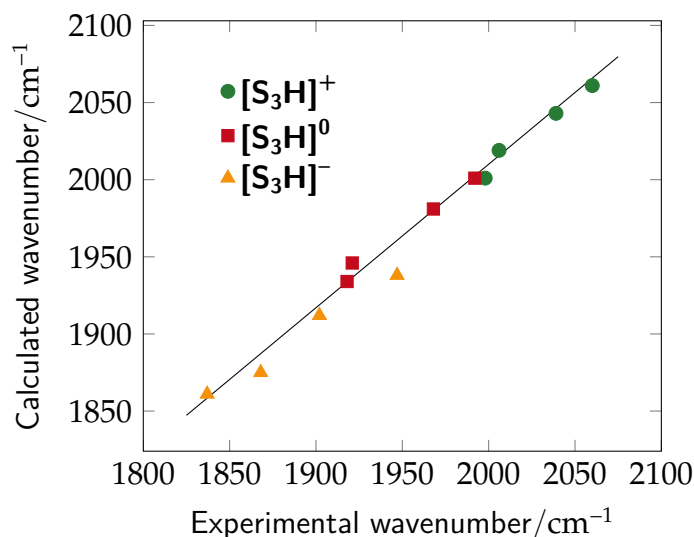


Figure 81: Comparison of observed and calculated infrared frequencies for $[\text{S}_3\text{H}]^+$, $[\text{S}_3\text{H}]^0$ and $[\text{S}_3\text{H}]^-$; the solid line shows the least-squares fit for all data points

The peak patterns and shifts calculated *in silico* are also in close agreement with those obtained experimentally (Figure 82).

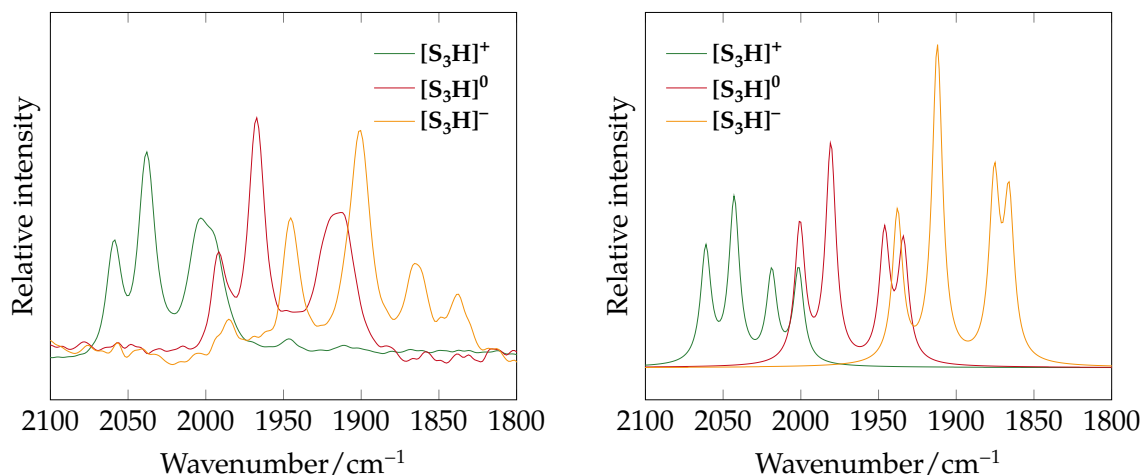


Figure 82: Left: infrared spectra from SEC experiments for reduction of $[\text{S}_3\text{H}]^+$; Right: simulated infrared spectra for reduction of $[\text{S}_3\text{H}]^+$; the calculated vibrational frequencies are *unscaled*

4.3.3 Attempted (Electro)Chemical Synthesis of the *Super-Reduced* State

An attempt to generate the *super-reduced* complexes in bulk has been carried out employing electrolysis of $[\text{S}_3\text{H}]^+$ and $[\text{pdtH}]^+$ complexes using a large vitreous carbon working electrode. Figure 83 shows current measured *versus* time.

The number of electrons (n) involved in the process can be obtained from Equation 27 in which the charge passed (Q) is calculated from the integral of the area beneath the curve (N is moles of complex used and F is the Faraday constant).

$$Q = nNF \quad (27)$$

It was found that reduction of $[\text{S}_3\text{H}]^+$ and $[\text{pdtH}]^+$ in bulk consumes 1 electron per molecule of complex and generates only the unprotonated parent complexes S_3 and pdt respectively. This is attributed to the reaction between the parent cation in the bulk solution and the reactive one-electron reduced product generated at the electrode (Scheme 38). Even though the hydrogen release was not measured, electrolysis is expected to produce H_2 in the process based on the behaviour of related diiron subsite models.¹⁷²

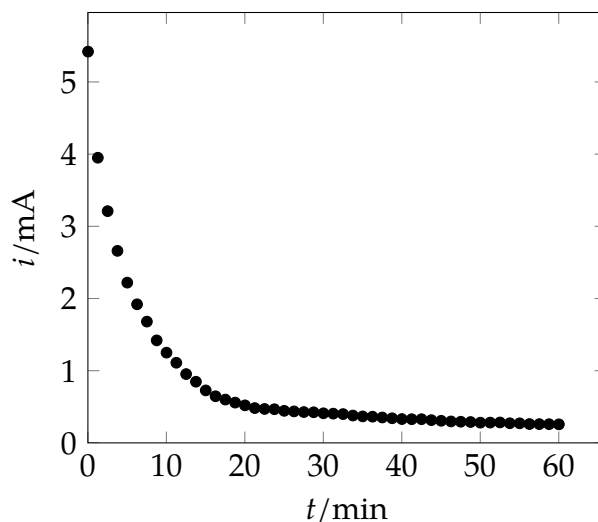
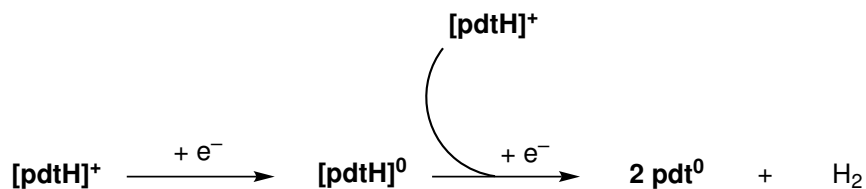


Figure 83: Controlled-potential electrolysis of $[\text{pdtH}]^+$ (7.2 mM) in $[\text{Bu}_4\text{N}][\text{BF}_4]\text{-MeCN}$ using a vitreous carbon working electrode; potential held at $-1.16\text{ V vs Ag/AgCl}$ reference electrode

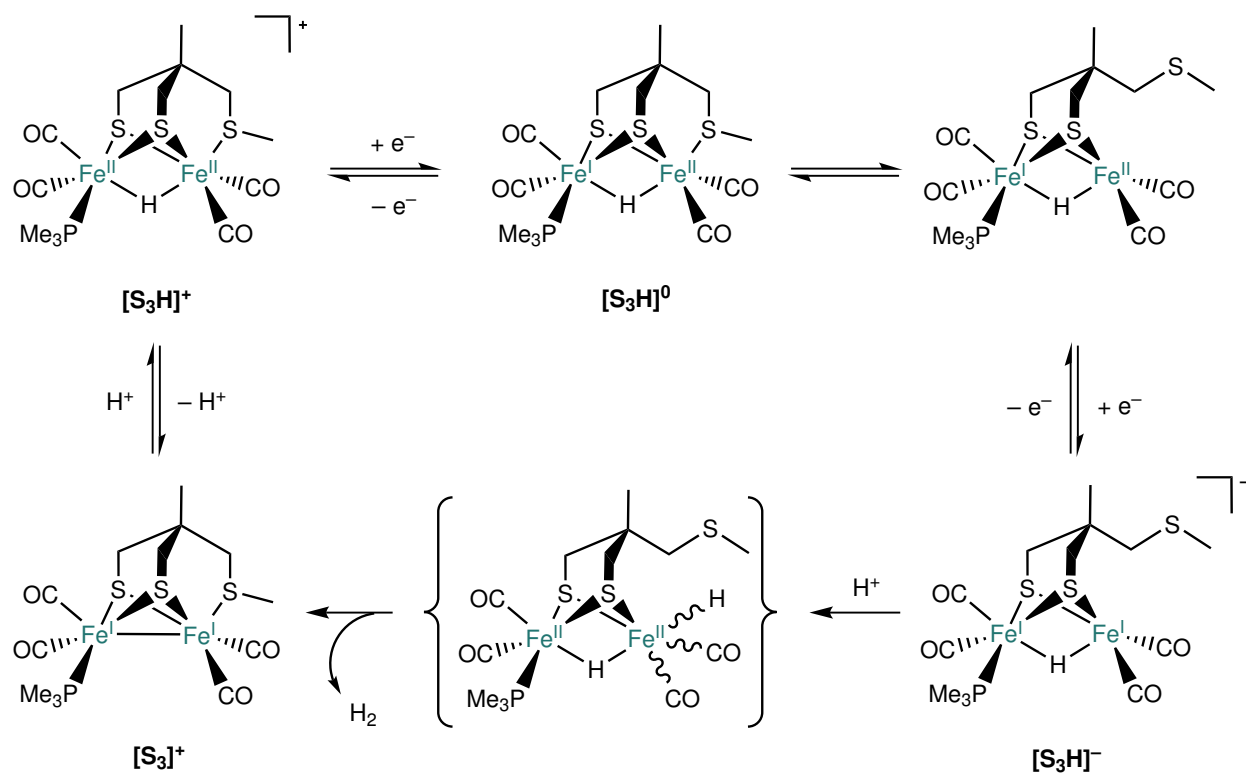


Scheme 38: Proposed parent-child reaction observed during the bulk electrolysis

Attempted electrolysis over the stirred mercury pool as the working electrode was anticipated to proceed faster, thus avoiding the parent-child reaction. However, once again only the unprotonated material was obtained. Rapid manual mixing of the chemical reductant and the diiron complex yielded the same results. Slow introduction of the metal complex to the solution containing excess of Cp^*_2Co *via* a syringe pump could not produce the *super-reduced* states either.

Attempts were made to collect the *super-reduced* complexes from a sequence of shots using the stopped-flow IR technique. However the acquired solutions were difficult to handle due to their low oxygen and moisture tolerance and the complexes decomposed after a few minutes. The reactivity of the paramagnetic intermediate and the following slow ligand rearrangement also precludes examination of any electrocatalytic hydrogen

production by the *super-reduced* complexes. However, the mechanism by which the catalytic H₂ production is anticipated to occur is depicted in Scheme 39.



Scheme 39: Proposed formation and behaviour of the *super-reduced* state for [S₃H]⁻ complex

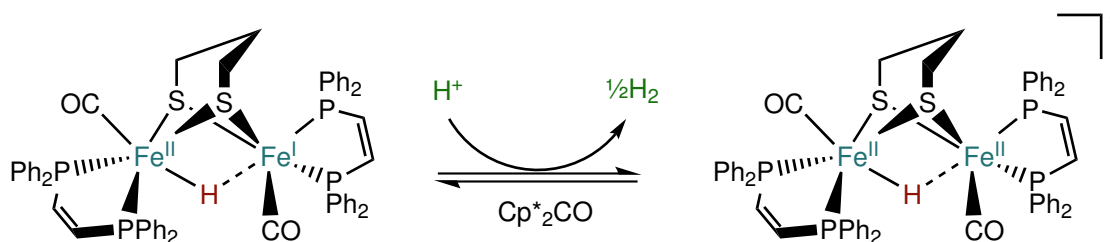
These attempted experiments not only highlight the difficulty in accessing the *super-reduced* states, but also highlights the importance of rapid techniques such as spectroelectrochemistry and stopped-flow. Only the presence of the thin layer in the former and efficient mixing in the latter allows observation of these unprecedented species.

4.3.4 Related Studies

Generation of several paramagnetic bridging hydride species has been first reported in 1991 by Krusic and co-workers.¹⁷³ This was achieved by the low-temperature UV photolysis of Fe(CO)₅ in the presence of H₂S, producing many species including Fe₂(CO)₆(μ-SH)₂-

(μ -H). These transient complexes have only been observed by EPR spectroscopy and have not been characterised by other spectroscopic means or isolated. Since then, the first *fully* spectroscopically characterised paramagnetic diiron dithiolates bearing μ -hydrides have been reported by the author and co-workers. This work has served as a reference point for a number of other studies concerned with paramagnetic hydrides at (bi)metallic centres.^{174–176}

Following on from this work Rauchfuss has reported the crystallographic characterisation of related paramagnetic bridging hydride system bearing bidentate phosphine ligands.¹¹¹ Interestingly, contrary to his previous assertions, the μ -hydride ligand in this complex was found to behave as a spectator ligand upon attack by protons (Scheme 40).



Scheme 40: Spectroscopically and crystallographically characterised mixed-valence diiron μ -hydride system reported by Rauchfuss¹¹¹

Soon after, Rauchfuss and co-workers have published another unique system containing *both* the bridging and the terminal hydride.⁹⁹ The complex has a substantial hydridic character and even weak acids induce H₂ evolution. This contrasts starkly with previous examples of diiron hydrides which are unaffected by mild acids or oxidants. This is attributed to the neutral charge of the complex and the donor strength of the bridging hydride. The system is also conceptually related to the *super-reduced* species discussed in this chapter, because it represents a second protonation of the *super-reduced* state. This lends some support to the mechanism outlined in Scheme 39.

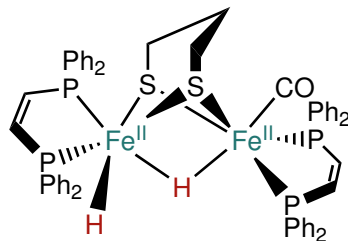


Figure 84: Spectroscopically and crystallographically characterised mixed-valence diiron system containing *both* a terminal and a bridging hydride as reported by Rauchfuss⁹⁹

These synthetic efforts highlight the importance of hydride derivatives at Fe(I)–Fe(II) centres in probing the catalytic cycle of hydrogen production more deeply. More importantly, this begins to give some control over design of these catalytically active systems providing tools for their improvement and spectroscopic handles for their examination. This has the potential to aid the reproduction of the active \mathbf{H}_{red} and \mathbf{H}_{ox} states of the enzyme and construction of more efficient catalysts for H_2 production.

4.4 Summary

In summary, paramagnetic metallo-hydrides are likely to be key intermediates in enzymic and molecular catalysis involving metallosulfur assemblies. The use of advanced FT-IR spectroelectrochemical cell, DFT calculations and EPR spectroscopy enabled characterization of the first set of discrete mixed-valence bridging hydride systems at both {2Fe2S} and {2Fe3S} cores. These have been shown to be valence-delocalized systems, possessing a substantial radical character on the μ -hydrides. SEC measurements have also provided evidence that further electron transfer and dissociation of coordinating ligands lead to formation of an unprecedented *super-reduced* Fe(I)(μ -H)Fe(I) states. In the enzyme, the super-reduced \mathbf{H}_{sred} state may be implicated in the catalytic hydrogen production, and while $[\mathbf{S}_3\mathbf{H}]^-$ is not a close model for \mathbf{H}_{sred} , it is notable that the accessibility of discrete Fe(I)–Fe(I) hydrides has been confirmed.

Beyond the relevance of paramagnetic hydrides to synthetic and natural diiron catalysis, there is a wider aspect of their role in other hydrogen-evolving or carbon dioxide-fixating bioinorganic systems. These include [Ni-Fe]-hydrogenases, carbon monoxide dehydrogenases and nitrogenases. The latter concomitantly evolves dihydrogen with nitrogen fixation. Fe-(μ -H)-Fe intermediates have been proposed in the four-electron reduced state of the FeMo-co centre of nitrogenase on the basis of EPR and electron-nuclear double resonance (ENDOR) measurements.¹⁷⁷ Remarkable progress towards identifying these transient species is steadily unveiling catalytic mechanisms occurring in biological systems.

4.5 Experimental

Unless otherwise stated, reactions were carried out under nitrogen using conventional air-sensitive techniques. Solvents were degassed using a nitrogen purge and dried using an M. Braun solvent purifier unit before use. Starting materials were purchased from Aldrich or Alfa Aesar and were used without further purification. Compounds [**pdthH**]⁺ and [**edthH**]⁺ were prepared according to literature methods.^{121,129}

Electrochemical measurements

Cyclic voltammetry measurements were carried out in 0.1 M [Bu₄N][BF₄]-MeCN or 0.2 M [Bu₄N][BF₄]-THF using a three compartment cell fitted with a glassy carbon working electrode (diameter 3 mm), a platinum counter electrode and a silver wire *pseudo*-reference electrode interfaced with an Autolab PGSTAT30 potentiostat. Potentials were calibrated using ferrocenium/ferrocene as an internal standard.

Spectroelectrochemical measurements

Infra-red spectroelectrochemical measurements were carried out in a custom-made Spectroelectrochemistry Partners SP-02 cell mounted on a Pike MIRacle ATR fitted with single-bounce silicon top plate. The ATR was fitted with a Northumbria Optical

Coatings filter (pass band 4.76 μm to 5.60 μm). Spectra were recorded on a Bruker Vertex 80 spectrometer equipped with a mercury cadmium telluride (MCT) detector. Data were collected at 4 cm^{-1} resolution. Typically, 80 time points were recorded for each experiment. The SP-02 cell was fitted with a glassy carbon working electrode (diameter 3 mm), a platinum counter electrode and a silver wire *pseudo*-reference electrode. These were attached to a Princeton Applied Research VersaSTAT 3 potentiostat. Data collection was controlled by the Bruker Opus package, interfaced to the potentiostat using a custom Opus3D script and TTL connection. IR data was processed and analysed using the Fit_3D application¹⁵⁵ and curve fitting was carried out using SciDAVis.

In a typical run, the cell was purged with nitrogen for some minutes before introduction of the solution for analysis. With the working electrode moved some distance from the ATR crystal (several 100 μm), CV data were acquired to estimate the $E_{1/2}$ value. A series of SEC runs were then carried out, moving the working electrode to within 10 μm of the ATR crystal. After each SEC run, the solution in the cell was allowed to equilibrate with unreacted material.

EPR measurements

For [pdtH]⁰: A solution of acenaphthalene (16 mg, 0.10 mmol) and [NBu₄][BF₄] (328 mg, 1.0 mmol) was prepared in dry THF (10 ml). A small amount of finely-divided sodium was added, and the solution was sonicated for approximately one hour, after which time the solution was brown. A second solution of [pdtH]⁰ (90 mg, 0.14 mmol) and [NBu₄][BF₄] (328 mg, 1.0 mmol) was prepared in dry THF (10 ml). Both solutions were then cooled to 195 K. A small portion of the reductant (roughly 0.25 ml) was taken up into a syringe, followed by an equal volume of the substrate solution. These were added to a silica EPR tube and rapidly frozen in liquid nitrogen.

For [S₃H]⁰: A solution of acenaphthalene (6 mg, 0.04 mmol) was prepared in dry THF (10 ml). A small amount of finely-divided sodium was added, and the solution was sonicated for approximately one hour, after which time the solution was brown. A second solution of [S₃H]⁰ (7.2 mg, 0.012 mmol) was prepared in dry THF (2 ml). Both

solutions were then cooled to 195 K. A small portion of the reductant (roughly 0.1 ml) was taken up into a syringe, followed by an equal volume of the substrate solution. These were added to a silica EPR tube and rapidly frozen in liquid nitrogen.

Continuous wave EPR spectra were recorded at X-band (9.43 GHz) using a ELEXSYS 500 spectrometer. The samples were warmed to just above the melting point. Temperature control was achieved using a Bruker ER4131VT N₂ Temperature Controller. EPR spectra were simulated using the computer programme WINEPR SinFonia (Bruker Analytische Messtechnik GmbH).

DFT calculations

All calculations were performed using the Gaussian 09¹⁵⁶ computational package. Geometry optimisation and frequency calculations have been carried out using the Tao–Perdew–Staroverov–Scuseria¹⁵⁷ (TPSS) density functional. Phosphorus, sulfur and iron atoms are described by the the Hay and Wadt LANL2DZ^{158,159} basis set with effective core potential (ECP). In the case of iron, the two outermost p functions were replaced with reoptimised 4p functions.¹⁶⁰ For sulfur and phosphorus, additional p and d polarisation functions were added.¹⁶¹ All other atoms employ the all electron 6-31+G** basis set. Structures were geometry optimised in the gas phase with the default convergence criteria and confirmed as minima through frequency calculations.

Chapter 5

Exploratory Studies and Future Directions

5.1 Probing the [Fe–Fe]-Hydrogenase Subsite Using Muon Spectroscopy

Discrete mixed-valence hydrides have now been successfully identified and characterised at both {2Fe2S} and {2Fe3S} cores of the [Fe–Fe]-hydrogenase subsite models. Such paramagnetic hydride species are considered as key intermediates in hydrogen production by the hydrogenases, the nitrogenases and carbon dioxide-fixating bioinorganic systems. It is no surprise that exploration of these transient species is receiving great attention in hopes to unravel the catalytic mechanisms occurring in biological systems. One promising technique which can aid in this endeavour is muon spectroscopy, which thus far has not been applied to bioinorganic systems. Here it is shown that utilizing this technique can provide information on short-lived muonium analogues of hydride chemistry.

Muon spectroscopy or μ SR uses muon spin to investigate (usually) solid state structures, providing new and often unique insights into the fundamental physical and chemical processes in materials.¹⁷⁸ The term was first coined by Crowe, Portis and Yamazaki in 1984, providing the following definition:

' μ SR stands for Muon Spin Relaxation, Rotation, Resonance, Research, or

what have you. The intention of the mnemonic acronym is to draw attention to the analogy with NMR and ESR, the range of whose applications is well known. Any study of the interactions of the muon spin by virtue of the asymmetric decay is considered μ SR, but this definition is not intended to exclude any peripherally related phenomena, especially if relevant to the use of the muon's magnetic moment as a delicate probe of matter.¹⁷⁹

Muons are fundamental subatomic particles 207 times heavier than an electron.¹⁸⁰ Once implanted in the sample they decay and can form a variety of chemical species. One of these is muonium (μ^+e^- or Mu), which might be regarded as a light isotope of hydrogen in which muon has retained the electron acquired in its path of flight. It can add to unsaturated centres or empty orbitals and form a muoniated radical species, aiding in characterisation of the chemical environment they reside in. Since these particles are remarkably sensitive to static and dynamic microscopic magnetic fields, it is possible to probe structural, magnetic and electronic properties of materials under investigation.

Currently μ SR is predominantly employed to study magnets, superconductors, semiconductors and insulators. Until now, application of muon spectroscopy to organometallic systems has been confined to ferrocene.¹⁸¹ However, very recently the author and co-workers have carried out exploratory studies on two [Fe-Fe]-hydrogenase subsite models in order to probe the reactions of muons with these systems on the nano second time scale (Figure 85).

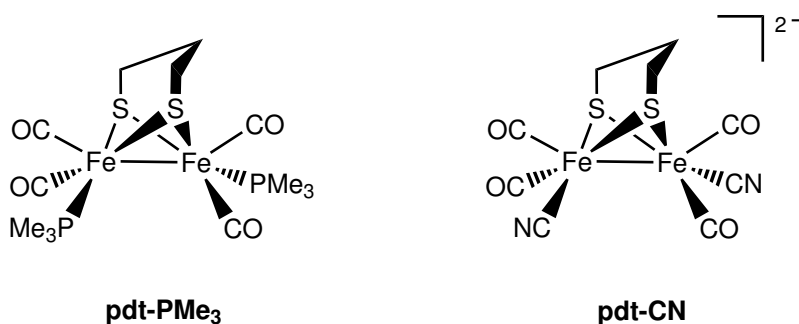


Figure 85: Complexes investigated by muon spectroscopy

Introduction of Mu to diiron subsite models can be viewed as analogues to a simultaneous addition of a proton and an electron to the complex. Experiments on solid state samples of **pdt-PMe₃** and **pdt-CN** have been carried out using EMU and HIFI instruments at the ISIS pulsed muon facility at the Rutherford Appleton Laboratory (RAL). These experiments have successfully confirmed the presence of paramagnetic species in diiron complexes upon addition of muonium.

In a typical experiment, spin-polarised muons are generated by collisions between the proton beam and a thin carbon target. Positive muons are then implanted in a sample, where it can acquire an electron to form muonium and chemically bind to a molecule. The experimental output is the evolution of the muon-polarisation with time, which is analogous to spin relaxation in conventional magnetic resonance techniques. The types of radicals formed and their hyperfine coupling constants can be deduced from repolarisation curves.¹⁸² These are plots of the asymmetry as a function of the applied field.

The repolarisation curves of **pdt-PMe₃** are characterised by a strong recovery at *ca* 100 G (Figure 86, left) and a weaker recovery at higher fields. On the basis of theoretical simulations the former is associated with a radical formation directly at the iron centres while the latter is speculated to arise from the S–Mu radical (Figure 87). Determining the precise muon binding sites is of direct interest to paramagnetic hydride intermediates and to the role of sulfur in mediating proton transfer to metal sites.⁹⁶

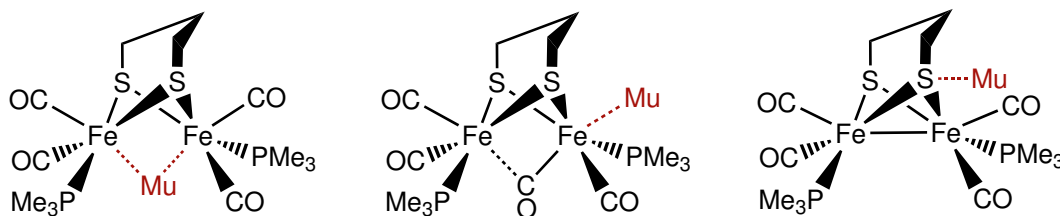


Figure 87: Some of the potential muon binding sites for **pdt-PMe₃**

The recovery in **pdt-CN** at 300 K occurs at a well-defined field when compared to the low temperature data (Figure 86, right). At 5 K the signals are extended over a wide

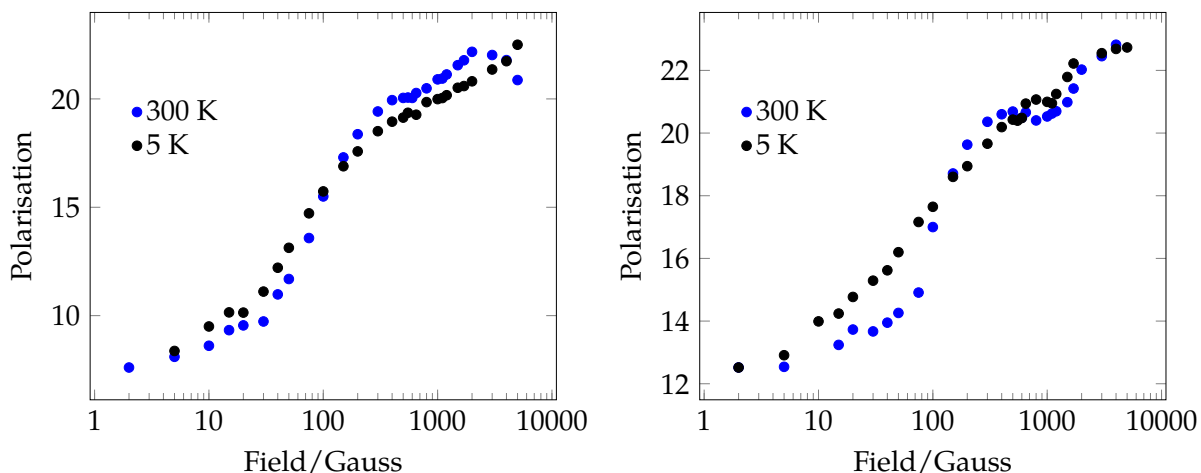


Figure 86: Repolarisation curves of solid state **pdt-PMe₃** (left) and **pdt-CN** (right) field range, potentially signifying the presence of multiple radicals, the origins of which are yet to be identified.

The assignment of the spectral features to precise binding sites on the diiron complexes requires further investigation, with some liquid state experiments pending to be conducted at PSI, Switzerland, later this year. The preliminary data acquired at RAL-ISIS demonstrate the great potential of the muon-based techniques in studying chemically interesting systems and providing unique insights into reaction pathways occurring on nano second time scales. This has the promise to not only aid in detecting transient paramagnetic intermediates in systems relevant to hydrogen production, but also shed light on other organometallic systems rendering muon spectroscopy a more widely used tool.

5.2 Future Avenues

There has been tremendous progress in identifying and modelling various catalytically active states of [Fe-Fe]-hydrogenase active site in both natural and synthetic models. In the last few years diiron complexes with rotated state geometry have emerged, the issue of identifying the central atom the in bridgehead position has been resolved and systems capable of both catalytic hydrogen oxidation and reduction have been designed.

The generation and characterisation of first discrete mixed-valence bridging-hydride species and *super-reduced* states outlined in this work have sparked efforts to obtain crystallographic characterisation of related systems elsewhere. These include successful attempts by Rauchfuss to crystallise a paramagnetic μ -hydride complex, a terminal hydride intermediate with a protonated amine cofactor and a unique system possessing both a bridging and a terminally-bound hydride.^{95,99,111} Extensive stopped-flow UV-vis, IR, spectroelectrochemical and electrochemical measurements have uncovered a linear free energy relationship between the activation energy of protonation and the energy level of the HOMO. Both the steric bulk introduced on the dithiolate bridgehead and the electron-donating abilities of the co-ligands were found to have a profound effect on the reactivity of these systems. This can serve as a tool in designing better catalytic systems, providing some measure of control over electronic and steric properties and reactivity of the structural and functional analogues of the [Fe–Fe]-hydrogenase.

Despite the latest breakthroughs there are still many areas of hydrogenase chemistry that demand attention. Hydrides in biological cycle of hydrogen production are yet to be identified and a question whether the \mathbf{H}_{sred} state is on the catalytic pathway remains open as is its exact structure. Thus, isolation of the *super-reduced* state in synthetic models is of great importance.

Another difficulty is obtaining rotated state geometries and retaining them throughout the catalytic cycles, which highlights the need to emulate the steric shielding of the active site that is naturally provided by the protein. Addition of an outer coordination sphere capable of hydrogen bonding to the diiron dithiolates might solve the issue, stabilising these states and highly sensitive cyanide coligands. The lack of cyanide-containing subsite models also remains one of the great concerns and challenges.

The chemistry of mixed-valence models for the active site of [Fe–Fe]-hydrogenase is rapidly evolving. New, better, more robust and more active catalysts for H_2 transduction are being designed ever year. The efforts are focused on equipping chemists with the tools necessary for providing control over chemical and steric properties of these systems. These data presented here has the potential to guide further efforts to understand the

intricate chemistry of hydrogenases and bring the future of hydrogen economy one step closer.

References

- (1) *Climate Change 2013: The Physical Science Basis*, ed. T. F. Stocker, D. Qin, G.-K. Plattner, M. M. Tignor, S. K. Allen, J. Boschung, A. Nauels, Y. Xia, V. Bex and P. M. Midgley, Cambridge University Press, Cambridge, United Kingdom and New York, 2013.
- (2) *Special Report on Renewable Energy Sources and Climate Change Mitigation*, ed. O. Edenhofer, R. Pichs-Madruga, Y. Sokona, K. Seyboth, P. Matschoss, S. Kadner, T. Zwickel, P. Eickemeier, G. Hansen, S. Schlömer and C. von Stechow, Cambridge University Press, Cambridge, United Kingdom and New York, 2011, p. 10.
- (3) *BP Statistical Review of World Energy*, tech. rep., BP, 2013.
- (4) S. Shafiee and E. Topal, *Energy Policy*, 2009, **37**, 181–189.
- (5) *2010 Survey of Energy Resources*, tech. rep., World Energy Council, 2010.
- (6) N. S. Lewis and D. G. Nocera, *Proc. Natl. Acad. Sci. USA*, 2006, **103**, 15729–15735.
- (7) T. R. Cook, D. K. Dogutan, S. Y. Reece, Y. Surendranath, T. S. Teets and D. G. Nocera, *Chem. Rev.*, 2010, **110**, 6474–6502.
- (8) O. Morton, *Nature*, 2006, **443**, 19–22.
- (9) L. R. Webster, S. K. Ibrahim, J. A. Wright and C. J. Pickett, *Chem. Eur. J.*, 2012, **18**, 11798–11803.
- (10) P. Chenevier, L. Mugerli, S. Darbe, L. Darchy, S. DiManno, P. D. Tran, F. Valentino, M. Iannello, A. Volbeda, C. Cavazza and V. Artero, *C. R. Chim.*, 2013, **16**, 491–505.

- (11) C. Madden, M. D. Vaughn, I. Díez-Perez, K. A. Brown, P. W. King, D. Gust, A. L. Moore and T. A. Moore, *J. Am. Chem. Soc.*, 2012, **134**, 1577–1582.
- (12) T. W. Woolerton, S. Sheard, Y. S. Chaudhary and F. A. Armstrong, *Energy Environ. Sci.*, 2012, **5**, 7470–7490.
- (13) F. A. Armstrong, *Curr. Opin. Chem. Biol.*, 2004, **8**, 133–140.
- (14) P. M. Vignais and B. Billoud, *Chem. Rev.*, 2007, **107**, 4206–4272.
- (15) R. K. Thauer, A. R. Klein and G. C. Hartmann, *Chem. Rev.*, 1996, **96**, 3031–3042.
- (16) R. K. T. Seigo Shima, *Chem. Rec.*, 2007, **7**, 37–46.
- (17) T. Hiromoto, K. Ataka, O. Pilak, S. Vogt, M. S. Stagni, W. Meyer-Klaucke, E. Warkentin, R. K. Thauer, S. Shima and U. Ermler, *FEBS Lett.*, 2009, **583**, 585–590.
- (18) K. A. Vincent, A. Parkin and F. A. Armstrong, *Chem. Rev.*, 2007, **107**, 4366–4413.
- (19) M. W. Adams, *Biochim. Biophys. Acta*, 1990, **1020**, 115–145.
- (20) M. Frey, *ChemBioChem*, 2002, **3**, 153–160.
- (21) T. Kramer, M. Kampa, W. Lubitz, M. van Gestel and F. Neese, *ChemBioChem*, 2013, **14**, 1898–1905.
- (22) J. W. Peters, W. N. Lanzilotta, B. J. Lemon and L. C. Seefeldt, *Science*, 1998, **282**, 1853–1858.
- (23) Y. Nicolet, C. Piras, P. Legrand, C. E. Hatchikian and J. C. Fontecilla-Camps, *Structure*, 1999, **7**, 13–23.
- (24) J. C. Fontecilla-Camps, A. Volbeda, C. Cavazza and Y. Nicolet, *Chem. Rev.*, 2007, **107**, 4273–4303.
- (25) B. Bennett, B. J. Lemon and J. W. Peters, *Biochemistry*, 2000, **39**, 7455–7460.
- (26) S. T. Stripp, G. Goldet, C. Brandmayr, O. Sanganas, K. A. Vincent, M. Haumann, F. A. Armstrong and T. Happe, *Proc. Natl. Acad. Sci. USA*, 2009, **106**, 17331–17336.

- (27) A. Volbeda, L. Martin, C. Cavazza, M. Matho, B. W. Faber, W. Roseboom, S. P. J. Albracht, E. Garcin, M. Rousset and J. C. Fontecilla-Camps, *J. Biol. Inorg. Chem.*, 2005, **10**, 239–249.
- (28) D. Sehnal, R. S. Vereckova, K. Berka, L. Pravda, V. Navratilova, P. Banas, C. M. Ionescu, M. Otyepka and J. Koca, *Cheminformatics*, 2013, **5**, 39.
- (29) P.-P. Liebgott, A. L. de Lacey, B. Burlat, L. Cournac, P. Richaud, M. Brugna, V. M. Fernandez, B. Guigliarelli, M. Rousset, C. Leger and S. Dementin, *J. Am. Chem. Soc.*, 2011, **133**, 986–997.
- (30) M.-E. Pandelia, V. Fourmond, P. Tron-Infossi, E. Lojou, P. Bertrand, C. Léger, M.-T. Giudici-Orticoni and W. Lubitz, *J. Am. Chem. Soc.*, 2010, **132**, 6991–7004.
- (31) M. Stephenson and L. H. Stickland, *Biochem. J.*, 1931, **25**, 205–214.
- (32) D. W. Mulder, E. S. Boyd, R. Sarma, R. K. Lange, J. A. Endrizzi, J. B. Broderick and J. W. Peters, *Nature*, 2010, **465**, 248–252.
- (33) M. L. Singleton, N. Bhuvanesh, J. H. Reibenspies and M. Y. Darensbourg, *Angew. Chem. Int. Ed.*, 2008, **47**, 9492–9495.
- (34) A. S. Pandey, T. V. Harris, L. J. Giles, J. W. Peters and R. K. Szilagyi, *J. Am. Chem. Soc.*, 2008, **130**, 4533–4540.
- (35) A. Silakov, B. Wenk, E. Reijerse and W. Lubitz, *Phys. Chem. Chem. Phys.*, 2009, **11**, 6592–6599.
- (36) Ö. F. Erdem, L. Schwartz, M. Stein, A. Silakov, S. Kaur-Ghymaan, P. Huang, S. Ott, E. J. Reijerse and W. Lubitz, *Angew. Chem. Int. Ed.*, 2011, **50**, 1439–1443.
- (37) U. Ryde, C. Greco and L. De Gioia, *J. Am. Chem. Soc.*, 2010, **132**, 4512–4513.
- (38) G. Berggren, A. Adamska, C. Lambertz, T. R. Simmons, J. Esselborn, M. Atta, S. Gambarelli, J.-M. Mouesca, E. Reijerse, W. Lubitz, T. Happe, V. Artero and M. Fontecave, *Nature*, 2013, **499**, 66–69.

- (39) J. Esselborn, C. Lambertz, A. Adamska-Venkatesh, T. Simmons, G. Berggren, J. Noth, J. Siebel, A. Hemschemeier, V. Artero, E. Reijerse, M. Fontecave, W. Lubitz and T. Happe, *Nat. Chem. Biol.*, 2013, **9**, 607–609.
- (40) W. Lubitz, E. Reijerse and M. van Gestel, *Chem. Rev.*, 2007, **107**, 4331–4365.
- (41) A. Adamska, A. Silakov, C. Lambertz, O. Rüdiger, T. Happe, E. Reijerse and W. Lubitz, *Angew. Chem. Int. Ed.*, 2012, **51**, 11458–11462.
- (42) W. Roseboom, A. L. D. Lacey, V. M. Fernandez, E. C. Hatchikian and S. P. J. Albracht, *J. Biol. Inorg. Chem.*, 2006, **11**, 102–118.
- (43) D. W. Mulder, M. W. Ratzloff, E. M. Shepard, A. S. Byer, S. M. Noone, J. W. Peters, J. B. Broderick and P. W. King, *J. Am. Chem. Soc.*, 2013, **135**, 6921–6929.
- (44) B. J. Lemon and J. W. Peters, *Biochemistry*, 1999, **38**, 12969–12973.
- (45) A. Silakov, C. Kamp, E. Reijerse, T. Happe and W. Lubitz, *Biochemistry*, 2009, **48**, 7780–7786.
- (46) M. W. W. Adams and E. I. Stiefel, *Curr. Opin. Chem. Biol.*, 2000, **4**, 214–220.
- (47) G. D. Cody, N. Z. Boctor, T. R. Filley, R. M. Hazen, J. H. Scott, A. Sharma and J. Yoder, Hatten S., *Science*, 2000, **289**, 1337–1340.
- (48) M. Y. Darensbourg, E. J. Lyon, X. Zhao and I. P. Georgakaki, *Proc. Natl. Acad. Sci. USA*, 2003, **100**, 3683–3688.
- (49) H. von Reihlen, A. Gruhl and G. von Hessling, *Liebigs Ann. Chem.*, 1929, **472**, 268–287.
- (50) F. A. Cotton and G. Wilkinson, *Advanced Inorganic Chemistry, Fifth Edition*, John Wiley & Sons, 1988.
- (51) L. F. Dahl, W. R. Costello and R. B. King, *J. Am. Chem. Soc.*, 1968, **90**, 5422–5429.
- (52) L. F. Dahl and C.-H. Wei, *Inorg. Chem.*, 1963, **2**, 328–333.
- (53) M. Weller, T. Overton, J. Rourke and F. Armstrong, *Inorganic Chemistry*, Oxford University Press, 6th edn., 2014.

- (54) W. Hieber and P. Spacu, *Anorg. Allg. Chem.*, 1937, **233**, 353–364.
- (55) K. Fauvel, R. Mathieu and R. Poilblanc, *Inorg. Chem.*, 1976, **15**, 976–978.
- (56) D. Seyferth and R. S. Henderson, *J. Am. Chem. Soc.*, 1979, **101**, 508–509.
- (57) A. Shaver, P. J. Fitzpatrick, K. Steliou and I. S. Butler, *J. Am. Chem. Soc.*, 1979, **101**, 1313–1315.
- (58) S. Lotz, P. H. V. Rooyen and M. M. V. Dyk, *Organometallics*, 1987, **6**, 499–505.
- (59) X. Wu, K. S. Bose, E. Sinn and B. A. Averill, *Organometallics*, 1989, **8**, 251–253.
- (60) D. Seyferth, G. B. Womack, M. K. Gallagher, M. Cowie, B. W. Hames, J. P. Fackler and A. M. Mazany, *Organometallics*, 1987, **6**, 283–294.
- (61) C. Tard and C. J. Pickett, *Chem. Rev.*, 2009, **109**, 2245–2274.
- (62) E. J. Lyon, I. P. Georgakaki, J. H. Reibenspies and M. Y. Darensbourg, *Angew. Chem. Int. Ed.*, 1999, **38**, 3178–3180.
- (63) A. Le Cloirec, S. P. Best, S. Borg, S. C. Davies, D. J. Evans, D. L. Hughes and C. J. Pickett, *Chem. Commun.*, 1999, **35**, 2285–2286.
- (64) H. Li and T. B. Rauchfuss, *J. Am. Chem. Soc.*, 2002, **124**, 726–727.
- (65) S. Ezzaher, J.-F. Capon, F. Gloaguen, F. Y. Pétilon, P. Schollhammer, J. Talarmin and N. Kervarec, *Inorg. Chem.*, 2009, **48**, 2–4.
- (66) J. D. Lawrence, H. Li, T. B. Rauchfuss, M. Bernard and M.-M. Rohmer, *Angew. Chem. Int. Ed.*, 2001, **40**, 1768–1771.
- (67) A. K. Justice, G. Zampella, L. De Gioia and T. B. Rauchfuss, *Chem. Commun.*, 2007, **43**, 2019–2021.
- (68) T. Liu and M. Y. Darensbourg, *J. Am. Chem. Soc.*, 2007, **129**, 7008–7009.
- (69) C.-H. Hsieh, Ö. F. Erdem, S. D. Harman, M. L. Singleton, E. Reijerse, W. Lubitz, C. V. Popescu, J. H. Reibenspies, S. M. Brothers, M. B. Hall and M. Y. Darensbourg, *J. Am. Chem. Soc.*, 2012, **134**, 13089–13102.

- (70) C. Tard, X. Liu, S. K. Ibrahim, L. De Gioia, S. C. Davies, X. Yang, L.-S. Wang, G. Sawers and C. J. Pickett, *Nature*, 2005, **433**, 610–613.
- (71) J. M. Camara and T. B. Rauchfuss, *Nat. Chem.*, 2012, **4**, 26–30.
- (72) M. Razavet, S. J. Borg, S. J. George, S. P. Best, S. A. Fairhurst and C. J. Pickett, *Chem. Commun.*, 2002, **36**, 700–701.
- (73) A. K. Justice, T. B. Rauchfuss and S. R. Wilson, *Angew. Chem. Int. Ed.*, 2007, **46**, 6152–6154.
- (74) A. K. Justice, L. De Gioia, M. J. Nilges, T. B. Rauchfuss, S. R. Wilson and G. Zampella, *Inorg. Chem.*, 2008, **47**, 7405–7414.
- (75) J. M. Camara and T. B. Rauchfuss, *J. Am. Chem. Soc.*, 2011, **133**, 8098–8101.
- (76) M. Karnahl, S. Tschierlei, Ö. F. Erdem, S. Pullen, M.-P. Santoni, E. J. Reijerse, W. Lubitz and S. Ott, *Dalton Trans.*, 2012, **41**, 12468–12477.
- (77) M. Razavet, S. C. Davies, D. L. Hughes, J. E. Barclay, D. J. Evans, S. A. Fairhurst, X. Liu and C. J. Pickett, *Dalton Trans.*, 2003, **32**, 586–595.
- (78) J. D. Lawrence, H. Li and T. B. Rauchfuss, *Chem. Commun.*, 2001, 1482–1483.
- (79) J. Windhager, M. Rudolph, S. Bräutigam, H. Görls and W. Weigand, *Eur. J. Inorg. Chem.*, 2007, 2748–2760.
- (80) M.-Q. Hu, C.-B. Ma, Y.-T. Si, C.-N. Chen and Q.-T. Liu, *J. Inorg. Biochem.*, 2007, **101**, 1370–1375.
- (81) L.-C. Song, Z.-Y. Yang, Y.-J. Hua, H.-T. Wang, Y. Liu and Q.-M. Hu, *Organometallics*, 2007, **26**, 2106–2110.
- (82) K. Charreteur, J.-F. Capon, F. Gloaguen, F. Y. Pétilion, P. Schollhammer and J. Talarmin, *Eur. J. Inorg. Chem.*, 2011, 1038–1042.
- (83) F. Gloaguen and T. B. Rauchfuss, *Chem. Soc. Rev.*, 2009, **38**, 100–108.
- (84) F. Gloaguen, J. D. Lawrence, T. B. Rauchfuss, M. Bernard and M.-M. Rohmer, *Inorg. Chem.*, 2002, **41**, 6573–6582.

- (85) F. Wang, M. Wang, X. Liu, K. Jin, W. Donga and L. Sun, *Dalton Trans.*, 2007, 3812–3819.
- (86) D. Morvan, J.-F. Capon, F. Gloaguen, A. L. Goff, M. Marchivie, F. Michaud, P. Schollhammer, J. Talarmin and J.-J. Yaouanc, *Organometallics*, 2007, **26**, 2042–2052.
- (87) B. E. Barton, G. Zampella, A. K. Justice, L. De Gioia, T. B. Rauchfuss and S. R. Wilson, *Dalton Trans.*, 2010, **39**, 3011–3019.
- (88) P.-Y. Orain, J.-F. Capon, F. Gloaguen, F. Y. Pétilion, P. Schollhammer and J. Talarmin, *Inorg. Chem.*, 2010, **49**, 5003–5008.
- (89) S. Ghosh, G. Hogarth, N. Hollingsworth, K. B. Holt, I. Richards, M. G. Richmond, B. E. Sancheza and D. Unwina, *Dalton Trans.*, 2013, **42**, 6775–6792.
- (90) S. L. Matthews and D. M. Heinekey, *Inorg. Chem.*, 2010, **49**, 9746–9748.
- (91) B. E. Barton, C. M. Whaley, T. B. Rauchfuss and D. L. Gray, *J. Am. Chem. Soc.*, 2009, **131**, 6942–6943.
- (92) B. M. Hoffman, D. Lukoyanov, D. R. Dean and L. C. Seefeldt, *Acc. Chem. Res.*, 2013, **46**, 587–595.
- (93) S. Tschierlei, S. Ott and R. Lomoth, *Energy Env. Sci.*, 2011, **4**, 2340–2352.
- (94) J. I. van der Vlugt, T. B. Rauchfuss, C. M. Whaley and S. R. Wilson, *J. Am. Chem. Soc.*, 2005, **127**, 16012–16013.
- (95) M. E. Carroll, B. E. Barton, T. B. Rauchfuss and P. J. Carroll, *J. Am. Chem. Soc.*, 2012, **134**, 18843–18852.
- (96) R. Zaffaroni, T. B. Rauchfuss, D. L. Gray, L. De Gioia and G. Zampella, *J. Am. Chem. Soc.*, 2012, **134**, 19260–19269.
- (97) S. Ezzaher, J.-F. Capon, F. Gloaguen, F. Y. Pétilion, P. Schollhammer and J. Talarmin, *Inorg. Chem.*, 2007, **46**, 3426–3428.
- (98) B. E. Barton, M. T. Olsen and T. B. Rauchfuss, *J. Am. Chem. Soc.*, 2008, **130**, 16834–16835.

- (99) W. Wang, T. B. Rauchfuss and L. Zhu, *J. Am. Chem. Soc.*, 2014, **136**, 5773–5782.
- (100) J. A. Wright and C. J. Pickett, *Chem. Commun.*, 2009, **45**, 5719–5721.
- (101) A. Jablonskytė, J. A. Wright and C. J. Pickett, *Dalton Trans.*, 2010, **39**, 3026–3034.
- (102) C. Liu, J. N. T. Peck, J. A. Wright, C. J. Pickett and M. B. Hall, *Eur. J. Inorg. Chem.*, 2011, 1080–1093.
- (103) G. A. N. Felton, A. K. Vannucci, J. Chen, L. T. Lockett, N. Okumura, B. J. Petro, U. I. Zakai, D. H. Evans, R. S. Glass and D. L. Lichtenberger, *J. Am. Chem. Soc.*, 2007, **129**, 12521–12530.
- (104) S. Ghosh, G. Hogarth, N. Hollingsworth, K. B. Holt, S. E. Kabir and B. E. Sanchez, *Chem. Commun.*, 2014, **50**, 945–947.
- (105) L. Sun, B. Åkermark and S. Ott, *Coord. Chem. Rev.*, 2005, **249**, 1653–1663.
- (106) J. Ekström, M. Abrahamsson, C. Olson, J. Bergquist, F. B. Kaynak, L. Eriksson, L. Sun, H.-C. Becker, B. Åkermark, L. Hammarström and S. Ott, *Dalton Trans.*, 2006, 4599–4606.
- (107) L.-C. Song, M.-Y. Tang, S.-Z. Mei, J.-H. Huang and Q.-M. Hu, *Organometallics*, 2007, **26**, 1575–1577.
- (108) J.-F. Capon, F. Gloaguen, P. Schollhammer and J. Talarmin, *J. Electroanal. Chem.*, 2006, **595**, 47–52.
- (109) R. J. Wright, W. Zhang, X. Yang, M. Fasuloa and T. D. Tilley, *Dalton Trans.*, 2012, **41**, 73–82.
- (110) S. Borg, T. Behrsing, S. P. Best, M. Razavet, X. Liu and C. J. Pickett, *J. Am. Chem. Soc.*, 2004, **126**, 16988–16999.
- (111) W. Wang, M. J. Nilges, T. B. Rauchfuss and M. Stein, *J. Am. Chem. Soc.*, 2013, **135**, 3633–3639.
- (112) M. T. Olsen, B. E. Barton and T. B. Rauchfuss, *Inorg. Chem.*, 2009, **48**, 7507–7509.
- (113) N. Wang, M. Wang, Y. Wang, D. Zheng, H. Han, M. S. G. Ahlquist and L. Sun, *J. Am. Chem. Soc.*, 2013, **135**, 1688–13691.

- (114) S. J. George, Z. Cui, M. Razavet and C. J. Pickett, *Chem. Eur. J.*, 2002, **8**, 4037–4046.
- (115) M. Razavet, S. C. Davies, D. L. Hughes and C. J. Pickett, *Chem. Commun.*, 2001, **37**, 847–848.
- (116) V. K. Aggarwal, I. W. Davies, R. Franklin, J. Maddock, M. F. Mahon and K. C. Molloy, *J. Chem. Soc. Perkin Trans. 1*, 1994, **17**, 2363–2368.
- (117) E. L. Eliel and R. O. Hutchins, *J. Am. Chem. Soc.*, 1969, **91**, 2703–2715.
- (118) S. Mirilashvili, N. Chasid-Rubinstein and A. Albeck, *Eur. J. Org. Chem*, 2008, 3461–3464.
- (119) M. S. Newman and J. Harper, Robert J., *J. Am. Chem. Soc.*, 1958, **80**, 6350–6355.
- (120) E. J. Lyon, I. P. Georgakaki, J. H. Reibenspies and M. Y. Darensbourg, *J. Am. Chem. Soc.*, 2001, **123**, 3268–3278.
- (121) X. Zhao, I. P. Georgakaki, M. L. Miller, R. Mejia-Rodriguez, C.-Y. Chiang and M. Y. Darensbourg, *Inorg. Chem.*, 2002, **41**, 3917–3928.
- (122) P. Li, M. Wang, C. He, G. Li, X. Liu, C. Chen, B. Åkermark and L. Sun, *Eur. J. Inorg. Chem.*, 2005, 2506–2513.
- (123) C. Kolomyjec, J. Whelan and B. Bosnich, *Inorg. Chem.*, 1983, **22**, 2343–2345.
- (124) A. Maisonnat, J. Devillers and R. Poilblanc, *Inorg. Chem.*, 1987, **26**, 1502–1507.
- (125) C. A. Ghilardi, S. Midollini, A. Orlandini and A. Vacca, *J. Chem. Soc. Dalton Trans.*, 1993, 3117–3121.
- (126) C. A. Ghilardi, S. Midollini, A. Orlandini and G. Scapacci, *Inorg. Chim. Acta*, 1997, **266**, 113–116.
- (127) S. Ibrahim, P. M. Woi, Y. Aliasb and C. J. Pickett, *Chem. Commun.*, 2010, **46**, 8189–8191.
- (128) S. K. Ibrahim, X. Liu, C. Tard and C. J. Pickett, *Chem. Commun.*, 2007, 1535–1537.
- (129) X. Zhao, I. P. Georgakaki, M. L. Miller, J. C. Yarbrough and M. Y. Darensbourg, *J. Am. Chem. Soc.*, 2001, **123**, 9710–9711.

- (130) M. T. Olsen, M. Brushci, L. De Gioia, T. B. Rauchfuss and S. R. Wilson, *J. Am. Chem. Soc.*, 2008, **130**, 12021–12030.
- (131) J. W. Tye, M. Y. Darensbourg and M. B. Hall, *Inorg. Chem.*, 2006, **45**, 1552–1559.
- (132) L.-C. Song, Z.-Y. Yang, H.-Z. Bian and Q.-M. Hu, *Organometallics*, 2004, **23**, 3082–3084.
- (133) T. R. Simmons, Unpublished work.
- (134) M. L. Singleton, R. M. Jenkins, C. L. Klemashevich and M. Y. Darensbourg, *C. R. Chimie*, 2008, **11**, 861–874.
- (135) A. Jablonskytė, J. A. Wright and C. J. Pickett, *Eur. J. Inorg. Chem.*, 2011, 1033–1037.
- (136) *CrystalClear-SM Expert*, Rigaku Corporation, Tokyo, Japan, 2012.
- (137) *CrysAlisPro*, Agilent Technologies, Yarnton, UK, 2012.
- (138) A. Altomare, G. Cascarano, C. Giacovazzo and Guagliardi, *J. Appl. Cryst.*, 1994, **27**, 435.
- (139) A. Altomare, M. C. Burla, M. Camalli, G. L. Cascarano, C. Giacovazzo, A. Guagliardi, A. G. G. Moliterni, G. Polidori and R. Spagna, *J. Appl. Cryst.*, 1999, **32**, 115–119.
- (140) G. M. Sheldrick, *Acta Crystallogr., Sect. A*, 2008, **64**, 112–122.
- (141) B. E. Barton and T. B. Rauchfuss, *Inorg. Chem.*, 2008, **47**, 2261–2263.
- (142) J. A. Wright, L. Webster, A. Jablonskytė, P. M. Woi, S. K. Ibrahim and C. J. Pickett, *Faraday Discuss.*, 2011, **148**, 359–371.
- (143) J. D. Tolland and R. N. F. Thorneley, *Biochemistry*, 2005, **44**, 9520–9527.
- (144) S. J. George, S. Kurkin, R. N. F. Thorneley and S. P. J. Albracht, *Biochemistry*, 2004, **43**, 6808–6819.
- (145) R. A. Henderson, S. K. Ibrahim, K. E. Oglieve and C. J. Pickett, *J. Chem. Soc., Chem. Commun.*, 1995, 1571–1572.
- (146) S. Kurkin, S. J. George, R. N. F. Thorneley and S. P. J. Albracht, *Biochemistry*, 2004, **43**, 6820–6831.

- (147) S. J. George, Z. Cui, M. Razavet and C. J. Pickett, *Chem. Eur. J.*, 2002, **8**, 4037–4046.
- (148) A. J. Bard and L. R. Faulkner, *Electrochemical Methods: Fundamentals and Applications*, 2nd Ed. John Wiley & Sons, Inc., 2001.
- (149) M. B. Hall, R. F. Fenske and L. F. Dahl, *Inorg. Chem.*, 1975, **14**, 3103–3117.
- (150) E. L. Andersen, T. P. Fehlner, A. E. Foti and D. R. Salahub, *J. Am. Chem. Soc.*, 1980, **102**, 7422–7429.
- (151) B. Walther, H. Hartung, J. Reinhold, P. G. Jones, C. Mealli, H. C. Bottcher, U. Baumeister, A. Krug and A. Mockelt, *Organometallics*, 1992, **11**, 1542–1549.
- (152) A. C. Sarapu and R. F. Fenske, *Inorg. Chem.*, 1975, **14**, 247–253.
- (153) G. Zampella, P. Fantucci and L. D. Gioia, *J. Am. Chem. Soc.*, 2009, **131**, 10909–10917.
- (154) P.-Y. Orain, J.-F. Capon, F. Gloaguen, F. Y. Pétilion, P. Schollhammer and J. Talarmin, *Inorg. Chem.*, 2010, **49**, 5003–5008.
- (155) S. J. George, *Fit_3D*, 2014, http://abex.lbl.gov/~simon/Instrument_Development.html.
- (156) M. J. Frisch, G. W. Trucks, H. B. Schlegel, G. E. Scuseria, M. A. Robb, J. R. Cheeseman, G. Scalmani, V. Barone, B. Mennucci, G. A. Petersson, H. Nakatsuji, M. Caricato, X. Li, H. P. Hratchian, A. F. Izmaylov, J. Bloino, G. Zheng, J. L. Sonnenberg, M. Hada, M. Ehara, K. Toyota, R. Fukuda, J. Hasegawa, M. Ishida, T. Nakajima, Y. Honda, O. Kitao, H. Nakai, T. Vreven, J. A. Montgomery, Jr., J. E. Peralta, F. Ogliaro, M. Bearpark, J. J. Heyd, E. Brothers, K. N. Kudin, V. N. Staroverov, R. Kobayashi, J. Normand, K. Raghavachari, A. Rendell, J. C. Burant, S. S. Iyengar, J. Tomasi, M. Cossi, N. Rega, J. M. Millam, M. Klene, J. E. Knox, J. B. Cross, V. Bakken, C. Adamo, J. Jaramillo, R. Gomperts, R. E. Stratmann, O. Yazyev, A. J. Austin, R. Cammi, C. Pomelli, J. W. Ochterski, R. L. Martin, K. Morokuma, V. G. Zakrzewski, G. A. Voth, P. Salvador, J. J. Dannenberg, S. Dapprich, A. D. Daniels, Ö. Farkas, J. B. Foresman, J. V. Ortiz, J. Cioslowski and D. J. Fox, *Gaussian09 Revision C.01*, Gaussian Inc., Wallingford CT, USA, 2009.

- (157) J. Tao, J. P. Perdew, V. N. Staroverov and E. G. Scuseria, *Phys. Rev. Lett.*, 2003, **91**, 146401–146405.
- (158) P. J. Hay and W. R. Wadt, *J. Chem. Phys.*, 1985, **82**, 270–283.
- (159) P. J. Hay and W. R. Wadt, *J. Chem. Phys.*, 1985, **82**, 284–298.
- (160) M. Couty and M. B. Hall, *J. Comput. Chem.*, 1996, **17**, 1359–1370.
- (161) C. E. Check, T. O. Faust, J. M. Bailey, B. J. Wright, T. M. Gilbert and L. S. Sunderlin, *J. Phys. Chem. A*, 2001, **105**, 8111–8116.
- (162) J. A. Wright, P. J. Turrell and C. J. Pickett, *Organometallics*, 2010, **29**, 6146–6156.
- (163) P. Amara, J.-M. Mouesca, A. Volbeda and J. C. Fontecilla-Camps, *Inorg. Chem.*, 2011, **50**, 1868–1878.
- (164) W. Dong, M. Wang, X. Liu, K. Jin, G. Li, F. Wang and L. Sun, *Chem. Commun.*, 2006, **40**, 305–307.
- (165) G. Zampella, C. Greco, P. Fantucci and L. D. Gioia, *Inorg. Chem.*, 2006, **45**, 4109–4118.
- (166) A. Jablonskytė, J. A. Wright, S. A. Fairhurst, J. N. T. Peck, S. K. Ibrahim, V. S. Oganessian and C. J. Pickett, *J. Am. Chem. Soc.*, 2011, **133**, 18606–18609.
- (167) J. A. Weil and J. R. Bolton, *Electron Paramagnetic Resonance: Elementary Theory and Practical Applications, 2nd Ed.* John Wiley & Sons, Inc., 2007.
- (168) N. G. Connelly and W. E. Geiger, *Chem. Rev.*, 1996, **96**, 877–910.
- (169) W. Kaim and J. Fiedler, *Chem. Soc. Rev.*, 2009, **38**, 3373–3382.
- (170) S. P. Best, *Coord. Chem. Rev.*, 2005, **249**, 1536–1554.
- (171) D. Sholl and J. A. Steckel, *Density Functional Theory: A Practical Introduction*, John Wiley & Sons, 2011.
- (172) T. R. Simmons, Ph.D. Thesis, School of Chemistry, UEA, 2011.
- (173) P. N. Keizer, P. J. Krusic, J. R. Morton and K. F. Preston, *J. Am. Chem. Soc.*, 1991, **113**, 5454–5456.

- (174) T. R. Dugan, E. Bill, K. C. MacLeod, W. W. Brennessel and P. L. Holland, *Inorg. Chem.*, 2014, **53**, 2370–2380.
- (175) M. Plois, W. Hujo, S. Grimme, C. Schwickert, E. Bill, B. Bruin, R. Pöttgen and R. Wolf, *Angew. Chem. Int. Ed.*, 2013, **52**, 1314–1318.
- (176) R. A. Kinney, C. T. Saouma, J. C. Peters and B. M. Hoffman, *J. Am. Chem. Soc.*, 2012, **134**, 12637–12647.
- (177) R. Y. Igarashi, M. Laryukhin, P. C. D. Santos, H.-I. Lee, D. R. Dean, L. C. Seefeldt and B. M. Hoffman, *J. Am. Chem. Soc.*, 2005, **127**, 6231–6241.
- (178) *Muon Science: Muons in Physics, Chemistry and Materials*, ed. S. L. Lee, R. Cywinski and S. Kilcoyne, The Scottish Universities Summer School in Physics, 1999.
- (179) K. M. Crowe, A. M. Portis and T. Yamazaki, *Muon SR Newsletter*, 1984, **29**, 1473–1607.
- (180) J. Caparthy, *Muons: New Research*, Nova Science Publishers, 2005.
- (181) U. A. Jayasooriya, R. Grinter, P. L. Hubbard, G. M. Aston, J. A. S. G. A. Hopkins, L. Camus, I. D. Reid, S. P. Cottrell and S. F. J. Cox, *Chem. Eur. J.*, 2007, **13**, 2266–2276.
- (182) *Fluxional Organometallic and Coordination Compounds*, ed. M. Gielen, R. Willem and B. Wrackmeyer, John Wiley & Sons, 2005.